

# Peptide-conjugated dextran hybrids: Generation of a versatile module for cytosolic delivery of biomolecular cargoes



TECHNISCHE  
UNIVERSITÄT  
DARMSTADT

Vom Fachbereich Chemie  
der Technischen Universität Darmstadt

zur Erlangung des Grades  
Doctor rerum naturalium (Dr. rer. nat.)

Dissertation

von

Bastian Becker, M.Sc.  
aus Lindenfels

Erstgutachter: Prof. Dr. Harald Kolmar  
Zweitgutachterin: Prof. Dr. Katja Schmitz

Darmstadt 2021

---

---

Becker, Bastian: Peptide-conjugated dextran hybrids: Generation of a versatile module for cytosolic delivery of biomolecular cargoes.

Darmstadt, Technische Universität Darmstadt,

Jahr der Veröffentlichung der Dissertation auf TUprints: 2021

**Tag der Einreichung:** 29. Juni 2021

**Tag der mündlichen Prüfung:** 25. Oktober 2021

Veröffentlicht unter CC BY-SA 4.0 International

<https://creativecommons.org/licenses/>

---

---

Der experimentelle Teil der vorliegenden Arbeit wurde unter der Leitung von Herrn Prof. Dr. Harald Kolmar am Clemens-Schöpf-Institut für Organische Chemie und Biochemie der Technischen Universität Darmstadt im Zeitraum von Oktober 2016 bis März 2020 angefertigt.

---

### Publications derived from this work:

**B. Becker**, S. Englert, H. Schneider, D. Yanakieva, S. Hofmann, C. Dombrowsky, A. Macarrón Palacios, S. Bitsch, A. Elter, T. Meckel, B. Kugler, A. Schirmacher, O. Avrutina, U. Diederichsen, H. Kolmar, Multivalent dextran hybrids for efficient cytosolic delivery of biomolecular cargoes., *Journal of Peptide Science* **2021**, *27*, e3298.

### Further publications during PhD thesis:

H. Schneider, D. Yanakieva, A. Macarrón, L. Deweid, **B. Becker**, S. Englert, O. Avrutina, H. Kolmar, TRAIL-Inspired Multivalent Dextran Conjugates Efficiently Induce Apoptosis upon DR5 Receptor Clustering., *ChemBioChem* **2019**, *20*, 3006-3012.

H. Schneider, L. Deweid, T. Pirzer, D. Yanakieva, S. Englert, **B. Becker**, O. Avrutina, H. Kolmar, Dextramabs: A Novel Format of Antibody-Drug Conjugates Featuring a Multivalent Polysaccharide Scaffold., *ChemistryOpen* **2019**, *8*, 354-357.

N.E. Juettner, S. Schmelz, A. Kraemer, S. Knapp, **B. Becker**, H. Kolmar, A. Scrima, and H.-L. Fuchsbauer, Structure of a glutamine donor mimicking inhibitory peptide shaped by the catalytic cleft of microbial transglutaminase., *FEBS Journal* **2018**, *285*, 4684-4694.

---

“Nothing compares to the simple pleasure of a bike ride.”  
J. F. Kennedy

---

---

## Table of Contents

---

1	Introduction	1
1.1	The cell membrane	1
1.2	Intracellular delivery of biomacromolecules	3
1.2.1	Basics of endocytosis	3
1.2.2	Delivery strategies	5
1.2.2.1	Cell-penetrating peptides	6
1.2.3	Endosomal escape	8
1.3	Brief success of CPPs and peptides applied in this work	9
1.3.1	Antimicrobial peptide aurein 1.2	10
1.3.2	M-lycotoxin derived peptide L17E	11
1.4	Dextran as versatile scaffold for multimerization of cargo	12
1.5	Chemical and biological conjugation methods: A brief overview	14
1.5.1	Copper-catalyzed and strain-promoted azide-alkyne 1,3-cycloaddition	14
1.5.2	Maleimide chemistry and inverse electron-demand Diels-Alder reaction	15
1.5.3	Microbial transglutaminase	16
1.5.4	Lipoic acid protein ligase A	16
1.6	Mis-splicing correction assay	17
2	Objective	19
3	Results and Discussion	20
3.1	Aurein1.2-mediated cytosolic delivery	20
3.1.1	Design of a multicomponent model conjugate: Trastuzumab-aurein1.2-doxorubicin 1	20
3.1.2	Synthesis of a multicomponent model conjugate	22
3.1.2.1	Synthesis of constituent A: Trastuzumab-LLQG-BCN 2	22
3.1.2.2	Synthesis of constituent B: Ac-Orn(N <sub>3</sub> )-VC-aurein1.2-Lys(maleimide)-NH <sub>2</sub> 3 and constituent B-NC: Ac-Orn(N <sub>3</sub> )-VC-GS-Lys(maleimide)-NH <sub>2</sub> 6	23
3.1.2.3	Synthesis of constituent C: Ac-Cys-Val-Cit-Gly-Dox 4	24
3.1.2.4	Maleimide-thiol conjugation: Synthesis of azide-aurein1.2-doxorubicin 8 and azide-doxorubicin 9	24
3.1.2.5	SPAAC assembly of ultimate conjugates Trastuzumab-aurein1.2-doxorubicin 1 and Trastuzumab-doxorubicin 10	26
3.1.3	Cell viability assay applying Trastuzumab-aurein1.2-doxorubicin 1e and Trastuzumab-doxorubicin 10	29
3.2	M-lycotoxin variant L17E covalently linked to cargo: Protein-L17E fusion	30
3.2.1	Cellular uptake assay	31
3.3	Peptide-dextran hybrids: Multiple copies of Aurein1.2 and L17E on polysaccharide scaffold	31
3.3.1	Dextran modification	31
3.3.1.1	Reductive amination: Synthesis of dextran- <i>N</i> -Boc-cadaverine 13	32
3.3.1.2	Synthesis of maleimide-dextran- <i>N</i> -Boc-cadaverine compounds	33
3.3.1.3	Synthesis of N <sub>3</sub> -dextran-cadaverine compounds	36
3.3.1.4	Synthesis of red-end functionalized N <sub>3</sub> -dextran compounds	39
3.3.2	Aurein1.2-dextran and L17E-dextran hybrids – a comparison	42

3.3.2.1	Maleimide-thiol conjugation I: Synthesis of TAMRA-labeled aurein1.2- and L17E-dextran compounds	43
3.3.2.2	Maleimide-thiol conjugation II: Synthesis of doxorubicin-labeled L17E-dextran	44
3.3.2.3	Cellular uptake assay: Comparison of aurein1.2-dextran and L17E-dextran	45
3.3.3	Potential cytotoxic effect of L17E-dextran module	47
3.3.3.1	CuAAC assembly of L17E-dextran module	42
3.3.3.2	UV/Vis photometric quantification	49
3.3.3.3	Cell viability assay applying L17E-dextran module	51
3.4	L17E-dextran as module for intracellular delivery	52
3.4.1	L17E-dextran mediated intracellular delivery of bioactive PNA	52
3.4.1.1	Maleimide-thiol conjugation: Synthesis of L17E-PNA-dextran	43
3.4.1.2	Mis-splicing correction assay applying L17E-PNA-dextran	43
3.4.2	L17E-dextran mediated protein delivery	54
3.4.2.1	L17E-dextran-eGFP conjugate design	55
3.4.2.2	L17E(4.3)-dextran-eGFP 44 conjugate synthesis	56
3.4.2.3	Cellular uptake assay	57
3.4.2.4	L17E(4.8)-dextran-eGFP 52 conjugate synthesis II	59
3.4.2.5	Cellular uptake assay at 4 °C	60
3.4.3	Site-specific dextran-to-protein conjugation	61
3.4.3.1	LplA <sup>W37V</sup> -mediated site-specific eGFP modification with methyltetrazine	62
3.4.3.2	L17E(4.8)-dextran-eGFP 57 synthesis applying LplA <sup>W37V</sup> mediated site-specific dextran-to-protein conjugation	63
3.4.3.3	Cellular uptake assay	66
4	Tabular summary of generated dextran-based delivery modules	68
5	Summary and Outlook	69
6	Zusammenfassung und Ausblick	72
7	Experimental Part	75
7.1	General	75
7.1.1	Solvents	75
7.1.2	Reagents	75
7.1.3	Buffers and solutions	75
7.1.4	Lyophilization	76
7.1.5	Removal of organic solvents	76
7.2	Characterization	76
7.2.1	High performance liquid chromatography (HPLC)	76
7.2.2	Size exclusion chromatography (SEC)	77
7.2.3	Hydrophobic interaction chromatography (HIC)	77
7.2.4	Mass spectrometry (MS)	77
7.2.5	Nuclear magnetic resonance spectroscopy (NMR)	77
7.2.6	Infrared spectroscopy (IR)	77
7.2.7	UV/Vis spectroscopy	77
7.2.8	Microscopy	77
7.2.9	Fluorescence-activated cell sorting (FACS)	78

7.3	Biological materials and methods	78
7.3.1	Bacterial strains	78
7.3.2	Mammalian cell lines	78
7.3.3	Sodium dodecyl sulfate polyacrylamide gel electrophoresis (SDS-PAGE)	78
7.3.4	eGFP-L17E fusion protein production	78
7.3.5	Transformation of <i>E. coli</i> by electroporation	79
7.3.6	Protein expression in <i>Escherichia coli</i>	79
7.3.7	Protein concentration measurement	80
7.3.8	Data of proteins applied in this work	80
7.3.8.1	eGFP-L17E fusion protein	80
7.3.8.2	Enhanced green fluorescent protein	80
7.3.8.3	Lipoic acid protein ligase A	81
7.3.9	Immobilized metal affinity chromatography (IMAC)	81
7.3.10	Protein A affinity chromatography	82
7.3.11	Cell culture	82
7.3.12	Cellular uptake assay	82
7.3.13	Cell viability assay	82
7.3.14	PNA mis-splicing correction assay	82
7.4	Enzymatic conjugation methods	83
7.4.1	Microbial transglutaminase (mTG) mediated conjugation	83
7.4.2	Lipoic acid protein ligase A (LplA <sup>W37V</sup> ) mediated conjugation	83
7.5	General peptide synthesis	83
7.5.1	Automated peptide synthesis on CEM Liberty blue <sup>®</sup>	83
7.5.2	General procedure for manual SPPS steps	83
7.5.2.1	Loading onto 2-chlorotriyl chloride (2-ctc) resin	83
7.5.2.2	Loading onto Rink amide (RAM) resin	84
7.5.2.3	Fmoc-deprotection	84
7.5.2.4	Coupling step	84
7.5.2.5	Acetylation of the <i>N</i> -terminus	84
7.5.3	Cleavage from solid support	85
7.5.4	Post-cleavage work-up	85
7.6	Synthesis of aurein1.2 based peptides	85
7.6.1	Synthesis of Ac-Orn(N <sub>3</sub> )-VC-aurein1.2-Lys(maleimide)-NH <sub>2</sub> 3	85
7.6.2	Synthesis of Ac-Orn(N <sub>3</sub> )-VC-GS-Lys(maleimide)-NH <sub>2</sub> 6	86
7.6.3	Synthesis of aurein1.2-Cys 33	87
7.7	Synthesis of M-Lycotoxin derived L17E peptides	87
7.7.1	Synthesis of L17E 12	87
7.7.2	Synthesis of L17E-Cys 34	88
7.7.3	Synthesis of L17E-Pra 41	88
7.8	Synthesis of constituent C: Ac-Cys-VC-Gly-Dox 4	89
7.8.1	Synthesis of Ac-Cys( <i>StBu</i> )-VC-Gly 7: SPPS	89
7.8.2	Synthesis of Ac-Cys( <i>StBu</i> )-VC-Gly-Dox 4-PG: Doxorubicin conjugation	89
7.8.3	Synthesis of Ac-Cys-VC-Gly-Dox 4: Thiol deprotection	90

7.9	Synthesis of azide-aurein1.2-doxorubicin conjugate 8	91
7.10	Synthesis of azide-doxorubicin conjugate 9 w/o aurein1.2	92
7.11	Assembly of Trastuzumab-conjugates	93
7.11.1	mTG mediated BCN-modification of Trastuzumab-LLQG	93
7.11.2	SPAAC test conjugation: Trastuzumab-aurein1.2-doxorubicin 1a-d	93
7.11.3	SPAAC conjugation: Synthesis of Trastuzumab-aurein1.2-doxorubicin 1e	94
7.11.4	SPAAC conjugation: Synthesis of Trastuzumab-doxorubicin 10	94
7.12	Cathepsin B test cleavage	95
7.12.1	Synthesis of cathepsin B test peptide 5	95
7.12.2	Cathepsin B cleavage of test peptide 5	95
7.13	Dextran modification	96
7.13.1	Synthesis of dextran- <i>N</i> -Boc-cadaverine 13	96
7.13.2	General procedure for dextran modifications	97
7.13.2.1	Carboxyethylation: Synthesis of 2-CE-dextran- <i>N</i> -Boc-cadaverine	97
7.13.2.2	Maleimide conjugation: Synthesis of maleimide-dextran- <i>N</i> -Boc-cadaverine	97
7.13.2.3	Azide conjugation: Synthesis of N <sub>3</sub> -dextran- <i>N</i> -Boc-cadaverine	98
7.13.2.4	Removal of the Boc-protecting group	98
7.13.3	Synthesis of <i>N</i> -(2-aminoethyl)maleimide 14	99
7.13.4	Synthesis of maleimide(6.5)-dextran- <i>N</i> -Boc-cadaverine 18	100
7.13.5	Synthesis of maleimide(7.8)-dextran- <i>N</i> -Boc-cadaverine 19	100
7.13.6	Synthesis of maleimide(10.5)-dextran- <i>N</i> -Boc-cadaverine 20	101
7.13.7	Synthesis of <i>N</i> -(5-aminopentyl)-2-azidoacetamide 21	101
7.13.8	Synthesis of N <sub>3</sub> (4.8)-dextran-cadaverine 24	102
7.13.9	Synthesis of N <sub>3</sub> (4.8)-dextran-cadaverine 25	102
7.13.10	Synthesis of N <sub>3</sub> (4.3)-dextran-cadaverine 26	103
7.13.11	Synthesis of N <sub>3</sub> (4.3)-dextran-norbornene 29, 30	104
7.13.12	Synthesis of N <sub>3</sub> (4.8)-dextran-norbornene 31	104
7.13.13	Synthesis of N <sub>3</sub> (4.8)-dextran-biotin 32	105
7.14	Thiol-maleimide addition of maleimide-functionalized dextran and thiol-modified cargo	106
7.14.1	Synthesis of TAMTA-thiol 35	106
7.14.2	Synthesis of TAMRA-aurein1.2(4.5)-dextran- <i>N</i> -Boc-cadaverine 36	106
7.14.3	Synthesis of TAMRA-L17E(3.8)-dextran- <i>N</i> -Boc-cadaverine 37	107
7.14.4	Synthesis of doxorubicin-thiol 40	108
7.14.4.1	Synthesis of Ac-Cys( <i>St</i> Bu)-OH 67	108
7.14.4.2	Synthesis of Ac-Cys-Dox 40	108
7.14.5	Synthesis of doxorubicin-L17E(5.2)-dextran- <i>N</i> -Boc-cadaverine 39	109
7.14.6	Synthesis of TAMRA-dextran- <i>N</i> -Boc-cadaverine 38	109
7.14.7	Synthesis of L17E-PNA-dextran- <i>N</i> -Boc-cadaverine 43	110
7.15	CuAAC conjugation of azide-functionalized dextran and alkyne-modified cargo	111
7.15.1	Synthesis of L17E(4.8)-dextran-cadaverine 42	111
7.15.2	Synthesis of L17E(4.3)-dextran-norbornene 45	111
7.15.3	Synthesis of L17E(4.8)-dextran-biotin 60	112
7.16	General synthesis of L17E-dextran-protein conjugates	113

7.16.1	General modification of eGFP with methyltetrazine functionality	113
7.16.1.1	eGFP modification with NHS-activated methyltetrazine derivative	113
7.16.1.2	Site-specific eGFP modification with methyltetrazine mediated by LplA <sup>W37V</sup>	113
7.16.2	General iEDDA dextran-to-protein conjugation	114
7.16.3	General biocompatible CuAAC	115
7.16.4	Alternative strategy: Dextran-to-protein conjugation applying pre-assembled L17E-dextran-norbornene 45	115
7.16.4.1	Synthesis of eGFP-MeTet 69	115
7.16.4.2	Alternative strategy: Synthesis of L17E(4.3)-dextran-eGFP 46	116
7.17	Synthesis of L17E(4.3)-dextran-eGFP 44	117
7.17.1	Synthesis of eGFP-MeTet 48	117
7.17.2	Synthesis of N <sub>3</sub> (4.3)-dextran-eGFP 49	117
7.17.3	Synthesis of L17E(4.3)-dextran-eGFP 44	118
7.18	Synthesis of L17E(4.8)-dextran-eGFP 52	118
7.18.1	Synthesis of eGFP-MeTet 50	118
7.18.2	Synthesis of N <sub>3</sub> (4.8)-dextran-eGFP 51	119
7.18.3	Synthesis of L17E(4.8)-dextran-eGFP 52	119
7.19	Synthesis of L17E(4.8)-dextran-eGFP 57 applying LplA <sup>W37V</sup> -mediated site-specific dextran-to-protein conjugation	120
7.19.1	LplA <sup>W37V</sup> -mediated synthesis of eGFP-MeTet 54, 55	120
7.19.2	LplA <sup>W37V</sup> -mediated synthesis of eGFP-MeTet 56	121
7.19.3	Synthesis of N <sub>3</sub> (4.8)-dextran-eGFP 58	121
7.19.4	Synthesis of L17E(4.8)-dextran-eGFP 57	122
8	Supporting information	123
8.1	Supplementary microscope images	123
8.1.1	TAMRA-dextran- <i>N</i> -Boc-cadaverine 38	123
8.1.2	TAMRA-dextran- <i>N</i> -Boc-cadaverine 38 with L17E 12 coinubation	123
8.1.3	TAMRA-L17E(3.8)-dextran- <i>N</i> -Boc-cadaverine 37	124
8.1.4	TAMRA- aurein1.2(4.5)-dextran- <i>N</i> -Boc-cadaverine 36	124
8.1.5	Dox-L17E(5.2)-dextran- <i>N</i> -Boc-cadaverine 39	125
8.1.6	L17E(4.3)-dextran-eGFP X	125
8.2	Analytical data of Ac-Orn(N <sub>3</sub> )-VC-aurein1.2-Lys(maleimide)-NH <sub>2</sub> 3	126
8.3	Analytical data of Ac-Orn(N <sub>3</sub> )-VC-GS-Lys(maleimide)-NH <sub>2</sub> 6	126
8.4	Analytical data of aurein1.2-Cys 33	127
8.5	Analytical data of L17E 12	127
8.6	Analytical data of L17E-Cys 34	128
8.7	Analytical data of L17E-Pra 41	129
8.8	Analytical data of Ac-Cys( <i>StBu</i> )-VC-Gly 7	129
8.9	Analytical data of Ac-Cys( <i>StBu</i> )-VC-Gly-Dox 4-PG	130
8.10	Analytical data of Ac-Cys-VC-Gly-Dox 4	130
8.11	Analytical data of azide-aurein1.2-doxorubicin conjugate 8	131
8.12	Analytical data of azide-doxorubicin conjugate 9 w/o aurein1.2	132
8.13	Analytical data of SPAAC test conjugation 1a-d	133

8.14	Analytical data of Trastuzumab-aurein1.2-doxorubicin 1e and Trastuzumab-doxorubicin	10 135
8.15	Analytical data of cathepsin B test peptide	5 135
8.16	Analytical data of cathepsin B mediated cleavage of test peptide	5 136
8.17	Analytical data of dextran- <i>N</i> -Boc-cadaverine	13 137
8.18	Analytical data of <i>N</i> -(2-aminoethyl)maleimide 14 and intermediates 65, 66	 137
8.19	Analytical data of maleimide(6.5)-dextran- <i>N</i> -Boc-cadaverine	18 139
8.20	Analytical of maleimide(7.8)-dextran- <i>N</i> -Boc-cadaverine	19 140
8.21	Analytical data of maleimide(10.5)-dextran- <i>N</i> -Boc-cadaverine	20 140
8.22	Analytical data of <i>N</i> -(5-aminopentyl)-2-azidoacetamide	21 141
8.23	Analytical data of N <sub>3</sub> (4.8)-dextran-cadaverine	24 141
8.24	Analytical data of N <sub>3</sub> (4.8)-dextran-cadaverine	25 143
8.25	Analytical data of N <sub>3</sub> (4.3)-dextran-cadaverine	26 144
8.26	Analytical data of N <sub>3</sub> (4.3)-dextran-norbornene	29 144
8.27	Analytical data of N <sub>3</sub> (4.8)-dextran-norbornene	31 145
8.28	Analytical data of N <sub>3</sub> (4.8)-dextran-biotin	32 145
8.29	Analytical data of TAMRA-thiol	35 146
8.30	Analytical data of TAMRA-aurein1.2(4.5)-dextran- <i>N</i> -Boc-cadaverine	36 147
8.31	Analytical data of TAMRA-L17E(3.8)-dextran- <i>N</i> -Boc-cadaverine	37 147
8.32	Analytical data of Ac-Cys(StBu)-OH	67 148
8.33	Analytical data of Dox-thiol (Ac-Cys-Dox)	40 148
8.34	Analytical data of doxorubicin-L17E(5.2)-dextran- <i>N</i> -Boc-cadaverine	39 149
8.35	Analytical data of TAMRA- dextran- <i>N</i> -Boc-cadaverine	38 149
8.36	Analytical data of L17E(4.8)-dextran-cadaverine	42 150
8.37	Analytical data of L17E(4.3)-dextran-norbornene	45 151
8.38	Analytical data of L17E(4.8)-dextran-biotin	60 152
8.39	Analytical data of L17E(4.3)-dextran-eGFP 46, assembled via alternative strategy: Dextran-to-protein conjugation applying pre-assembled L17E(4.3)-dextran-norbornene	45 152
8.40	Analytical data of L17E(4.3)-dextran-eGFP	44 153
8.41	Analytical data of L17E(4.8)-dextran-eGFP	52 153
8.42	Analytical data of LpLA <sup>W37V</sup> -mediated site-specific eGFP modification with methyltetrazine	154
8.43	Protein productions: IMAC purification	155
8.43.1	eGFP-L17E 11 fusion	155
8.43.2	LpLA <sup>W37V</sup> batch 1 and batch 2	156
	References	157
	Abbreviations	162
	List of figures	164
	List of schemes	171
	List of tables	174
	Danksagung	175
	Appendix	clxxvi

---

## 1 Introduction

---

In 1982, the introduction of recombinant human insulin marked the beginning of protein-based therapeutics.<sup>[1]</sup> Since then, the interest in development of novel pharmaceutical agents based on biologicals like e.g. peptides, proteins, enzymes, nucleic acids, antibodies, or antibody-drug-conjugates (ADCs) for treatment of various diseases, among them cancer, immunological or metabolic disorders, increased steadily. To date, hundreds of biopharmaceuticals have been approved,<sup>[2]</sup> and in 2017 seven out of the top-ten selling drugs were the protein-based ones.<sup>[3]</sup> The success of these structurally highly complex macromolecules can be explained by their beneficial properties like the ability to modulate cellular processes with high efficacy and specificity.<sup>[4]</sup> However, the size of these sophisticated macromolecular architectures entails their major drawback – in contrast to small-molecule drugs, biopharmaceuticals are not able to cross the cellular membrane for entering the cytosol, thus limiting their application to extracellular targets.<sup>[5]</sup> Certainly, approximately two-thirds of the human proteome is located intracellularly and therefore inaccessible for membrane-impermeable molecules.<sup>[6]</sup> Although many small molecules can cross the cell membrane by passive diffusion or via membrane transporters,<sup>[7]</sup> only a minor part of the human proteome, approximately a several hundred proteins, are addressable with these small molecules.<sup>[8]</sup> This is due to the fact that small molecules are limited to modulate protein function of either intracellular or extracellular targets possessing binding sites in form of deep binding pockets. However, in a therapeutic context many proteins do not exhibit such binding sites and depend on formation of macromolecular complexes by protein-protein interactions (PPI). Hence, for modulation of protein functions, relying on PPIs, these targets must be addressed with suitable biologicals. As such molecules are not able to cross the plasma membrane for reaching the cytosol, their action and potential application field is drastically limited to extracellular targets, leaving a lot of intracellular targets “undruggable”.<sup>[5]</sup> The possibility to improve intracellular uptake of proteins by overcoming the main barrier – the cell membrane – would open up the ways to a plethora of intracellular targets, among them important oncology ones, such as the drivers of tumorigenic processes RAS and MYC.<sup>[9]</sup>

### 1.1 The cell membrane

All cells have at least one fact in common, they all feature a boundary, which separates the interior of the cell from the surrounding extracellular environment: the cell membrane. The cell membrane, which is also called plasma membrane, amongst others, serves as physical barrier which gives cells the opportunity to regulate their composition and properties. It is composed of amphiphilic phospholipids, which self-aggregate with the polar head units facing the aqueous exterior and the hydrophobic fatty acyl chains, associating under water exclusion to form the hydrophobic interior of the 5-8 nm thick lipid bilayer.<sup>[10]</sup> The three main types of lipids present in the cell membrane are glycerophospholipids, sphingolipids, and sterols (**Figure 1**).

Glycerophospholipids represent the major structural lipids in eukaryotes. They are composed of the hydrophobic diacylglycerol (DAG), a glycerol esterified with two saturated or *cis*-unsaturated fatty acid chains of various length, and the polar phosphate head unit, which is esterified with the third glycerol hydroxylic group. The phosphate group in turn is esterified with different alcohols like choline, ethanolamine, serine, or inositol, resulting in phosphatidylcholine (PtdCho), phosphatidylethanolamine (PtdEtn), phosphatidylserine (PtdSer), or phosphatidylinositol (PtdIns).<sup>[11]</sup> In eukaryotic membranes, PtdCho is the predominant lipid representing more than 50% of the phospholipids, whereat most PtdCho molecules carry one *cis*-unsaturated fatty acid chain, such as *cis*-9 monounsaturated oleic acid.<sup>[12]</sup> The polar head units of PtdSer und PtdIns are negatively charged. Due to the asymmetric distribution in the membrane composition, with PtdSer and PtdIns occurring predominantly on the cytosolic membrane surface, a negative charge with a potential difference is generated.<sup>[10]</sup>

Sphingolipids represent the second class of structural lipids. In contrast to the DAG backbone of glycerophospholipids, sphingolipids are based on ceramide (Cer). This hydrophobic structure is yielded by amide bond formation between a fatty acid and the C2 amine group of sphingosine. Decoration of

Cer with either phosphocholine or with saccharides leads to formation of sphingomyelin (SM) respectively glycosphingolipids (GSL), which are the two major sphingolipids in mammalian cells.<sup>[11]</sup> Featuring unsaturated fatty acids, the kink of aliphatic chains in phospholipids, is caused by predominant *cis*-conformation of the double bond and leads to lower packing density and therefore membrane fluidity.<sup>[12]</sup> While sphingolipids exhibit either saturated or *trans*-unsaturated acyl chains, which cause higher packing density in the bilayer. The higher packing density results in less fluidity and solid-gel phase of the membrane.<sup>[11]</sup>

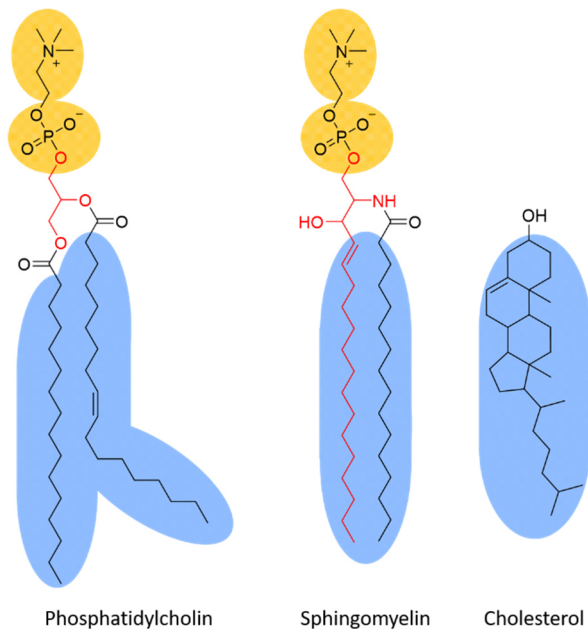


**Figure 1:** Three main classes of membrane lipids with most common prototypes in mammals. Glycerophospholipid (left): Phosphatidylcholine based on Glycerol (red) esterified with palmitic acid, oleic acid, and phosphocholine. Sphingolipid (middle): Sphingomyelin based on Sphingosine (red) esterified with palmitic acid and phosphocholine. Sterol (right): Cholesterol. Hydrophobic chains marked in blue and polar head units marked in yellow.

The third type of membrane lipids, the non-polar sterols, prevent formation of the solid-gel phase by interfering with the acyl-chain packing. Thus, over a broad range of different lipid compositions and temperatures, sterols keep the membrane fluid, while simultaneously increasing the membrane rigidity, thickness, and impermeability of solutes. In mammalian cells, the predominant sterol is cholesterol. In plasma membranes, the cholesterol content is up to 40 mol %, explaining the increased thickness of the plasma membrane compared to the intracellular ones, like the membrane of the endoplasmic reticulum, which exhibits a significantly lower cholesterol content of around 5 mol %.<sup>[12-13]</sup>

The three types of lipid classes, combined with the variety of fatty acid molecules differing in length and saturation level, the variable phosphoesters bound to DAG or Cer, or the different saccharides bound to Cer, create a huge diversity of lipids. This lipid diversity in membrane constitution provides stable and robust composition as well as impermeability of the membrane under local alterations of environmental conditions. Furthermore, diversity enables functional features of the membrane like e.g. membrane or vesicular trafficking or modulation of membrane protein function by interaction with different lipids.<sup>[13-14]</sup>

In addition to the complexity and diversity of lipid composition, the plasma membrane also differs from pure lipid bilayers as it contains membrane proteins. Dependent on the cell type, the molecular protein-to-lipid ratio approximately amounts to 1:40, or expressed in percentage by weight, of more than 50%.<sup>[15]</sup> Membrane proteins have a wide range of functions, from transporters of solutes or ion-channels to receptors of extracellular signals regulating cellular functions. Membrane proteins are classified in two classes –peripheral and integral membrane proteins. Peripheral proteins are not directly bound to the membrane, rather indirectly by intermolecular interactions with membrane areas or bound proteins. The integral membrane proteins are divided into anchored and transmembrane ones. The anchored variants are either glycosylphosphatidylinositol (GPI)- or lipid-anchored on the membrane surface, while the transmembrane proteins are further divided into multi-pass and single-pass transmembrane proteins. While in single-pass transmembrane proteins the amino acid sequence spans the membrane only once, in multi-pass transmembrane proteins the protein chain crosses the membrane multiply. In the transmembrane region, the underlying secondary structures are often  $\alpha$ -helices with hydrophobic amino acid residues facing the membrane interior, or in some cases  $\beta$ -sheets forming a  $\beta$ -barrel.<sup>[16]</sup> Two well-known members of transmembrane proteins, and the largest group of membrane receptors, are G-protein-coupled receptors (GPCRs) and receptor tyrosine kinases (RTKs). Both are involved in signal pathways regulating various cellular functions and associated with different diseases, among them certain kinds of cancer. GPCRs are multi-pass transmembrane proteins with seven transmembrane

helical motifs spanning the cell membrane. Upon ligand binding, the intracellularly coupled heterotrimeric G-protein dissociates modulating the activity of different second messengers, and thus regulates various cellular functions.

RTKs, including epidermal growth factor receptors (EGFRs), are single-pass transmembrane proteins with intracellular protein tyrosine kinase domain. Ligand binding leads to dimerization of the RTKs, followed by autophosphorylation and activated signaling pathways, which regulate important cellular functions like cell growth or differentiation.<sup>[17]</sup>

In the last decades, the paradigm of cell membrane architecture has changed. Formerly, according to the fluid mosaic model (**Figure 2 A**), the membrane was considered a homogenous fluid phase containing the membrane proteins.<sup>[18]</sup> Meanwhile it has turned out that parts of the membrane can separate into microdomains possessing different lipid and protein compositions. The lipid raft model (**Figure 2 B**) describes subcompartmentalization in dynamic self-organized membrane domains. The lipid raft domains are rich in sphingolipids, cholesterol, and proteins, which associate driven by lipid-lipid, protein-lipid, or protein-protein interactions. These lipid rafts are involved in coordination of different cellular processes like post-Golgi trafficking, signaling, and endocytosis.<sup>[19]</sup>

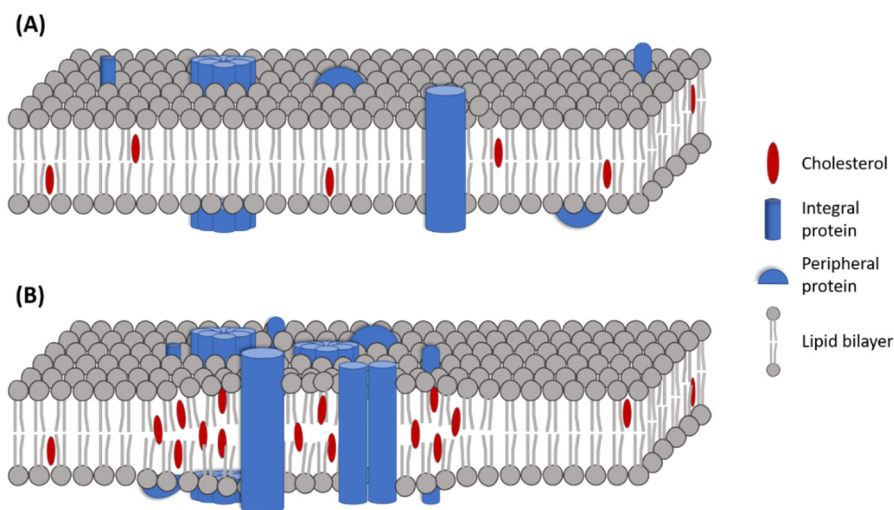


**Figure 2:** Schematic depiction of cell membrane architectures according to homogenous phase in fluid mosaic model (A) and subcompartmentalized domains in the lipid raft model (B), adapted from<sup>[18-19]</sup>.

## 1.2 Intracellular delivery of biomacromolecules

### 1.2.1 Basics of endocytosis

Small molecules can pass the plasma membrane via passive diffusion, which is the case for small and slight polar to nonpolar molecules. Alternatively, small molecules can pass the membrane via active protein transporters, carriers, or channels in case of more polar molecules like amino acids, sugars, nucleosides, or ions. However, cellular uptake of macromolecules usually occurs via membrane-bound vesicles. The vesicle formation is a result of invagination of parts of the plasma membrane, followed by pinching off the resulting vesicle, and is known as endocytosis. Endocytosis is basically divided into the uptake of large particles and uptake of fluids and solutes, referred to as phagocytosis and pinocytosis. Phagocytosis mainly occurs in specialized mammalian cells, for example during disposal of pathogens or debris of dead cells by macrophages. In contrast, pinocytosis is performed in all cells and is classified in four mechanisms of endocytic pathway: macropinocytosis, clathrin-mediated endocytosis, caveolae-mediated endocytosis and clathrin- and caveolin-independent endocytosis (**Figure 3**).<sup>[20]</sup>

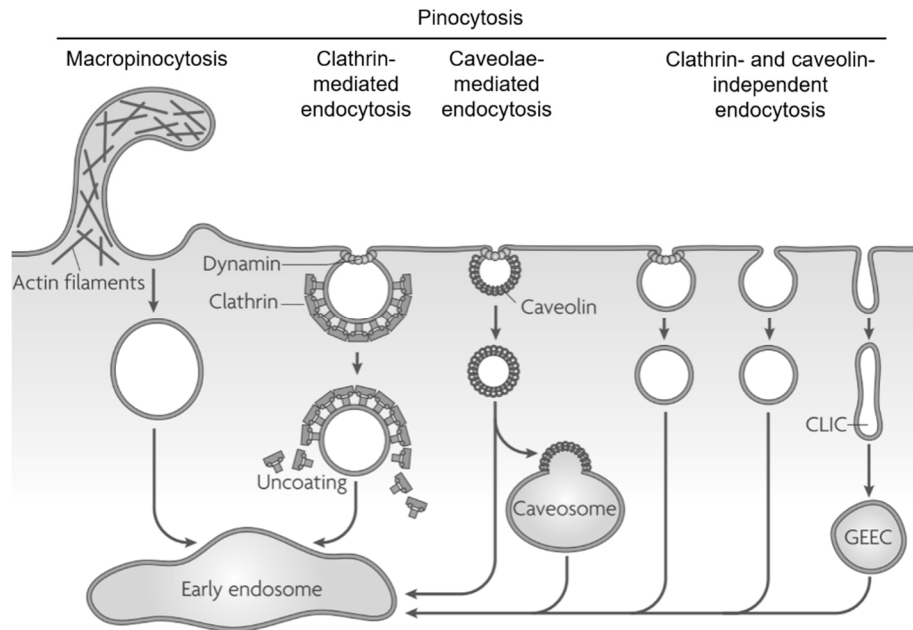


**Figure 3:** Schematic depiction of pinocytotic pathways and following endocytosis, intracellular trafficking to the early endosome, adapted from.<sup>[21]</sup>

Lipid rafts play a crucial role in endocytic pathways. Macropinocytosis (**Figure 3**) depends on actin-rich lipid rafts and is a signal-dependent form of endocytosis. Upon growth factor stimulation actin rearrangement induces membrane ruffling. Following collapse of the ruffled membrane and membrane fusion, respectively closure of the membrane, the fluid-phase uptake results in formation of endocytic vesicles called macropinosomes.<sup>[22]</sup>

Clathrin-mediated endocytosis (**Figure 3**) is the most common pathway of cellular entry. As in most endocytic pathways, clathrin-mediated endocytosis is triggered after receptor-ligand binding. The plasma membrane domain invaginates, mediated by the enriched clathrin protein. Clathrin-coated pits are formed and pinch off, resulting in clathrin-coated vesicles. These clathrin-coated vesicles contain the concentrated receptor-ligand complex, which finally reaches the early endosomes.<sup>[20]</sup>

Caveolae are flask-shaped invaginations of the plasma membrane, including caveolin as structuring membrane protein (**Figure 3**). Caveola pinch off and if the enclosed content is not recycled by fusion with the plasma membrane, it reaches the early endosome with possible detour over intermediary caveosomes. Contrary to other endosomal compartments, caveosomes are endosomal vesicles with neutral pH.<sup>[20-21, 23]</sup>

The clathrin- and caveolae independent endocytic pathways as well as the dependent variants and macropinocytosis are based on different lipid raft microdomains. The cholesterol-sensitive clathrin- and caveolin-independent variants can be further classified in different pathways: A dynamin-dependent variant and a variant, which dynamin independently but actin-dependently forms the so-called clathrin- and dynamin-independent carriers (CLIC). These CLIC compartments then build GPI-anchored protein enriched early endosomal compartments (GEEC) (**Figure 3**).<sup>[24]</sup>

The efficiency of endocytosis is associated with binding to the cell membrane. Unspecific binding of endocytosed solutes with the cell membrane can increase uptake efficiency. Even higher efficiency is achieved by interaction of ligands with the respective high-affinity receptors embedded in the plasma membrane, respectively in the invaginations of the cell membrane like clathrin-coated pits or caveolae. The endocytic uptake mediated through ligand-receptor interaction is also known as receptor-mediated endocytosis. However, it is not possible to draw a conclusion from the process of receptor-mediated endocytosis towards the underlying endocytic pathway mechanism, because several pinocytotic pathways are triggered by ligand-receptor interactions.<sup>[20]</sup>

All pinocytosis pathways have something fundamental in common. Following vesicular trafficking, the internalized macromolecular cargo is entrapped in the early endosome. The interior of an early endosome presents an enclosed extracellular environment, which is still separated from the cytoplasm by the endosomal lipid membrane. In the early endosome, the internalized cargo is sorted for either recycling back to the plasma membrane, transport to the trans-Golgi network via retrograde trafficking, or degradation in the lysosome. Accompanied by proton pump that ensures decrease of pH value, early endosomes mature into late endosomes and, finally, lysosomes. In the lysosome, endocytosed biomacromolecules, such as antibodies or other proteins, are proteolytically degraded, if they have not been recycled or already left the endosome. Thus, the endocytosed cargo must cross the endosomal membrane barrier to reach the cytoplasm and to escape the endosome before degradation.<sup>[24]</sup> Alternatively, a possibility to avoid the need for endosomal release of molecules, in terms of cytoplasmic uptake, is to prevent endosomal entrapment by circumvention of endocytic uptake. To this end, direct entrance of naturally membrane impermeable molecules into the cytoplasm is required, mediated by delivery agents that enable their transport across the cell membrane.

### 1.2.2 Delivery strategies

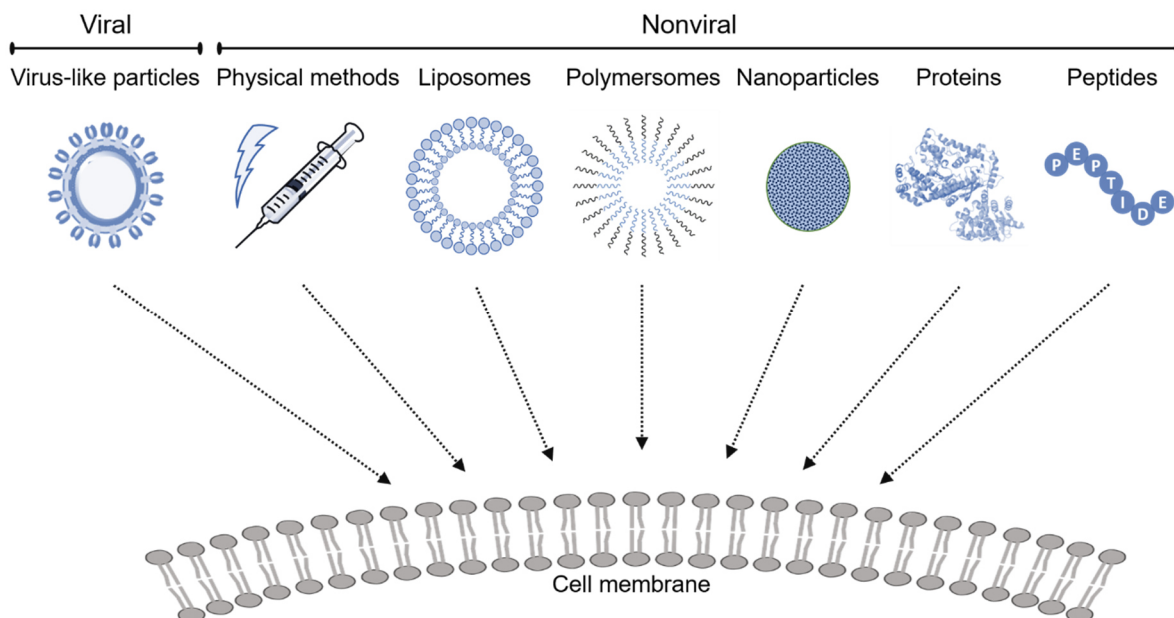


**Figure 4:** Schematic depiction of delivery strategies applying viral and nonviral systems.

Over the years, different strategies for intracellular delivery of macromolecular cargoes, among them proteins, have been reported (**Figure 4**). First, the delivery strategies can be separated into viral and nonviral systems. Viruses are capable to deliver their viral genome into the cytosol of host cells by either direct translocation across the cell membrane or, most common, by escaping the endosomal compartment after endocytosis. Therefore, enveloped viruses, such as influenza A virus, can fuse with the membrane and release their content into the cytoplasm, while non-enveloped viruses either must lyse the membrane or generate pores.<sup>[25]</sup> The idea behind virus-based systems for intracellular protein delivery is to mimic viral entry. Therefore, the cargo protein is packed into virus-like particles to facilitate the delivery into the cytoplasm.<sup>[26]</sup>

Besides viral delivery systems, a number of nonviral delivery systems based on different approaches have been introduced. Physical methods using mechanical membrane disruption like electroporation or microinjections have successfully been investigated for intracellular delivery of diverse cargoes. However, these methods are restricted to *in vitro* experiments and are not applicable under clinical conditions due to their invasive nature, which causes cell damage.<sup>[27]</sup>

---

The methods are more promising that are based on chemical modification or attachment of the cargo to intracellular delivery systems in an either covalent or non-covalent manner, with liposome-, polymer-, or inorganic nanoparticle-based systems being the most prominent examples. Liposomes are lipid-bilayer-surrounded vesicular particles, in which cargo molecules like proteins can be encapsulated. pH-sensitive liposomes contain pH-sensitive lipids. Endocytic uptake of liposomes, followed by acidification in endosomal compartments, leads to destabilizing of the liposomal structure. Upon either fusion with or disruption of the endosomal membrane, the encapsulated cargo is released into the cytoplasm.<sup>[28]</sup> Another liposome-based strategy is to generate fusogenic liposomes for intracellular delivery of proteins. Those modules avoid endocytic uptake and endosomal trafficking through direct fusion upon contact with the cell membrane, and release of their content into the cytoplasm.<sup>[29]</sup> Similar to the liposome approach, synthetic polymer vesicles, called polymersomes, composed of self-assembling pH-sensitive diblock copolymers, can encapsulate protein cargo in their interior. Following endocytic uptake and decrease of pH value during endosomal maturation, the polymersomes dissociate quickly. This leads to osmotically damage of the membrane and clears the way to cytoplasmic delivery of encapsulated cargo.<sup>[30]</sup> According to the enhanced permeability and retention effect, nano-sized particles are known to accumulate in tumor tissue.<sup>[31]</sup> Hence, mesoporous silica or organosilica nanoparticles were reported to successfully mediate intracellular delivery of encapsulated protein cargo.<sup>[32]</sup>

Furthermore, delivery strategies have been developed based on proteins exhibiting the ability to form pores or channels in cellular membranes. Some plants and bacteria produce protein toxins, which commonly inhibit protein synthesis in the affected organism. To that end, the respective toxins must enter the target cells and reach the cytosol.<sup>[33]</sup> Therefore, a strategy has been evolved that enables the toxin to specifically bind the target cell, enter it and to escape from the endosome. These toxins are composed of an enzymatic protein fragment A, which is responsible for inhibition of protein synthesis and a second fragment B, which mediates specific receptor binding on the cell surface as well as entry into the cell. Two representatives of these so-called AB-toxins, which directly escape the endosome after receptor-mediated endocytosis, are anthrax toxin (*Bacillus anthracis*) and diphtheria toxin (*Corynebacterium diphtheria*). Following receptor binding and endocytosis, the B fragments of anthrax and diphtheria toxins both form translocation pores in the endosomal membranes, which enables the escape from the endosomal compartments. While anthrax toxin forms rigid membrane spanning  $\beta$ -barrel pores, diphtheria toxin forms flexible  $\alpha$ -helical pores. These ability to bind and enter mammalian cells followed by endosomal escape aroused interest in protein engineering of AB-toxin-based modules for intracellular cargo delivery.<sup>[34]</sup> Several strategies have successfully been introduced using anthrax toxin-derived systems for delivery of bioactive cargo, from oligonucleotides<sup>[35]</sup> to peptides or proteins.<sup>[36]</sup>

### 1.2.2.1 Cell-penetrating peptides

Recently, cell-penetrating peptides (CPPs) have emerged as powerful delivery vehicle. They are able to mediate cytoplasmic or nuclear translocation of various macromolecular cargoes, such as peptides, proteins, or oligonucleotides, in cells of different types. CPPs are oligopeptides with a length of up to 30 amino acid residues, possessing a high content of basic amino acids, a positive charge at physiological pH and often amphipathic character.<sup>[22b, 37]</sup> In 1988, the attention was drawn to delivery vehicles based on peptides when it has been shown that the Tat-protein from human immunodeficiency virus 1 (HIV-1) was rapidly taken up by cells and translocated into the nucleus.<sup>[38]</sup> Moreover, chemically synthesized Tat-protein as well as its truncated mutants<sup>[39]</sup> up to shortened peptide version Tat-(48-60) (GRKKRRQRRRPPQ)<sup>[40]</sup> were shown to cross the plasma membrane and to accumulate in the nucleus. The similar ability to translocate across cell membranes was shown for penetratin, a 16 amino acid residue peptide, derived of the third helix of antennapedia homeodomain found in *Drosophila*.<sup>[41]</sup> These findings led to intense research in the field of CPP-based delivery system for translocation of bioactive macromolecular cargo.

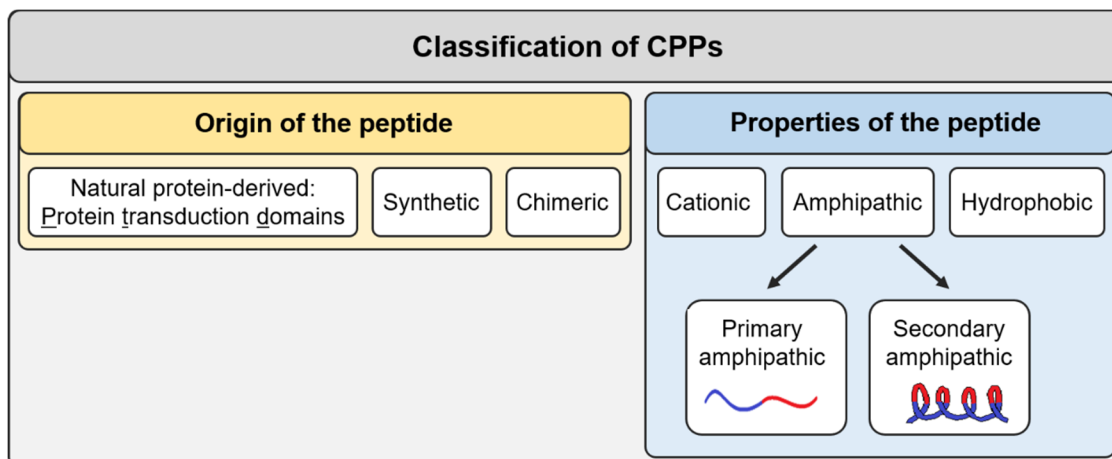


**Figure 5:** Classification of CPPs according to either origin or properties of the peptide.

CPPs can get classified in different ways (**Figure 5**). First, it can be distinguished between the origin of the peptide. Variants derived of natural proteins, such as Tat or penetratin, are also called protein transduction domains (PTDs). Chimeric CPPs combine two or more motifs of different peptides or proteins and synthetic CPPs like polyarginines<sup>[42]</sup> represent the third class. Another possibility is the differentiation into cationic CPPs with high positive net charge, amphipathic CPPs, containing both polar and non-polar regions, and the rarely occurring hydrophobic CPPs, bearing only nonpolar amino acids.<sup>[43]</sup> The rather short cationic CPPs belong to the group of non-amphipathic peptides while the amphipathic CPPs can be split in primary and secondary ones. In the first group, the amphipathic character is caused by the - usually - rather long (more than 20 amino acids) primary structure with sequential assembly of hydrophobic and hydrophilic domains. Peptides of the second group are often shorter than the primary counterparts, and their amphipathic character is caused by the conformational formation of  $\alpha$ -helices or  $\beta$ -sheets upon interaction with the phospholipid bilayer.<sup>[22b, 44]</sup>

The characteristics of the peptide, such as primary structure, overall charge, or charge distribution, determine the mode of interaction between a CPP and the cell membrane or molecules on the cell surface. The successful intracellular translocation of CPPs and cargo molecules has frequently been reported in the literature. However, the underlying uptake mechanisms and pathways of entry into the cells are not totally elucidated to date. The possible modes of internalization are numerous, and (in addition to the CPP characteristics) also depend on the respective cargo, cell type, and employed concentration. The internalization can occur following two major pathways, via direct translocation across the plasma membrane or by endocytosis. The direct translocation is a passive and energy-independent process, while endocytosis is an active and energy-dependent two-step route, comprising endocytic uptake followed by essential endosomal escape. It is known that endocytic uptake is the most common mechanism at low peptide concentrations. Cationic arginine-rich CPPs such as oligo/polyarginine or Tat peptide have been reported to often enter cells following one pathway of endocytosis, namely, macropinocytosis.<sup>[22b]</sup> In contrast, high peptide concentrations can stimulate direct translocation across the plasma membrane.<sup>[22b]</sup> For cell entry via direct translocation, which requires the interaction of cationic CPPs with negatively charged membrane components, several mechanisms have been proposed (**Figure 6**):

**Pore formation** is one of the postulated mechanisms for direct translocation across the cell membrane. Two different kinds of pores can be generated, according to the barrel stave or toroidal models. Following the barrel stave model, primary amphipathic,  $\alpha$ -helical peptides, which are long enough to span the membrane, form a barrel-shaped bundle. The hydrophobic regions of the helices interact with the lipids, while the hydrophilic ones are directed to the center and form the hydrophilic pore.<sup>[22b]</sup> In the toroidal model, peptides form an  $\alpha$ -helical structure upon interaction with the membrane. Following interaction of positively charged amino acid residues of the peptide with negatively charged phospholipid head units and penetration into the membrane, the lipid layer bends

towards the interior and forms a hydrophilic gap. The hydrophilic pore is formed by the hydrophilic regions of the peptide as well as the phospholipid head units.<sup>[22b]</sup>

In the **carpet model** and membrane-thinning model, the positively charged peptides do not penetrate the membrane. Instead, they are oriented parallel to the cell surface and electrostatically bound to negatively charged phospholipid head units. The peptides cover the membrane like a carpet and cause membrane destabilization. Potential hydrophobic peptide residues are embedded in the lipid interior, leading to structural membrane reorganization and possible translocation of the peptide, if a certain concentration is reached.<sup>[22b]</sup>

The **inverted micelle** model was already postulated as uptake mechanism for penetratin in 1996.<sup>[45]</sup> It has been hypothesized that positively charged peptide areas electrostatically interact with negatively charged phospholipid head units. The lipid heads surround the peptide and form the inverted micelle, which includes the peptide in its hydrophilic interior. Destabilization and reopening of the inverted micelle can release its content into the cell interior.<sup>[22b]</sup>

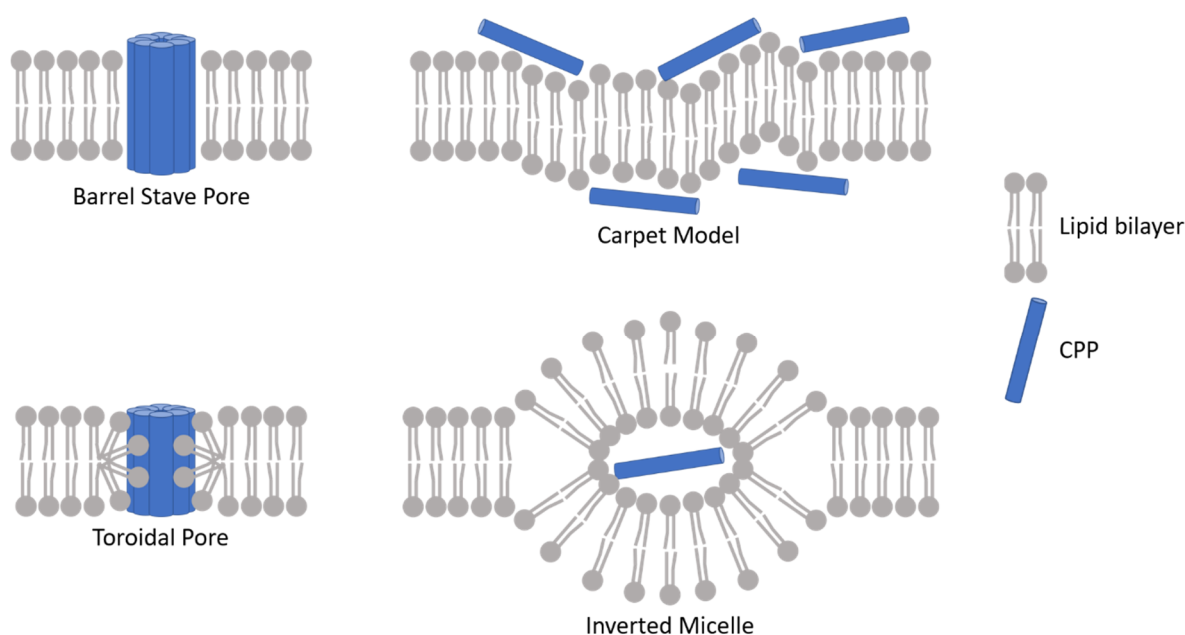


**Figure 6:** Schematic depiction of the postulated mechanism for direct translocation across the cell membrane of cell-penetrating peptides. Adapted from <sup>[22b]</sup>

In any case, electrostatic interactions between peptide and plasma membrane play a crucial role in cell entry of CPPs via both direct translocation and endocytic uptake.<sup>[22b, 37]</sup> In case of dominating uptake via a pathway of endocytosis, the CPP or CPP-cargo complex is entrapped in endosomal compartments. Thus, to avoid degradation in the lysosome, escaping the endosome is highly required. The endosomal escape of delivery vehicle and cargo, no matter if mediated by CPPs or alternative strategies, still lacks efficiency and remains a bottleneck in cytoplasmic delivery of cargo molecules.<sup>[5, 46]</sup>

### 1.2.3 Endosomal escape

Escaping the endosome is a crucial step for cytoplasmic delivery of cargo molecules, equally using CPPs<sup>[47]</sup> or other delivery strategies.<sup>[5, 46]</sup> Different routes of endosomal escape and their mechanical background was extensively investigated, and different mechanisms of this process have been proposed:

**Pore formation**, as described for CPP-mediated direct translocation across the cell membrane, can occur in the endosomal membrane in the same way. As already described, bacterial toxins have been reported to successfully escape the endosome. Upon pH decrease in the endosomal compartment, the

---

respective domain undergoes conformational change, inserts into the endosomal membrane, and forms a translocation pore.<sup>[34]</sup> In the same way, it was proposed that CPPs mediate endosomal escape by pore formation in the endosomal membrane. It was hypothesized, that similar to CPP-mediated pore formation for direct translocation across the cell membrane, cationic amphipathic peptides can form either barrel-stave or toroidal translocation pores in the endosomal membrane.<sup>[5, 46]</sup>

**Proton sponge effect** hypothesis describes delivery agents, which have a high buffer capacity, absorb the protons, swell under protonation, and thus prevent endosomal acidification. Continuous proton transport leads to simultaneous chloride and water influx to keep the osmotic balance. This causes swelling of the endosome, eventually followed by rupture of the membrane and release of the entrapped content.<sup>[5]</sup> For example poly-histidine<sup>[48]</sup> or poly(amidoamine)<sup>[49]</sup> based delivery vehicles are thought to release their cargo by osmotic swelling and rupture of the endosome.

**Membrane fusion** describes either the interaction of liposomes or fusogenic peptides with the endosomal membrane. The lipid bilayer of endocytosed liposome-based delivery vehicles can fuse with the endosomal membrane and release the endosomal content into the cytosol.<sup>[5]</sup> Fusogenic peptides undergo a conformational change when the pH value is decreased in the endosome. For example, haemagglutinin, an influenza virus coat peptide, changes its conformation from negative hydrophilic coil at physiological pH to a hydrophobic helical conformation under acidified endosomal conditions. The adapted hydrophobic helical conformation leads to fusion of the peptide with the endosomal membrane, followed by rupture and leakage.<sup>[46]</sup>

**Membrane destabilization or disruption** is a hypothesis, which describes local charge-charge and/or hydrophilic interactions of either CPPs, cationic polymers, or the respective transporter-cargo conjugate, with the endosomal membrane. These electrostatic interactions can lead to local destabilization and permeability or local disruption of the endosomal membrane.<sup>[5]</sup>

**Vesicle budding and collapse** describes an escape mechanism, in which CPPs bind to the endosomal membrane, generate CPP-enriched lipid domains, which bud off and form small CPP and cargo enriched vesicles. The vesicular budding off is facilitated by accumulation of the CPPs at the budding neck. Thus, increased binding affinity between CPP and the membrane enhances the vesicle formation. For example, acidification of the endosomal content leads to increased membrane binding affinity of arginine-rich peptides, resulting in increased vesicle formation and pinch-off. The vesicular content is then released into the cytosol after disintegration and collapse of the vesicles. In contrast to the other proposed mechanisms, vesicle budding and collapse leaves the endosome intact and can happen multiple times.<sup>[5]</sup>

The reported endosomal escape mechanisms are hypotheses trying to explain the respective modes of action of the different delivery strategies. For CPP-mediated endosomal escape, the membrane fusion, membrane destabilization and disruption, as well as the vesicle budding and collapse mechanisms are thought to be the most suitable variants.<sup>[5, 46]</sup> Especially the vesicle budding and collapse mechanism seems to be suitable, particularly to cyclic arginine-containing peptides.<sup>[47]</sup>

### 1.3 Brief success of CPPs and peptides applied in this work

To date, a vast number of CPPs have been reported in the literature. A big part of effective CPPs is represented by arginine-rich peptides, whose translocation efficiency can be further increased by cyclization (cyclic CPP (cCPP)).<sup>[50]</sup> It has been shown that linear TAT peptide, covalently conjugated to GFP, did not lead to efficient translocation in living HeLa cells, while cyclic TAT conjugated to GFP was able to mediate cell entry, starting at conjugate concentrations of 50  $\mu\text{M}$ .<sup>[51]</sup> Another study revealed the potential of cyclic TAT to promote cellular delivery of functional nanobodies at low micromolar concentrations. The replacement of cyclic TAT by relatively simple cyclic poly-arginine (cR10) peptide threefold increased the intracellular delivery of conjugated nanobodies. Thus, for construction of cell-permeable protein conjugates, cR10 seems to be preferable over cyclic TAT.<sup>[52]</sup> Furthermore, the potency of cCPPs was validated, when cR10 was shown to efficiently transport mCherry protein to desired

---

intracellular loci, such as the actin cytoskeleton or the nucleus. Therefore the respective localization peptide sequence was fused to the protein and the cCPP was conjugated via an intracellularly cleavable linker.<sup>[53]</sup>

Another approach in terms of CPP-enhanced intracellular delivery was introduced by Mier and coworkers.<sup>[54]</sup> A tetrameric CPP construct was attached to two different antibodies, matuzumab and trastuzumab, as well as to ado-trastuzumab-emtansine ADC, namely *Kadcyla*<sup>®</sup>. Eight different CPP (homo)tetramers were analyzed, among them tetramers composed of TAT, nona-arginine, or penetratin. The tetrameric-TAT variant was the most promising one. It was able to fourfold increase the internalization efficiency of matuzumab-tetrameric-TAT construct compared to matuzumab alone and a threefold increase was determined compared to a matuzumab-monomeric-TAT variant. Similar findings were made for the conjugates comprising trastuzumab and *Kadcyla*<sup>®</sup>. Additionally, the tetrameric-TAT conjugate showed strongly increased cytotoxicity of *Kadcyla*<sup>®</sup>, with a sixfold lower EC<sub>50</sub> compared to solitary *Kadcyla*<sup>®</sup>.<sup>[54]</sup>

Beside the arginine-rich peptides, CPPs based on pH-sensitive endosomolytic peptides were comparably reported. A prominent representative of pH-sensitive peptides is the synthetic GALA-peptide, which was extensively studied and efficiently applied for gene delivery.<sup>[55]</sup> A strategy pursued by Futaki and coworkers is to make use of haemolytic cationic peptides.<sup>[56]</sup> Insertion of glutamate (Glu) residues into the hydrophobic helix-face attenuates their membrane lytic behavior in extracellular environment, which is restored upon protonation in acidified endosomes. The M-lycotoxin derived L17E peptide<sup>[56]</sup> is one subject of this work and discussed in detail in the following section. In subsequent investigations, the relevance of the position of glutamate insertion was further analyzed and Glu insertion between hydrophobic and hydrophilic faces of lytic peptides, such as melittin, showed even more promising results in intracellular delivery of proteins.<sup>[57]</sup> Membrane-lytic peptides also showed their potential when applied as fusion peptide. Combining a membrane-lytic peptide with a peptide that induces macropinocytotic uptake, was reported to efficiently mediate cytoplasmic delivery of protein and nucleic acid cargo upon coinubation.<sup>[58]</sup>

In the latter strategies, cell-penetrating peptide mediated cargo delivery was based on coinubation of CPP and cargo. An alternative approach that has been shown to efficiently mediate intracellular delivery, was the introduction of a covalent connection between CPP and cargo molecule.<sup>[51-52, 59]</sup> Based on covalent linkage between a CPP and a cargo, some CPPs have shown enhanced cellular uptake when presented in multiple copies on a suitable scaffold, as reported for both arginine-rich and arginine-lacking CPPs.<sup>[60]</sup> However, increased delivery efficiency was accompanied by simultaneous increase of cytotoxicity. A similar multivalency effect was also observed in case of a dextran scaffold, which was equipped with multiple copies of nonaarginine. The construct was reported to efficiently deliver a proapoptotic peptide into the cytoplasm of human Jurkat cells,<sup>[61]</sup> while its cytotoxicity was strongly increased compared to monomeric nonaarginine.<sup>[62]</sup>

### 1.3.1 Antimicrobial peptide aurein 1.2

Antimicrobial peptides (AMPs) represent a broad class of host defence peptides, which can be found in nearly all organisms from prokaryotes to plants, animals, and humans. They are known to have selective defence activity against bacteria, fungi, yeast, and viruses, while only showing minimal toxicity towards mammalian cells. These water-soluble membrane-active and perturbing peptides, with a length between 10 and 50 amino acid residues, commonly possess positively charged amino acids as well as the hydrophobic ones and adopt an amphipathic secondary structure, at least when interacting with membranes.<sup>[63]</sup> Natural AMPs with defined activity and sequence are registered in *The Antimicrobial Peptide Database*<sup>[64]</sup> which comprises more than 3000 AMPs, to date.

Aurein 1.2 comprises 13 amino acid residues (GLFDIHKIAESF-NH<sub>2</sub>) and is secreted in the dorsal skin glands of the Southern bell frog *Litoria raniformis*.<sup>[65]</sup> It was reported to be the most bioactive peptide of the aurein family and the shortest anuran peptide which exhibits both antibiotic and anticancer activity.

---

Meanwhile, it does not affect red blood cells in concentrations up to  $100\ \mu\text{g}\times\text{mL}^{-1}$ , which is above the required concentration for antibacterial and anticancer activity. Proved by NMR analysis, the membrane-active peptide, when located in membrane environment, adopts an  $\alpha$ -helical and amphipathic structure with well-defined hydrophilic and hydrophobic areas.<sup>[66]</sup> The membrane perturbing activity of aurein 1.2 was thought to be based on interaction with membranes according to the carpet mechanism.<sup>[67]</sup>

As reported in the literature,<sup>[68]</sup> featuring membrane perturbing activity, aurein 1.2 has the ability to act as an agent that enhances the intracellular delivery of proteins into the cytoplasm by mediating endosomal escape of endocytosed proteins. A Cre-recombination assay, generating tdTomato fluorescence upon nuclear Cre delivery, was performed. It turned out, that the antimicrobial aurein 1.2 peptide, fused to supercharged GFP-Cre fusion protein, tenfold increased the cytoplasmic respectively nuclear delivery of the construct compared with supercharged GFP-Cre fusion protein lacking conjugated aurein 1.2. In doing so, the cell viability was nearly not affected. Additionally, similar findings were reported for nonendosomal protein delivery *in vivo*. Conjugated aurein 1.2 was able to 20-fold increase the delivery of supercharged GFP-Cre recombinase enzyme into the hair cells of the inner ear of live Cre-reporter transgenic mice, leading to tdTomato fluorescence upon recombination.

These results suggest the antimicrobial peptide aurein 1.2 to be a possible candidate to mediate cytoplasmic protein delivery by enhancing the endosomal escape of entrapped cargo upon endocytic uptake.

### 1.3.2 M-lycotoxin derived peptide L17E

Recently, a novel lipid-sensitive endosomolytic peptide derived from M-lycotoxin was introduced by the Futaki working group.<sup>[56]</sup> M-lycotoxin is an antimicrobial and haemolytic cationic peptide with amphiphilic  $\alpha$ -helical structure, identified from the wolf spider *Lycosa carolinensis* venom.<sup>[69]</sup> Starting from this highly membrane-lytic peptide, they inserted one or two glutamic acid residues in the hydrophobic face of the helix. The idea behind the Glu insertion was, that at physiological pH the negatively charged Glu residue prevents hydrophobic interaction with the cell membrane and thus reduces the lytic activity. Meanwhile, the cationic residues in the hydrophilic face of the helix were thought to still enable the electrostatic interaction with the cellular membrane, leading to the uptake and entrapment in the endosome. In the acidified endosomal environment, protonation of the Glu residue was thought to recover the hydrophobic face and thus the membrane-perturbing activity. Additionally, the cationic character of the peptide was thought to lead to enhanced electrostatic interaction with the more negatively charged endosomal membrane compared with the cell membrane. These features should give the peptide the ability to selectively disrupt endosomal membranes and enable entrapped cargo to reach the cytosol.<sup>[56]</sup>

One M-lycotoxin variant L17E (IWLTKLFLGKHAAKHEAKQQLSKL-NH<sub>2</sub>), with replacement of leucine by glutamic acid, showed a 30-fold diminished cytotoxicity compared to M-lycotoxin and successfully enabled cytoplasmic delivery of functional proteins from Cre recombinase up to full-length antibodies upon coincubated with  $40\ \mu\text{M}$  peptide.<sup>[56]</sup> Interestingly, in contrast to the intended effect of Glu insertion, L17E showed no pH-sensitive membrane disruption. Nevertheless, the membrane perturbation was endosome-selective, presumably as a result of the electrostatic interaction of the cationic peptide with the endosomal membrane.<sup>[56]</sup>

Further analysis by Futaki and coworkers led to introduction of a novel major uptake mechanism (Figure 7) of L17E-mediated cytoplasmic delivery: transient membrane permeabilization.<sup>[70]</sup> Accordingly, the interaction of L17E with the plasma membrane assumedly induces actin rearrangement, which causes membrane ruffling followed by macropinocytosis. Applying different inhibitors, it turned out that inhibition of actin polymerization and membrane ruffling both led to inhibited L17E-mediated macromolecule uptake, while inhibition of membrane fusion prior to macropinosome formation did not affect L17E-mediated uptake. Therefore, L17E was thought to rupture the ruffled membrane before macropinosome formation is accomplished. Thus, L17E paves the way of direct cargo entry into the

cytoplasm without involving macropinosomes or endosomal pathway. The proposed novel concept of permeabilization mechanism via actin-mediated membrane ruffling differs from known mechanisms like direct translocation across the cell membrane or endocytic uptake followed by endosomal escape.<sup>[70]</sup>

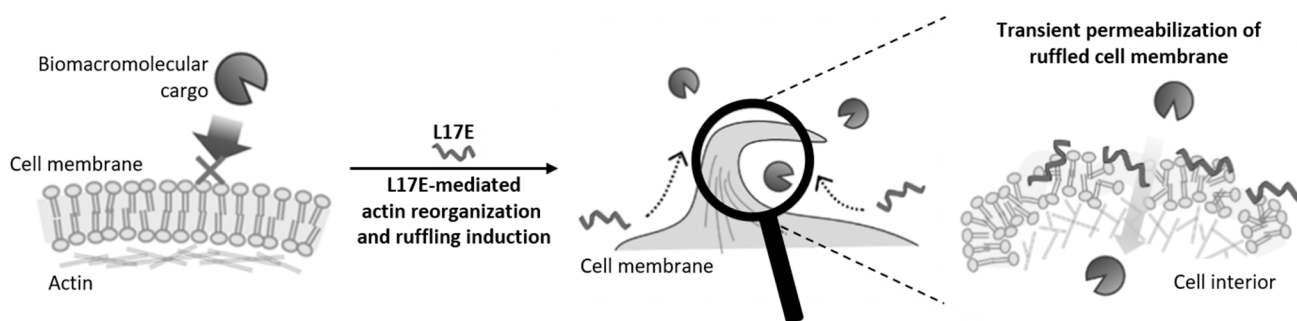


**Figure 7:** L17E-mediated cytoplasmic delivery of biomacromolecular cargoes via transient cell membrane permeabilization upon L17E-induced actin reorganization. Uptake mechanism introduced by and depiction adapted from Futaki and coworkers.<sup>[70]</sup>

These promising ability of M-lycotoxin variant L17E to mediate cytoplasmic delivery of macromolecular cargo up to antibodies upon coincubation suggest the peptide to be a possible candidate for generation of a transport vehicle for intracellular delivery of biomacromolecules.

#### 1.4 Dextran as versatile scaffold for multimerization of cargo

Dextran is a hydrophilic and biocompatible polysaccharide produced by bacteria such as *Leuconostoc mesenteroides*. It is composed of D-glucose repeating units linked via  $\alpha$ -(1-6) glycosidic bonds with little amount of branching via  $\alpha$ -(1-3) connection (**Figure 8**). In case of *L. mesenteroides* dextran is a predominant linear polymer with only 5% branched (1-3) linkages.<sup>[71]</sup>

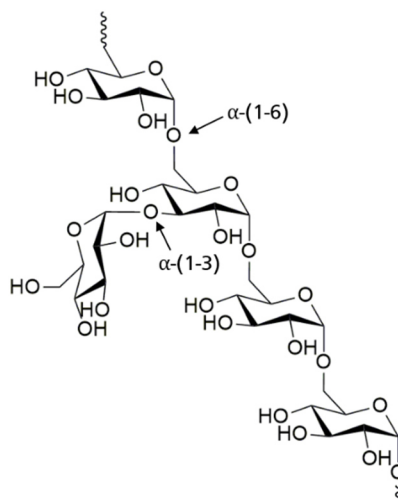


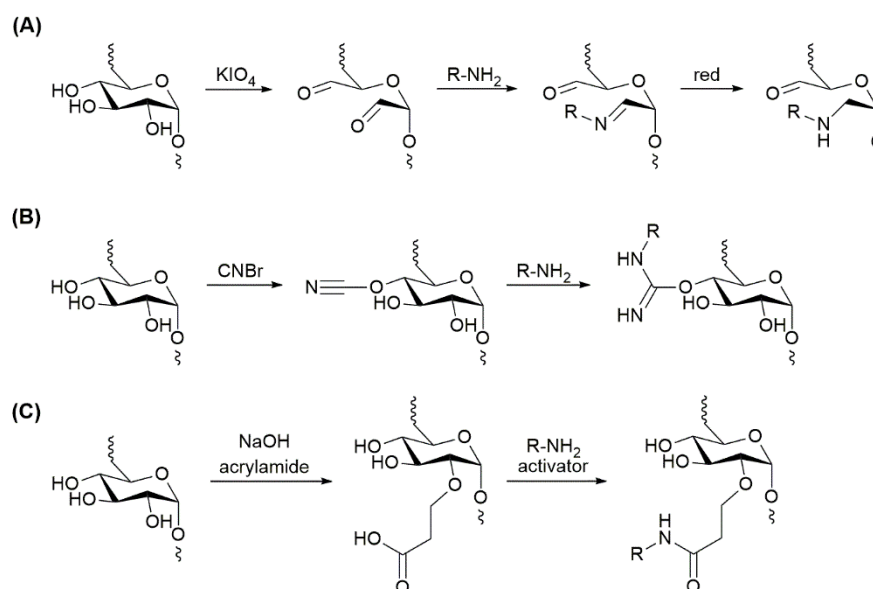
**Figure 8:** Structure of dextran polysaccharide showing linear  $\alpha$ -(1-6) glycosidic bonds of the D-glucose repeating units with little branching of  $\alpha$ -(1-3) linkages.

In the clinic, FDA-approved solutions containing dextran with either 40 kDa or 70 kDa average molecular weight, are used as blood-flow enhancer as well as plasma volume expander. Dextran is always a mixture of polysaccharide chains of different length. The molecular mass distribution is characterized by the degree of polydispersity, which is the quotient of weight average to number average molecular weight. For use in research, dextran with an average molecular weight between 4 and 200 kDa and polydispersity of approximately 1.5 is commercially available.<sup>[72]</sup> The good water solubility, biocompatibility, stability

under mild acidic and basic conditions, as well as the numerous possibilities for chemical modification, make this polymer an attractive carrier of different cargo from drugs to proteins.<sup>[72]</sup> Thereby, dextran does not only act as carrier, in addition it is able to improve properties of the conjugated cargo. For example, it can reduce immunogenicity of conjugated proteins,<sup>[73]</sup> improve their bioavailability<sup>[74]</sup> or plasma half-life,<sup>[75]</sup> and is a valuable, solubility-mediating tool for generation of antibody-drug conjugates (ADCs) with high drug-to-antibody ratio, called Dextramabs.<sup>[76]</sup>

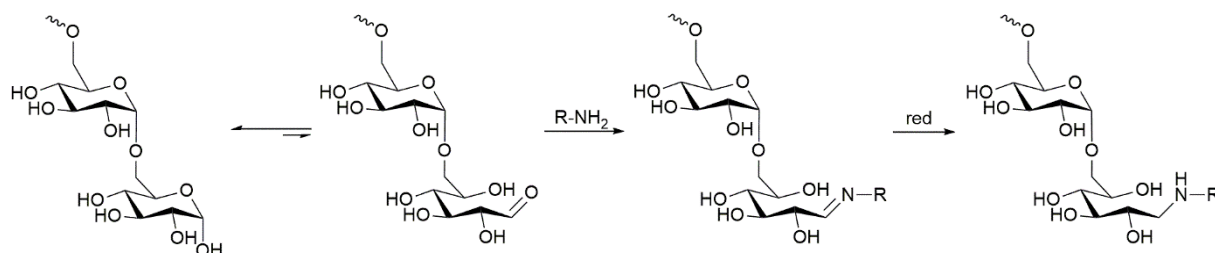
Several possibilities exist for chemical modification of dextran. The large number of hydroxyl groups at the glucose repeating units can be addressed in different ways. For example, periodate oxidation leads to opening of the glucose ring and formation of a dialdehyde, which can be further addressed with amine groups. The formed *Schiff* bases are subsequently stabilized by reduction (**Scheme 1 (A)**). The hydroxyls can also get activated with cyanogen bromide and afterwards addressed with an amine counterpart (**Scheme 1 (B)**). Both strategies have their drawbacks by creating unspecific heterogenic product mixtures and different byproducts.<sup>[71, 75b]</sup>

An elegant method is the carboxyethylation of dextran, which selectively introduces carboxy functionalities at the glucose C2 hydroxy groups. Thereby the ratio of introduced carboxy groups per dextran can be adjusted by regulating the amount of applied acrylamide starting material.<sup>[61]</sup> In a following step, the yielded 2-carboxyethyl-dextran (2-CED) is accessible for further modification via amide-bond formation with amine-functionalized molecules of interest (**Scheme 1 (C)**).<sup>[61, 76]</sup>



**Scheme 1:** Different strategies for chemical modification of hydroxy groups of glucose repeating units: **(A)** periodate oxidation and subsequent addressing of the dialdehyde with amine functionality; **(B)** cyanogen bromide activated amine conjugation; **(C)** glucose C2-hydroxy selective carboxyethylation followed by amide bond formation with amine-functionalities.<sup>[61, 71, 75b, 76]</sup>

In addition to the glucose repeating units, the dextran polysaccharide provides a second addressable conjugation site, its reducing end. The terminal glucose unit differs from the remaining glucose units in the C1 hydroxy group, the hemiacetal group, which is not involved in glycosidic bond and therefore addressable with nucleophiles. The cyclic hemiacetal form of the terminal glucose unit is in equilibrium with the open free aldehyde form, which is addressable with amine functionalized agents. Upon nucleophilic attack of the amine to the carbonyl group an imine (*Schiff* base) is formed and subsequently reduced into the stable amine (**Scheme 2**). Due to the low amount of free aldehyde form at equilibrium compared to the cyclic hemiacetal form, the process of reductive amination is slow and proceeds several days.<sup>[77]</sup>



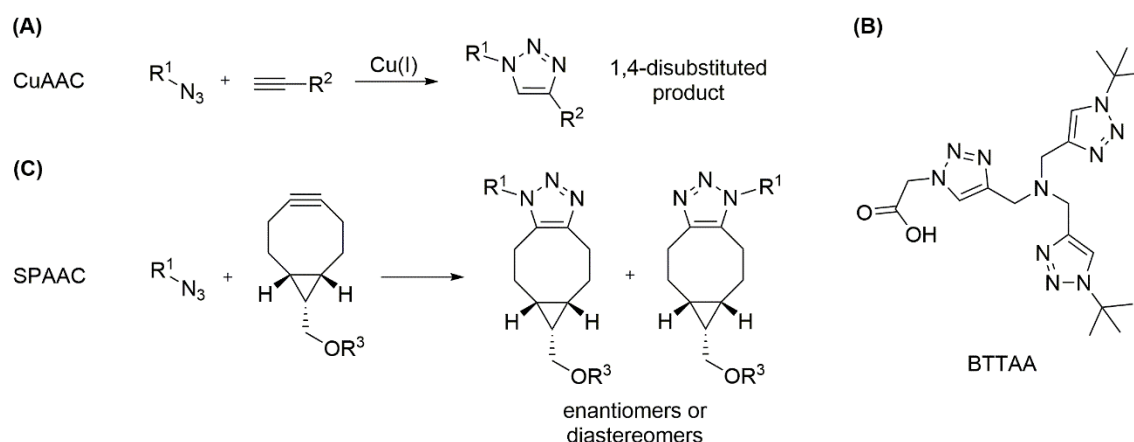
**Scheme 2:** Modification of the polysaccharide reducing end via reductive amination: Schiff base formation followed by reduction into the stable amine.<sup>[77]</sup>

In general, as reported in the literature,<sup>[76, 78]</sup> the beneficial properties of dextran, such as hydrophilicity, flexibility, or multiple functionalization possibilities, make dextran a versatile scaffold for conjugation of various cargo in multiple copies. The orthogonal dextran modification scheme, which combines addressing the polysaccharide reducing end via reductive amination and carboxyethylation of the glucose repeating units, enables decoration of dextran with adjustable amount of cargo molecules and simultaneous protein conjugation at the reducing end. Thus, this multivalent scaffold was successfully used for generation of potent ADCs with high drug-to-antibody ratio<sup>[76]</sup> and as tumor cell apoptosis inducing multimerization platform, equipped with multiple receptor-binding peptides.<sup>[78]</sup>

## 1.5 Chemical and biological conjugation methods: A brief overview

### 1.5.1 Copper-catalyzed and strain-promoted azide-alkyne 1,3-cycloaddition

The copper(I)-catalyzed azide-alkyne cycloaddition (CuAAC) can be seen as the prototype of the “click-chemistry” concept, established by Sharpless and coworkers in 2001.<sup>[79]</sup> The 1,2,3-triazole-forming azide-alkyne 1,3-dipolar cycloaddition was investigated in detail by Huisgen in the 1960s.<sup>[80]</sup> Later, two groups found out independently, that addition of copper(I) not only strongly accelerated the 1,3-cycloaddition but also selectively yielded the 1,4-disubstituted 1,2,3-triazole regioisomer (**Scheme 3 (A)**), while the original Huisgen reaction leads to 1,4- and 1,5-disubstituted regioisomer mixture.<sup>[81]</sup> One major drawback of the broad applied CuAAC is the toxicity of copper species towards biological systems. The use of Cu(I)-binding ligands, such as 2-(4-((bis((1-*tert*-butyl)-1H-1,2,3-triazol-4-yl)methyl)amino)methyl)-1H-1,2,3-triazol-1-yl)acetic acid (BTAA) (**Scheme 3 (B)**), maintains the Cu(I) oxidation state, thus accelerating the reaction speed and simultaneously protecting biological systems or biomolecules by preventing oxidative damage.<sup>[82]</sup>

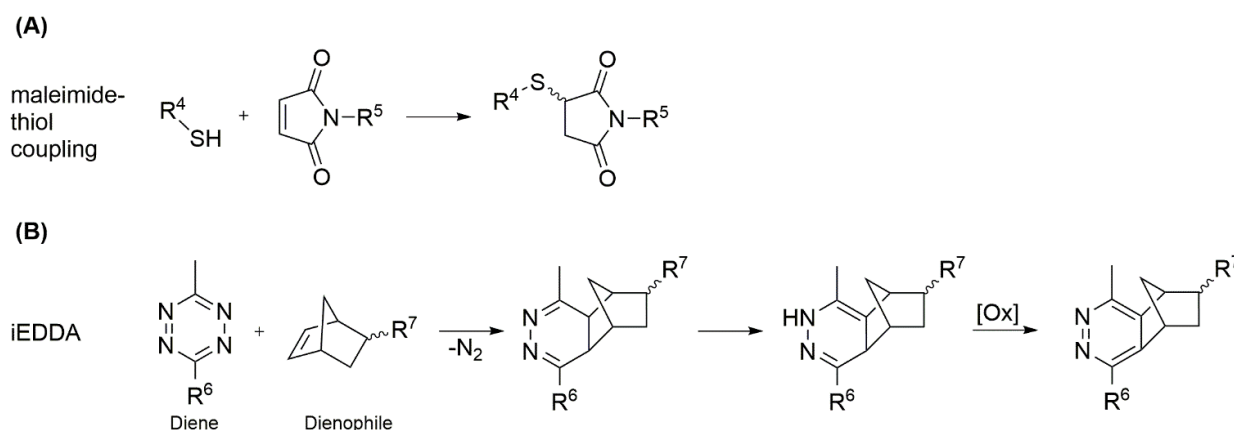


**Scheme 3:** General reaction scheme of **(A)** Cu(I)-catalyzed (CuAAC)<sup>[81]</sup> and **(C)** strain-promoted (SPAAC)<sup>[83]</sup> azide-alkyne cycloaddition. SPAAC shows cycloaddition applying BCN derivative; **(B)** Cu(I)-binding ligand BTAA.<sup>[82]</sup>

To circumvent the problem of copper toxicity, bioorthogonal conjugation methods were introduced by Bertozzi and coworkers: Bioorthogonality means, the reaction and the involved functional groups are nontoxic and compatible with biological systems, do not interact or interfere with them, and the specific and high reactivity is retained under biocompatible conditions.<sup>[83b, 84]</sup> One prominent representative of bioorthogonal conjugation methods is the strain-promoted azide-alkyne 1,3-cycloaddition (SPAAC), which fulfills all requirements of bioorthogonality. Similar to CuAAC, SPAAC is based on the reaction between azide and alkyne functionalities. However, due to the pre-activated nature of the alkyne functionalities in strained cyclooctynes, there is no more need for copper(I) catalyst.<sup>[83b]</sup> Various ring-strained cyclooctynes have been reported and successfully used,<sup>[85]</sup> among them bicyclo[6.1.0]nonyne (BCN).<sup>[83a]</sup> An advantage of SPAAC applying BCN is the formation of a single regioisomer only, while most cyclooctyne derivatives form a regioisomer product mixture. Due to the nature of BCN, its SPAAC conjugation product is a mixture of enantiomers or diastereomers (**Scheme 3 (C)**), depending on the chirality of the azide counterpart. However, the isomer formation is usually not seen as drawback in bioorthogonal conjugation.

### 1.5.2 Maleimide chemistry and inverse electron-demand Diels-Alder reaction

Maleimide-thiol chemistry is a well-known and widespread method in bioconjugation. It is based on addressing a maleimide functionality with a free thiol moiety following a Michael-type addition (**Scheme 4 (A)**).<sup>[86]</sup> Despite some drawbacks, such as retro-Michael addition of the thiosuccinimide product or thiol exchange reaction, this practicable conjugation method is not only frequently applied in bioinspired research, but also used for assembly of clinically approved ADCs brentuximab vedotin and adotrastuzumabemtansine.<sup>[86-87]</sup>

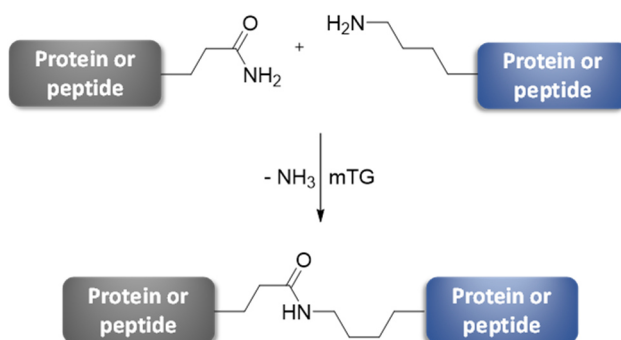


**Scheme 4:** General reaction scheme of maleimide-thiol conjugation<sup>[86]</sup> and inverse electron-demand Diels-Alder reaction.<sup>[88]</sup>

Recently, the inverse electron-demand Diels-Alder reaction (iEDDA), cycloaddition of 1,2,4,5-tetrazines acting as electron-poor diene and electron-rich dienophiles, became more and more important. Starting with the reaction of tetrazines with unsaturated compounds, known as Carboni-Lindsey reaction,<sup>[89]</sup> iEDDA emerged as the state-of-the-art method for totally bioorthogonal and metal-free “click”-conjugation of biomolecules.<sup>[88]</sup> The electron-deficient heterocyclic tetrazine-derivative reacts with diverse electron-rich dienophiles, ranging from *trans*-cyclooctene (TCO), over BCN, and norbornene to cyclopentene, following a Diels-Alder [4+2] cycloaddition with inverse electron-demand. Following this rate-determining step, a *retro*-Diels-Alder reaction releases nitrogen, what makes the conjugation irreversible. Subsequent isomerization yields the 1,4-dihydropyridazin product (**Scheme 4 (B)**). In presence of oxidative agents, the respective pyridazine-derivative is formed. The oxidation step is not crucial, if using iEDDA as conjugation method. Beside beneficial properties such as biocompatibility, selectivity, irreversibility, high yield and full orthogonality to other conjugation methods, such as CuAAC or SPAAC even in one-pot reactions,<sup>[88d]</sup> iEDDA conjugation stands out for its remarkably fast reaction kinetics. iEDDA conjugation reaches reaction rates of notable  $3.8 \times 10^5 \text{ M}^{-1}\text{s}^{-1}$ , applying TCO<sup>[88d]</sup> and still

1-10 M<sup>-1</sup>s<sup>-1</sup>, applying more stable but less reactive norbornene counterpart,<sup>[88d, 90]</sup> while SPAAC using BCN only reaches rates of 0.1 M<sup>-1</sup>s<sup>-1</sup>.<sup>[83b]</sup>

### 1.5.3 Microbial transglutaminase



**Scheme 5:** mTG mediated bond formation between glutamine side chain, acting as acyl donor and  $\epsilon$ -amine of lysine, acting as acyl acceptor.

Transglutaminases are bond-forming enzymes, which belong to the  $\gamma$ -glutamyltransferases and can be found in microorganisms, plants, invertebrates, fish, birds, and mammals. In nature, the enzyme modifies proteins by intramolecular cross-linking or by intermolecular isopeptide bond formation. To this end, it catalyzes the ammonia-releasing transamidation between  $\gamma$ -carboxamides of glutamine side chains (acyl donor) and primary  $\epsilon$ -amine groups of lysine side chains (acyl acceptor) (**Scheme 5**). Several transglutaminases with diverse biological functions have been found in humans, such as fibrin clots stabilizing factor XIIIa or transglutaminase 2, which shapes the extracellular matrix and is involved in pathogenesis of celiac disease.<sup>[91]</sup>

Regarding biotechnological applications, bacterial transglutaminases have several advantages such as cofactor independency, small size, and reduced deamidation activity (side reaction, converting glutamines in glutamic acid).<sup>[91b, 92]</sup> One of the most intensive studied variants is microbial transglutaminase (mTG) from *Streptomyces mobaraensis*. Beside its use in food industry, mTG gained interest for biotechnological and pharmaceutical applications and became a versatile and frequently used tool for site-specific bioconjugation.<sup>[91b, 92]</sup> mTG-mediated formation of protein-protein,<sup>[93]</sup> protein-DNA,<sup>[94]</sup> and protein-polymer<sup>[95]</sup> conjugates have been reported as well as the mTG-catalyzed assembly of ADCs.<sup>[76, 96]</sup> For enzymatic recognition, the acyl donor glutamine must be located in a suitable recognition sequence. Beside the primary structure, the secondary structure as well as flexibility in the sequence motif have impact on the mTG specificity. Regarding acyl acceptor substrate specificity, mTG is quite promiscuous. Besides the natural lysine substrate and aliphatic amines, mTG also accepts primary amines, functionalized with azide or alkyne moieties. Thus, mTG conjugation enables site-specific introduction of “click”-chemistry functionalities into biomolecules.<sup>[91b, 92]</sup>

### 1.5.4 Lipic acid protein ligase A

Lipoic acid protein ligase A (LplA) is a ligation enzyme that is involved in the oxidative metabolism in *Escherichia coli*. Dependent on ATP and Mg<sup>2+</sup>, it catalyzes the amide bond formation between lipoic acid and specific lysine residues of three acceptor proteins in *E. coli*.<sup>[97]</sup> Beside the natural substrate specificity for lipoic acid, LplA shows substrate promiscuity and has been reported to accept carboxylic acid derivatives, among them azide functionalized carboxylic acids.<sup>[98]</sup> A specific recognition sequence in form of a 13 amino acid lipoic acid acceptor peptide (LAP) has been engineered, that can be fused to proteins of interest.<sup>[97b, 98]</sup>



cellular permeability and are not effectively taken up by cells. Therefore, efforts have been made for intracellular respectively nuclear PNA delivery, including CPP-based strategies.<sup>[106]</sup>

The mis-splicing correction assay is based on HeLa-eGFP654 cells, which are stably transfected with enhanced green-fluorescent protein (eGFP) gene. The introduced eGFP gene is interrupted by an inserted mutant intron 2 of human  $\beta$ -globin (IVS2-654). This leads to activation of an aberrant splice site at position 654, resulting in translation of non-functional eGFP due to retention of intron fragment in the spliced mRNA. Antisense oligomers, directed towards position 654, such as the 18-mer PNA (gctattacctaaccag), restore correct splicing upon hybridization, finally leading to production of functional eGFP (**Figure 11**).<sup>[107]</sup> Thus, emerging eGFP fluorescence validates cytoplasmic delivery and nuclear translocation of PNA biomolecules. A similar assay, using luciferase reporter instead of eGFP, has already been reported for CPP-mediated PNA uptake studies.<sup>[106, 108]</sup>

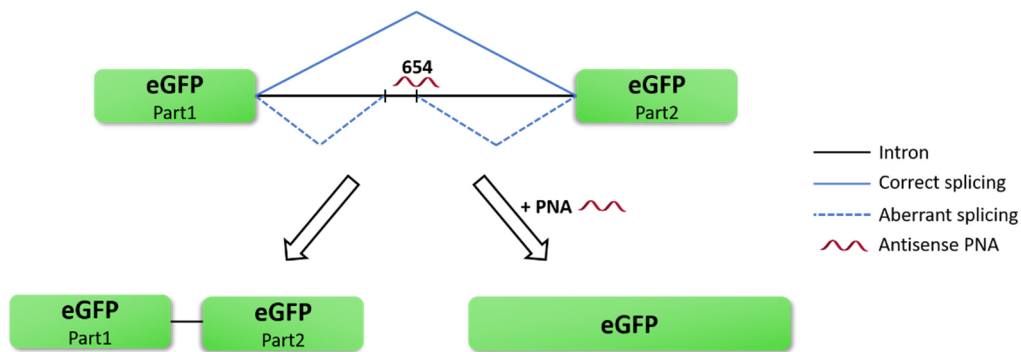


**Figure 11:** Schematic depiction of aberrant splicing and mis-splicing correction upon hybridization of antisense PNA. Adapted from<sup>[107]</sup>

---

## 2 Objective

---

The present work was aimed at the development of an approach for cytoplasmic delivery of biomolecular cargoes. Novel pharmaceutical agents based on biologicals, such as peptides, proteins, or nucleic acids, are often limited to extracellular targets as these molecules are not able to cross the plasma membrane and to reach the cytosol. To overcome this limitation and to expand their potential application range towards intracellular targets, development of efficient delivery systems is of great importance.

To this end, the capability of two different cell-penetrating peptides to mediate intracellular uptake of covalently conjugated biomacromolecular cargo should be investigated. Since it turned out that both CPPs did not succeed in enhancing intracellular uptake when conjugated to model cargo as a solitaire, it should be studied whether oligomerization of the CPPs on a suitable scaffold can improve delivery. For that purpose, hydrophilic dextran polysaccharide should be functionalized in multivalent fashion and decorated with multiple copies of the respective CPP. Upon treatment of mammalian cells, the intracellular distribution of the generated fluorophore-labeled peptide-dextran hybrid macromolecules should be analyzed.

To evaluate the potential application as delivery module, a possible cytotoxic effect of the superior peptide-dextran hybrid, decorated with multiple copies of cationic amphiphilic M-lycotxin variant L17E, should be assessed. Afterwards, the cytosolic and even nuclear uptake of the L17E-dextran hybrid should be validated. To this end, a mis-splicing correction assay should be performed, applying a dextran macromolecule decorated with multiple copies of both L17E peptide units and bioactive peptide nucleic acid cargo molecules.

In the further course of the work, the ability of L17E-dextran module to mediate intracellular delivery of covalently conjugated protein cargo should be investigated in a proof-of-concept study. Applying combinatorial set of orthogonal chemical conjugation methods, the eGFP model protein should be covalently conjugated to the polysaccharide reducing end of L17E-decorated dextran. Following treatment of mammalian cells, intracellular distribution of the compound, combining covalently connected counterparts L17E peptide, dextran, and eGFP model protein, should be examined. Finally, regarding prospective application of L17E-dextran as module for intracellular delivery of functional proteins, assembly of the L17E-dextran-protein conjugate should be evolved towards more sophisticated dextran-to-protein conjugation. To this end, the chemical functionality, required for subsequent linkage with the polysaccharide reducing end, should be introduced into the model protein, applying site-specific enzyme catalysis.

## 3 Results and Discussion

### 3.1 Aurein1.2-mediated cytosolic delivery

#### 3.1.1 Design of a multicomponent model conjugate: Trastuzumab-aurein1.2-doxorubicin 1

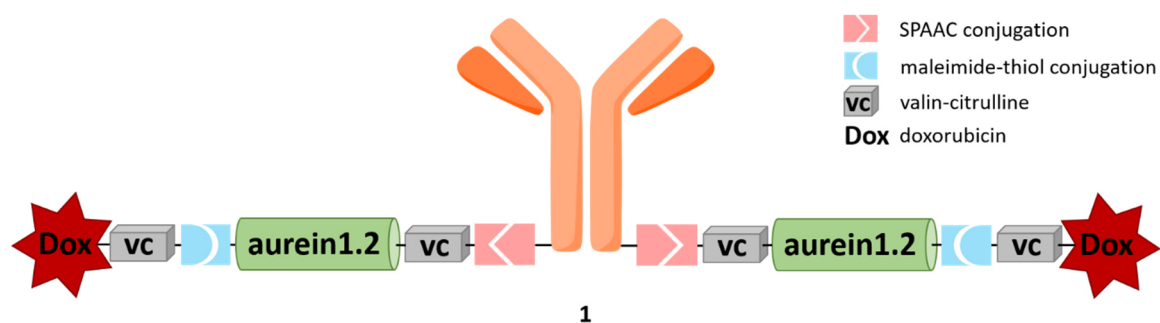


**Figure 12:** Schematic depiction of the multicomponent model conjugate Trastuzumab-aurein1.2-doxorubicin 1.

The antimicrobial and membrane-lytic peptide aurein1.2 was reported<sup>[68]</sup> to enhance the intracellular delivery of proteins into the cytoplasm by enhancing endosomal escape of endocytosed proteins. The aim of this part of the work was the verification of the membrane-perturbing ability of aurein1.2 on basis of a multicomponent synthetic model conjugate **1** (**Figure 12**). To investigate, whether the covalent incorporation of aurein1.2 possibly led to enhanced intracellular delivery of proteins into the cytoplasm by enhancing endosomal escape, model conjugate **1** was designed. The multicomponent model conjugate design was based on an antibody as targeting protein component, due to the internalization characteristics and mode of action of antibody-drug conjugates (ADCs).<sup>[109]</sup> Briefly: ADCs are targeted therapeutics, which combine the specificity of an antibody and the efficacy of a high potent cytotoxic compound, and where the counterparts are connected via chemical linkers. Following target binding on the cell surface, an ADC is internalized via receptor-mediated endocytosis. As a result, the ADC-receptor complex is entrapped in endosomal compartments. Within the endosome-lysosome pathway, the cytotoxic drug must be cleaved from the antibody, released and enter the cytosol to reach its target. Depending on the type of the linkage used, the drug cleavage can either occur enzymatically in the endosome, chemically under acidic conditions in endosomal/lysosomal compartments, or via lysosomal degradation.<sup>[109]</sup>

The designed conjugate **1** consisted of the monoclonal anti-HER2 antibody trastuzumab, featuring synthetic modules at the heavy chain C-termini, which comprised the antimicrobial peptide aurein1.2 and the cytotoxic drug doxorubicin (Dox). Between all components, a covalent but enzyme-cleavable connection was introduced, applying combination of orthogonal chemical and enzymatic conjugation methods.

It should be investigated, whether the incorporated aurein1.2 component was able to enhance endosomal escape and release of doxorubicin upon endocytosis and entrapment of conjugate **1** in endosomal compartments. Aurein1.2-mediated facilitation of doxorubicin release was thought to increase cytotoxicity of conjugate **1** compared to an equivalent conjugate lacking the aurein1.2 sequence.



comparable constructs involving *para*-aminobenzyloxycarbonyl (PABC) linker.<sup>[110]</sup> PABC has been successfully used as cleavable linker in antibody-drug conjugate research,<sup>[111]</sup> but synthetically is much more difficult to access. A major advantage of PABC is self-immolative and traceless release of the toxin. Applying glycine spacer, the toxin is released non-tracelessly in form of a Gly-Dox compound. However, doxorubicin has been reported<sup>[112]</sup> to still show cytotoxicity when released in a non-traceless fashion; therefore glycine was chosen as steric spacer between Val-Cit cleavage site and doxorubicin in constituent C. Enzymatic cleavage of Val-Cit-Gly site was validated via cathepsin B catalyzed cleavage of a test peptide **5**, containing Val-Cit-Gly sequence. Meanwhile, there is no need for steric spacer following the cathepsin B cleavage site in the aurein1.2 constituent B, due to following amino acid sequence continuing with glycine anyway.

As a negative control, the construct was designed lacking the aurein1.2 sequence. To that end, the 13 amino acid sequence of aurein1.2 in constituent B was replaced by a single glycine-serine spacer, leading to constituent B-negative control (Ac-Orn(N<sub>3</sub>)-VC-GS-Lys(maleimide)-NH<sub>2</sub>) **6** (Figure 14 B-NC).

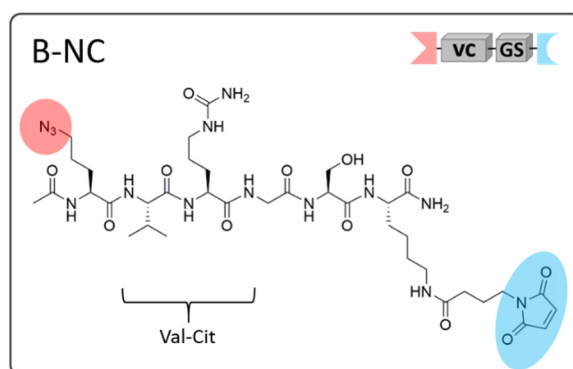
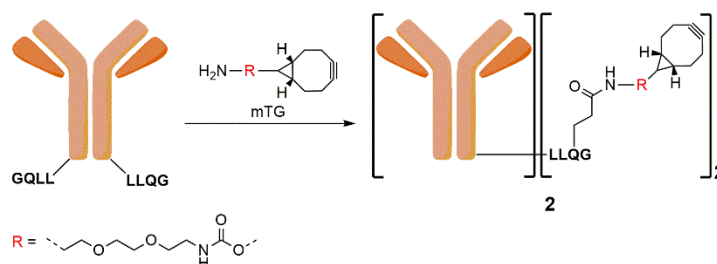


**Figure 14:** Depiction of constituent B-NC (Ac-Orn(N<sub>3</sub>)-VC-GS-Lys(maleimide)-NH<sub>2</sub>) **6** for assembly of a negative control lacking aurein1.2. Schematic abbreviation in the upper right corner.

### 3.1.2 Synthesis of a multicomponent model conjugate

#### 3.1.2.1 Synthesis of constituent A: Trastuzumab-LLQG-BCN **2**



**Scheme 7:** mTG mediated synthesis of constituent A: Trastuzumab-LLQG-BCN **2**.

To incorporate a specific conjugation site addressable in strain-promoted azide-alkyne cycloaddition, the monoclonal antibody trastuzumab, featuring LLQG enzyme recognition tag at the C-termini of the heavy chains, was modified with a BCN functionality in a microbial transglutaminase-catalyzed reaction. To this end, mTG selectively mediated isopeptide bond formation between the glutamine of the LLQG recognition sequence and a BCN-amine derivative, yielding Trastuzumab-LLQG-BCN **2** (constituent A). The product was immobilized on protein A column for purification and the following conjugation step.

### 3.1.2.2 Synthesis of constituent B: Ac-Orn(N<sub>3</sub>)-VC-aurein1.2-Lys(maleimide)-NH<sub>2</sub> **3** and constituent B-NC: Ac-Orn(N<sub>3</sub>)-VC-GS-Lys(maleimide)-NH<sub>2</sub> **6**

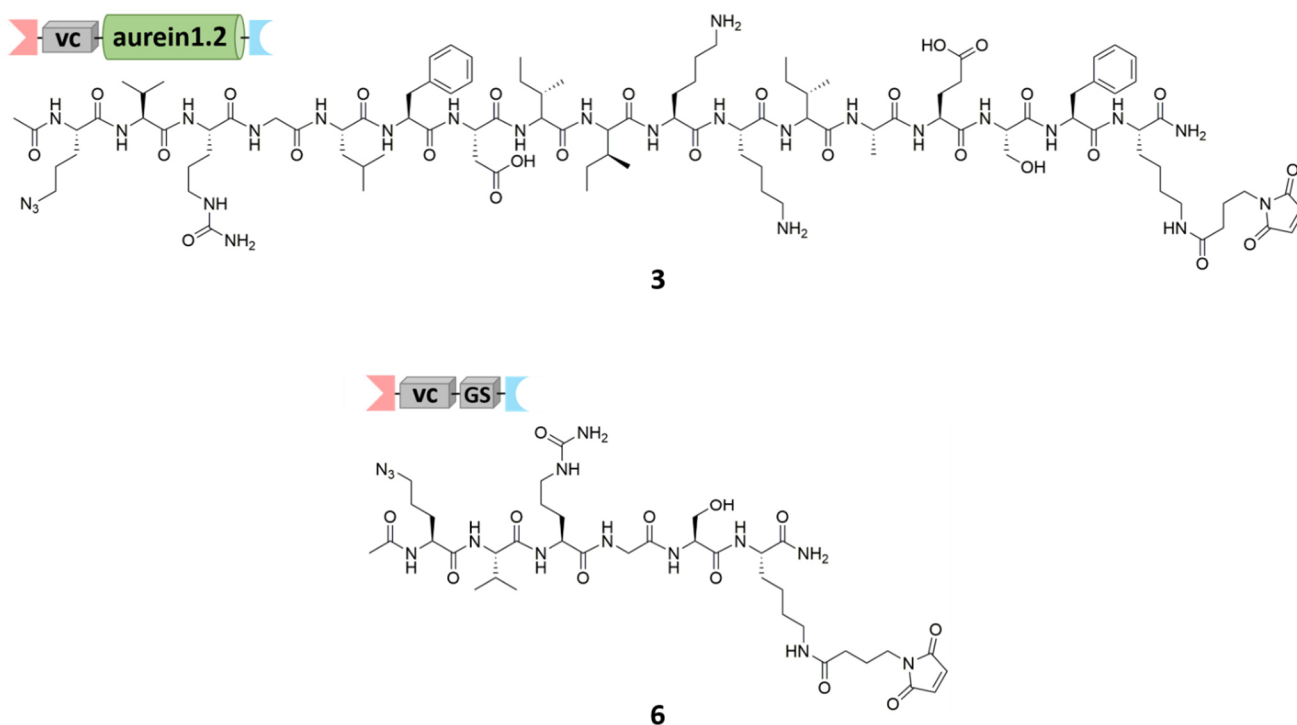


**Figure 15:** Structure of constituent B: Ac-Orn(N<sub>3</sub>)-VC-aurein1.2-Lys(maleimide)-NH<sub>2</sub> **3** and constituent B-NC: Ac-Orn(N<sub>3</sub>)-VC-GS-Lys(maleimide)-NH<sub>2</sub> **6**.

To enable selective conjugation, two orthogonal functionalities accessible for azide-alkyne cycloaddition and maleimide-thiol Michael-type addition, were incorporated into the peptide sequence of constituent **B 3**. To this end, the *N*-terminus of aurein1.2 was extended with azide modified ornithine as well as valine and citrulline forming an enzyme cleavage site. The *C*-terminus was extended with an additional lysine, whose  $\epsilon$ -amine was converted into a maleimide functionality. Acetylation of the *N*-terminus prevented side reactions during incorporation of the maleimide moiety. Constituent B-NC **6** lacked the aurein1.2 sequence, which was replaced by unfunctional glycine-serine linker.

Both peptides Ac-Orn(N<sub>3</sub>)-VC-aurein1.2-Lys(maleimide)-NH<sub>2</sub> **3** and Ac-Orn(N<sub>3</sub>)-VC-GS-Lys(maleimide)-NH<sub>2</sub> **6** were synthesized via standard 9 fluorenyl-methoxycarbonyl (Fmoc) solid-phase peptide synthesis (SPPS). Application of Fmoc-lysine building block, bearing 4,4-dimethyl-2,6-dioxocyclohex-1-ylidene ethyl (Dde)  $\epsilon$ -amine protection, enabled on-resin introduction of a maleimide functionality via amide bond formation with 4-maleimidobutyric acid. Following cleavage from the solid support and purification, the obtained peptides **3** and **6** were validated via mass spectrometric analysis (see section 7.6.1 and 7.6.2).

### 3.1.2.3 Synthesis of constituent C: Ac-Cys-Val-Cit-Gly-Dox 4

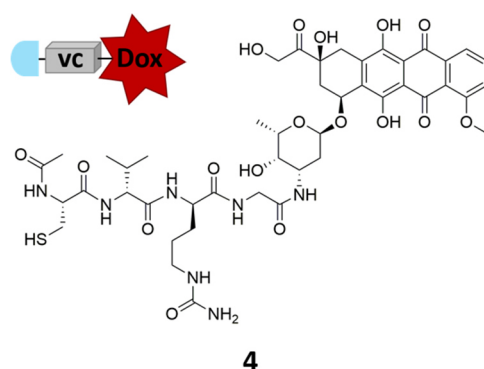


Figure 16: Structure of constituent C: Ac-Cys-VC-Gly-Dox 4.

To synthesize constituent C 4 comprising *N*-terminal cysteine, valine-citrulline cleavage site, glycine spacer, and *C*-terminally attached doxorubicin, the peptidic backbone Ac-Cys(*StBu*)-VC-Gly-OH 7 was generated, initially. To this end, peptide 7 was synthesized via standard Fmoc SPPS using Fmoc-cysteine building block with *tert*-butylthiol (*StBu*) disulfide protection. The peptide was cleaved from the solid support under preservation of *StBu* protection. Following in-solution conjugation of doxorubicin to NHS-activated *C*-terminus of the assembled peptide 7, *StBu* cysteine protecting group was removed. The product 4 was isolated via semi-preparative chromatography and validated via mass spectrometric analysis (see section 7.8).

### 3.1.2.4 Maleimide-thiol conjugation: Synthesis of azide-aurein1.2-doxorubicin 8 and azide-doxorubicin 9

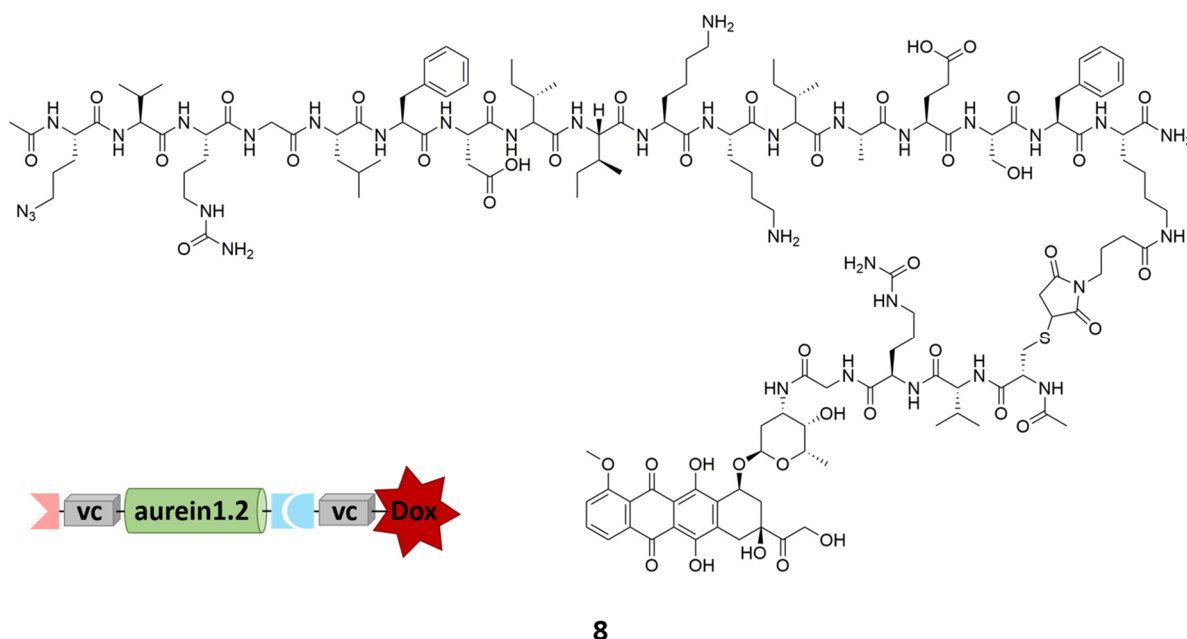


Figure 17: Structure of azide-aurein1.2-doxorubicin 8, conjugation product of maleimide-thiol addition of constituent B + C.

To join the cytotoxic doxorubicin component 4 with the membrane-lytic aurein1.2 containing constituent B 3, the *C*-terminal maleimide functionality of Ac-Orn( $N_3$ )-VC-aurein1.2-Lys(maleimide)-NH<sub>2</sub> 3 was addressed with the *N*-terminal cysteine residue of Ac-Cys-VC-Gly-Dox 4. The Michael-type maleimide-thiol addition, performed in 2-(*N*-morpholino)ethanesulfonic acid (MES) buffer at pH 6.5, resulted in

azide-aurein1.2-doxorubicin **8** (Figure 17) (94.0 %) upon separation via semi-preparative chromatography.

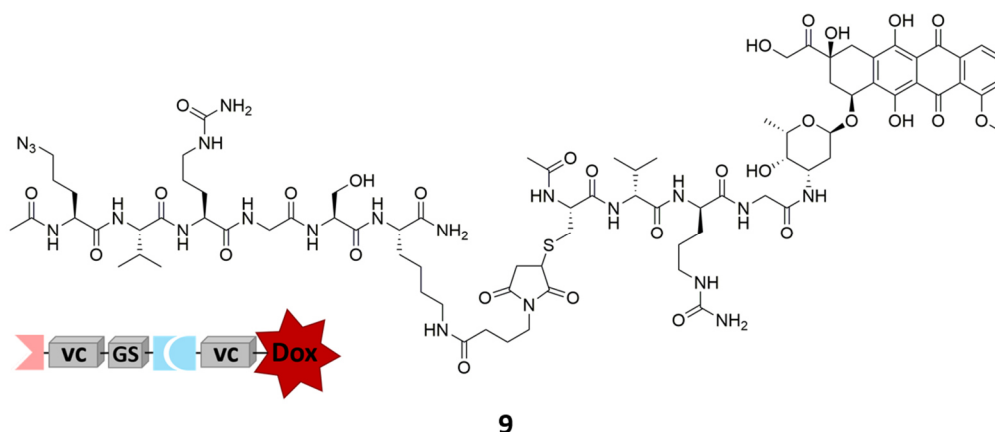


Figure 18: Structure of azide-doxorubicin **9**, conjugation product of maleimide-thiol addition of constituent B-NC + C.

Similarly, the addition of the Ac-Orn(N<sub>3</sub>)-VC-GS-Lys(maleimide)-NH<sub>2</sub> **6** and Ac-Cys-VC-Gly-Dox **4** was performed, yielding azide-doxorubicin **9** (Figure 18) (73.0 %) upon separation via semi-preparative chromatography. Successful formation of both products, azide-aurein1.2-doxorubicin **8**, as well as azide-doxorubicin **9**, was validated via mass spectrometry (Figure 19).

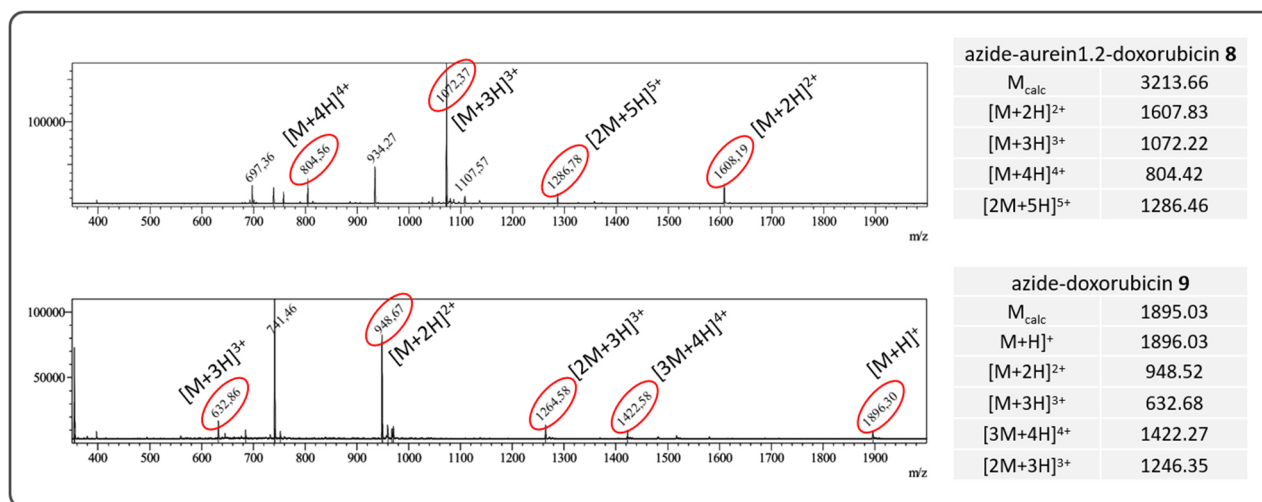
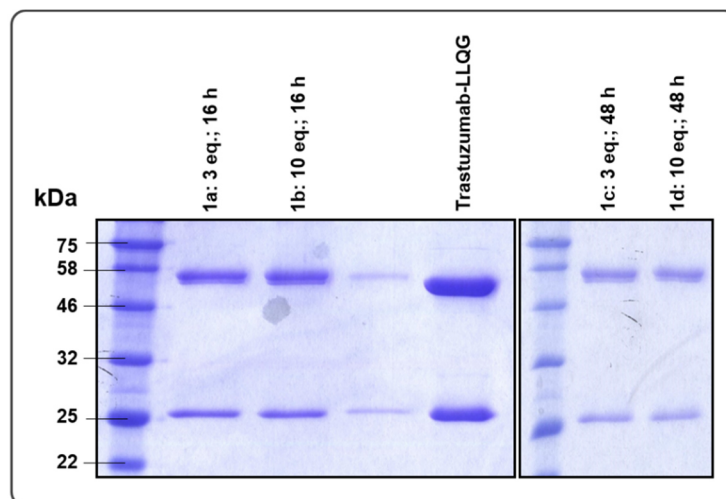


Figure 19: LC-MS analysis of azide-aurein1.2-doxorubicin **8** (upper) and azide-doxorubicin **9** (lower).





**Figure 21:** Coomassie stained SDS-PAGE analysis of Trastuzumab-aurein1.2-doxorubicin **1a-d** conjugation under different reaction conditions: Comparison of threefold and tenfold molar excess of azide-aurein1.2-doxorubicin **8**, applying 16- or 48-hours reaction time.

In ideal circumstances, complete conjugation would result in a final construct Trastuzumab-aurein1.2-doxorubicin **1** featuring two modules at the heavy chain C-termini, comprising the antimicrobial peptide aurein1.2 and the cytotoxic drug doxorubicin (Dox). To this end, complete conversion would premise entirely mTG mediated introduction of BCN functionality to both LLQG-tagged heavy chains. However, SDS-PAGE analysis of the final construct revealed its incomplete formation, visualized through occurrence of a double band in the Coomassie-stained SDS-PAGE gel, located in the corresponding area of 50 kDa (**Figure 21**). Complete conjugation, when both heavy chains are decorated with an aurein1.2-doxorubicin unit, would have led to shift in SDS-PAGE of the entire heavy chain band to bigger size. However, the expected shift occurred only for approximately half amount of the heavy chain band. This led to the assumption, that conjugation efficiency was only about 50 %, implying that trastuzumab was only decorated with one aurein1.2-doxorubicin unit on average. Possible reasons for incomplete conjugation could have either been incomplete SPAAC conjugation during final assembly of the construct, or incomplete mTG-mediated introduction of the BCN-functionality to only one of both heavy chain LLQG-tags. For further analysis, hydrophobic interaction chromatography (HIC) was performed.

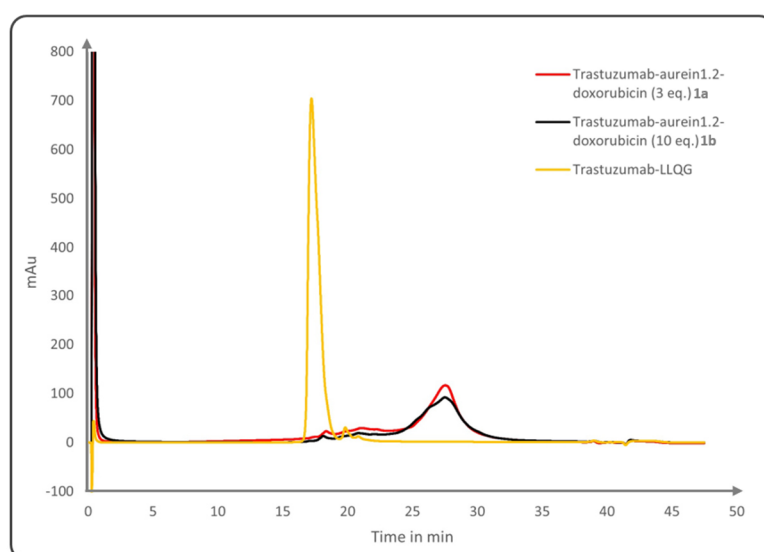


**Figure 22:** HIC-chromatogram of Trastuzumab-LLQG (orange) and conjugates Trastuzumab-aurein1.2-doxorubicin **1a** and **1b**, synthesized applying 3 eq. (red) respectively 10 eq. (black) molar excess azide-aurein1.2-doxorubicin **8** and 16 h reaction time.

HIC chromatograms of final conjugates Trastuzumab-aurein1.2-doxorubicin **1a** and **1b**, compared to unmodified Trastuzumab-LLQG (**Figure 22**), revealed a hydrophobic shift of the product to longer retention times. The product chromatogram revealed disappearance of the signal, corresponding to unmodified Trastuzumab-LLQG, and appearance of one new signal with longer retention time. This indicated conversion of Trastuzumab-LLQG into one single product species and not into a mixture of unmodified trastuzumab-LLQG, trastuzumab-LLQG decorated with one aurein1.2-doxorubicin unit and trastuzumab-LLQG decorated with two units.

Together with the information of about 50 % conjugation efficiency, resulting from the SDS-PAGE analysis, it was assumed, that the SPAAC conjugation of azide-aurein1.2-doxorubicin **8** with Trastuzumab-LLQG-BCN **2** ran completely, but previous mTG mediated formation of Trastuzumab-LLQG-BCN **2** seemed to be incomplete. Presumably, the BCN functionality was introduced to one of both LLQG-tagged heavy chains only. This resulted in a mono-decorated final conjugate, equipped with one aurein1.2-doxorubicin unit per antibody only. Taking into consideration that SDS-PAGE analysis was performed under denaturing conditions, the mono-decorated antibody generated the double band, with the lower band representing the unmodified heavy chain and the upper band being the modified one. While in the non-reducing HIC analysis, the mono-decorated antibody was represented by one single signal, emerging at more hydrophobic prolonged retention time.

In following conjugations, the efficiency of mTG mediated BCN introduction could not be increased. Nevertheless, knowing conjugate assembly yielded mono-decorated products, Trastuzumab-aurein1.2-doxorubicin **1** and Trastuzumab-doxorubicin **10** conjugates were applied to analyze a possible effect of incorporated aurein1.2 on intracellular delivery of doxorubicin.

As reported for the synthesis of conjugate **1a**, the procedure was repeated yielding Trastuzumab-aurein1.2-doxorubicin **1e**. Analogous, for synthesis of Trastuzumab-doxorubicin **10**, Trastuzumab-LLQG-BCN **2**, immobilized on protein A column, was treated with threefold molar excess of azide-doxorubicin **9**. SPAAC resulted in Trastuzumab-doxorubicin **10**, which was eluted after purification and re-buffered for following cell viability assay. SDS-PAGE analysis of conjugates **1e** and **10** revealed similar conjugation efficiency as seen in previous conjugation of compounds **1a-d**.

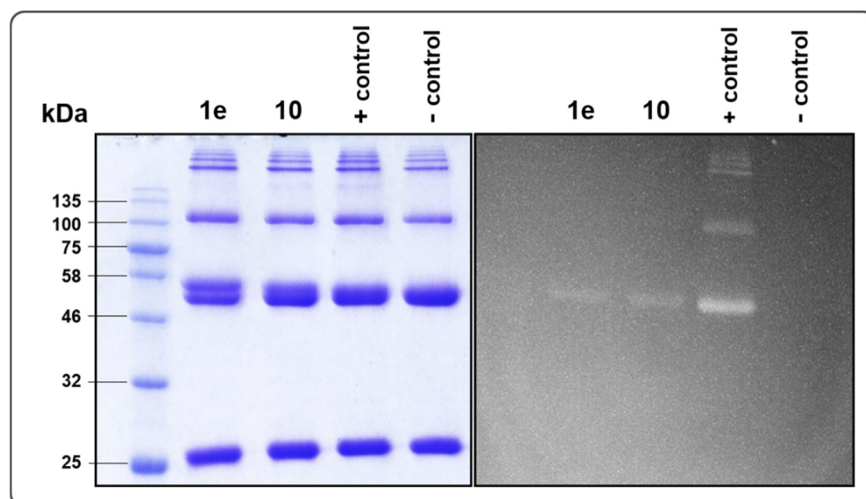


**Figure 23:** Left: Coomassie stained SDS-PAGE analysis of Trastuzumab-aurein1.2-Dox **1e**; Trastuzumab-Dox **10**; Trastuzumab-BCN + TAMRA-N<sub>3</sub> as positive control for preceding Trastuzumab-LLQG-BCN formation; Trastuzumab-LLQG-BCN as negative control. Right: Irradiated SDS-PAGE before staining: Doxorubicin fluorescent Trastuzumab-aurein1.2-Dox **1e**; doxorubicin fluorescent Trastuzumab-Dox **10**; TAMRA fluorescent Trastuzumab-BCN + TAMRA-N<sub>3</sub> positive control; Trastuzumab-LLQG-BCN negative control.

### 3.1.3 Cell viability assay applying Trastuzumab-aurein1.2-doxorubicin **1e** and Trastuzumab-doxorubicin **10**

Aurein1.2 has been reported to enhance the escape of endosomally entrapped cargo. To assess a potential effect of antimicrobial and membrane-lytic peptide aurein1.2, incorporated in the multicomponent model conjugate, on the intracellular delivery of a cytotoxic drug, and therefore on cytotoxicity, cell viability assay was performed. To this end, HER2-positive SK-BR-3 cells were treated with the multicomponent conjugate Trastuzumab-aurein1.2-doxorubicin **1e** comprising trastuzumab, covalently decorated with a module that combines the antimicrobial aurein1.2 peptide and cytotoxic component doxorubicin. Furthermore, SK-BR-3 cells were treated with Trastuzumab-doxorubicin **10**, as negative control, lacking the aurein1.2 sequence. Following 72 h incubation with the constructs (7.8 – 2000 nM) in medium, MTS assay was performed.

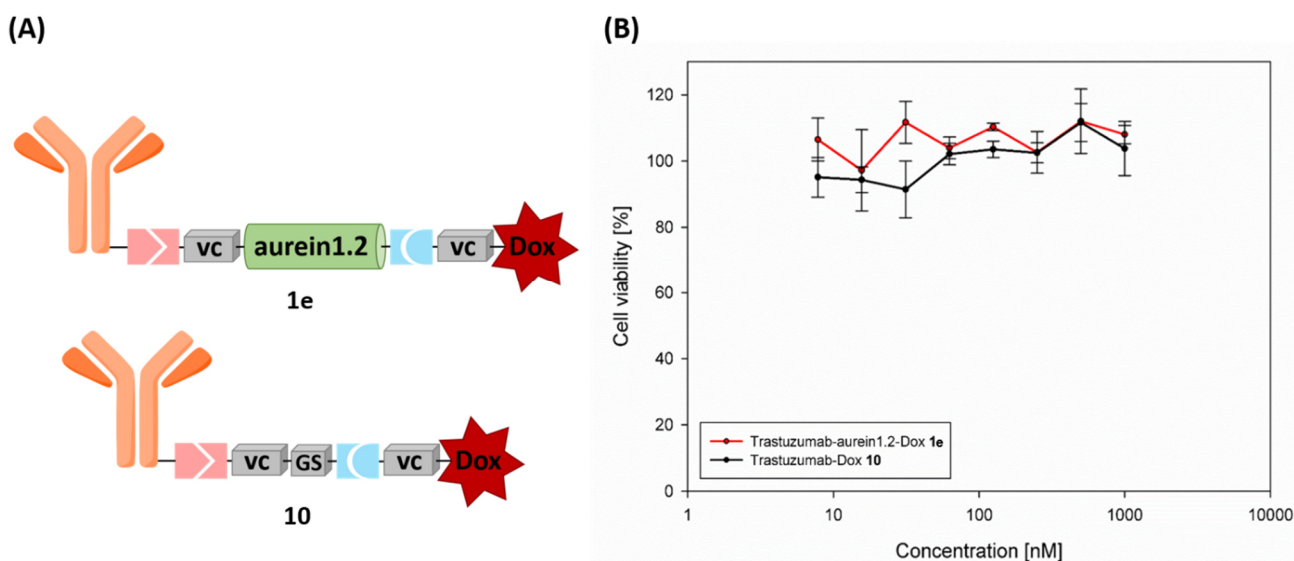


**Figure 24:** (A) Schematic depiction of Trastuzumab-aurein1.2-doxorubicin **1e** and Trastuzumab-doxorubicin **10**; (B) Effect of both conjugates on cell viability of SK-BR-3 cell line.

Interestingly, both constructs did not affect the cell viability (**Figure 24 (B)**), even at the highest concentration. Neither construct **1e** including membrane-lytic aurein1.2, nor construct **10** lacking aurein1.2 did show any effects.

The idea behind designing the multicomponent model conjugate was to investigate if incorporated membrane-lytic peptide aurein1.2 influences intracellular delivery of the cytotoxin, and therefore cytotoxicity. To this end, a construct was designed, combining an antibody, aurein1.2 and the low potent cytotoxin doxorubicin. It was thought, starting from an agent with low cytotoxic potency, a possible effect of incorporated aurein1.2 peptide on efficacy would be rather better observable than starting from a conjugate with already high potency. It is known from the literature,<sup>[113]</sup> that BR96-doxorubicin, an ADC comprising anti-Lewis Y antigen monoclonal antibody BR96, decorated with eight doxorubicin, showed IC<sub>50</sub> values between 100-200 nM. Thus, decoration of trastuzumab with two doxorubicin payloads was thought to result in a conjugate with low potency and low micromolar IC<sub>50</sub> value. However, no effect on cell viability was observed when incubating HER2-positive SK-BR-3 cells with Trastuzumab-doxorubicin **10** in concentrations up to 2 μM. Probably, a reason for no observable cytotoxic effect could be the insufficient conjugation efficiency, seen during conjugate assembly, leading to decoration of trastuzumab with one cytotoxic unit only instead of intended two units. Another reason could be the non-traceless cleavage of the cytotoxic component in form of glycine-doxorubicin instead of free doxorubicin, which presumably lowers the potency of the drug.

The construct comprising incorporated membrane-lytic aurein1.2, Trastuzumab-aurein1.2-doxorubicin **1e**, also did not affect cell viability, when incubating HER2-positive SK-BR-3 cells with concentrations up to 2  $\mu$ M. No cytotoxicity-enhancing effect of incorporated aurein1.2 was detectable. Possibly, due to the general non-observable cytotoxic effect of Trastuzumab-doxorubicin **10**, a possible effect of aurein1.2 lay out of range of applied construct concentrations. Or probably, the one-to-one ratio, aurein1.2-to-antibody (or 2:1 in ideal case of complete conjugate assembly) was not sufficient to cause an effect in terms of enhancing endosomal escape of entrapped cargo. Probably, applying a higher concentration of aurein1.2, respectively incorporation of the peptide in multiple copies would be preferable.

Hence, these results led to the idea to investigate, whether the membrane-lytic antimicrobial peptide aurein1.2 has the ability to mediate non-endosomal intracellular delivery when applied in multiple copies, covalently bound on a suitable scaffold.

### 3.2 M-lycotoxin variant L17E covalently linked to cargo: Protein-L17E fusion

The cationic amphiphilic 25 amino acid residue L17E peptide was reported<sup>[56]</sup> to efficiently mediate cytosolic delivery of different protein cargo up to full-length antibodies. Being derived from naturally haemotoxic M-lycotoxin, the variant L17E with leucine exchanged by glutamic acid showed diminished cytotoxicity and enabled cytosolic protein delivery upon coincubation with 40  $\mu$ M peptide. Until now, no efforts have been made to introduce a covalent linkage between cargo protein and the L17E peptide transporter. So far, reported uptake experiments were based on coincubation only. To investigate whether the uptake mediating ability of L17E was retained upon introduction of a covalent connection between the peptide and the cargo, a fusion protein was generated applying eGFP as model cargo. To this end, separated from a glycine-serine spacer, the 25 amino acid sequence of L17E was C-terminally fused to an eGFP variant, including an internal 13 amino acid recognition sequence towards lipotic acid protein ligase A (LplA). As reported in the literature,<sup>[114]</sup> the lipotic acid acceptor peptide (LAP), was located at a loop of the  $\beta$ -barrel structure between E172 and D173 of eGFP.

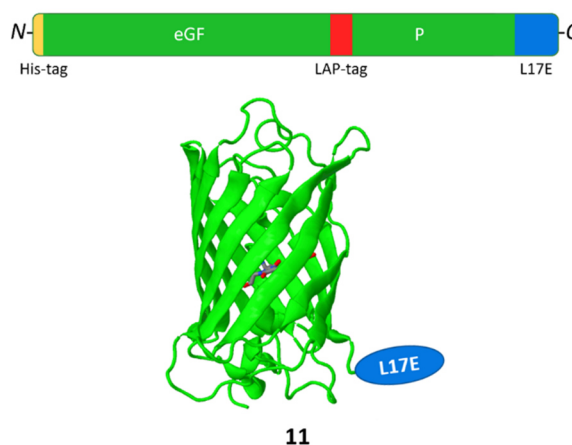


**Figure 25:** Schematic depiction of eGFP-L17E fusion protein **11** with L17E sequence C-terminally fused to eGFP. Protein structure adapted from.<sup>[115]</sup>

Following primer encoded L17E fusion to eGFP gene and insertion into the respective vector by restriction cloning using *NotI* and *XbaI*, eGFP-L17E **11** was produced in *E. coli* and purified via IMAC. The capability of eGFP-L17E **11** to enter the cytosol was determined in a cellular uptake assay and compared with L17E-mediated delivery of eGFP upon coincubation with solitary peptide, as reported in the literature.<sup>[56]</sup> For that purpose, L17E peptide **12** was synthesized via Fmoc SPPS and in accordance with the literature applied in 40  $\mu$ M, co-incubated with unmodified eGFP. To provide a comparable corresponding L17E concentration, incubation of cells with eGFP-L17E **11** was performed in 40  $\mu$ M also.

---

### 3.2.1 Cellular uptake assay

HeLa cells were incubated with unmodified eGFP (8  $\mu$ M) as negative control, unmodified eGFP (8  $\mu$ M) coincubated with 40  $\mu$ M solitary L17E **12**, and 40  $\mu$ M eGFP-L17E fusion protein **11** in serum free medium for 1 h each. Following further 3 h incubation in medium, cellular distribution of eGFP fluorescence signal was analyzed with fluorescence microscopy. Cells only treated with eGFP did not show any fluorescence both inside the cell and on the cell surface. Interestingly, also no fluorescence signals were observed in cells treated with both eGFP applying 40  $\mu$ M solitary L17E coincubation and eGFP-L17E fusion protein (data not shown).

Albeit the M-lycotoxin variant L17E was reported as efficient delivery agent, in this setup, neither solitary L17E **12** in the coincubation experiment nor L17E peptide sequence covalently linked to the cargo were able to mediate cellular uptake of eGFP model cargo. Presumably, the one-to-one protein-to-L17E ratio in eGFP-L17E fusion protein was insufficient and did not promote intracellular protein delivery. Hence, it remained to be investigated whether L17E peptide was capable to mediate intracellular delivery of covalently connected cargo, when applied in multiple copies.

### 3.3 Peptide-dextran hybrids: Multiple copies of Aurein1.2 and L17E on polysaccharide scaffold

Antimicrobial and membrane lytic aurein1.2, known to mediate non-endosomal intracellular delivery by enhancing endosomal escape,<sup>[68]</sup> as well as M-lycotoxin variant L17E, known for cytosolic delivery of proteins,<sup>[56]</sup> both did not show ability to enhance or mediate intracellular uptake, when covalently bound to a model conjugate in single copy. This resulted in the idea to investigate, whether multiple copies of the peptides, covalently bound to a suitable scaffold, could cause the effects associated with multivalency that enable intracellular uptake of covalently bound cargo molecules. To that purpose, dextran polysaccharide was chosen as hydrophilic scaffold, resulting in peptide-dextran hybrids upon covalently decoration with multiple copies of the respective peptide.

#### 3.3.1 Dextran modification

Dextran polysaccharide has already been reported as versatile tool for different kinds of applications, among them usage as hydrophilic scaffold for generation of potent high-DAR antibody-drug conjugates<sup>[76]</sup> or as flexible multimerization platform for apoptosis inducing peptides.<sup>[78]</sup>

As reported in the literature,<sup>[76, 78]</sup> dextran offers a dual derivatization possibility: The hydroxy groups of the glucose repeating units on the one hand and the polysaccharide reducing end on the other hand. Thus, dextran polysaccharide could be an ideal scaffold for covalent oligomerization of cell-penetrating peptides, to investigate a possible multivalency effect on intracellular uptake efficiency and cytoplasmic cargo delivery. To this end, the modified hydroxy groups of the glucose repeating units could be decorated with multiple copies of the respective peptide, while the reducing end offers the possibility for introduction of a functionality, accessible for cargo conjugation.

For this purpose, dextran modification started with incorporation of cadaverine at the polysaccharide reducing end via reductive amination. Following carboxyethylation and subsequent conversion of the introduced carboxyl moieties into either maleimide- or azide-functionalities, as described in the following sections, resulted in versatile dextran scaffolds, decorated with variable amount and kind of chemical handles (**Figure 26**).

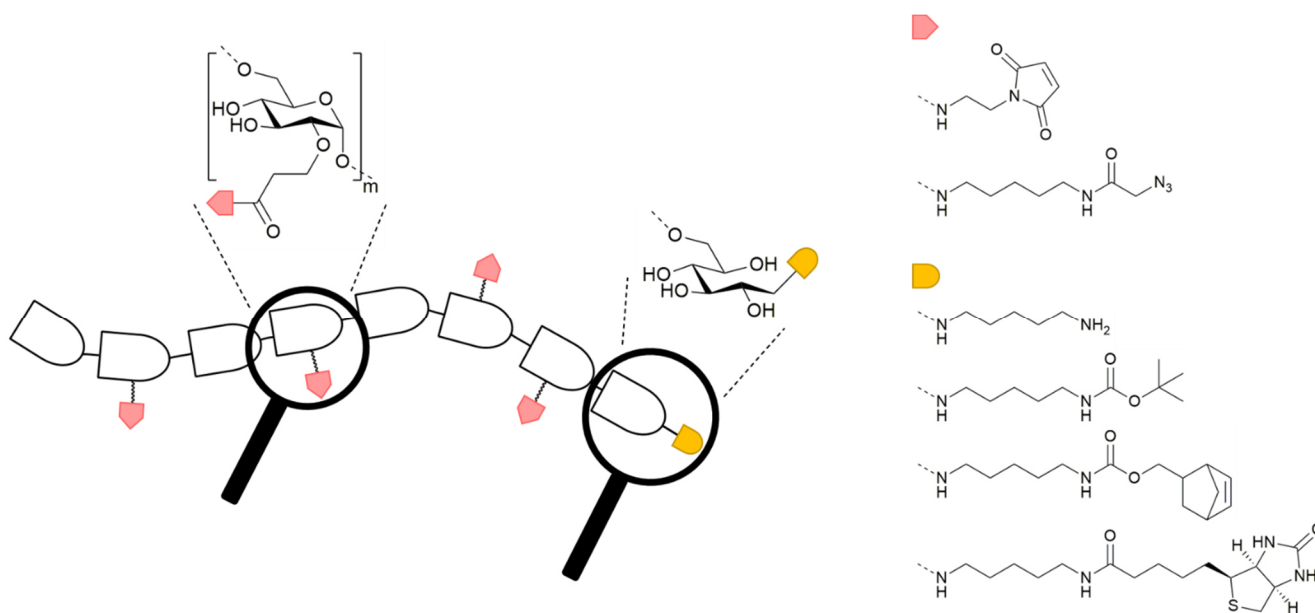
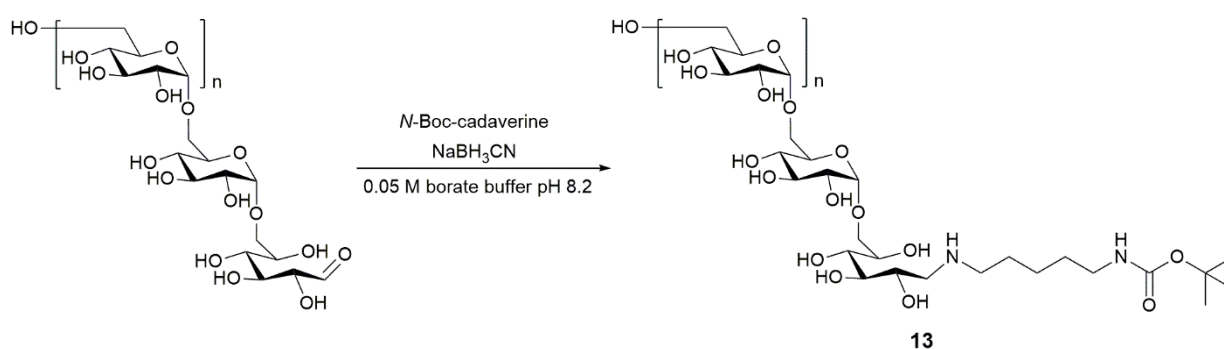


**Figure 26:** Schematic depiction of dextran modification: Introduction of conjugation sites at the repeating units (red) and at the polysaccharide reducing end (orange).

### 3.3.1.1 Reductive amination: Synthesis of dextran-*N*-Boc-cadaverine **13**



**Scheme 8:** Synthesis of dextran-*N*-Boc-cadaverine **13** via reductive amination.

To introduce a terminal conjugation site, a mono-protected diaminoalkane was incorporated at the polysaccharide reducing end via reductive amination. Therefore the 10 kDa dextran starting material from *Leuconstoc mesenteroides* (average Mol. Wt. 9000-11000; minimal branching of ca. 5 %) was addressed with *N*-Boc-cadaverine and the resulting imine was selectively reduced with sodium cyanoborohydride reducing agent, as previously described in the literature.<sup>[76]</sup> The mono-Boc-protected cadaverine derivative was chosen to prevent formation of dextran dimers and to protect the introduced amine functionality from participation in subsequent reactions. The longer aliphatic chain of cadaverine compared to e.g. ethylenediamine was thought to be advantageous in terms of accessibility. The dextran-*N*-Boc-cadaverine **13** product was obtained in a yield of 95 % and product formation was analyzed via <sup>1</sup>H NMR spectroscopy. Appearance of the signals, corresponding to aliphatic protons of cadaverine and the Boc protecting group, validated successful conversion (**Figure 27**).

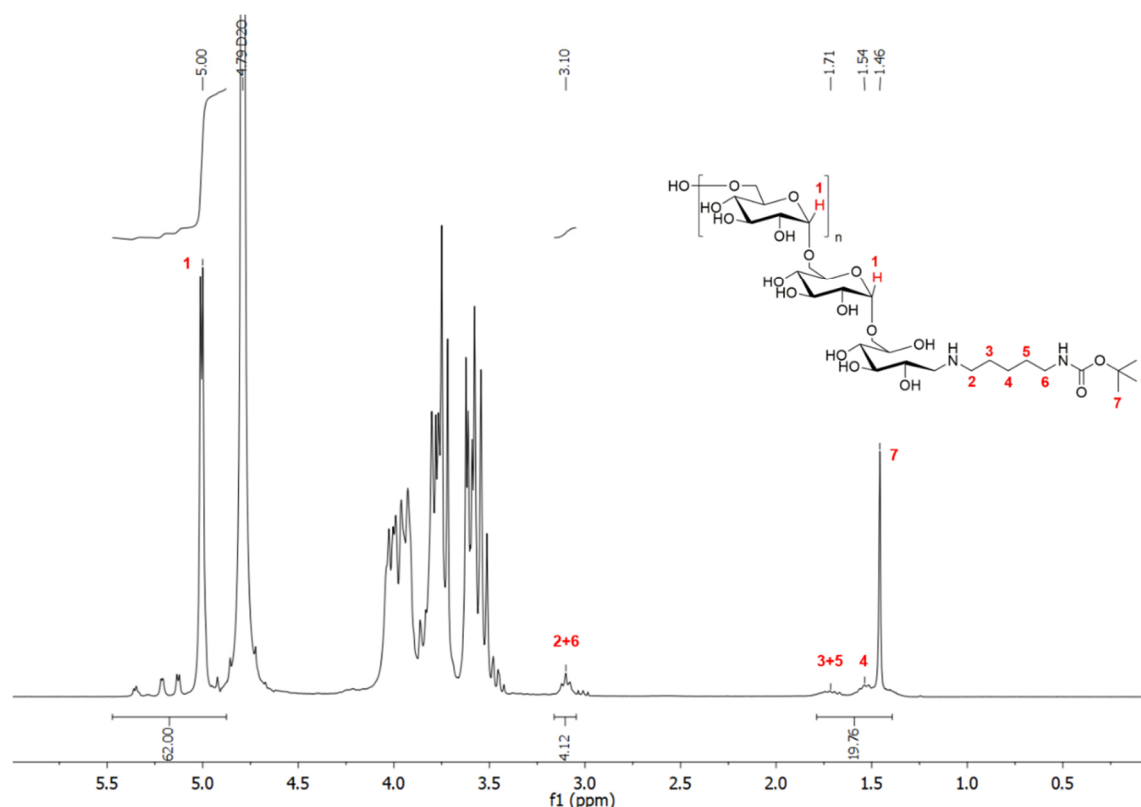
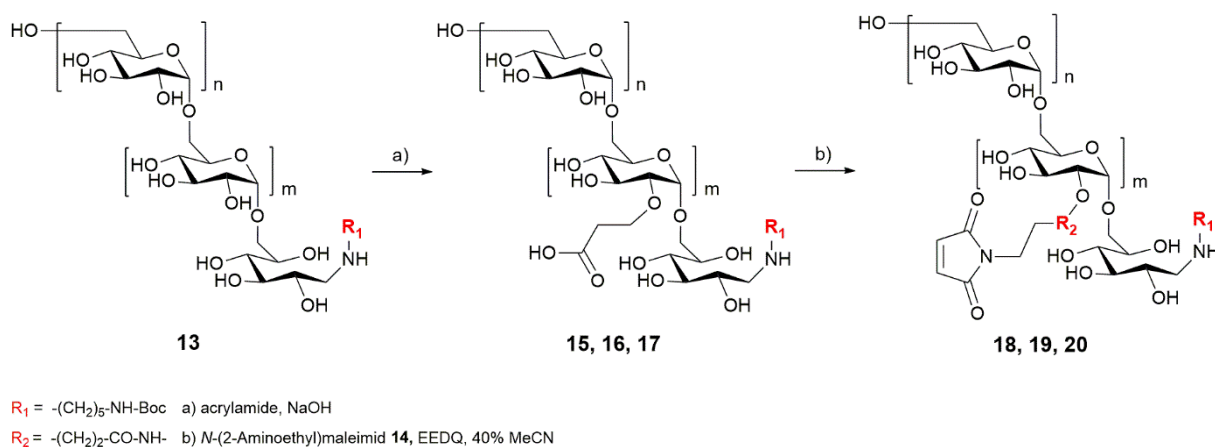


**Figure 27:**  $^1\text{H}$  NMR spectrum of dextran-*N*-Boc-cadaverine **13**: Depicted correlation of adequate protons and proton signals displayed successful introduction of *N*-Boc-cadaverine via reductive amination.

### 3.3.1.2 Synthesis of maleimide-dextran-*N*-Boc-cadaverine compounds



**Scheme 9:** General synthesis of maleimide-dextran-*N*-Boc-cadaverine: Dextran-*N*-Boc-cadaverine **13** modification via carboxyethylation followed by EEDQ activated conjugation of *N*-(2-aminoethyl)maleimide **14**.

To introduce maleimide-functionalities into the glucose repeating units of dextran-*N*-Boc-cadaverine **13**, a two-step procedure comprising carboxyethylation and subsequent amide-bond formation with a maleimide- and amine-bifunctionalized linker was performed. In the literature,<sup>[61]</sup> 2D-NMR analysis validated that carboxyethylation, the modification of dextran with acrylamide in presence of sodium hydroxide, introduced carboxyethyl groups selectively to the C2 positions of the glucose repeating units. It was known<sup>[76]</sup> that approximately 40 % of applied acrylamide was conjugated to the glucose repeating units. Hence, the amount of incorporated 2-carboxyethyl groups per dextran was adjustable by regulating the amount of applied acrylamide. About 2.5 equivalents excess acrylamide were required for

introduction of one 2-CE group per dextran. Accordingly, carboxyethylation of dextran-*N*-Boc-cadaverine **13** was performed to obtain three different 2-CE-dextran-*N*-Boc-cadaverine compounds, decorated with low, medium, and high intended number of 2-CE groups per dextran in a range between six and ten. Afterwards, the incorporated carboxy moieties of 2-CE-dextran-*N*-Boc-cadaverine compounds **15**, **16** and **17** were converted into maleimide functionalities by EEDQ-activated amide-bond formation<sup>[76]</sup> with *N*-(2-aminoethyl)maleimide **14**. To validate successful product formation, and to determine the number of incorporated maleimide moieties per dextran, the resulting maleimide-dextran-*N*-Boc-cadaverine compounds **18**, **19** and **20** were analyzed via <sup>1</sup>H NMR spectroscopy.

Quantification of introduced maleimide-functionalized 2-CE groups per dextran using <sup>1</sup>H NMR spectroscopy was performed as described in the literature.<sup>[61, 76]</sup> Quantification is exemplarily shown for maleimide(6.5)dextran-*N*-Boc-cadaverine **18** (Figure 28):

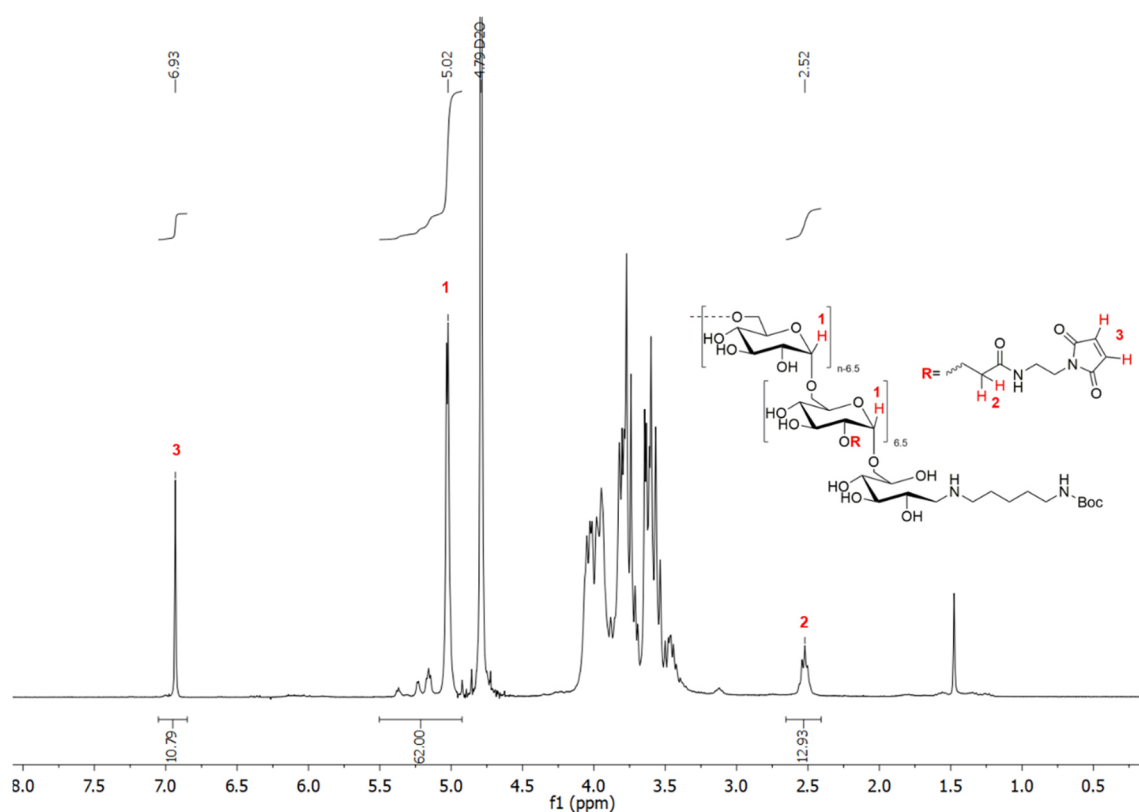


**Figure 28:** <sup>1</sup>H NMR spectrum of maleimide(6.5)-dextran-*N*-Boc-cadaverine **18**: Depicted correlation of adequate protons and proton signals used for quantification of introduced maleimide functionalities per dextran on average.

To determine the number of incorporated maleimide-functionalized 2-carboxyethyl groups per dextran, the proton signal resulting from the anomeric protons (signal **1**) of the glucose repeating units was set in ratio to the C2 proton signal of the introduced 2-CE groups. The average polysaccharide of dextran with average molecular weight of 10 kDa was composed of 62 glucose monomers. Consequently, the integral of proton signal **1**, which corresponds to anomeric protons of glucose repeating units, was set to 62, representing one single average dextran molecule. Proton signal **2** corresponded to the two protons at C2 position of introduced carboxyethyl groups, leading to following formula (2) for calculation of number of 2-CE groups per dextran molecule:

$$\frac{\text{number}}{\text{dextran}} = \frac{\text{integral (signal X)}}{\text{number of corresponding protons (signal X)}} \quad (1)$$

$$\frac{2 - \text{CE} - \text{groups}}{\text{dextran}} = \frac{\text{integral (signal 2)}}{\text{number of corresponding protons (signal 2)}} = \frac{12.93}{2} \approx 6.5 \quad (2)$$

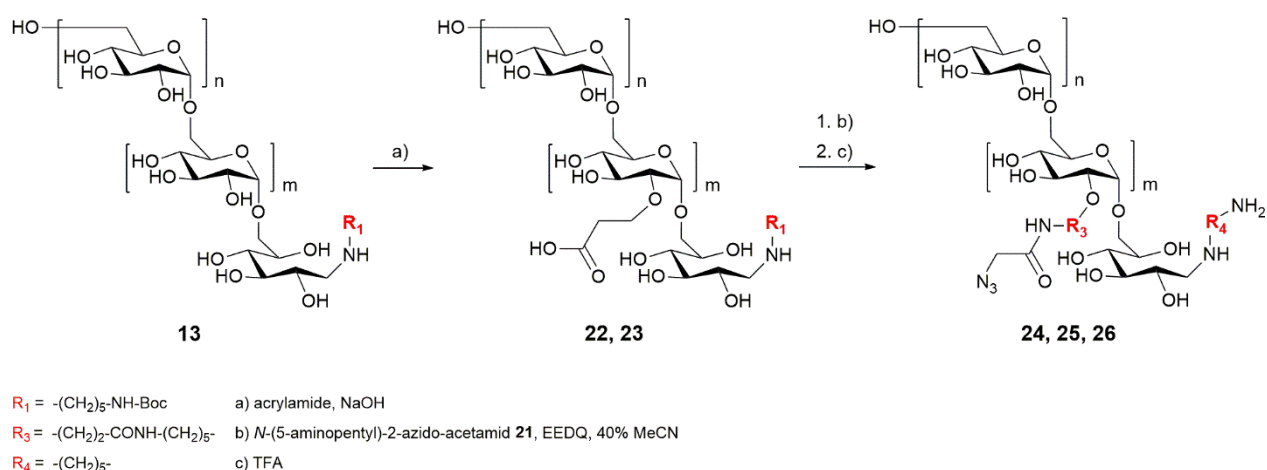
For quantification of the maleimide functionalities, signal **3** was used, which corresponded to the two unsaturated protons of the maleimide functionality. The protons which originated from the ethyl linker between maleimide and amine moiety in *N*-(2-aminoethyl)maleimide **14**, were not amenable for quantification, because the corresponding signals overlap with the bulky proton signals of the glucose backbone. The integral of signal **3** was slightly decreased compared to the expected integral for quantitative conversion of all 6.5 2-CE-groups per dextran on average into maleimide moieties. However, in the *N*-(2-aminoethyl)maleimide **14** starting material, the integral of the respective unsaturated protons compared to the ethyl-linker protons was reduced by exactly the same factor (**Figure 131**), thus leading to the assumption of quantitative amide-bond formation.

In the present work, three maleimide-dextran-*N*-Boc-cadaverine compounds **18**, **19**, and **20** (**Table 1**), decorated with on average 6.5, 7.8, and 10.5 maleimide functionalities at the glucose repeating units as well as a *N*-Boc-protected cadaverine functionality at the reducing end, were synthesized in yields ranging from 11-18 % referred to dextran-*N*-Boc-cadaverine **13**.

**Table 1:** Overview of maleimide-dextran-*N*-Boc-cadaverine compounds synthesized in the present work.  $R_1 = \text{-(CH}_2\text{)}_5\text{-NH-Boc}$ ;  
 $R_2 = \text{-(CH}_2\text{)}_2\text{-CO-NH-}$ .

Compound	#	Structure	Average maleimide moieties per dextran	Yield
maleimide(6.5)-dextran- <i>N</i> -Boc-cadaverine	<b>18</b>		6.5	17 %
maleimide(7.8)-dextran- <i>N</i> -Boc-cadaverine	<b>19</b>		7.8	18 %
maleimide(10.5)-dextran- <i>N</i> -Boc-cadaverine	<b>20</b>		10.5	11 %

### 3.3.1.3 Synthesis of N<sub>3</sub>-dextran-cadaverine compounds



**Scheme 10:** General synthesis of N<sub>3</sub>-dextran-cadaverine: Dextran-*N*-Boc-cadaverine **13** modification via carboxyethylation followed by EEDQ activated conjugation of *N*-(5-aminopentyl)-2-azido-acetamid **21** and final removal of the Boc protecting group.

According to generation of maleimide-dextran-*N*-Boc-cadaverine compounds, synthesis of N<sub>3</sub>-dextran-cadaverine compounds were performed following a similar procedure. Carboxyethylation of dextran-*N*-Boc-cadaverine **13** was planned to obtain 2-CE-dextran-*N*-Boc-cadaverine, decorated with approximately five 2-CE groups per dextran on average. Subsequently the incorporated 2-CE groups were addressed with azide- and amine-bifunctionalized *N*-(5-aminopentyl)-2-azido-acetamide **21** in an EEDQ-activated amide bond formation. Following introduction of the azide moieties, the Boc-protecting group of the cadaverine modification at the polysaccharide reducing end was removed by treatment with trifluoroacetic acid. The deprotection yielded N<sub>3</sub>-dextran-cadaverine compounds, decorated with approximately five azide functionalities at the glucose repeating units and an orthogonal amine conjugation site at the polysaccharide reducing end. To validate successful product formation and to quantify the number of incorporated azide functionalities per dextran, <sup>1</sup>H NMR spectroscopy was performed. Additionally, IR-spectroscopy was performed and the characteristic azide-band at wavenumbers between 2114-2116 cm<sup>-1</sup> validated the presence of azide functionalities.

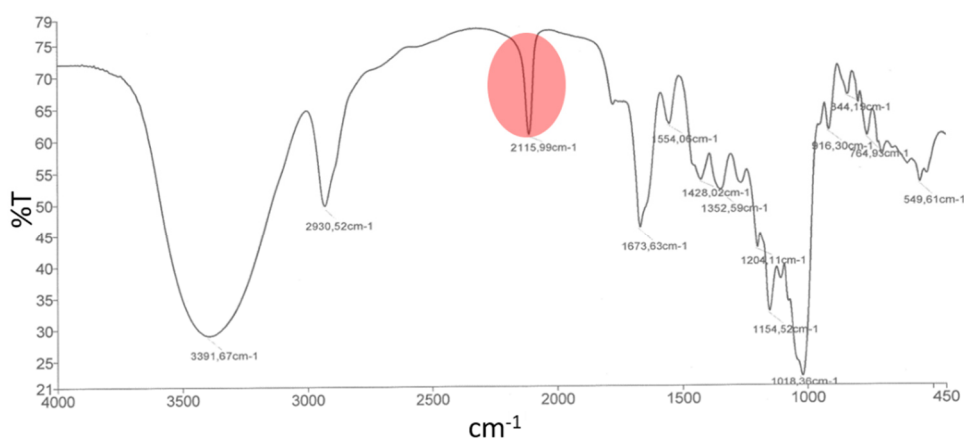


**Figure 29:** IR-spectrum of azide modified dextran-cadaverine **24** showing the characteristic azide band (marked in red) at a wavenumber of 2116 cm<sup>-1</sup>.

Quantitative Boc deprotection was validated via <sup>1</sup>H NMR analysis. Disappearance of the proton signal, corresponding to the three methyl groups of Boc, was exemplarily shown in the spectra of N<sub>3</sub>(4.8)-

dextran-cadaverine **24** compared with the corresponding  $N_3$ -dextran-*N*-Boc-cadaverine intermediate (**Figure 30**).

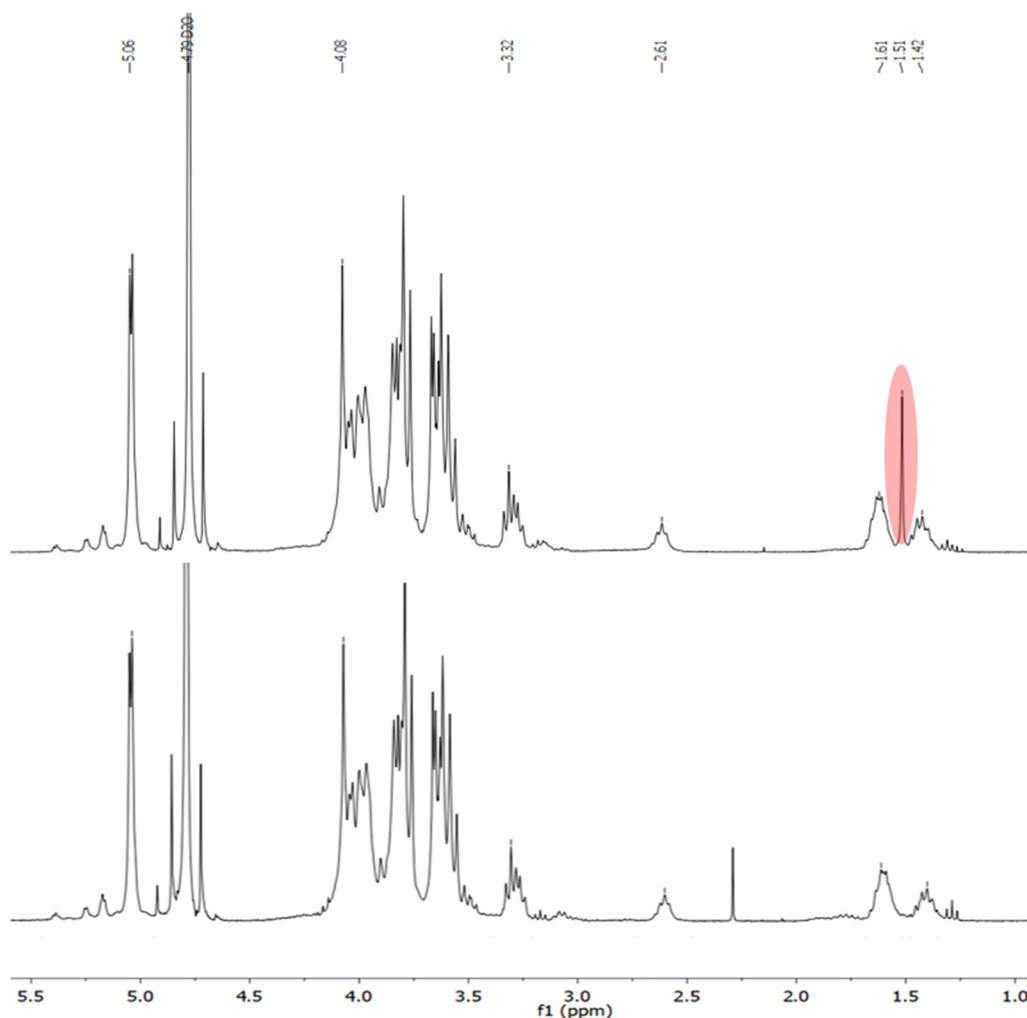


**Figure 30:** Comparison of  $^1\text{H}$  NMR spectra of  $N_3(4.8)$ -dextran-cadaverine **24** (lower) and the  $N_3$ -dextran-*N*-Boc-cadaverine intermediate (upper). Disappearance of the Boc signal (marked in red) upon deprotection.

Quantification of introduced azide functionalities per dextran was performed as reported in the literature<sup>[61, 76]</sup> and already described for quantification of maleimide functionalities in dextran compounds **18**, **19**, and **20**. Quantification is briefly exemplified by  $^1\text{H}$  NMR spectroscopic data (**Figure 31**) of  $N_3(4.8)$ -dextran-cadaverine **24**.

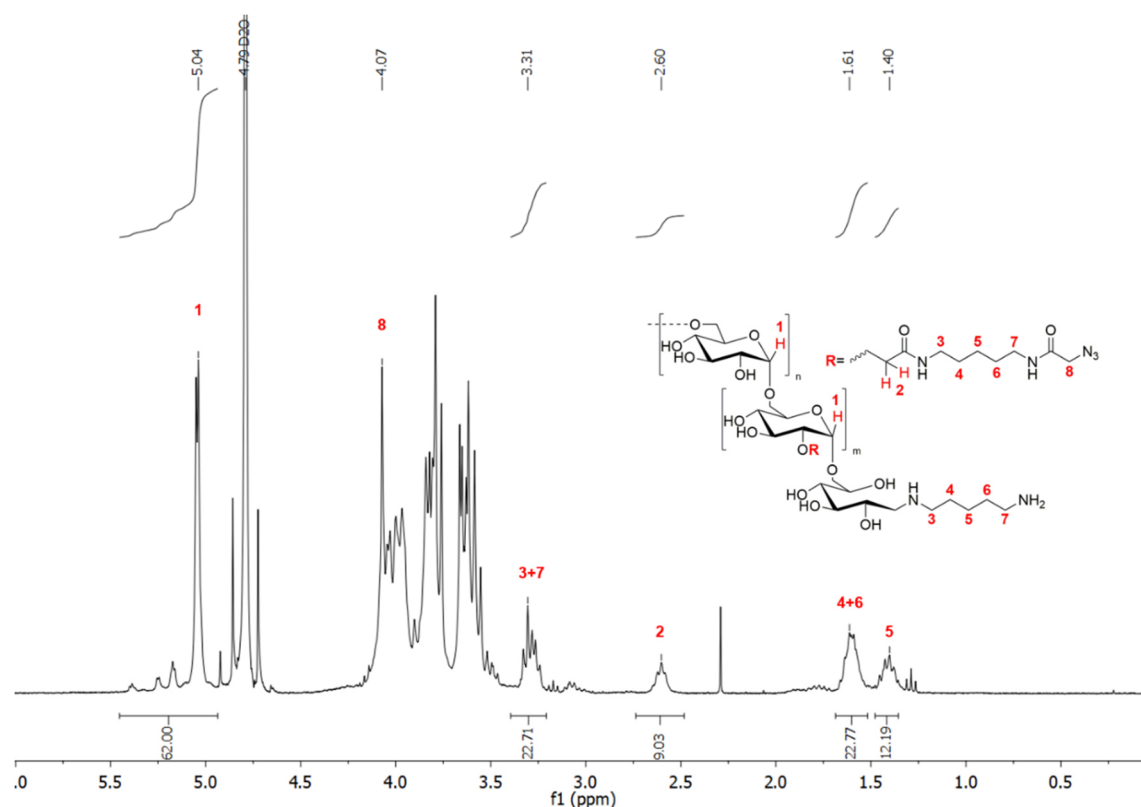


**Figure 31:**  $^1\text{H}$  NMR spectrum of  $\text{N}_3(4.8)$ -dextran-cadaverine **24**: Depicted correlation of adequate protons and proton signals used for quantification of introduced azide functionalities per dextran on average.

To determine the number of incorporated azide-functionalized 2-carboxyethyl groups per dextran, the integral of the anomeric proton signal **1** of the glucose repeating units was set to 62. Proton signal **2**, corresponding to the two C2 protons of the carboxyethyl group, signal **3+7**, **4+6**, and **5**, corresponding to the aliphatic protons **3-7**, were used for quantification. The respective number per dextran was calculated using formula (1). In case of aliphatic protons **3-7** it must be pointed out, that the protons and corresponding signals did not only originate from incorporated azide-functionalized 2-CE groups, but also from the cadaverine residue at the polysaccharide reducing end. Thus, for quantification of azide-groups per dextran, the respective number of red-end-originated cadaverine protons had to be subtracted from the corresponding integral value. The final number of azide groups per dextran on average was calculated as the mean value of the individual calculations of each signal:

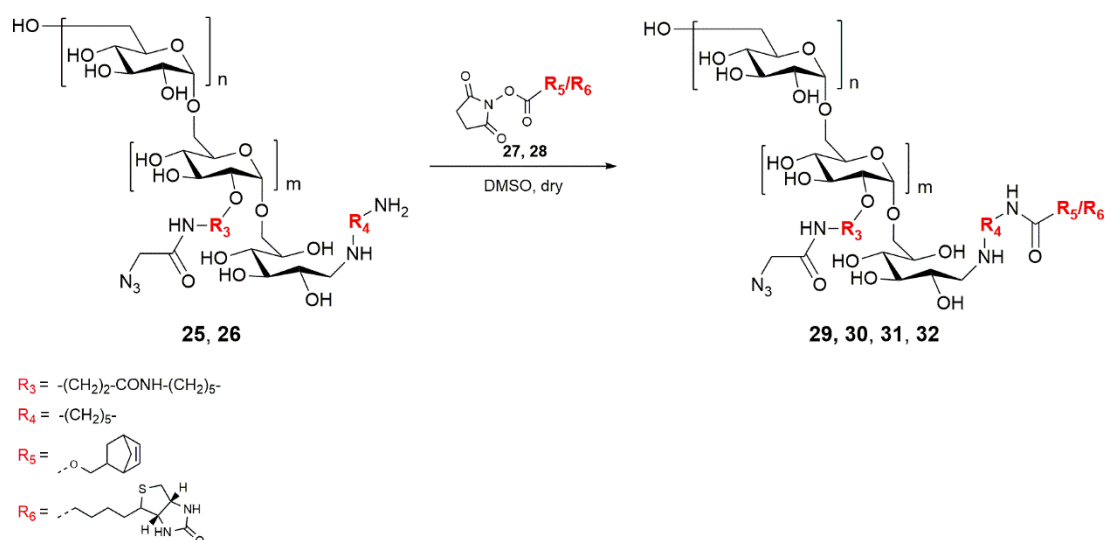
$$\frac{N_3 - \text{groups}}{\text{dextran}} = \frac{\frac{22.71 - 4}{4} + \frac{9.03}{2} + \frac{22.77 - 4}{4} + \frac{12.19 - 2}{2}}{4} \approx 4.8 \quad (3)$$

In the present work, three  $\text{N}_3$ -dextran-cadaverine compounds **24**, **25**, and **26** (Table 1) were synthesized, decorated with on average 4.8, 4.8, and 4.3 azide functionalities at the glucose repeating units as well as an orthogonal cadaverine conjugation site at the reducing end. Products **24**, **25**, and **26** were obtained in yields ranging from 35-56 % referred to dextran-*N*-Boc-cadaverine **13**.

**Table 2:** Overview of N<sub>3</sub>-dextran-cadaverine compounds synthesized in the present work. R<sub>3</sub> = -(CH<sub>2</sub>)<sub>2</sub>-CONH-(CH<sub>2</sub>)<sub>5</sub>-;  
R<sub>4</sub> = -(CH<sub>2</sub>)<sub>5</sub>-.

Compound	#	Structure	Average azide moieties per dextran	Yield
N <sub>3</sub> (4.8)-dextran-cadaverine	24		4.8	35 %
N <sub>3</sub> (4.8)-dextran-cadaverine	25		4.8	56 %
N <sub>3</sub> (4.3)-dextran-cadaverine	26		4.3	46 %

### 3.3.1.4 Synthesis of red-end functionalized N<sub>3</sub>-dextran compounds



**Scheme 11:** General synthesis of N<sub>3</sub>-dextran derivatives bearing red-end functionalization: Amide-bond formation of N<sub>3</sub>-dextran-cadaverine with NHS-activated norbornene **27** or biotin **28** derivative.

In order to facilitate accessibility of the cadaverine conjugation site, incorporated at the polysaccharide reducing end of azide-decorated dextran, the amine moiety was further modified and converted into

either norbornene or biotin functionalities. Introduction of norbornene-functionality should enable conjugation of counterpart-labeled cargo following iEDDA, fully orthogonal to CuAAC-addressable azide moieties at the glucose repeating units. Biotinylation of the polysaccharide reducing end should enable the non-covalent but extremely stable linkage of modified dextran and streptavidin protein in prospective experiments.

To this end, the amine-moieties at the reducing end of the respective  $N_3$ -dextran-cadaverines were addressed with the respective NHS-activated norbornene **27** or biotin **28** derivatives. Amide-bond formation was qualitatively monitored via  $^1\text{H}$  NMR spectroscopy (**Figure 32** and **Figure 33**). If the turnover occurred quantitatively, was not further analyzed. Excessive NHS-activated derivatives were removed. Yielded products were not separated from potential unmodified  $N_3$ -dextran-cadaverine starting materials, which do not take part in or affect subsequent conjugations.

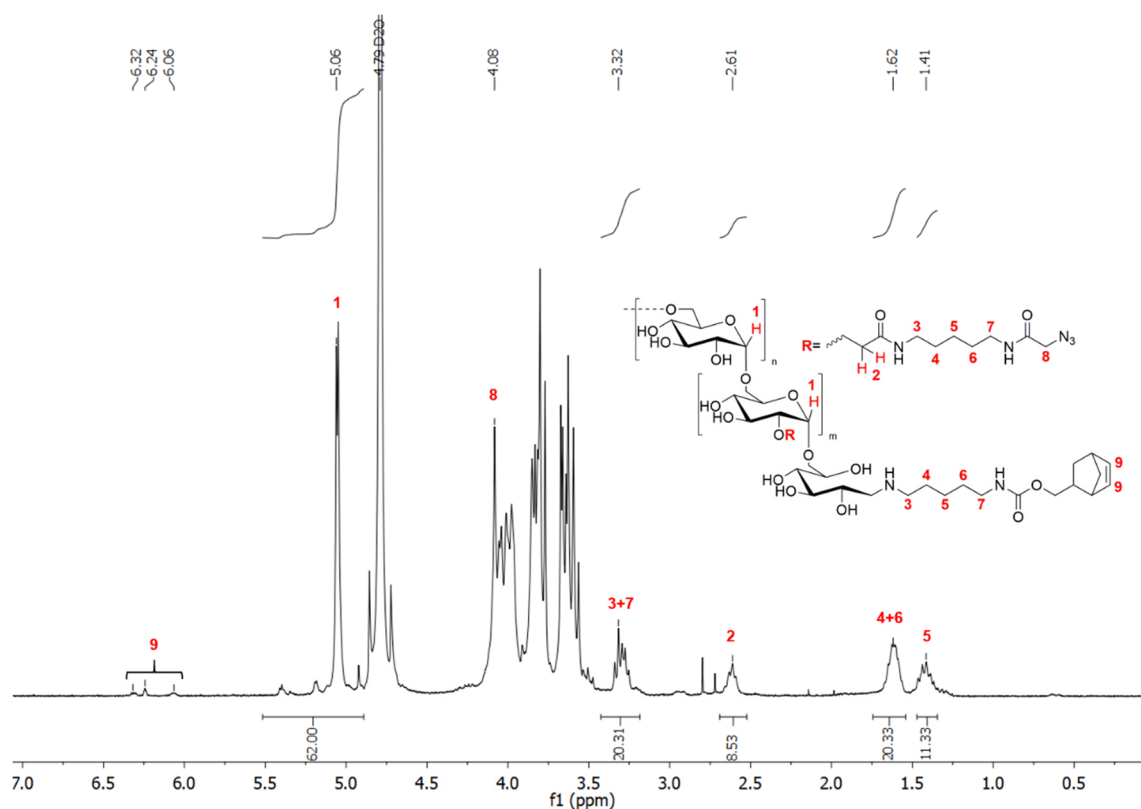


**Figure 32:**  $^1\text{H}$  NMR spectrum of  $N_3(4.3)$ -dextran-norbornene **29**: Depicted correlation of unsaturated norbornene protons and proton signals (9) as qualitative validation of norbornene introduction.

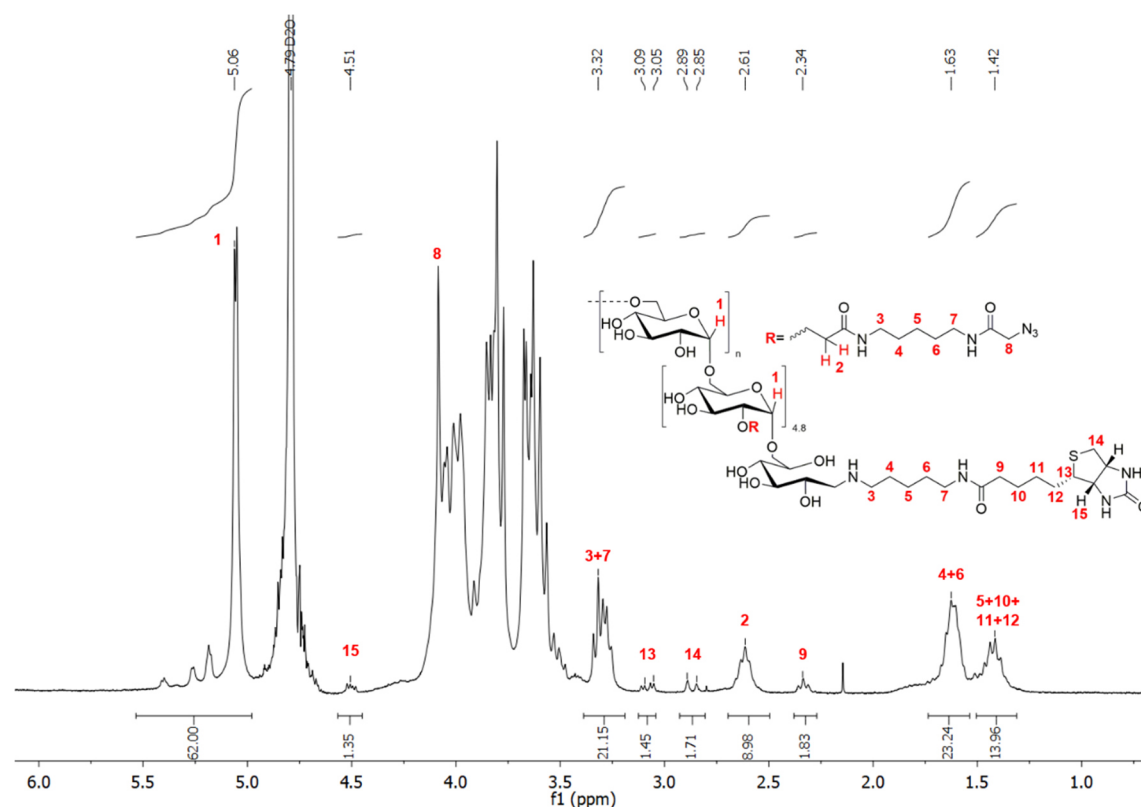


**Figure 33:**  $^1\text{H}$  NMR spectrum of  $\text{N}_3(4.8)$ -dextran-biotin **32**: Depicted correlation of biotin protons and proton signals (15 + 13 + 14 + 9) as qualitative validation of biotin introduction.

In the present work, three norbornene red-end-functionalized dextran variants, decorated with on average 4.3 or 4.8 azide functionalities at the glucose repeating units, and one red-end-biotinylated dextran, decorated with on average 4.8 azide groups per dextran, were synthesized in yields ranging from 76-95 % (**Table 3**).

**Table 3:** Overview of  $\text{N}_3$ -dextran-norbornene/biotin compounds synthesized in the present work.  $\text{R}_3 = -(\text{CH}_2)_2\text{-CONH-}(\text{CH}_2)_5-$ ;  $\text{R}_4 = -(\text{CH}_2)_5-$ .

Compound	#	Structure	Average azide moieties per dextran	Yield
$\text{N}_3(4.3)$ -dextran-norbornene	29		4.3	86 %
$\text{N}_3(4.3)$ -dextran-norbornene	30		4.3	83 %

N <sub>3</sub> (4.8)-dextran-norbornene	<b>31</b>		4.8	76 %
N <sub>3</sub> (4.8)-dextran-biotin	<b>32</b>		4.8	95 %

### 3.3.2 Aurein1.2-dextran and L17E-dextran hybrids – a comparison

To investigate, whether oligomerisation of aurein1.2, respectively L17E, on dextran could cause a multivalency effect that enables intracellular uptake of yielded peptide-dextran hybrid macromolecules, 10 kDa dextran was covalently decorated with multiple copies of the respective peptide. Additional introduction of a fluorescent label (TAMRA) enabled detection of intracellular distribution via fluorescence microscopy upon intracellular uptake of yielded peptide-dextran hybrids.

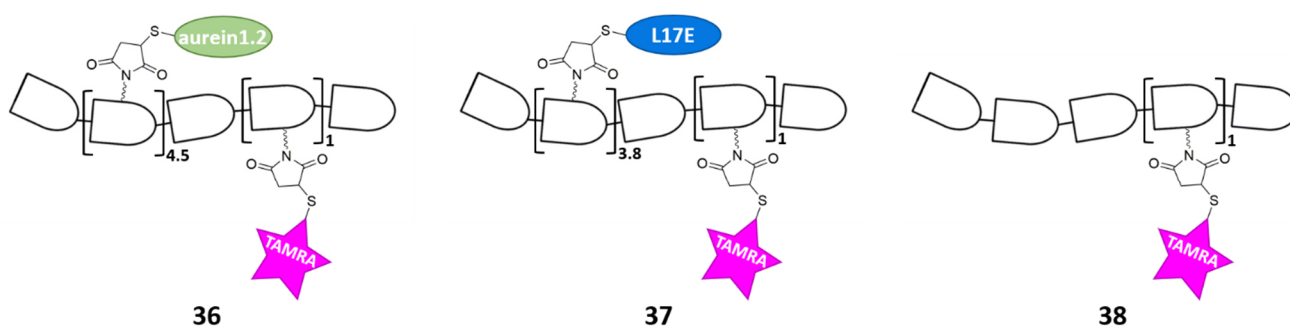
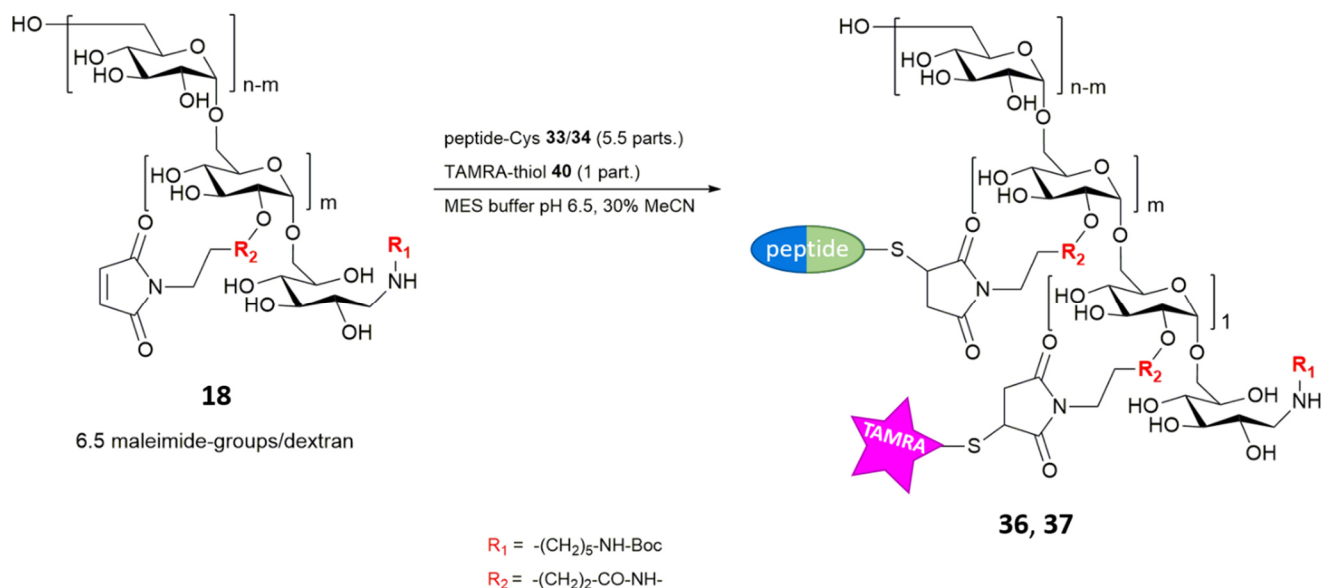


**Figure 34:** Schematic depiction of dextran decorated with TAMRA fluorophore and multiple copies of aurein1.2 **36** respectively L17E **37** as well as dextran decorated with TAMRA-label only **38**.

TAMRA-labeled peptide-dextran hybrids (**Figure 34**) were synthetically accessed by addition of thiol-modified peptide, respectively thiol-modified TAMRA fluorophore, to functionalized dextran, decorated with maleimide moieties at the glucose repeating units. For that purpose, both peptides, aurein1.2 as well as L17E, were synthesized via Fmoc-SPPS with an additional cysteine at the C-termini, yielding thiol-modified peptide variants aurein1.2-Cys **33** and L17E-Cys **34**. In the same way TAMRA-labeled dextran **38**, lacking peptide decoration, was synthesized as negative control, by addressing maleimide-dextran with thiol-modified TAMRA.

### 3.3.2.1 Maleimide-thiol conjugation I: Synthesis of TAMRA-labeled aurein1.2- and L17E-dextran compounds



**Scheme 12:** Synthesis of dextran compounds, decorated with TAMRA fluorophore and multiple copies of aurein1.2 **36** respectively L17E **37** via maleimide-thiol conjugation.

Maleimide(6.5)-dextran-*N*-Boc-cadaverine **18**, decorated with 6.5 maleimide functionalities per dextran on average and *N*-Boc-cadaverine modification at the reducing end, was chosen as starting material. To incorporate a single fluorophore per dextran, the maleimide-thiol addition was stoichiometrically controlled and dextran **18** was addressed with a mixture of aurein1.2-Cys **33**, respectively L17E-Cys **34** and TAMRA-thiol **35**, containing peptide-thiol and TAMRA-thiol in ratio 5.5:1, respectively.

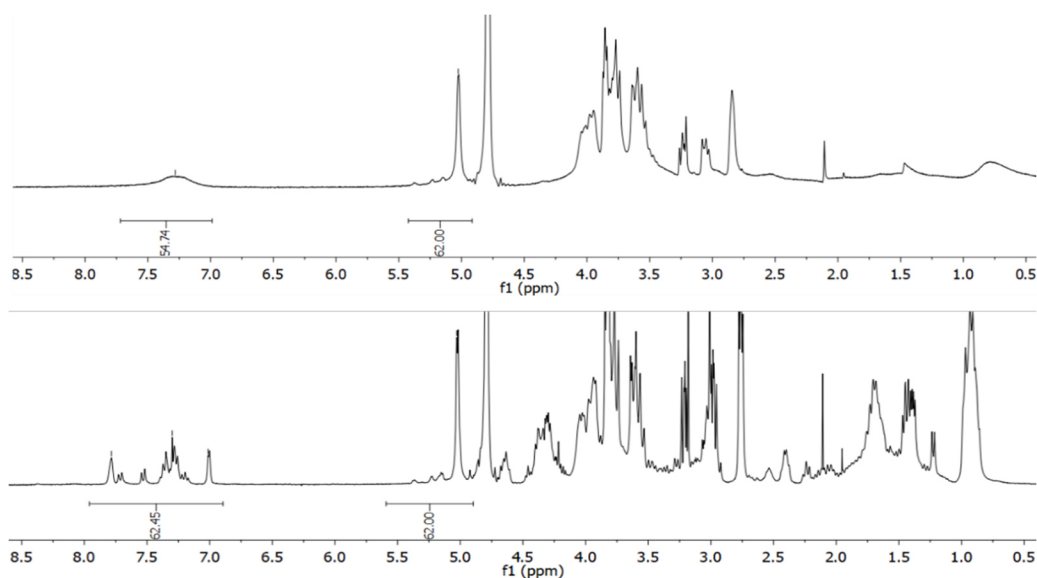


**Figure 35:**  $^1\text{H}$  NMR spectra of TAMRA-aurein1.2(4.5)-dextran-*N*-Boc-cadaverine **36** (upper) and TAMRA-L17E(3.8)-dextran-*N*-Boc-cadaverine **37** (lower) used for quantification of number of conjugated peptides per dextran on average.

To quantify the number of incorporated peptides per dextran,  $^1\text{H}$  NMR analysis was performed (**Figure 35**). Therefore integrated signals of the anomeric protons of the dextran glucose repeating units were set to a value of 62 and compared with the integrated aromatic signals. The aurein1.2 conjugation

product exhibited 54.74 aromatic protons per dextran, while the L17E conjugation product exhibited 62.45 aromatic protons per dextran. It was known, that L17E comprises 14 aromatic protons, aurein1.2 comprises 10 aromatic protons, further it was assumed that 1 TAMRA fluorophore, corresponding to 9 aromatic protons, was conjugated per dextran each. This resulted in compounds TAMRA-aurein1.2(4.5)-dextran-*N*-Boc-cadaverine **36**, equipped with on average 4.5 aurein1.2 per dextran, and TAMRA-L17E(3.8)-dextran-*N*-Boc-cadaverine **37**, equipped with on average 3.8 conjugated L17E per dextran.

As negative control, lacking both aurein1.2 and L17E, TAMRA-dextran-*N*-Boc-cadaverine **38** was synthesized, decorated with a TAMRA fluorescent label only, by addressing maleimide(7.8)-dextran-*N*-Boc-cadaverine **18** with one equivalent TAMRA-thiol **35**.

### 3.3.2.2 Maleimide-thiol conjugation II: Synthesis of doxorubicin-labeled L17E-dextran

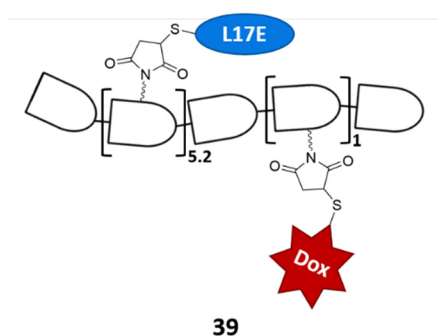
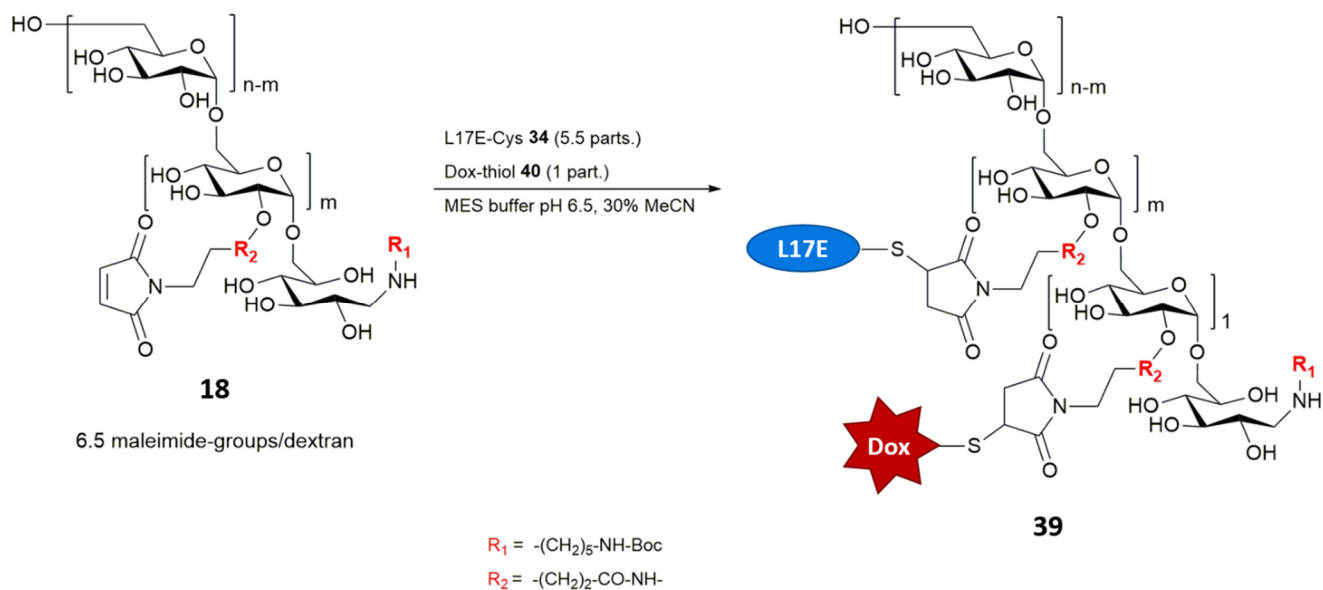


**Figure 36:** Schematic depiction of dextran **39** decorated with doxorubicin as fluorescent label and multiple copies of L17E.

Dextran **39** was decorated with multiple copies of L17E peptide molecules and a doxorubicin, replacing the TAMRA fluorescent label in the corresponding TAMRA-L17E(3.8)-dextran **37**. Briefly, doxorubicin is a fluorescent and cytostatic anthracycline drug, whose cytotoxicity is based on intercalation into the DNA.<sup>[116]</sup> The idea behind exchanging TAMRA by doxorubicin was to make use of the affinity between doxorubicin and DNA, which was thought to lead to accumulation of the construct in the nucleus upon cytosolic delivery.



**Scheme 13:** Synthesis of L17E-decorated dextran **39** equipped with doxorubicin as fluorescent label.

---

Corresponding to the synthesis of TAMRA-labeled and aurein1.2- respectively L17E-decorated dextran compounds **36** and **37**, maleimide(6.5)-dextran-*N*-Boc-cadaverine **18** bearing 6.5 maleimide functionalities per dextran on average, was addressed with a mixture of L17E-Cys **34** (5.5 parts) and Dox-thiol **40** (1 part). As reported for compounds **36** and **37**, quantification was performed via <sup>1</sup>H NMR analysis. The obtained product, Dox-L17E(5.2)-dextran-*N*-Boc-cadaverine **39**, was equipped with on average 5.2 copies of L17E peptide molecules per dextran.

### 3.3.2.3 Cellular uptake assay: Comparison of aurein1.2-dextran and L17E-dextran

In the literature,<sup>[56]</sup> L17E was reported to mediate cytosolic uptake of various biomacromolecules upon co-incubation with 40 μM L17E peptide. Initially, the uptake-mediating ability of the peptide was demonstrated by delivery of fluorescently labeled dextran (10 kDa) macromolecules. To this end, in the cited literature, HeLa cells were incubated with 25 μM fluorescently labeled dextran and co-incubated with 40 μM L17E. A similar procedure was applied for uptake assay in the present work.

HeLa cells were incubated in medium for 1 h with TAMRA-labeled dextran **38** (25 μM), TAMRA-labeled dextran **38** (25 μM) co-incubated with solitary L17E peptide **12** (40 μM), and peptide-decorated dextran hybrids TAMRA-aurein1.2(4.5)-dextran-*N*-Boc-cadaverine **36** (25 μM), TAMRA-L17E(3.8)-dextran-*N*-Boc-cadaverine **37** (3.13 μM) as well as Dox-L17E(5.2)-dextran-*N*-Boc-cadaverine **39** (12.5 μM). Following further 3 h incubation in medium only, the cellular distribution of the fluorescent constructs was analyzed by confocal laser scanning microscopy (CLSM).

Only weak uptake of the macromolecule was visible in cells treated with TAMRA-labeled dextran **38** (25 μM) in absence of L17E peptide (**Figure 37 (A)**; **Figure 90**), while cells co-incubated with 40 μM L17E peptide **12** showed enhanced uptake of TAMRA-labeled dextran **38** (25 μM) (**Figure 37 (B)**; **Figure 91**). Signals of intense TAMRA fluorescence were punctually distributed in the cytoplasm, leaving the area of the nucleus unaffected.

HeLa cells incubated with TAMRA-L17E(3.8)-dextran **37**, equipped with on average 3.8 copies of covalently bound L17E peptide units, showed significantly increased TAMRA fluorescence. Already at 3.13 μM compound concentration the fluorescence signals were spread all over the cytosol and even nucleus (**Figure 37 (C)**; **Figure 92**). The confocal images also revealed small spots and slightly degenerated cell morphology. Taken together it could be supposed that these spots are composed of membrane pieces and electrostatically attached compound molecules. These spots could be an indication for potential cytotoxic effects of the TAMRA-labeled and L17E-decorated dextran compound **37**.

Cells treated with TAMRA-aurein1.2(4.5)-dextran-*N*-Boc-cadaverine **36**, equipped with 4.5 copies of covalently bound aurein1.2 peptide molecules on average, even at high concentration (25 μM) showed weak uptake of the macromolecule only, with slight TAMRA fluorescent signals punctually distributed in the cytoplasm (**Figure 37 (D)**; **Figure 93**).

HeLa cells treated with Dox-L17E(5.2)-dextran-*N*-Boc-cadaverine **39**, equipped with 5.2 copies of covalently bound L17E peptide units on average and doxorubicin as fluorescent label (12.5 μM), showed fluorescence signals distributed in cytosol and nucleus (**Figure 37 (E)**; **Figure 94**). Higher compound concentration was required to reach similar intracellular distribution of fluorescence signals compared to cells treated with 3.13 μM TAMRA-L17E(3.8)-dextran **37**. Potentially, this was due to hampered detection of the doxorubicin labeled compound, respectively of the fluorescence signal of doxorubicin, which has a lower quantum yield compared to TAMRA fluorophore. The higher compound concentration applied, corresponding to higher L17E concentration, led to increased loss of membrane integrity and cell damage. Possibly, the cytotoxic nature of doxorubicin itself led to increased cell damage, albeit incubation time was thought to be short enough to not observe a cytotoxic effect. Altogether, replacing TAMRA fluorophore by doxorubicin did not show expected doxorubicin-DNA affinity induced increased accumulation of fluorescence signal inside the nucleus. However, the TAMRA-labeled compound **37**, already showed considerable nuclear translocation.

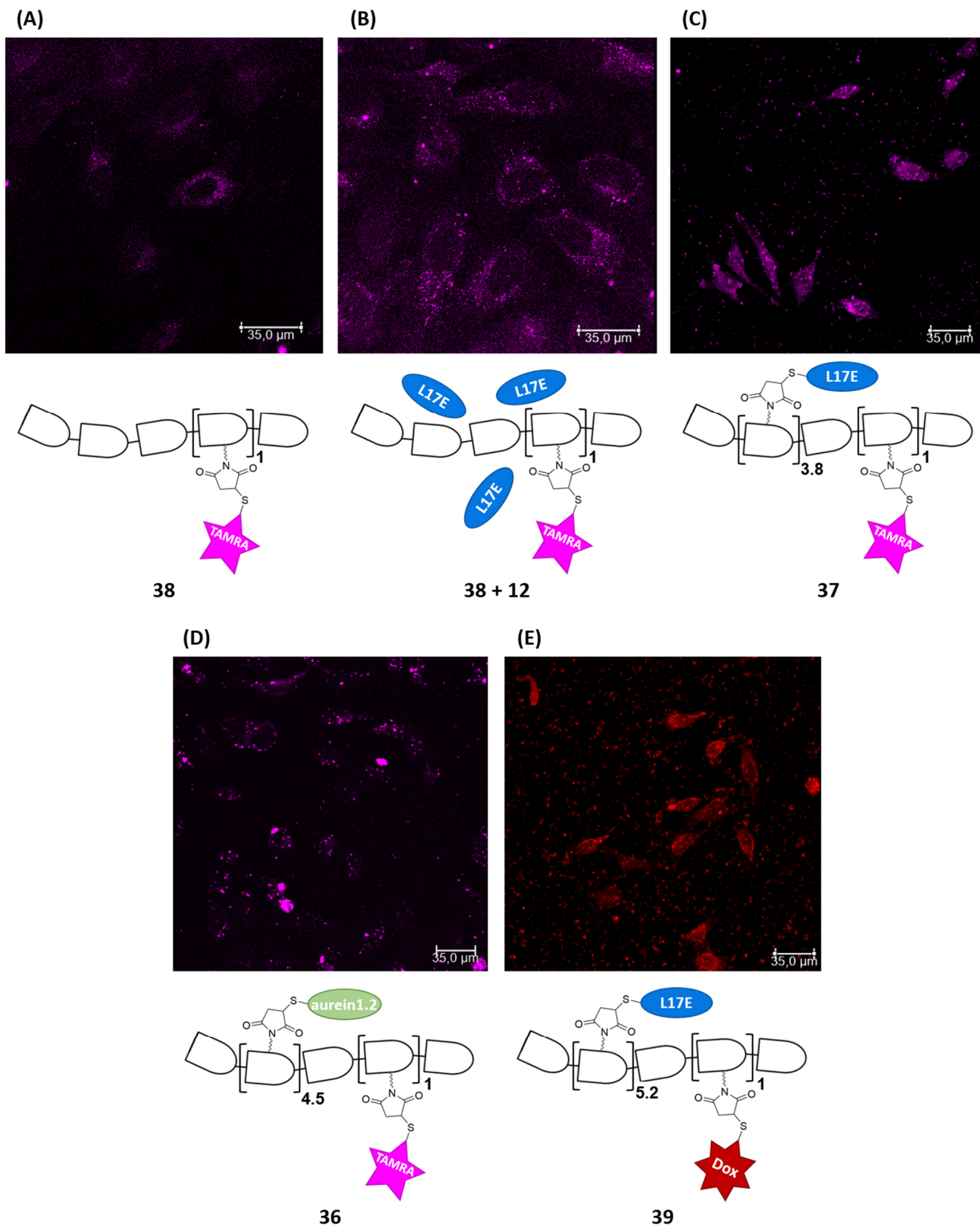


**Figure 37:** CLSM images (20 $\times$ ) of HeLa cells treated with different fluorophore-labeled peptide-dextran hybrids. TAMRA-fluorescence channel: **(A)** HeLa cells incubated with 25  $\mu$ M TAMRA-labeled dextran **38**; **(B)** HeLa cells incubated with 25  $\mu$ M TAMRA-labeled dextran **38** plus coincubation with 40  $\mu$ M solitary L17E **12**; **(C)** HeLa cells incubated with 3.13  $\mu$ M TAMRA-L17E(3.8)-dextran **37**; **(D)** HeLa cells incubated with 25  $\mu$ M TAMRA-aurein1.2(4.5)-dextran **36**. Doxorubicin-fluorescence channel: **(E)** HeLa cells incubated with 12.5  $\mu$ M Dox-L17E(5.2)-dextran **39**.

---

Taken together, compared to all other compounds enhanced intracellular uptake of TAMRA-L17E(3.8)-dextran **37**, equipped with on average 3.8 L17E peptide units and TAMRA label, was observed. Incubation with construct **37** led to intense fluorescence signals distributed all over the cytosol and nucleus, already starting at 3.13  $\mu\text{M}$  concentration. These findings revealed the superior ability of L17E compared to aurein1.2 to mediate intracellular uptake of macromolecules. Disclosed beneficial properties of L17E led to exclusively focus on this peptide in following development of peptide-dextran hybrid as module for intracellular delivery of covalently conjugated cargo.

Furthermore, the enhanced cytosolic uptake of the L17E-equipped dextran **37** (3.13  $\mu\text{M}$ ), compared to TAMRA-labeled dextran **38** (25  $\mu\text{M}$ ) coincubated with 40  $\mu\text{M}$  L17E peptide **12**, was induced obviously by the covalent nature of peptide-polysaccharide connection. Remarkably, the enhanced uptake of construct **37** occurred at lower concentrations of fluorescently labeled dextran as well as lower corresponding concentration of uptake mediating L17E peptide. Possibly, this indicated a multivalency effect induced by multiple copies of L17E bound to dextran scaffold, which was beneficial for the uptake-mediating ability of the peptide.

Macromolecules in a size under approximately 30-40 kDa can diffuse into the nucleus via nuclear pores.<sup>[117]</sup> Interestingly, no to little nuclear uptake of TAMRA-dextran **38**, co-incubated with solitary L17E was visible, while L17E-decorated TAMRA-dextran **37** entered the nucleus. Though both compounds featured smaller sizes than 30 kDa. Possibly, minor cytosolic concentration of TAMRA-dextran **38**, delivered via L17E coincubation, decreased nuclear diffusion, compared to construct **37**. Either a higher cytosolic concentration of construct **37**, TAMRA-labeled dextran covalently decorated with multiple L17E units, enhanced diffusion into the nucleus, or the presence of covalently conjugated L17E units mediated enhanced nuclear uptake, or a combination of both.

These findings showed the potential of L17E peptide molecules covalently bound to dextran in multiple copies. Furthermore, these results were encouraging to apply the peptide-dextran hybrid, featuring multiple attached L17E, as uptake mediating module for intracellular delivery of conjugated cargo.

### 3.3.3 Potential cytotoxic effect of L17E-dextran module

The intracellular uptake of TAMRA-L17E(3.8)-dextran **37**, with fluorescence signals distributed all over the cytosol and nucleus upon incubation of HeLa cells with the macromolecule at low micromolar concentration, led to application of L17E-decorated dextran as uptake-mediating module for intracellular delivery of conjugated cargo. However, to synthesize L17E-dextran module, the maleimide-thiol conjugation strategy was changed. Presumably due to hydrolysis, the conjugation of L17E-Cys and TAMRA-thiol with maleimide-functionalized dextran did not enable quantitative conversion. Hence, maleimide-thiol conjugation was substituted for azide-alkyne 1,3-cycloaddition. To this end, dextran was functionalized with azide moieties, while an additional propargyl-glycine (Pra) was introduced in the L17E sequence C-terminally, yielding L17E-Pra **41** after Fmoc SPPS. Further advantage of azide-alkyne “click”-reaction was the orthogonality to the amine conjugation site at the polysaccharide reducing end and incorporated red-end functionalities.

To apply dextran scaffold, decorated with multiple copies of L17E peptide molecules, as uptake-mediating module for intracellular delivery of conjugated cargo, the potential cytotoxic effect of L17E-dextran module **42** (**Figure 38**) on living cells had to be assessed.

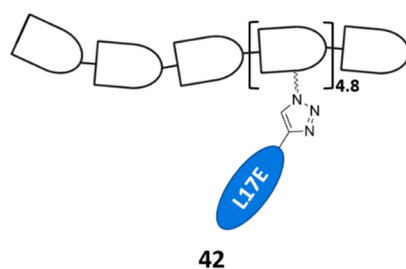
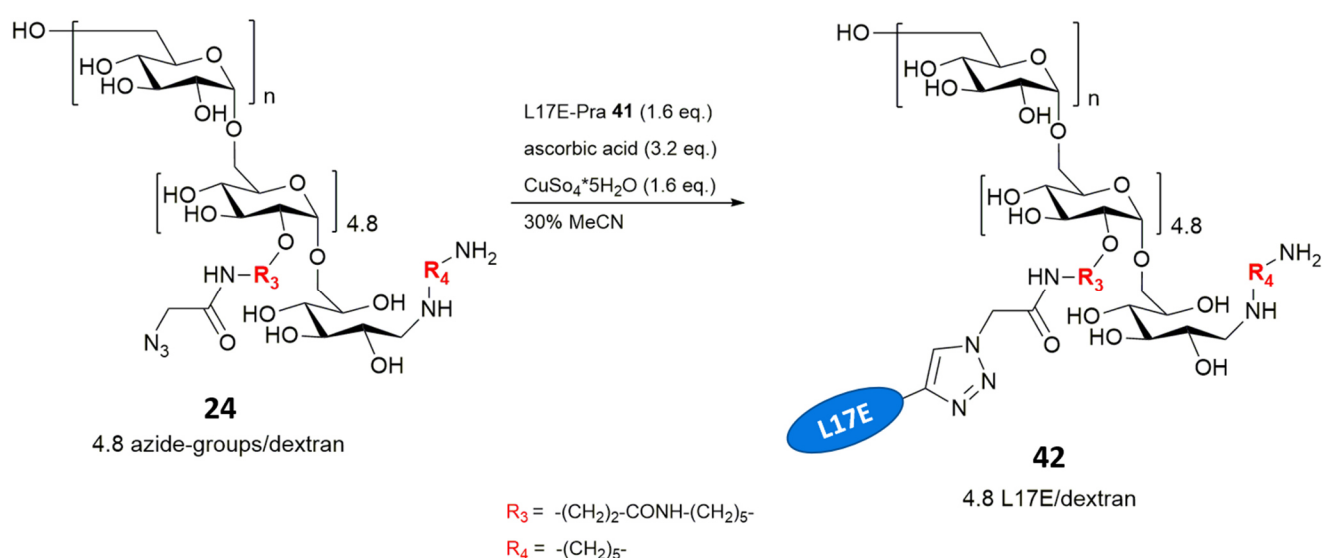


**Figure 38:** Schematic depiction of L17E-dextran module **42** decorated with multiple copies of L17E.

The L17E-dextran module **42** was synthetically accessed by copper catalyzed azide-alkyne cycloaddition of alkyne modified L17E-Pra peptide **41** and dextran, featuring azide functionalities at the glucose repeating units. To that end, upon carboxyethylation of dextran-*N*-Boc-cadaverine **13**, followed by EEDQ-activated conjugation of the azide linker **21** and removal of the Boc-protection, finally  $N_3(4.8)$ -dextran-cadaverine **24** (Scheme 10, Scheme 37) was accomplished, that possessed on average 4.8 azide functionalities per dextran accessible for further “click”-reaction.

### 3.3.3.1 CuAAC assembly of L17E-dextran module **42**



**Scheme 14:** Cu(I)-catalyzed azide-alkyne cycloaddition, yielding L17E(4.8)-dextran-cadaverine **42**.

To synthesize L17E-dextran module,  $N_3(4.8)$ -dextran-cadaverine **24** was addressed with L17E-Pra **41** in a Cu(I)-catalyzed azide-alkyne cycloaddition, resulting in L17E(4.8)-dextran-cadaverine **42**, decorated with on average 4.8 copies of L17E peptide and a cadaverine at the reducing end. To verify quantitative turnover and complete conversion of all 4.8 azide functionalities on average, the product was analyzed using IR-spectroscopy and UV/Vis spectroscopy. The IR spectrum of  $N_3$ -dextran-cadaverine starting material showed a characteristic azide-band at a wavenumber of around  $2116\text{ cm}^{-1}$ , which was no more visible in IR spectrum of the product after CuAAC (Figure 39). Disappearance of the azide-band was a qualitative evidence for complete turnover. To additionally verify the complete turnover quantitatively, the number of L17E peptide molecules per dextran on average was quantified via UV/Vis spectroscopy.

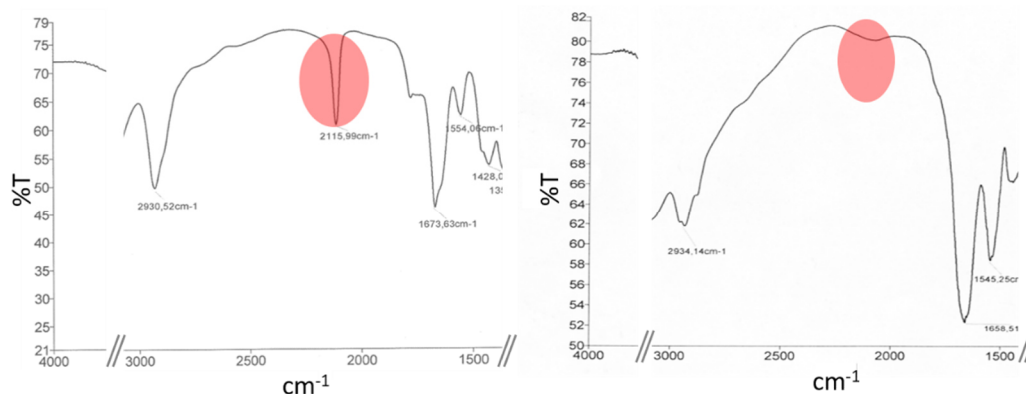


**Figure 39:** IR spectra of  $N_3(4.8)$ -dextran-cadaverine **24** starting material (left) and L17E(4.8)-dextran-cadaverine **42** product (right). The azide band at a wavenumber of 2116  $\text{cm}^{-1}$  disappeared after CuAAC.

### 3.3.3.2 UV/Vis photometric quantification

To quantify of the number of L17E peptide molecules per dextran on average in the CuAAC conjugation product **42**, UV/Vis photometry was performed. To that end, the molar extinction coefficient of L17E-Pra **41** at a wavelength of 280 nm was determined upon generation of a calibration curve (**Table 4**, **Figure 40**). A L17E-dextran-cadaverine **42** product sample with known concentration (weighted sample, assumed molecular weight of quantitative reaction product) was prepared and the absorption (280 nm) was measured. Using the determined molar extinction coefficient of L17E-Pra **41**, the resultant L17E concentration was calculated according to Lambert-Beer law (formula (6)). The number of L17E peptide molecules per dextran on average corresponds to the ratio of measured L17E concentration to sample concentration (formula (7)). The calculated ratio of 4.86, meaning 4.86 L17E units per dextran, coincided with the number of addressable azide groups per dextran in the  $N_3(4.8)$ -dextran-cadaverine **24** starting material, determined via  $^1\text{H}$ NMR spectroscopy. Together with the IR spectroscopical data, this result indicated the quantitative turnover of CuAAC. Hence, in this work, for all following decorations of azide functionalized dextran compounds with L17E-Pra peptide in Cu(I)-catalyzed azide-alkyne cycloaddition, a quantitative turnover of CuAAC conjugation was assumed and not analyzed repeatedly.

**Table 4:** Absorption measurement at 280 nm of serial dilutions of three different samples of L17E-Pra **41** for generation of a calibration curve and subsequent determination of the molar extinction coefficient.

c [mmol/L]	$A_{280}$ sample 1	$A_{280}$ sample 2	$A_{280}$ sample 3	$A_{280}$ mean	standard deviation
<b>0.176</b>	0.612	0.602	0.651	<b>0.622</b>	0.021
<b>0.117</b>	0.408	0.402	0.438	<b>0.416</b>	0.016
<b>0.078</b>	0.270	0.269	0.291	<b>0.277</b>	0.010
<b>0.052</b>	0.181	0.179	0.195	<b>0.185</b>	0.007
<b>0.035</b>	0.121	0.120	0.131	<b>0.124</b>	0.005
<b>0.023</b>	0.078	0.081	0.087	<b>0.082</b>	0.004
<b>0.015</b>	0.051	0.054	0.059	<b>0.055</b>	0.003
<b>0.010</b>	0.032	0.035	0.040	<b>0.036</b>	0.003
<b>0.007</b>	0.020	0.023	0.028	<b>0.024</b>	0.003
<b>0.005</b>	0.021	0.016	0.019	<b>0.019</b>	0.002
<b>0.003</b>	0.006	0.010	0.014	<b>0.010</b>	0.003

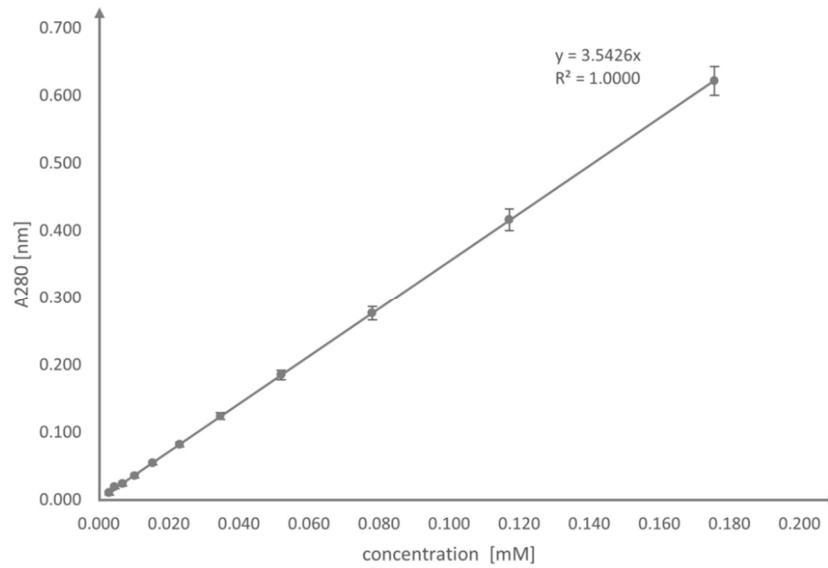


**Figure 40:** Calibration curve based on data shown in **Table 4**. The molar extinction coefficient of L17E-Pra **41** at 280 nm was determined to be 3542.6 L/(mol\*cm).

$$A = \varepsilon * c * d \quad (4)$$

$$c = \frac{A}{\varepsilon * d} \quad (5)$$

$$A_{280}(\text{sample}) = 0.302$$

$$d = 1 \text{ cm}$$

$$\varepsilon_{280}(\text{L17E-Pra}) = 3542.6 \frac{\text{L}}{\text{mol} * \text{cm}}$$

$$c(\text{sample}) = 1.75 * 10^{-5} \frac{\text{mol}}{\text{L}}$$

$$c(\text{L17E}) = \frac{A_{280}(\text{sample})}{\varepsilon_{280}(\text{L17E-Pra}) * d} = \frac{0.302}{3542.6 \frac{\text{L}}{\text{mol} * \text{cm}} * 1 \text{ cm}} = 8.5 * 10^{-5} \frac{\text{mol}}{\text{L}} \quad (6)$$

$$X = \frac{\text{L17E}}{\text{dextran}} = \frac{c(\text{L17E})}{c(\text{sample})} = \frac{8.5 * 10^{-5} \frac{\text{mol}}{\text{L}}}{1.75 * 10^{-5} \frac{\text{mol}}{\text{L}}} = 4.86 \quad (7)$$

### 3.3.3.3 Cell viability assay applying L17E-dextran module

To assess the potential cytotoxic effect of L17E-dextran module, in vitro cell viability assay was performed. Thus, HeLa cells were incubated in medium for 1 h with L17E-dextran module **42**, comprising dextran-cadaverine, decorated with 4.8 L17E per dextran on average ( $0.2 - 25 \mu\text{M}$ ), and solitary L17E peptide **12** ( $1 - 137 \mu\text{M}$ ). Following further 3 h incubation (B) respectively 24 h incubation (C) in medium only, MTS assay was performed. As already reported by Futaki et al.,<sup>[56]</sup> no decrease in cell viability was observable when incubating with high L17E peptide concentrations - up to  $70 \mu\text{M}$ . The L17E-dextran module **42** showed an  $\text{IC}_{50}$  value of approximately  $10 \mu\text{M}$  (Figure 41). Regarding the decoration of dextran-peptide hybrid with on average 4.8 L17E peptide units, the  $\text{IC}_{50}$  value corresponds to  $48 \mu\text{M}$  solitary L17E. Possibly, the nearly 1.5-fold increase in cytotoxicity could be induced by multivalency effects. Taking into consideration that L17E was derived from naturally haemotoxic lycotoxin, the  $\text{IC}_{50}$  value of approximately  $10 \mu\text{M}$  of L17E-dextran module **42** in the taken cell line is rather low. It is still in acceptable range and above concentration required to mediate intracellular delivery. No appreciable effect on cell viability was detectable when extending the second incubation period in medium only to 24 h.

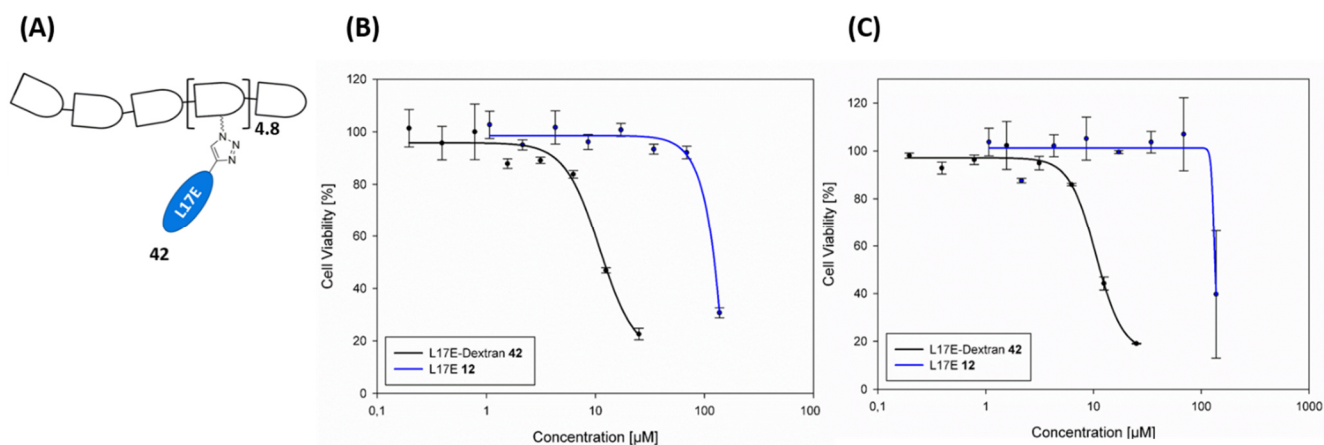


**Figure 41:** (A) Schematic depiction of L17E-dextran conjugate **42**, bearing 4.8 L17E per dextran on average, employed in cell viability assay on HeLa cell line. (B) Cell viability assay: HeLa cells treated 1 h with construct **42** and solitary L17E **12** in medium and subsequently 3 h in medium only. (C): Cell viability assay: HeLa cells treated 1 h with construct **42** and solitary L17E **12** in medium and subsequently 24 h in medium only.

Previously, uptake studies applying dextran **37**, equipped with on average 3.8 L17E units per dextran and TAMRA fluorescent label, in addition to remarkable uptake of the construct with widespread fluorescence inside the cytosol and nucleus, revealed slight indication for cytotoxic effects of the construct. This potential cytotoxic effect was observed at a concentration of  $3.13 \mu\text{M}$ , which was below the determined  $\text{IC}_{50}$  value of dextran **42**, decorated with 4.8 L17E units on average. In this context, it is important to mention, that introduction of a TAMRA label has been reported in the literature<sup>[118]</sup> to possibly induce an additional cytotoxic effect.

### 3.4 L17E-dextran as module for intracellular delivery

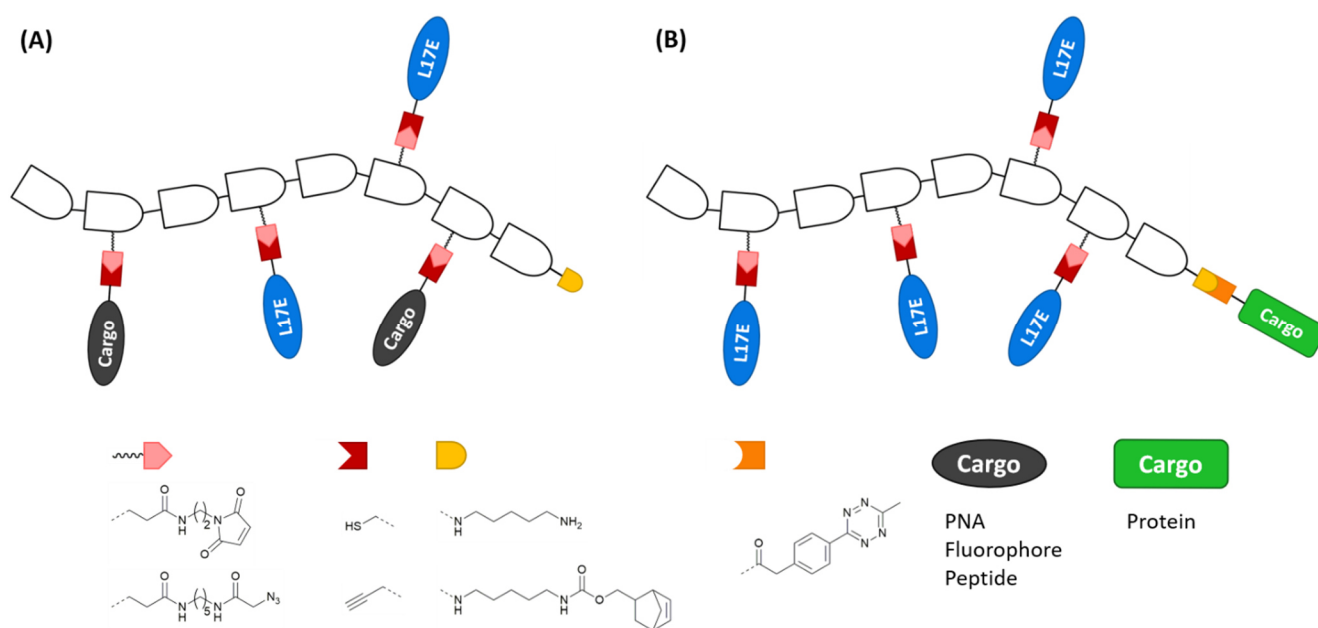


**Figure 42:** Depiction of two possible setups applying L17E-dextran module for intracellular delivery of cargo. **(A)** Dextran decorated with multiple copies of both L17E and cargo molecules at the glucose repeating units, offering a possible conjugation site for a second cargo at the reducing end. **(B)** Dextran decorated with multiple copies of L17E at the glucose repeating units and a conjugated cargo at the reducing end.

During development of L17E-dextran hybrid as uptake mediating module for intracellular delivery of conjugated cargo, two strategies evolved applying L17E-dextran in two different setups. One possibility was represented by the “mixed-decoration” approach, that enabled stoichiometrical decoration of the dextran glucose repeating units with multiple copies of both, L17E peptide units as well as cargo molecules. Simultaneously, this setup would have offered the possibility to address a further functionality at the polysaccharide reducing end with a second various payload, if desired (**Figure 42 (A)**). The “mixed-decoration” approach was beneficial for delivery of cargo molecules in multiple copies and was favorable in case of less space consuming payloads, such as PNA or peptides. Alternatively, the second setup featured decoration of modified hydroxy groups of the glucose repeating units with multiple L17E peptide molecules only, while a solitary cargo molecule was conjugated to the orthogonally functionalized reducing end (**Figure 42 (B)**). This setup seemed to be advantageous for delivery of demanding and bulky cargo, such as proteins.

#### 3.4.1 L17E-dextran mediated intracellular delivery of bioactive PNA

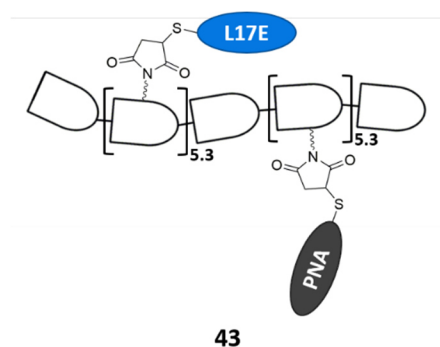


**Figure 43:** Schematic depiction of dextran 43 decorated with multiple copies of L17E and PNA.

To validate cytoplasmic delivery and even nuclear uptake, L17E-dextran was applied as delivery module for bioactive PNA payload. The experiment was performed in cooperation with Simon Englert, a colleague from the working group. To that end, according to the mixed-decoration setup (Figure 42 (A)), a dextran scaffold was decorated with multiple copies of both L17E and PNA molecules at the glucose repeating units (Figure 43) and applied in a mis-splicing correction assay.

As described in the introduction (1.6), the mis-splicing correction assay was based on HeLa-eGFP654 cells, which were stably transfected with eGFP gene containing a point mutation, that led to incorrect splicing and therefore translation of non-functional eGFP. Upon nuclear uptake of L17E-PNA-dextran 43 and hybridization of the antisense PNA with the mutated intron, splicing would be corrected and fluorescent eGFP would be produced (Figure 11). Hence, emerging eGFP fluorescence would validate cytoplasmic delivery and nuclear translocation of PNA biomolecules. Flow cytometry was used to relatively quantify the amount of intracellular eGFP that correlated with the amount of delivered PNA to the nucleus.

### 3.4.1.1 Maleimide-thiol conjugation: Synthesis of L17E-PNA-dextran 43

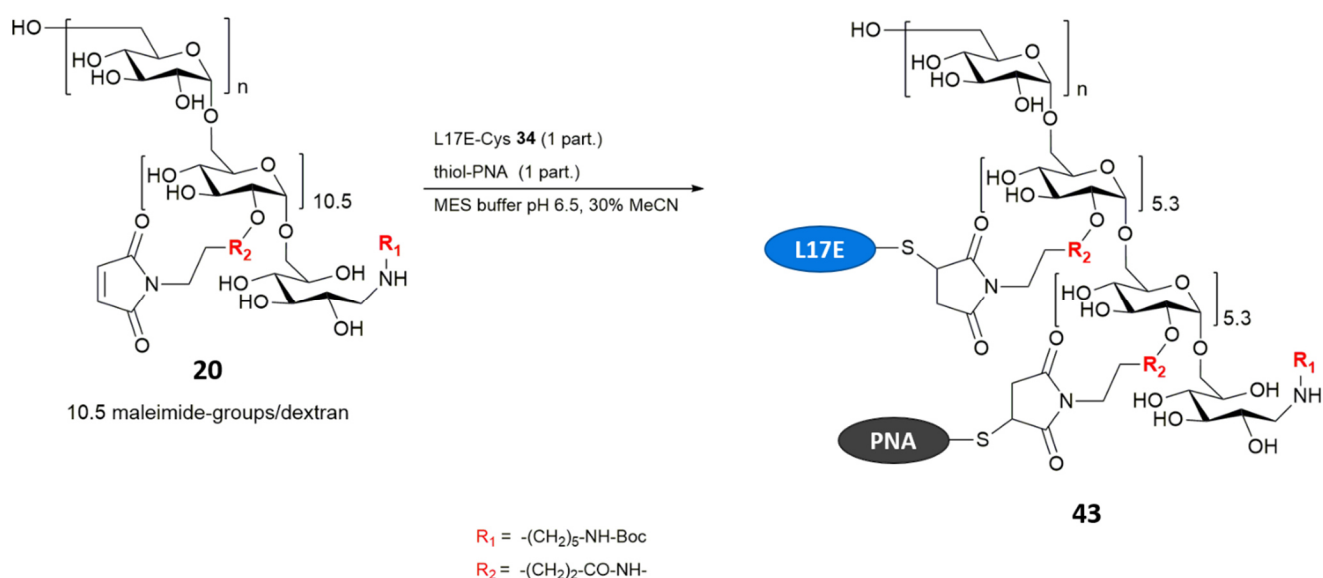


**Figure 44:** Maleimide-thiol conjugation of maleimide functionalized dextran with equimolar mixture of L17E-Cys 34 and thiol-PNA, yielding L17E-PNA-dextran conjugate 43.

To synthesize L17E and PNA decorated dextran 43, maleimide(10.5)-dextran-*N*-Boc-cadaverine 20, decorated with on average 10.5 maleimide functionalities per dextran and *N*-Boc-cadaverine modification at the reducing end, was addressed with an equimolar ratio of L17E-Cys 34 and thiol-PNA via Michael-like addition. The required 18mer PNA (*3-mercaptopropionic acid-gct-att-acc-tta-acc-cag-K-NH*<sub>2</sub>) was synthesized by Simon Englert via Fmoc SPPS including solubility enhancing C-terminal lysine and *N*-terminal modification with 3-mercaptopropionic acid as thiol conjugation site.

### 3.4.1.2 Mis-splicing correction assay applying L17E-PNA-dextran 43

In cooperation with Simon Englert, HeLa-eGFP654 cells were incubated with dextran 43, bearing L17E and PNA decoration in multiple copies, in serum-free medium at 37 °C for 30 min, followed by further incubation in serum-containing medium for 24 hours. Following trypsinization, cells were analyzed by flow cytometry (Figure 45 (B)). Cells incubated with L17E-PNA(10.5)-dextran conjugate 43 displayed higher fluorescence than untreated cells, even at low concentration of 2.5 μM (Figure 45 (B), top middle). In contrast, prior experiments performed in the working group, investigating uptake of free thiol-PNA, showed no significant shift in eGFP fluorescence (Figure 45 (B), top left). Interestingly,

despite structural complexity and the large size of about 54 kDa, the dextran conjugate **43**, decorated with multiple copies of L17E and PNA molecules was able to reach the nucleus where the PNA molecules were able to hybridize to the mutated intron. These findings validated cytoplasmic translocation of the macromolecule and furthermore revealed the potential of L17E-dextran module to mediate cytosolic and nuclear delivery of PNA.

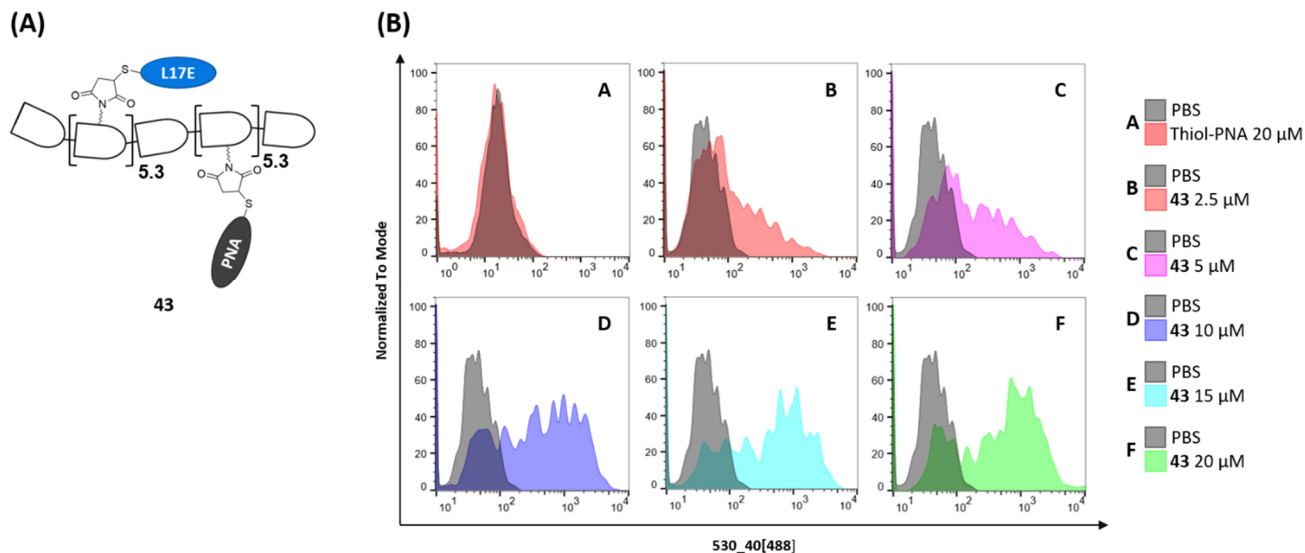


**Figure 45:** (A) Schematic depiction of L17E-PNA-dextran conjugate **43**. (B) Flow cytometric analysis (GFP-fluorescence on the x-axis) of HeLa-eGFP654 cells treated with thiol PNA (20  $\mu$ M) (top left) and different concentrations of **43** (top middle to bottom right). Grey histograms represent cells treated with PBS only.

### 3.4.2 L17E-dextran mediated protein delivery

Following the prior experiments, which recommended L17E-dextran as module for intracellular delivery and verified L17E-dextran mediated cytosolic and nuclear delivery of bioactive PNA, the module should be applied for intracellular delivery of covalently conjugated protein cargo. For the proof-of-concept, a cargo protein was covalently conjugated to the dextran reducing end, while the glucose repeating units were covalently decorated with multiple copies of L17E peptide molecules (**Figure 46**). Due to the intrinsic fluorescence, enhanced green fluorescent protein (eGFP) was chosen as model protein. Upon cellular uptake *in vitro*, the eGFP fluorescence facilitated detection of intracellular distribution of delivered protein payload via fluorescence microscopy.

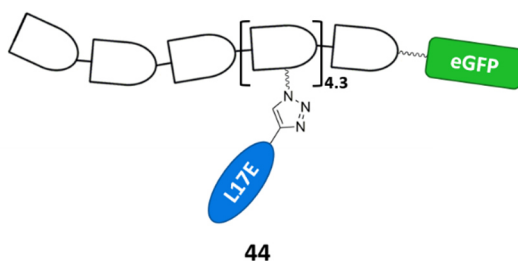


**Figure 46:** Schematic depiction of L17E-dextran module **44** decorated with multiple copies of L17E and covalently conjugated eGFP at the reducing end.

### 3.4.2.1 L17E-dextran-eGFP conjugate design

To assemble the conjugate **44** comprising L17E-dextran module, bearing multiple L17E at the glucose repeating units and covalently conjugated eGFP at the polysaccharide reducing end, an orthogonal strategy was developed, which combined dextran-to-protein conjugation via inverse electron-demand Diels-Alder (iEDDA) reaction followed by L17E conjugation in Cu(I)-catalyzed azide-alkyne cycloaddition (CuAAC) (**Figure 47**). To that end, a multi-functionalized dextran scaffold was required, featuring azide moieties at the glucose repeating units as well as norbornene functionality, accessible in iEDDA conjugation, located at the polysaccharide reducing end. Furthermore, methyltetrazine (MeTet) counterpart was introduced into the cargo protein via unspecific NHS-activated protein labeling.

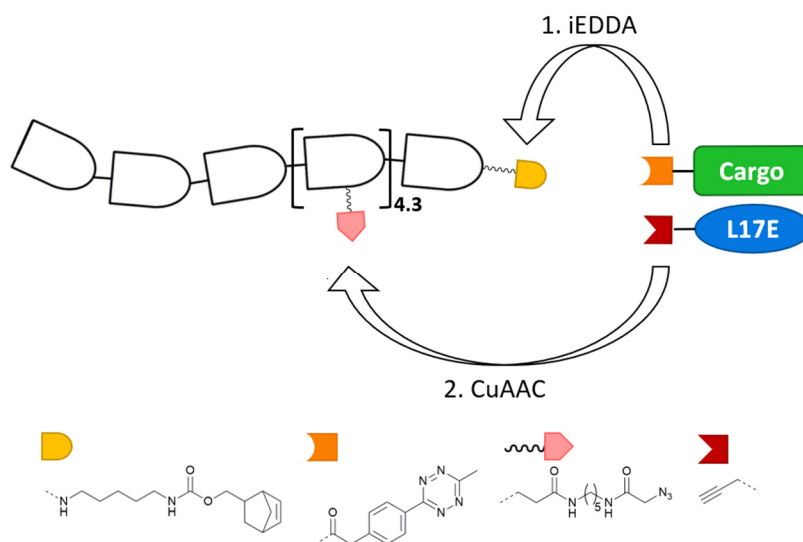


**Figure 47:** Synthesis strategy for assembly of L17E-dextran module, equipped with protein cargo at the reducing end. Dextran-to-protein conjugation via iEDDA applying  $N_3$ -dextran-norbornene and MeTet modified protein followed by addressing the azide groups at the glucose repeating units with L17E-Pra via CuAAC.

In face of possible negative impacts of copper catalyst on the protein during CuAAC, the conjugation steps had to be arranged in the order of protein conjugation first and L17E conjugation second, due to purification after dextran-to-protein conjugation. Excessive  $N_3$ -dextran-norbornene compound was removed via IMAC purification using the hexa-histidine-tag of the protein. It turned out, that IMAC purification following dextran-to-protein iEDDA conjugation, applying a CuAAC pre-assembled and already L17E-decorated dextran-norbornene **45**, was not possible. SDS-PAGE analysis of the dextran-to-protein conjugation product **46** revealed unsuccessful removal of excessive L17E-dextran-norbornene compound (**Figure 48 (B)**). Probably, presence of conjugated L17E peptide molecules led to interaction of histidine residues, originating from the L17E sequence, and immobilized nickel ions of the stationary phase. Hence, L17E-decoration of the glucose repeating units had to be performed following dextran-to-protein conjugation and purification. Application of copper(I)-ligand BTAA during CuAAC prevented copper-induced protein damage.

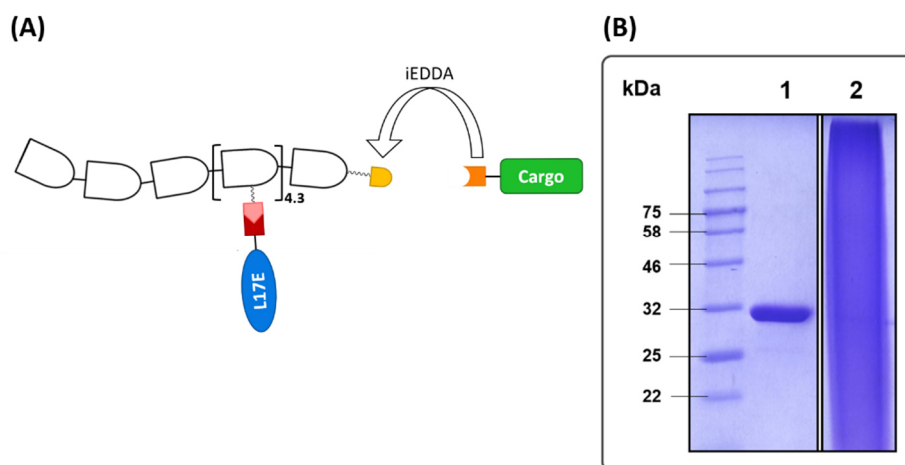
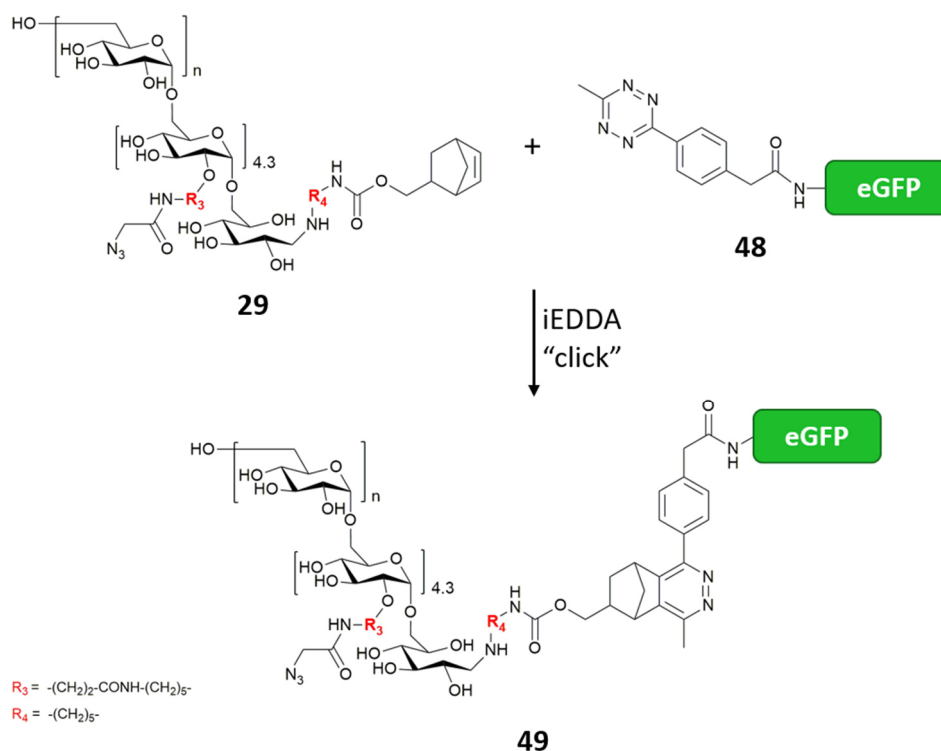


**Figure 48:** (A) Alternative synthesis strategy applying pre-assembled L17E-dextran-norbornene in dextran-to-protein conjugation via iEDDA. (B) Coomassie stained SDS-PAGE analysis 1: unmodified eGFP; 2: IMAC purified L17E-dextran-to-protein conjugation product: removal of excessive L17E-dextran-norbornene was not possible.

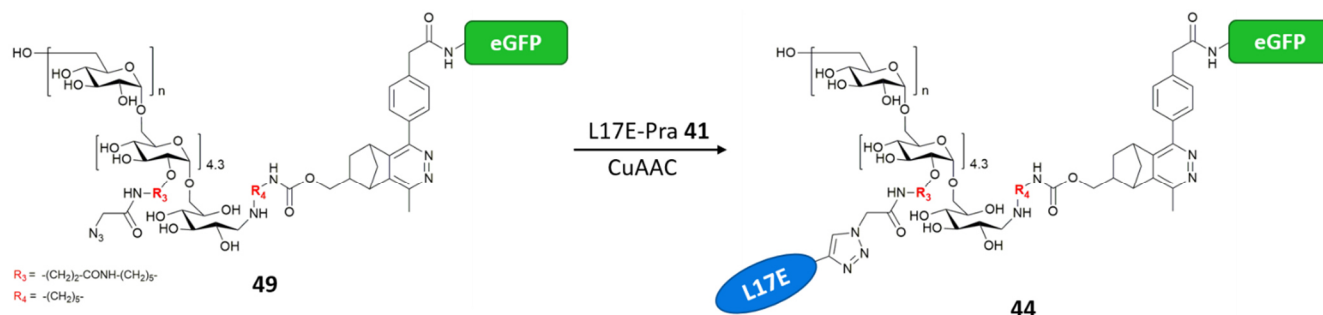
### 3.4.2.2 L17E(4.3)-dextran-eGFP 44 conjugate synthesis



**Scheme 15:** iEDDA dextran-to-protein conjugation of red-end functionalized  $N_3(4.3)$ -dextran-norbornene **29** and methyltetrazine modified eGFP **48** yielding dextran-to-protein conjugate  $N_3(4.3)$ -dextran-eGFP **49**.

To synthesize L17E-dextran module **44** with covalently conjugated eGFP payload, dextran **29**, bearing on average 4.3 azide moieties at the glucose repeating units and a norbornene functionality at the reducing end, was chosen as starting material. Following unspecific eGFP modification applying NHS-activated methyltetrazine derivative **47**, dextran-to-protein conjugation of eGFP-MeTet **48** and  $N_3(4.3)$ -dextran-norbornene **29** was achieved via iEDDA “click”-chemistry, yielding  $N_3(4.3)$ -dextran-eGFP **49** (**Scheme 15**). Following removal of excessive dextran **29** via IMAC, the conjugate was decorated with L17E peptide molecules. To this end, the azide moieties were addressed with L17E-Pra **41** in a Cu(I)-

catalyzed azide-alkyne cycloaddition (**Scheme 16**), applying Cu(I)-ligand BTAA for biocompatibilization. Upon purification, the ultimate conjugate L17E(4.3)-dextran-eGFP **44** was yielded, decorated with 4.3 L17E units on average and covalently conjugated eGFP at the reducing end.



**Scheme 16:** Addressing the azide functionalities of  $N_3(4.3)$ -dextran-eGFP **49** with L17E-Pra **41** in biocompatibilized Cu(I)-catalyzed azide-alkyne cycloaddition, yielding L17E(4.3)-dextran-eGFP **44**.

Coomassie stained SDS-PAGE analysis revealed successful and nearly complete dextran to protein conjugation, visualized by decrease of eGFP band (**Figure 49; 1**) and appearance of dextran typical smeared band (**Figure 49; 2**), whose intensity of Coomassie stain explicitly increased upon L17E peptide conjugation (**Figure 49; 3**). Final product concentration was determined via eGFP absorbance at 488 nm.

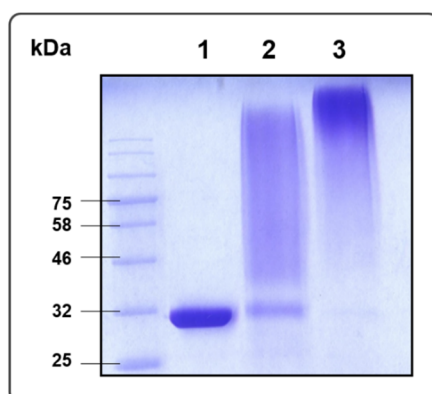
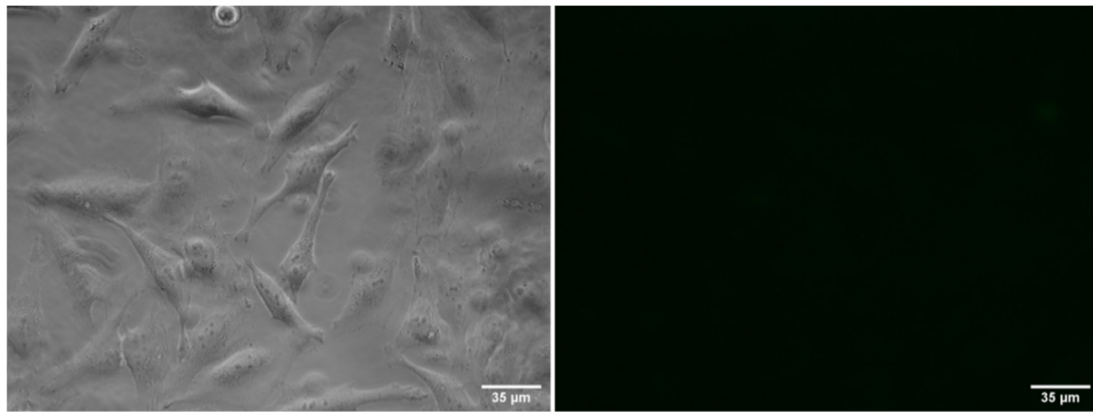


**Figure 49:** SDS-PAGE of 1: eGFP; 2:  $N_3(4.3)$ -dextran-eGFP **49**; 3: L17E(4.3)-dextran-eGFP **44**.

### 3.4.2.3 Cellular uptake assay

HeLa cells were incubated with unmodified eGFP ( $8 \mu\text{M}$ ) as negative control, unmodified eGFP ( $8 \mu\text{M}$ ) co-incubated with solitary L17E **12** ( $40 \mu\text{M}$ ), and L17E(4.3)-dextran-eGFP **44** at  $4 \mu\text{M}$  concentration in serum free medium for 1 h each. Following further 3 h incubation in medium, cellular distribution of the eGFP fluorescence signal was analyzed with fluorescence microscopy. Cells only treated with eGFP did not show any fluorescence both inside the cell and on the cell surface (data not shown). Cells treated with eGFP plus coinubation with  $40 \mu\text{M}$  solitary L17E peptide **12** also did not show any fluorescence (**Figure 50**), while cells treated with conjugate **44** showed widely spread fluorescence signal inside the cytosol (**Figure 51**).



(A)

(B)

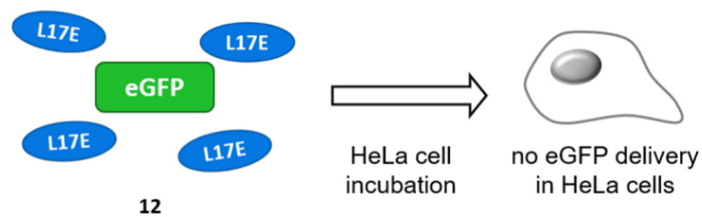
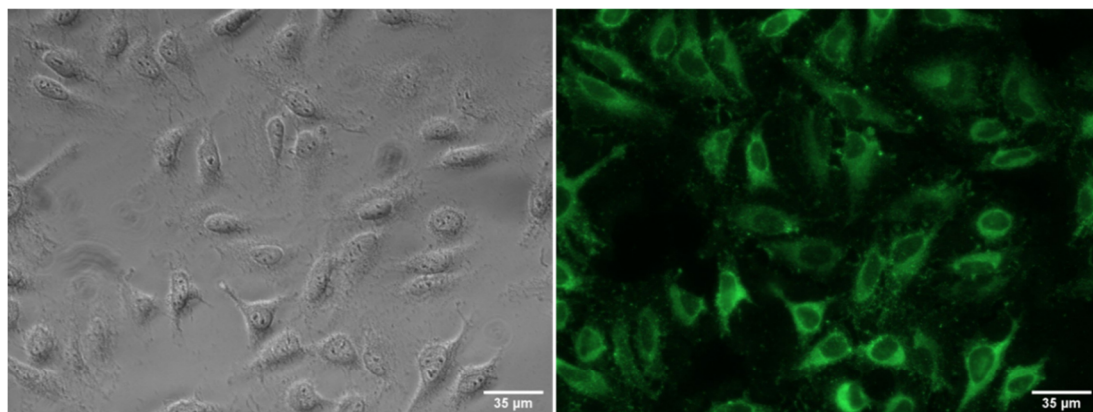


**Figure 50:** Fluorescence microscopy (20×) images of HeLa cells treated with eGFP (8 μM) co-incubated with 40 μM L17E 12 ((A): brightfield image; (B): eGFP fluorescence channel).



(C)

(D)

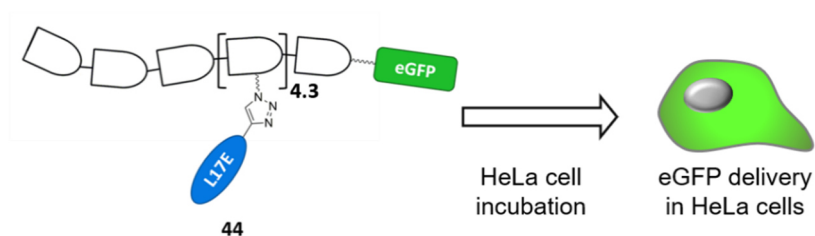


**Figure 51:** Fluorescence microscopy (20×) images of HeLa cells treated with L17E(4.3)-dextran-eGFP 44 (4 μM) ((C): brightfield image; (D): eGFP fluorescence channel).

The fluorescence microscopy analysis was repeated applying confocal laser scanning microscopy. Confocal images revealed the same results. Cells treated with eGFP (8 μM) only and cells treated with eGFP (8 μM) plus coincubation with L17E (40 μM) did not show eGFP fluorescence (data not shown), while evenly and widely spread fluorescence signal inside the cytosol was validated in cells treated with L17E(4.3)-dextran-eGFP 44 (4 μM) (Figure 52; Figure 95; Figure 96).

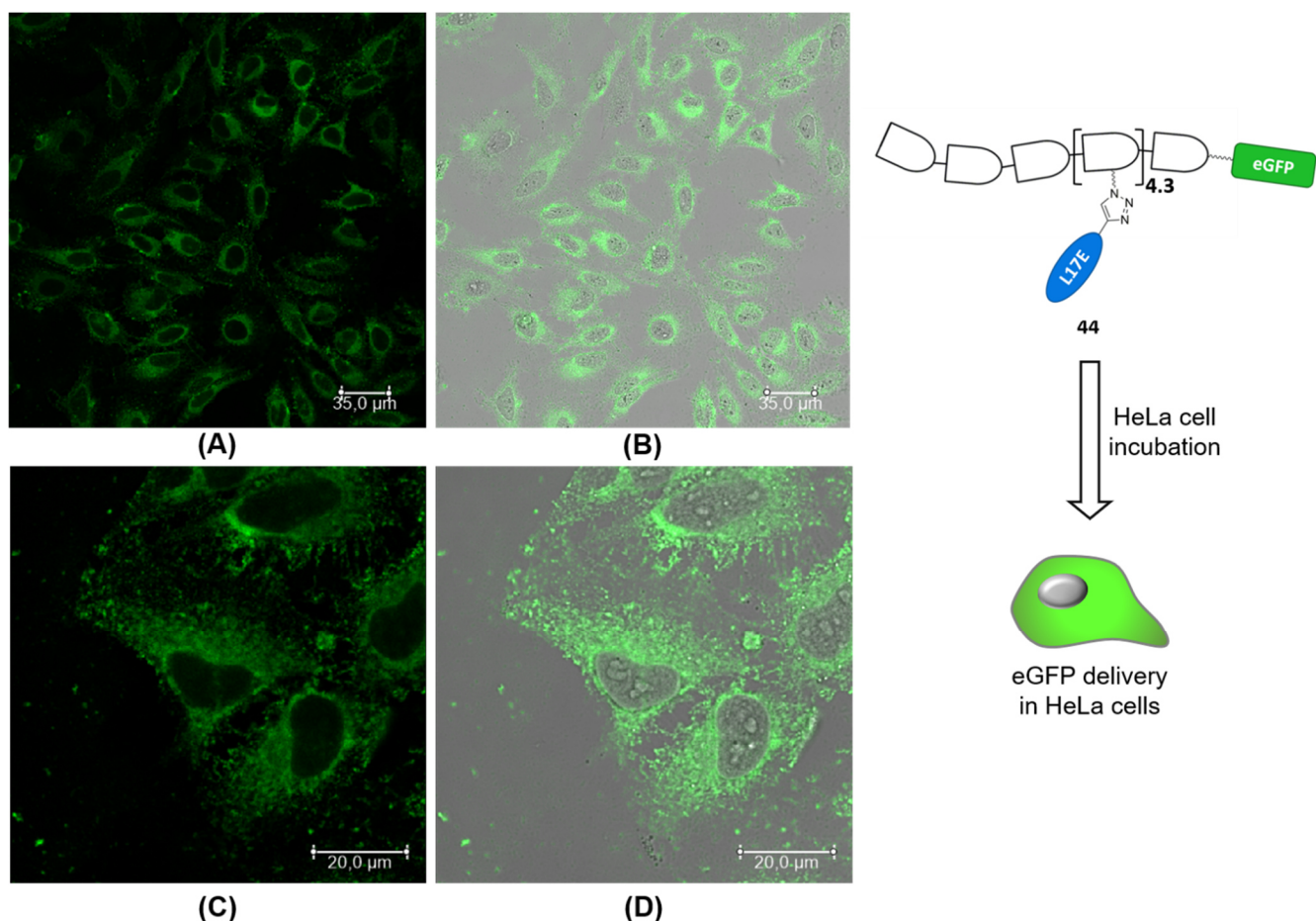


**Figure 52:** Cytosolic delivery of eGFP model protein mediated by covalently conjugated L17E-dextran delivery module. HeLa cells were treated with 4  $\mu$ M L17E(4.3)-dextran-eGFP **44** and analyzed via CLSM. **(A):** treated HeLa cells, eGFP fluorescence channel (20 $\times$ ). **(B):** Merge of eGFP fluorescence and brightfield image (20 $\times$ ). **(C):** treated HeLa cells, eGFP fluorescence channel (63 $\times$ ). **(D):** Merge of eGFP fluorescence and brightfield image (63 $\times$ ).

No unspecific uptake of unmodified eGFP in HeLa cells was detectable and no adherence of the protein on the cell membrane was visible. Furthermore, coincubation with 40  $\mu$ M L17E **12** did not lead to any intracellular eGFP fluorescence, respective did not mediate intracellular uptake of the model protein. Meanwhile, cytosolic eGFP fluorescence emerged in cells treated with conjugate **44**, comprising dextran equipped with on average 4.3 L17E peptide molecules at the glucose repeating units and covalently conjugated eGFP model protein at the polysaccharide reducing end. This revealed the ability of the developed L17E-dextran hybrid to promote cytosolic delivery of covalently conjugated protein cargo. The evenly and widespread eGFP fluorescence signals inside the cells, together with the knowledge from prior experiments, which validated L17E-dextran mediated cytosolic and nuclear uptake, led to the assumption of cytosolic and non-endosomal protein delivery, mediated by covalently connected L17E-dextran module.

#### 3.4.2.4 L17E(4.8)-dextran-eGFP **52** conjugate synthesis II

L17E-dextran module demonstrated its ability to promote intracellular uptake of a covalently conjugated eGFP model protein into the cytoplasm. In the literature,<sup>[70]</sup> for L17E-mediated uptake of macromolecules an uptake mechanism was proposed: Transient membrane permeabilization. This mechanism is based on macropinocytosis and therefore classified as energy-dependent endocytosis. Upon interaction with the cell membrane, L17E was thought to mediate actin rearrangement, causing membrane ruffling followed by macropinocytosis. Before membrane closure and formation of macropinosomes, L17E was thought to rupture the ruffled membrane and to enable direct influx of cargo

into the cell interior. To investigate, whether the underlying uptake mechanism could also prevail for dextran-coupled L17E, the energy dependence of L17E-dextran mediated cargo delivery was analyzed. To that end, the cellular uptake assay applying L17E-dextran with covalently conjugated eGFP model protein was repeated under ATP-depleted conditions at 4 °C. According to synthesis of L17E(4.3)-dextran-eGFP **44**, a similar conjugate was assembled based on dextran **31**, decorated with on average 4.8 azide moieties at the glucose repeating units and norbornene red-end functionalization. Upon iEDDA dextran-to-protein conjugation of N<sub>3</sub>(4.8)-dextran-norbornene **31** and eGFP-MeTet **50**, followed by addressment of N<sub>3</sub>(4.8)-dextran-eGFP **51** with L17E-Pra **41** in a Cu(I)-catalyzed azide-alkyne cycloaddition, final conjugate **52**, bearing L17E decoration and covalently conjugated eGFP was yielded (**Figure 53**). Final product concentration was determined via eGFP absorbance at 488 nm.

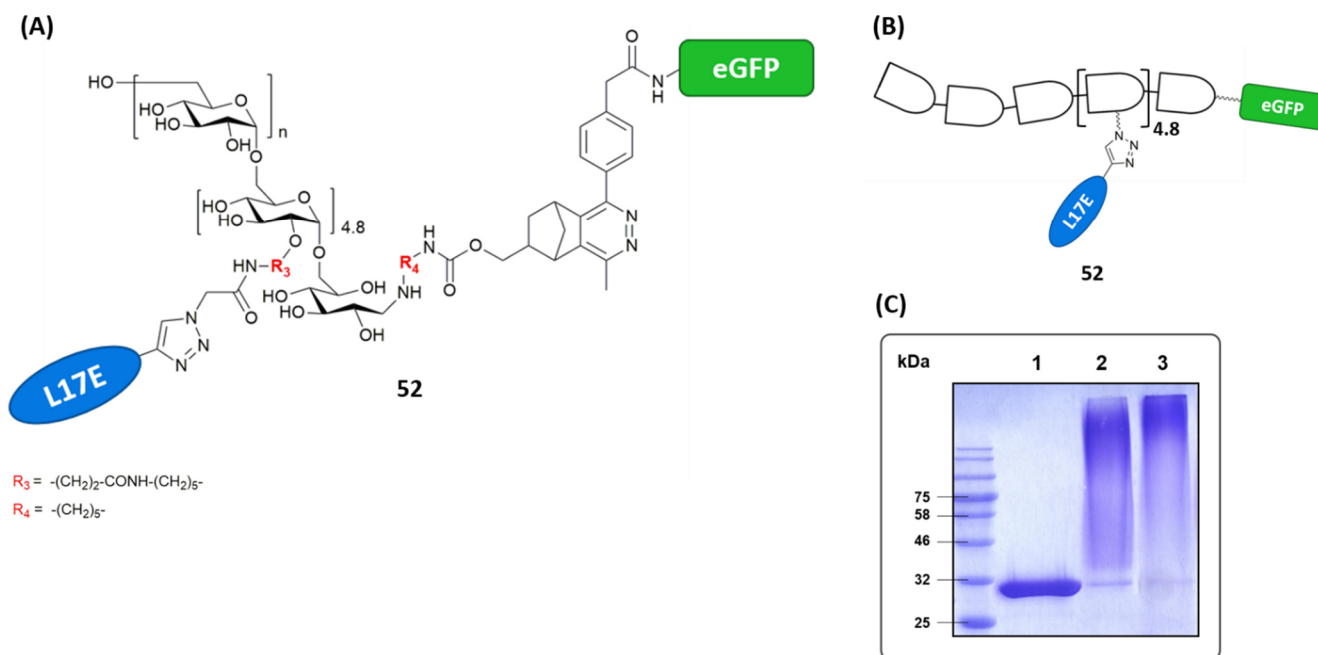


**Figure 53:** (A) Structure of L17E(4.8)-dextran-eGFP **52**; (B) Schematic depiction of conjugate **52**; (C) Coomassie stained SDS-PAGE analysis showing unmodified eGFP (1), N<sub>3</sub>(4.8)-dextran-eGFP **51** (2) and L17E(4.3)-dextran-eGFP **52** (3).

### 3.4.2.5 Cellular uptake assay at 4 °C

Following washing with cold PBS, HeLa cells were incubated with L17E(4.8)-dextran-eGFP **52** at 2  $\mu\text{M}$  concentration in serum free medium for 1 h at 4 °C. Following further 3 h incubation in medium at 4 °C, cellular distribution of the eGFP fluorescence signal was analyzed with fluorescence microscopy. Cells treated with conjugate **52** showed evenly and widely spread fluorescence signal inside the cytosol (**Figure 54**). Interestingly, in contrast to L17E-mediated uptake in the literature,<sup>[70]</sup> the reduced temperature in this experiment did not affect the ability of the L17E-dextran module to promote intracellular delivery of covalently conjugated protein cargo. In contrast to the transient membrane permeabilization uptake mechanism proposed in the literature<sup>[70]</sup> (for detailed description of the mechanism see section 1.3.2), these findings would have led to the assumption of energy-independent uptake mediated by L17E-dextran module. However, L17E-induced membrane ruffling and uptake of macromolecules following L17E-mediated rupture of the ruffled membrane prior to macropinosome formation, was reported to occur within a few minutes.<sup>[70]</sup> Probably, under the given ATP-depletion conditions, uptake of conjugate **52** was an artifact due to residual temperature, sufficient for macromolecule uptake within first minutes of incubation. The experiment remained to be repeated applying thoroughly pre-cooled HeLa cells and sodium azide induced ATP-depleted conditions. Furthermore, application of macropinocytosis inhibitors such as Cytochalasin D or 5-(*N*-ethyl-*N*-isopropyl)amiloride, inhibiting actin polymerization, respectively formation of ruffled membranes, both crucial elements for macropinocytosis, could shed light on L17E-dextran mediated uptake pathway.

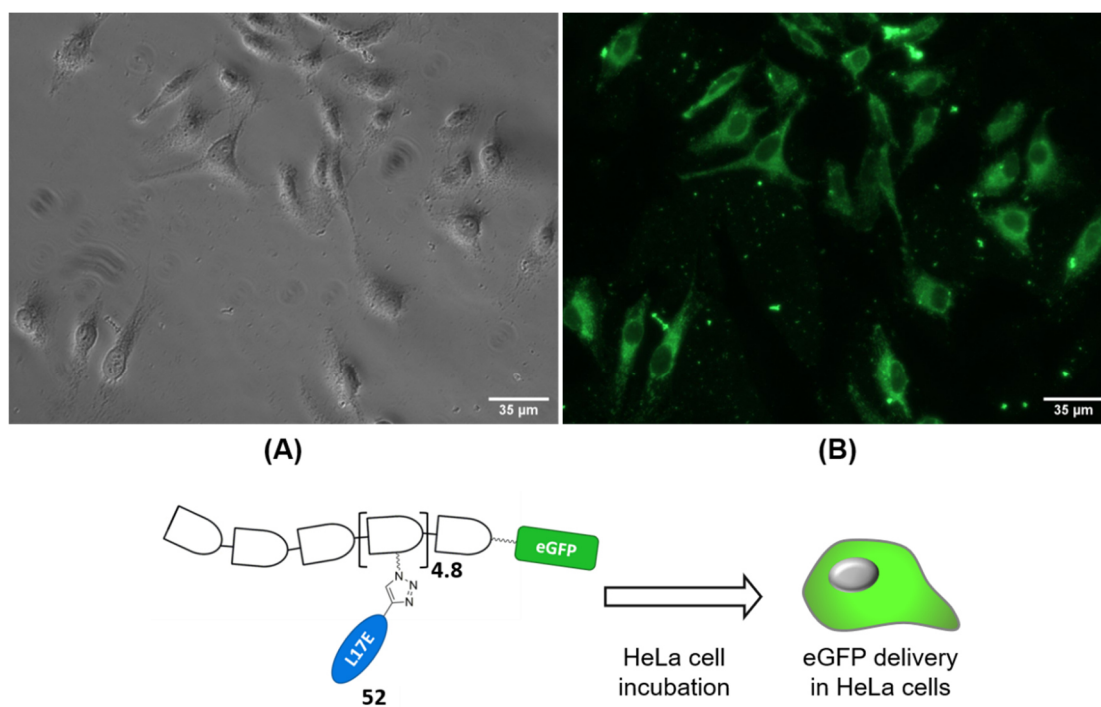


**Figure 54:** Fluorescence microscopy (20×) images of HeLa cells treated with L17E(4.8)-dextran-eGFP **52** (2 μM) at 4 °C ((A): brightfield image; (B): eGFP fluorescence channel).

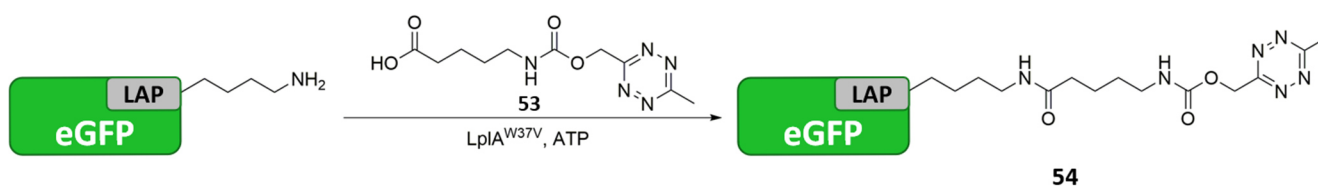
### 3.4.3 Site-specific dextran-to-protein conjugation

While solitary L17E peptide was not able to promote intracellular uptake of an eGFP model protein upon coincubation, L17E-dextran hybrid proved its ability to act as delivery module for both covalently conjugated protein cargo and multiple copies of covalently conjugated PNA molecules. Dextrans **44** and **52**, both decorated with multiple L17E peptides at the glucose repeating units and eGFP covalently conjugated to polysaccharide reducing end, resulted in considerable cytosolic eGFP fluorescence upon incubation of HeLa cells with the respective construct. Both conjugates were based on dextran-to-protein conjugation via iEDDA conjugation between norbornene functionality at the dextran red-end and a MeTet functionality introduced into the protein. So far, introduction of MeTet into the protein was achieved by unspecific addressment of accessible amine groups of eGFP with NHS-activated MeTet derivative. This led to heterogeneous product mixtures due to unspecific MeTet-labeling of different amine side chain functionalities of eGFP on the one hand and to possible decoration of the protein with multiple MeTet functions on the other hand. Introduction of more than one MeTet group would have led to conjugation of multiple dextran modules per protein in the following dextran-to-protein conjugation. To keep possible multifunctionalization of the protein in low range, the applied amount of NHS-activated MeTet compound was restricted to five-fold molar excess. For proof-of-concept studies, which successfully proved the ability of L17E-dextran module to mediate cytosolic delivery of protein cargo, the potential heterogeneous nature of the yielded conjugates did not matter.

However, homogenous dextran-to-protein conjugation product would be preferable. Especially when thinking about potential prospective application of L17E-dextran as module for intracellular delivery of functional proteins in a therapeutic context. To that end, it was obvious to benefit from the specificity of enzyme-mediated protein modification. In this respect, Wombacher and coworkers<sup>[102]</sup> presented an excellent protein labeling approach, which combined lipoic acid protein ligase A (LplA<sup>W37V</sup>) mediated site-specific introduction of novel diene substrates, such as methyltetrazine substrate, with subsequent biorthogonal iEDDA conjugation.

According to this approach, LplA was used to incorporate the required methyltetrazine functionality site-specifically into eGFP, equipped with lipoic acid acceptor peptide (LAP) recognition sequence.

### 3.4.3.1 LplA<sup>W37V</sup>-mediated site-specific eGFP modification with methyltetrazine



**Scheme 17:** LplA<sup>W37V</sup> mediated amide bond formation between lysine  $\epsilon$ -amine of the LAP-tagged eGFP and a methyltetrazine substrate derivative derived of liponic acid, yielding eGFP-MeTet **54**

For site-specific introduction of the methyltetrazine functionality into LAP-tagged eGFP, amide bond formation between lysine  $\epsilon$ -amine originating from the LAP-tag and the methyltetrazine substrate was catalyzed by LplA<sup>W37V</sup> (**Scheme 17**). The required liponic acid derived methyltetrazine substrate **53** was kindly provided by the Wombacher group, the enzyme was produced in the working group for prior experiments.

Enzyme reaction was performed applying 25 equivalents substrate and 1/10 equivalent LplA<sup>W37V</sup> at 37 °C for 1 h. The ligation product eGFP-MeTet **54** was analyzed via HIC. HIC analysis of unmodified eGFP, beside a minor impurity, showed one main signal with a retention time of 13.032 min (**Figure 55** green). Upon LplA<sup>W37V</sup> mediated amide bond formation with the MeTet substrate **53**, the eGFP-MeTet **54** chromatogram revealed total shift of the signal towards longer retention time of 15.843 min and nearly no signal of unmodified eGFP was visible (**Figure 55** blue). The prolonged retention time correlated with increasing hydrophobicity of modified eGFP, caused by the incorporation of the MeTet functionality.

These results verified quantitative introduction of methyltetrazine substrate into the protein, mediated by LplA<sup>W37V</sup>. For this reason, LplA<sup>W37V</sup> catalysis represents a suitable option for site-specific introduction of a chemical functionality into a protein of interest, equipped with LAP recognition sequence. Hence, LplA<sup>W37V</sup> mediated protein modification could enable site-specific dextran-to-protein conjugation, resulting in a homogenous product.

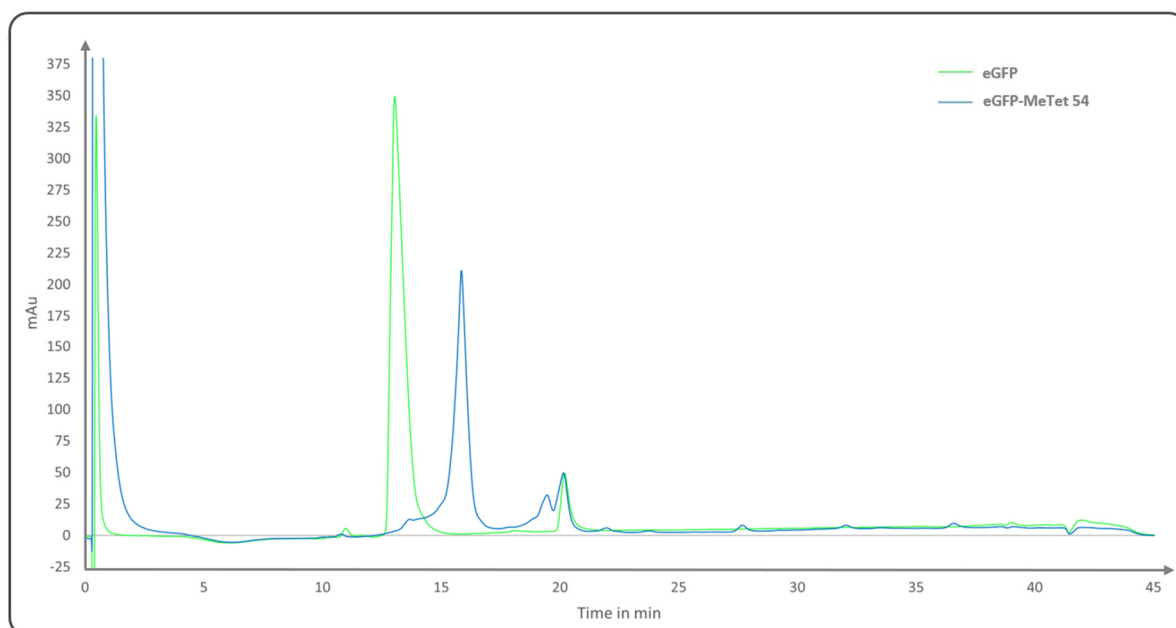


**Figure 55:** HIC chromatograms of eGFP (green) and eGFP-MeTet **54** (blue).

### 3.4.3.2 L17E(4.8)-dextran-eGFP 57 synthesis applying LpIA<sup>W37V</sup> mediated site-specific dextran-to-protein conjugation

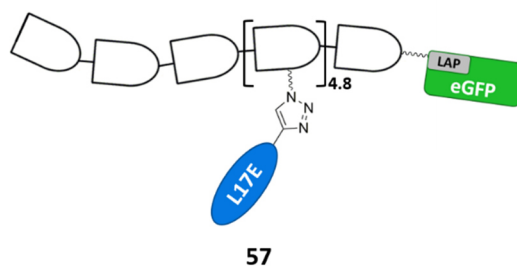
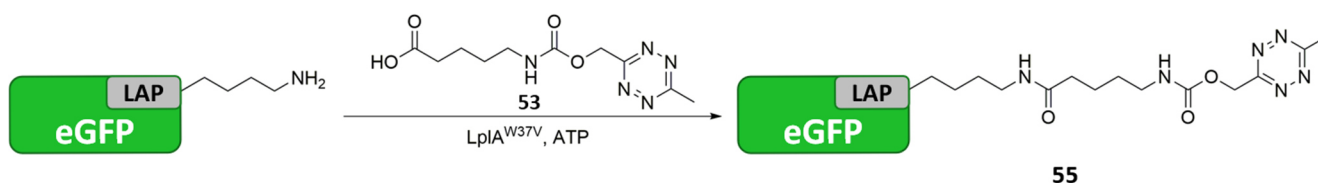


**Figure 56:** Schematic depiction of L17E-dextran module **57** decorated with multiple copies of L17E and site-specific conjugated eGFP at the reducing end.

To assemble compound **57**, comprising L17E-dextran module and covalently bound eGFP, applying site-specific dextran-to-protein conjugation, the methyltetrazine functionality had to be introduced to eGFP via LpIA<sup>W37V</sup> catalyzed amide bond formation, initially. To this end, the enzyme was produced in *E. coli* and a test ligation was performed as reported in section 3.4.3.1, applying 25 equivalents methyltetrazine substrate **53** and 1/10 equivalent LpIA<sup>W37V</sup> (batch 1) at 37 °C for 1 h (**Scheme 18**). The ligation product eGFP-MeTet **55** was analyzed via HIC.



**Scheme 18:** LpIA<sup>W37V</sup> (batch 1) mediated amide bond formation between lysine ε-amine of the LAP-tagged eGFP and a methyltetrazine substrate derivative derived of lipoic acid, yielding eGFP-MeTet **55**.

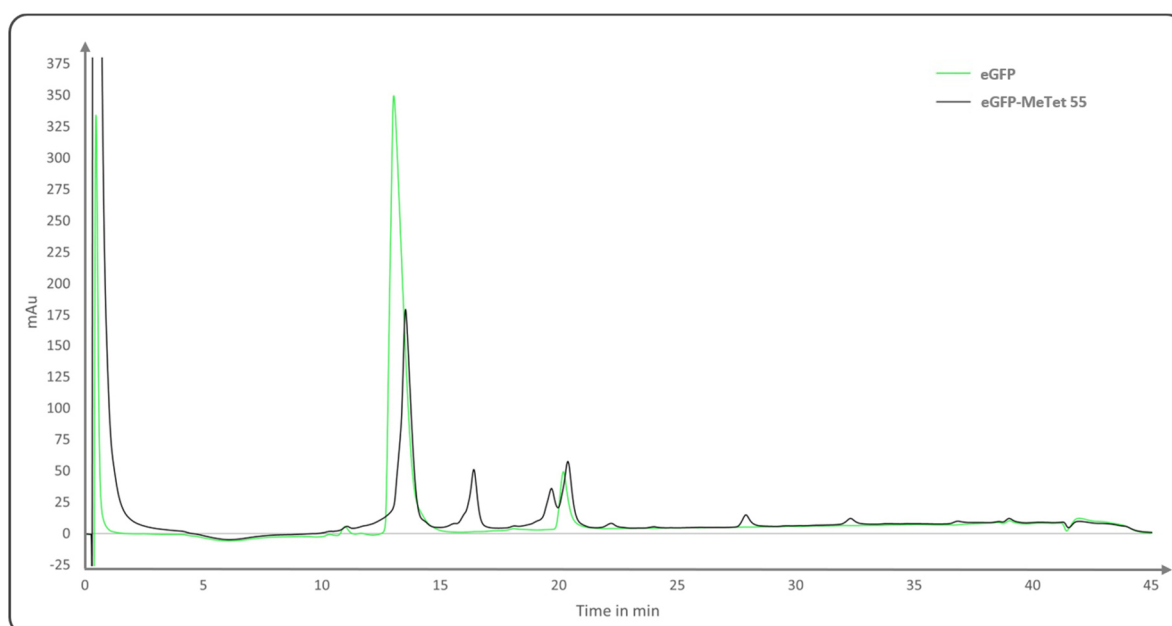
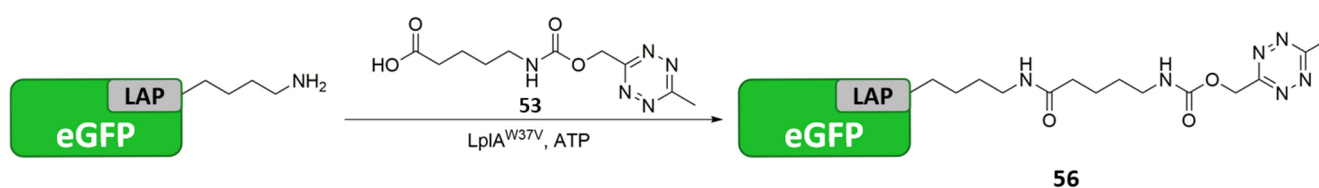


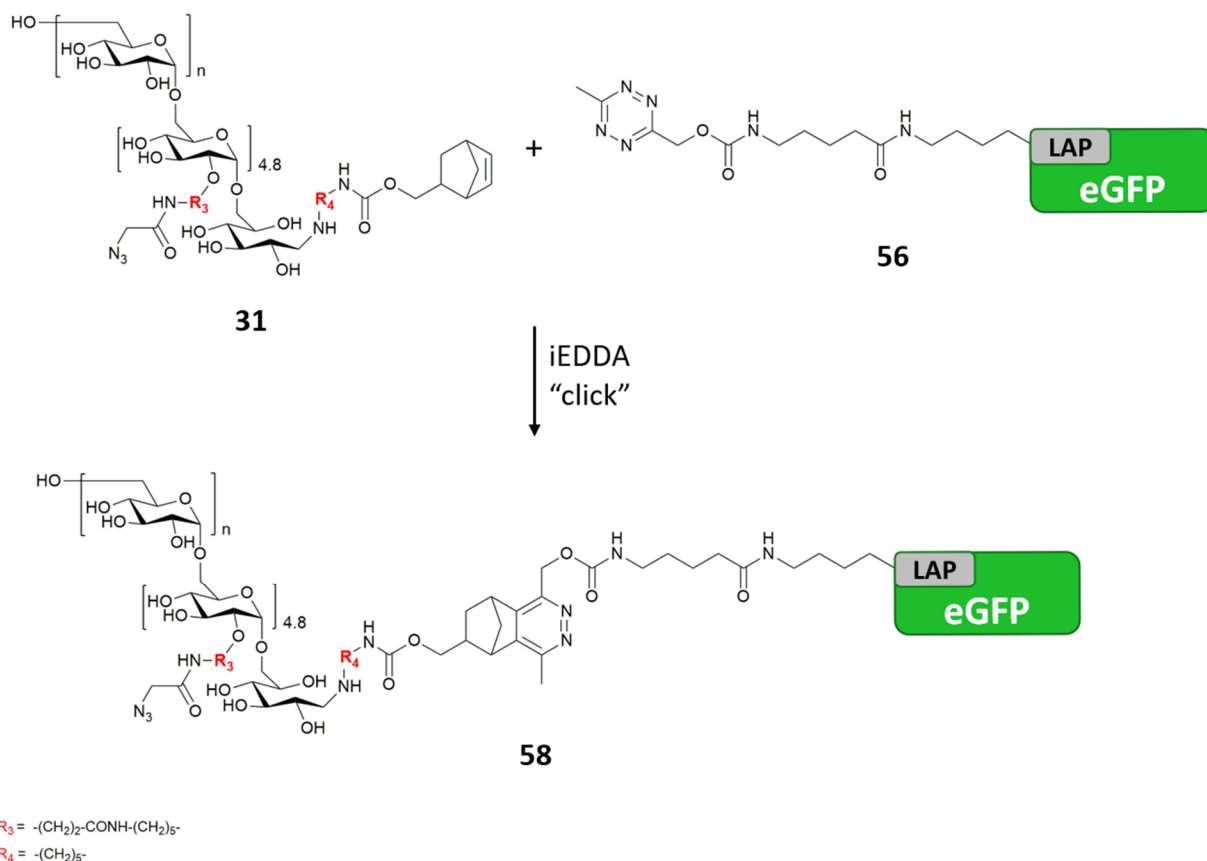
**Figure 57:** HIC chromatograms of eGFP (green) and eGFP-MeTet **55** (black).

In contrast to previous quantitative LplA<sup>W37V</sup> catalyzed formation of eGFP-MeTet **54**, HIC analysis of eGFP-MeTet **55** revealed partial product formation only (**Figure 57** black). Produced LplA<sup>W37V</sup> (batch 1) merely catalyzed conversion of about 16 % eGFP into eGFP-MeTet **55**. Following production in *E. coli* separation of LplA<sup>W37V</sup> (batch1) via IMAC did not result in totally pure protein (**Figure 169 (A)**). Probably, the amount of active enzyme in applied protein quantity was not sufficient to completely catalyze amide bond formation between eGFP, bearing LAP-tag, and the demanding methyltetrazine substrate. Hence, LplA<sup>W37V</sup> production in *E. coli* was repeated, resulting in improved IMAC separation of LplA<sup>W37V</sup> (batch 2) (**Figure 169(B)**). Unfortunately, due to limited availability of methyltetrazine substrate **53**, enzyme activity was not analyzed. Instead, residual substrate was applied in synthesis of eGFP-MeTet **56**, which was applied without further analysis for proof-of-concept assembly of final L17E-dextran-eGFP **57** conjugate based on LplA<sup>W37V</sup> mediated dextran-to-protein conjugation. To this end, enzyme catalyzed amide bond formation between methyltetrazine substrate **53** and LAP-tagged eGFP was performed at 37 °C for 1.5 h, applying LplA<sup>W37V</sup> (batch 2) and reduced substrate quantity (15 eq.), due to shortage (**Scheme 19**).



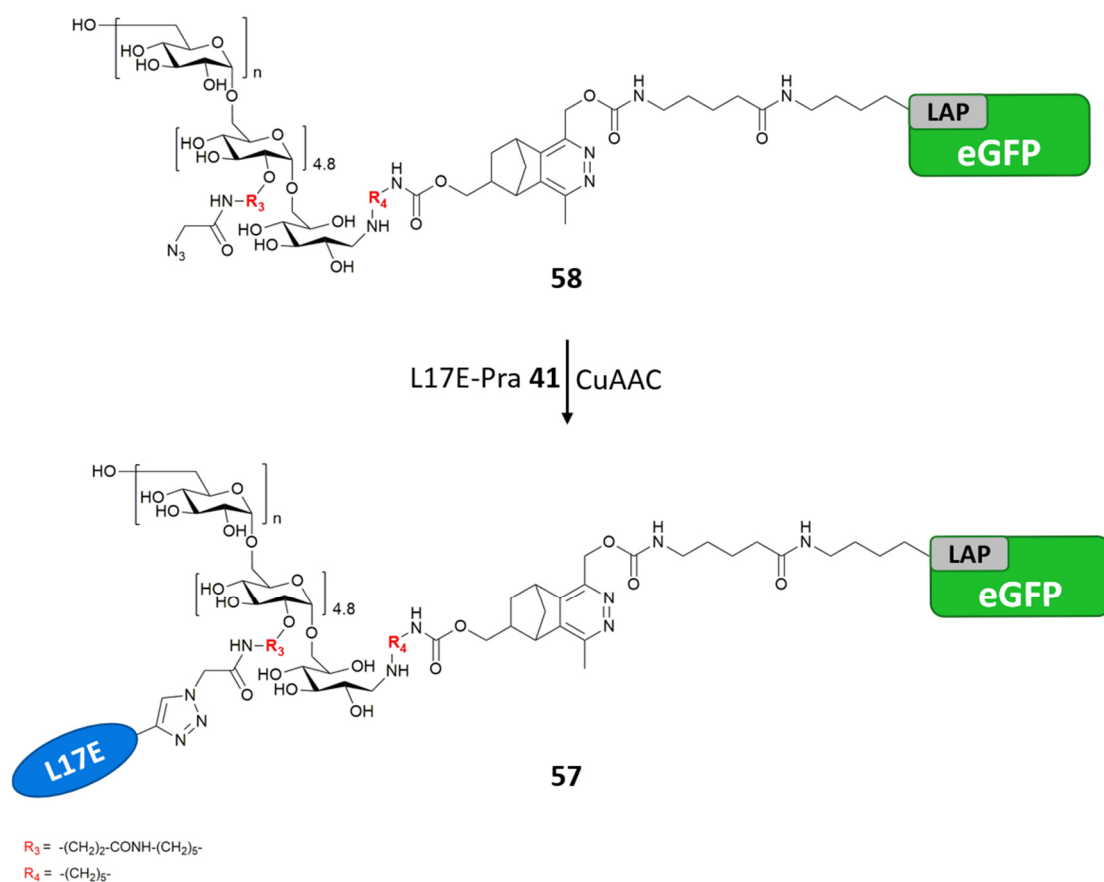
**Scheme 19:** LplA<sup>W37V</sup> (batch 2) mediated amide bond formation between lysine ε-amine of the LAP-tagged eGFP and a methyltetrazine substrate derivative derived of lipoic acid, yielding eGFP-MeTet **56**.

Following removal of excessive substrate, site-specifically modified eGFP-MeTet **56** was applied in subsequent dextran-to-protein conjugation without further analysis.



**Scheme 20:** iEDDA dextran-to-protein conjugation of red-end functionalized  $N_3(4.8)$ -dextran-norbornene **31** and eGFP-MeTet **56**, yielding conjugate  $N_3(4.8)$ -dextran-eGFP **58**.

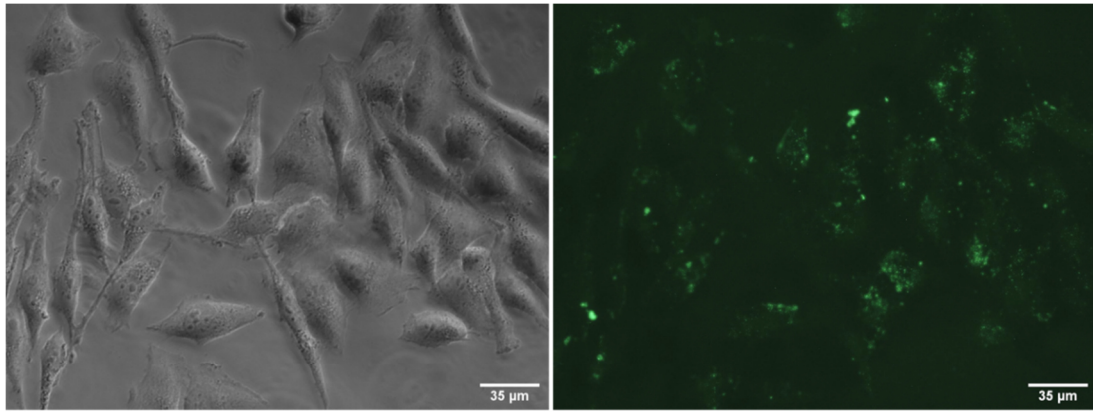
For dextran-to-protein conjugation via iEDDA “click” chemistry,  $N_3(4.8)$ -dextran-norbornene **31**, decorated with on average 4.8 azide moieties at the glucose repeating units and norbornene functionality at the reducing end, was addressed with eGFP-MeTet **56** (**Scheme 20**). Following removal of excessive dextran **31**, the azide functionalities of  $N_3(4.8)$ -dextran-eGFP **58** were addressed with L17E-Pra **41** in a copper(I) catalyzed azide-alkyne cycloaddition (**Scheme 21**). Upon removal of excessive L17E-Pra **41** and catalysts, final L17E(4.8)-dextran-eGFP **57** was yielded. SDS-PAGE analysis (data not shown) revealed incomplete dextran-to-protein conjugation, visualized by considerable residual band of eGFP, lacking dextran modification. Presumably, enzymatic activity of LpIA<sup>W37V</sup> (batch2), applied for eGFP-MeTet **56** synthesis, was insufficient repeatedly, as already seen for the preceding LpIA<sup>W37V</sup> (batch 1) production (**Figure 57**). Potentially, insufficient enzyme activity led to incomplete eGFP modification with methyltetrazine. Consequently, incomplete formation of eGFP-MeTet **56** resulted in partial dextran-to-protein conjugation only, and yielded a mixture of ultimate L17E(4.8)-dextran-eGFP **57** and unmodified eGFP, finally. In course of purification, unmodified eGFP was not removed, because the first IMAC purification step following dextran-to-protein conjugation was based on the eGFP His-tag, while the final purification using centrifugal filters only removed excessive L17E-Pra peptide and catalysts. Unfortunately, conjugation could not get repeated under improved conditions, due to unavailable methyltetrazine substrate combined with shortage of time. However, the mixture containing L17E(4.8)-dextran-eGFP **57** and unmodified eGFP was applied in cellular uptake assay. As previous uptake experiments revealed, unmodified eGFP was neither taken up by living HeLa cells nor adhered at the cell surface, and therefore did not influence uptake of compound **57**. Though, photometrical determination of product mixture concentration at 488 nm assessed concentration of present eGFP in total and did not distinguish between unmodified eGFP and eGFP covalently conjugated to L17E-dextran in module **57**. Hence, the actually applied L17E(4.8)-dextran-eGFP **57** compound concentration was unknown but definitely less than stated.



**Scheme 21:** Addressing  $N_3(4.8)$ -dextran-eGFP **58** with L17E-Pra **41** in Cu(I)-catalyzed azide-alkyne cycloaddition, yielding L17E(4.8)-dextran-eGFP **57**.

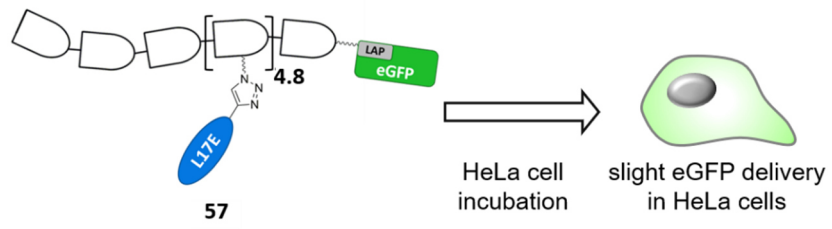
### 3.4.3.3 Cellular uptake assay

HeLa cells were incubated with the mixture L17E(4.8)-dextran-eGFP **57** / unmodified eGFP at  $4.1 \mu\text{M}$  total eGFP concentration in serum free medium for 1 h. Following further 3 h incubation in medium, cellular distribution of the eGFP fluorescence signal was analyzed with fluorescence microscopy. Cells treated with conjugate **57** showed slight intracellular eGFP fluorescence (**Figure 58**). Taking into consideration that not every eGFP molecule was equipped with covalently conjugated L17E-dextran module, the effective concentration of actually applied L17E(4.8)-dextran-eGFP **57** was definitely lower than  $4.1 \mu\text{M}$ . Therefore, intracellular eGFP fluorescence, caused by uptake of compound **57**, was expected to be decreased, compared to previous cellular uptake assays, applying L17E-dextran-eGFP compounds **44** and **52**. However, appearance of slight intracellular eGFP fluorescence confirmed the ability of L17E-module to also promote intracellular uptake upon dextran-to-protein conjugation based on site-specific LplA<sup>W37V</sup> mediated introduction of required chemical functionality into the cargo protein. Quantitative introduction of functional groups, addressable for subsequent iEDDA conjugation into LAP-tagged proteins mediated by LplA<sup>W37V</sup> has successfully been reported in the literature.<sup>[100, 102, 114a]</sup> Similarly, in the present work, LplA<sup>W37V</sup> catalyzed introduction of methyltetrazine derivative into LAP-tagged eGFP could be reproduced and resulted in quantitative eGFP-MeTet **54** formation (**Figure 55**). Unfortunately, in further productions, required enzyme activity could not be achieved and LplA<sup>W37V</sup> production remained to be improved. Nevertheless, upon improved enzyme production, quantitative site-specific functionalization of a protein of interest, bearing LAP recognition sequence, followed by covalent L17E-dextran-to-protein conjugation would be feasible. Thus, efficient cytosolic delivery of functional proteins of interest, addressing intracellular targets, could be achieved upon site-specific decoration with L17E-dextran module.



(A)

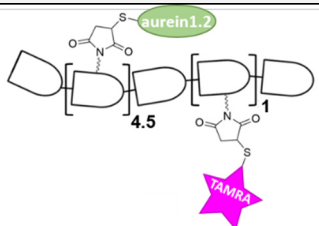
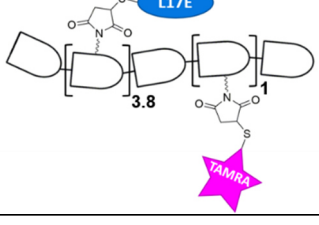
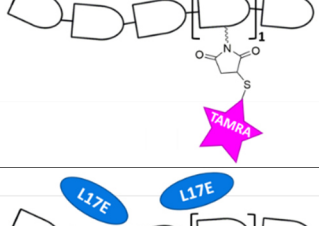
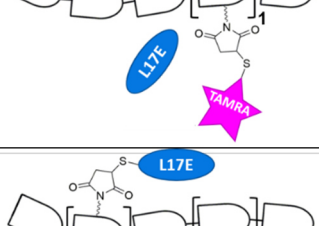
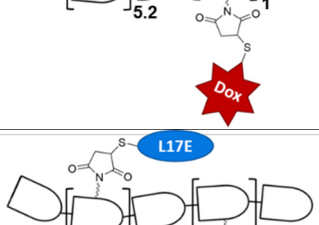
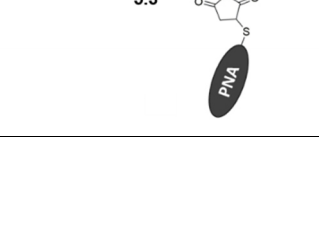
(B)

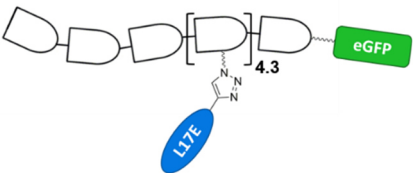
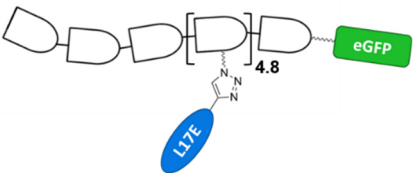
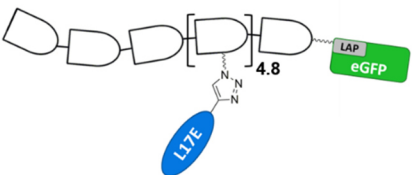


**Figure 58:** Fluorescence microscopy (20×) images of HeLa cells treated with L17E(4.8)-dextran-eGFP 57 / unmodified eGFP mixture (4 μM) ((A): brightfield image; (B): eGFP fluorescence channel).

#### 4 Tabular summary of generated dextran-based delivery modules

**Table 5:** Overview of dextran-based compounds generated in the present work as modules for cytosolic or even nuclear delivery of different kinds of cargoes. In addition to the schematic structures, the abilities of the respective compounds to mediate cytosolic and nuclear uptake are given (+++ effective uptake; ++ medium uptake; + slight uptake; — no uptake). \*Compounds differ in dextran-to-protein conjugation: Compound 52 based und unspecific and compound 57 based on site-specific LpIA<sup>W37V</sup>-mediated dextran-to-protein conjugation.

Compound	#	Schematic depiction	Cytosolic delivery	Nuclear delivery
TAMRA-aurein1.2(4.5)-dextran- <i>N</i> -Boc-cadaverine	36		+	—
TAMRA-L17E(3.8)-dextran- <i>N</i> -Boc-cadaverine	37		+++	+++
TAMRA-dextran- <i>N</i> -Boc-cadaverine	38		+	—
TAMRA-dextran- <i>N</i> -Boc-cadaverine + L17E co-incubation	38 + 12		++	—
Dox-L17E(5.2)-dextran- <i>N</i> -Boc-cadaverine	39		++	++
L17E-PNA-dextran- <i>N</i> -Boc-cadaverine	43		+++	+++

L17E(4.3)-dextran-eGFP	44		+++	-
L17E(4.8)-dextran-eGFP*	52*		+++	-
L17E(4.8)-dextran-eGFP*	57*		+	-

## 5 Summary and Outlook

Along with steadily increasing interest in biopharmaceuticals such as peptides, proteins, or nucleic acids, development of strategies for their effective cytosolic delivery gained comparable attention. Indeed, being very potent in frames of bioactivity, these macromolecules do not readily enter the cytosol. Therefore, their application field is often restricted to extracellular targets. To overcome this limitation, and to achieve the ability to address intracellular targets, different approaches have been done aiming at improved cellular uptake. Beside strategies based on delivery of macromolecules with liposomes,<sup>[28-29]</sup> polymersomes,<sup>[30]</sup> nanoparticles,<sup>[32]</sup> or pore-forming proteins,<sup>[35-36]</sup> cell-penetrating peptides have emerged as a versatile tool for intracellular delivery of different cargoes. In particular, arginine-rich CPPs and their even more potent cyclic versions have numerously been reported as efficient delivery vehicles.<sup>[50, 52]</sup>

In the frame of the present work, a system for efficient cytosolic delivery of biomolecular cargo was developed, based on CPP-bearing dextran hybrids. The initial study was focused on two arginine-free peptides. The 13 amino acid antimicrobial peptide aurein1.2 has been reported<sup>[68]</sup> to enhance cytoplasmic delivery by mediating endosomal escape of endocytosed proteins. The cationic amphiphilic 25 amino acid peptide L17E, a variant of haemolytic M-lycotoxin with diminished cytotoxicity, was reported<sup>[56]</sup> to promote cytosolic uptake of different functional proteins up to full-length antibodies. So far, L17E-mediated cargo delivery was induced upon co-incubation with the peptide merely, and no efforts have been made to introduce a covalent linkage between both components, peptide and cargo. In the present study, both aurein1.2 and L17E were not able to promote cellular uptake when covalently linked to model conjugate in single unit. Hence, it remained to be investigated, whether an uptake-increasing multivalency effect could be generated by linkage of the respective peptide on a suitable scaffold in multiple copies.

Comprising  $\alpha$ -(1-6) glycosidic bonds between D-glucose repeating units, biocompatible dextran polysaccharide has already been reported as a suitable hydrophilic scaffold for the generation of high-DAR antibody-drug conjugates<sup>[76]</sup> or multivalent platform for DR5-induced apoptosis.<sup>[78]</sup> The hydroxy groups of the glucose repeating units as well as the polysaccharide reducing end offered possibilities for multivalent functionalization of dextran.<sup>[61, 76, 78]</sup> Therefore, 10 kDa dextran was chosen as platform for covalent oligomerization of cell-penetrating peptides aurein1.2 and L17E. To this end, amine functionality was introduced to the polysaccharide reducing end via reductive amination and the hydroxy groups of the glucose repeating units were modified via carboxyethylation. Subsequent

---

conversion of the introduced carboxyl moieties into either maleimide- or azide-functionalities enabled peptide and/or cargo conjugation via maleimide-thiol addition or Cu(I)-catalyzed azide-alkyne cycloaddition.

Decoration of maleimide-functionalized dextran polysaccharide with multiple copies of aurein1.2, respectively L17E, and a fluorescent label gave peptide-dextran hybrids, whose intracellular distribution was analyzed upon uptake in HeLa cells. L17E-dextran hybrid showed considerable superior uptake compared to the aurein1.2 variant. HeLa cells treated with TAMRA-labeled and L17E-decorated dextran module **37** at low micromolar concentration showed effective uptake of the macromolecule with fluorescence signals spread all over the cytosol and even nucleus (**Figure 37**, **Figure 92**). Furthermore, TAMRA-labeled dextran **37**, covalently decorated with on average 3.8 L17E units, showed increased uptake compared to a TAMRA-labeled dextran co-incubated with solitary L17E peptide, as reported in the literature.<sup>[56]</sup> These encouraging findings led to development of a strategy for intracellular delivery of various cargo beyond fluorophore molecules, applying L17E-dextran hybrid as delivery module.

A possible cytotoxic effect of L17E-dextran module was assessed, applying dextran **42**, decorated with on average 4.8 L17E peptide units. In the taken cell line, an IC<sub>50</sub> value of approximately 10 μM (**Figure 41**) was determined, which was rather low and in an acceptable range when taken into consideration that L17E was derived from naturally haemotoxic lycotoxin.

L17E-dextran mediated cytosolic and nuclear delivery of peptide nucleic acid (PNA) was validated by mis-splicing correction assay in appropriate HeLa cells, stably transfected with enhanced green-fluorescent protein (eGFP) gene. Therefore dextran **43** was equipped with multiple copies of both L17E and PNA. The L17E-dextran module was able to deliver bioactive PNA into the nucleus of HeLa cells, whereupon the cargo PNA induced mis-splicing correction, leading to enhanced GFP fluorescence (**Figure 45**). This validated not only cytosolic, but even nuclear translocation of L17E-dextran module. Furthermore, the potential of dextran, equipped with multiple L17E peptides, was demonstrated to mediate intracellular uptake of PNA, that in general lacks cellular permeability and is not efficiently taken up by cells.

Finally, L17E-dextran module showed its ability to promote intracellular delivery of covalently conjugated protein cargo. To this end, a construct was designed, combining eGFP as model protein with L17E-decorated dextran serving as cytosolic uptake-promoting module. Synthesis was performed via iEDDA conjugation of a norbornene-functionalized dextran, bearing multiple orthogonal azide moieties, to a methyltetrazine-modified eGFP protein, followed by CuAAC “click” with alkyne-modified L17E peptide. At low micromolar concentration, yielded L17E-dextran-eGFP **44** was efficiently taken up by HeLa cells, visualized by widely spread and homogenic eGFP fluorescence inside the cytosol (**Figure 52**).

In conclusion, decoration of dextran polysaccharide with multiple copies of L17E peptides resulted in peptide-dextran hybrid, acting as a versatile uptake-mediating module. L17E-dextran promoted cytoplasmic delivery of covalently conjugated biomolecular cargo at low micromolar concentration without largely compromising cell viability. L17E has already been reported to promote cytosolic uptake of proteins, up to full-length antibodies, upon simple co-incubation of solitary L17E peptide with the cargo.<sup>[56]</sup> However, uptake-mediating ability was improved via combining the oligomerization of L17E peptide on polysaccharide scaffold with the introduction of covalent connections between all counterparts: peptide, cargo, and dextran. In this way, a modular delivery system was established, which enabled intracellular delivery of various cargo, from PNA to proteins. Dependent on type and nature of the cargo, the multifunctionalized dextran backbone could be decorated following two strategies (**Figure 59**): One possibility included decoration of glucose repeating units with multiple copies of L17E and with multiple copies of cargo molecules simultaneously, while a further conjugation site at the reducing end remained accessible for conjugation of a potential second type of cargo. This option seemed to be beneficial for delivery of cargo such as peptides or PNA. The second possibility was based on decoration of the glucose repeating units with multiple L17E only, while the cargo was conjugated to the

polysaccharide reducing end. The latter option seemed to be most suitable for more bulky cargo, such as proteins.

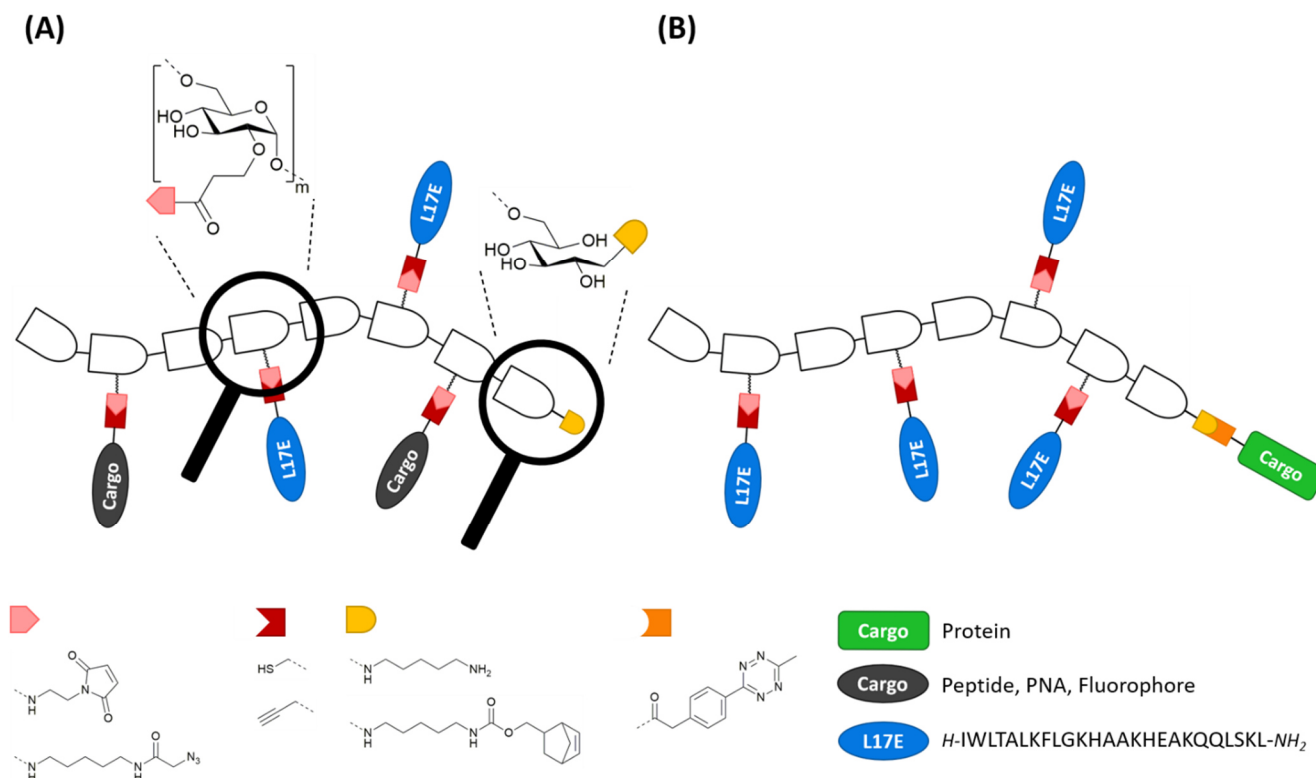


**Figure 59:** (A) Schematic depiction of L17E-dextran delivery module in the setup applying multiple copies of both L17E and cargo at the glucose repeating units and a possibility for conjugation of a second cargo at the polysaccharide reducing end. (B) L17E-dextran delivery module decorated with multiple copies of L17E at the glucose repeating units and protein cargo covalently conjugated to the reducing end.

In addition to the encouraging results of this proof-of-concept studies, several issues remain to be investigated. For solitary L17E co-incubation-mediated cytoplasmic cargo delivery an uptake mechanism was proposed based on transient membrane permeabilization. L17E was thought to induce actin rearrangement upon interaction with the cell membrane, leading to membrane ruffling followed by macropinocytosis. Before macropinosome formation was accomplished, L17E assumedly ruptured the ruffled membrane, thus paving the way of direct cargo entry into the cytoplasm.<sup>[70]</sup> It remains to be ascertained, whether the same mechanism is appropriate for L17E in its dextran-conjugated state.

Moreover, regarding L17E-dextran mediated delivery of covalently conjugated protein cargo, it remains to substitute eGFP model protein with a functional biomolecule of interest. A broad range of intracellular targets exist, whose specific binding or functional blocking could be of interest in a therapeutic context. Single-domain antibodies, also called nanobodies, could be ideal candidates for addressing intracellular targets. Therefore, cytosolic delivery of these macromolecules would be of great importance and in the future, potentially could be realized via site-specific conjugation to L17E-dextran delivery module.

---

## 6 Zusammenfassung und Ausblick

---

In den vergangenen Jahrzehnten hat das Interesse an der Entwicklung von therapeutischen Wirkstoffen, die auf biologischen Molekülen wie Peptiden, Proteinen oder Nukleinsäuren basieren, zunehmend an Bedeutung gewonnen. Damit einhergehend erweckte auch die Entwicklung von Strategien für einen effektiven Transport in das Zellinnere zunehmend an Aufmerksamkeit, da diese auf Biomakromolekülen basierenden Wirkstoffe meist nicht in der Lage sind die Zellmembran zu überwinden und in das Zytosol zu gelangen. Aus diesem Grund sind Biopharmazeutika in ihrer Anwendung häufig auf extrazelluläre Ziele begrenzt. Um diese Restriktion zu überwinden und auch intrazelluläre Anwendung zu ermöglichen, wurden bereits verschiedene Strategien zum verbesserten Transport diverser Biomakromoleküle in das Zytosol entwickelt. Neben Herangehensweisen, die auf Verwendung von Liposomen,<sup>[28-29]</sup> Polymersomen,<sup>[30]</sup> Nanopartikeln<sup>[32]</sup> oder porenbildenden Proteinen<sup>[35-36]</sup> basieren, hat sich auch der Einsatz sogenannter zellpenetrierender Peptide (cell-penetrating peptides CPPs) zum Transport von Biomakromolekülen in das Zytosol lebender Zellen als effektiv erwiesen. Vor allem CPPs, die eine Vielzahl an Argininen beinhalten, und insbesondere deren zyklisierte Varianten, stellen ein effektives Transportsystem dar.<sup>[50-51]</sup>

Im Rahmen der vorliegenden Arbeit wurde ein System zum effizienten Transport von Biomolekülen in das Zytosol von Säugerzellen entwickelt, das auf CPP-dekorierten Dextran Hybriden basiert. Zu Beginn der Entwicklung wurden zwei Arginin freie Peptide in Betracht gezogen: Das antimikrobielle 13 Aminosäuren Peptid Aurein1.2 soll die intrazelluläre zytoplasmatische Darreichung von Proteinen, die nach endozytotischer Aufnahme in Endosomen eingeschlossen sind, dadurch verbessern, dass es die Überführung aus dem Endosom ins Zytosol erleichtert.<sup>[68]</sup> Das kationische amphiphile 25 Aminosäuren Peptid L17E ist eine durch Aminosäureaustausch generierte Variante des hämolytischen M-Lykotoxins mit verminderter Zytotoxizität und ermöglicht effektiven Transport verschiedener funktioneller Proteine, bis hin zu Volllängen-Antikörpern, ins Zytosol.<sup>[56]</sup> Bisher wurde die L17E vermittelte zytoplasmatische Darreichung von Proteinen lediglich durch Koinkubation des jeweiligen Proteins mit L17E Peptid erzielt. Anstrengungen, um eine kovalente Bindung zwischen beiden Komponenten einzuführen, wurden bisher noch nicht unternommen. Unter den in dieser Arbeit zu Grunde gelegten Bedingungen konnten jedoch sowohl Aurein1.2 als auch L17E, jeweils in einzelner Ausfertigung kovalent an ein Modellprotein gebunden, nicht dessen intrazelluläre Aufnahme induzieren. Daher blieb zu analysieren, ob durch Verknüpfung mehrerer Kopien des jeweiligen Peptids auf einem geeigneten Rückgrat ein Multivalenzeffekt hervorgerufen werden kann, der den Transport von Biomakromolekülen ins Zytosol begünstigt.

Das biokompatible Polysaccharid Dextran, bestehend aus vornehmlich  $\alpha$ -(1-6) glycosidisch gebundenen D-Glukose Wiederholungseinheiten, wurde unter anderem bereits erfolgreich als hydrophiles Gerüst zur Erzeugung von high-DAR Antikörper-Wirkstoff Konjugaten<sup>[76]</sup> oder auch als multivalente Plattform für DR5-induzierte Apoptose<sup>[78]</sup> eingesetzt. Dextran bietet die Möglichkeit zur multivalenten Funktionalisierung, so können zum einen die Hydroxygruppen der Glukose Einheiten als auch das reduzierende Ende des Polysaccharids modifiziert werden.<sup>[61, 76, 78]</sup> Folglich wurde Dextran (10 kDa) als geeignete Plattform für die kovalente Oligomerisierung der zellpenetrierenden Peptide Aurein1.2 und L17E ausgewählt. Zu Beginn der Dextran Modifikation wurde mittels reduktiver Aminierung eine Aminfunktionalität am reduzierenden Ende eingeführt und anschließend die Hydroxygruppen der Glukose Wiederholungseinheiten durch Carboxyethylierung modifiziert. Durch Umwandlung der eingeführten Carboxygruppen in entweder Maleimid- oder Azid-Funktionalitäten, wurde die Konjugation von zellpenetrierendem Peptid und/oder von zu transportierendem Makromolekül durch Maleimid-Thiol Addition oder Cu(I)-katalysierter Azid-Alkin-Cycloaddition ermöglicht. Die Dekoration von Maleimid-funktionalisiertem Dextran mit mehreren Kopien von Aurein1.2 respektive L17E und einem Fluoreszenzfarbstoff ergab Peptid-Dextran Hybride, deren intrazelluläre Verteilung nach Aufnahme in HeLa Zellen analysiert wurde. TAMRA markiertes L17E-Dextran Hybrid zeigte im Vergleich zur mit Aurein1.2 ausgestatteten Variante eine deutlich gesteigerte Aufnahme. HeLa-Zellen, die mit TAMRA-markiertem und L17E-dekoriertem Dextran **37** in niedriger mikromolarer Konzentration

---

inkubiert wurden, zeigten eine effektive Aufnahme des Makromoleküls mit gleichmäßig über das gesamte Zytosol verteilten und auch im Zellkern sichtbaren Fluoreszenzsignalen (**Figure 37**, **Figure 92**). Darüber hinaus zeigte TAMRA-markiertes Dextran **37**, das kovalent mit durchschnittlich 3,8 L17E Einheiten ausgestattet war, verglichen mit TAMRA-markiertem Dextran, das wie in der Literatur<sup>[56]</sup> beschrieben mit solitärem L17E Peptid koinkubiert wurde, eine deutlich verbesserte Aufnahme in HeLa Zellen. Diese ermutigenden Ergebnisse führten zur Entwicklung einer Strategie, die unter Verwendung von L17E-Dextran den Transport von kovalent gebundenen Biomakromolekülen ins Zytosol von Säugerzellen ermöglichen sollte.

Eine mögliche zytotoxische Wirkung des L17E-Dextran Transportmoduls wurde unter Verwendung von Dextran **42** beurteilt, das mit durchschnittlich 4,8 L17E Peptideinheiten ausgestattet wurde. In der verwendeten HeLa Zelllinie wurde für L17E-Dextran **42** ein IC<sub>50</sub> Wert von ungefähr 10 µM bestimmt. In Anbetracht dessen, dass L17E von natürlich vorkommendem, hämotoxischem M-Lykotoxin abgeleitet wurde, wurde dieser Wert als relativ gering und innerhalb eines akzeptablen Bereichs angesehen.

Die Validierung des L17E-Dextran vermittelten Transports von Biomakromolekülen ins Zytosol und darüber hinaus auch in den Zellkern von HeLa Zellen erfolgte durch Peptid-Nukleinsäuren (PNA) induzierte Korrektur von Fehlspleißen. Zu diesem Zweck wurde Dextran **43** mit mehreren Kopien von sowohl L17E als auch der benötigten PNA ausgestattet. Das L17E-Dextran Transportmodul war in der Lage die bioaktive PNA in den Zellkern der speziellen, mit eGFP Gen transfizierten HeLa Zellen zu transportieren, woraufhin dort die PNA vermittelte Korrektur des Spleißens zu verstärkter eGFP-Fluoreszenz führte (**Figure 45**). Dadurch wurde nicht nur die zytoplasmatische, sondern auch die nukleare Translokation des L17E-Dextran Transportmoduls bestätigt. Darüber hinaus zeigte sich auf diese Weise auch das Potential von L17E-dekoriertem Dextran prinzipiell als Transporter von PNA Molekülen zu dienen, die im Allgemeinen Zellmembran impermeabel und solitär nicht in der Lage sind Zytosol und Zellkern zu erreichen.

Schließlich demonstrierte das L17E-Dextran Transportmodul seine Fähigkeit zur Vermittlung intrazellulärer Aufnahme kovalent konjugierter Proteine. Dazu wurde ein Konstrukt entworfen, das L17E-dekoriertes Dextran, fungierend als Komponente zur Vermittlung zytoplasmatischer Aufnahme, mit eGFP als Modellprotein kombinierte. Die Synthese des Konstrukts wurde durch iEDDA-Konjugation eines Norbornen-funktionalisierten und gleichzeitig mit mehreren orthogonalen Azid-Funktionalitäten dekorierten Dextrans an ein Methyltetrazin-modifiziertes eGFP Protein realisiert. Im Anschluss daran wurden die Azid-Funktionalitäten des Dextrans durch CuAAC-„Klick“ mit Alkin-modifiziertem L17E-Peptid adressiert. Das daraus resultierende L17E-Dextran-eGFP **44** zeigte eine effektive intrazelluläre Aufnahme in HeLa-Zellen, die durch eine weit verbreitete und homogene eGFP-Fluoreszenz im Zytosol visualisiert wurde (**Figure 52**).

Zusammenfassend lässt sich festhalten, dass die kovalente Dekoration von Dextran Polysaccharid mit mehreren Kopien von L17E Peptiden zu Peptid-Dextran Hybriden führte, die sich als vielseitiges Transportmodul zur Vermittlung intrazellulärer Aufnahme von Biomakromolekülen bewiesen. Bereits in geringer Konzentration vermittelte L17E-Dextran den Transport kovalent konjugierter Biomakromoleküle ins Zytoplasma, ohne dabei die Viabilität der Zellen maßgeblich zu beeinträchtigen. Es war bereits aus der Literatur<sup>[56]</sup> bekannt, dass L17E die zytoplasmatische Aufnahme von Proteinen bis hin zu Vollängen-Antikörpern durch einfache Koinkubation des entsprechenden Proteins mit solitärem L17E Peptid vermittelt. Diese Fähigkeit zur Vermittlung zytoplasmatischer Aufnahme konnte allerdings dadurch verbessert werden, dass Oligomerisierung des L17E Peptids auf einem Polysaccharid Rückgrat mit der gleichzeitigen Einführung kovalenter Bindungen zwischen allen beteiligten Komponenten, nämlich Peptid, Dextran und zu transportierendem Biomakromolekül, kombiniert wurde. Auf diese Weise konnte ein modulares System entwickelt werden, das die intrazelluläre Aufnahme verschiedener Biomakromoleküle wie PNA oder Proteine ermöglichte. Abhängig von der Art der zu transportierenden Makromoleküle konnte das multifunktionalisierte Dextran Rückgrat zwei unterschiedlichen Strategien folgend dekoriert werden (**Figure 60**). Eine Möglichkeit bestand darin die Glukose Wiederholungseinheiten gleichzeitig mit mehreren Kopien von L17E und mit mehreren Kopien von

Frachtmolekülen auszustatten, während am reduzierenden Ende eine weitere potentielle Konjugationsstelle zugänglich blieb. Diese Variante schien besonders für den Transport kleinerer Makromoleküle wie Peptide oder PNA geeignet zu sein. Die zweite Möglichkeit bestand darin die Glukose Wiederholungseinheiten ausschließlich mit L17E auszustatten, während das zu transportierende Makromolekül an das reduzierende Ende konjugiert wurde. Diese Option eignete sich vor allem für den L17E-Dextran vermittelten Transport von Proteinen.

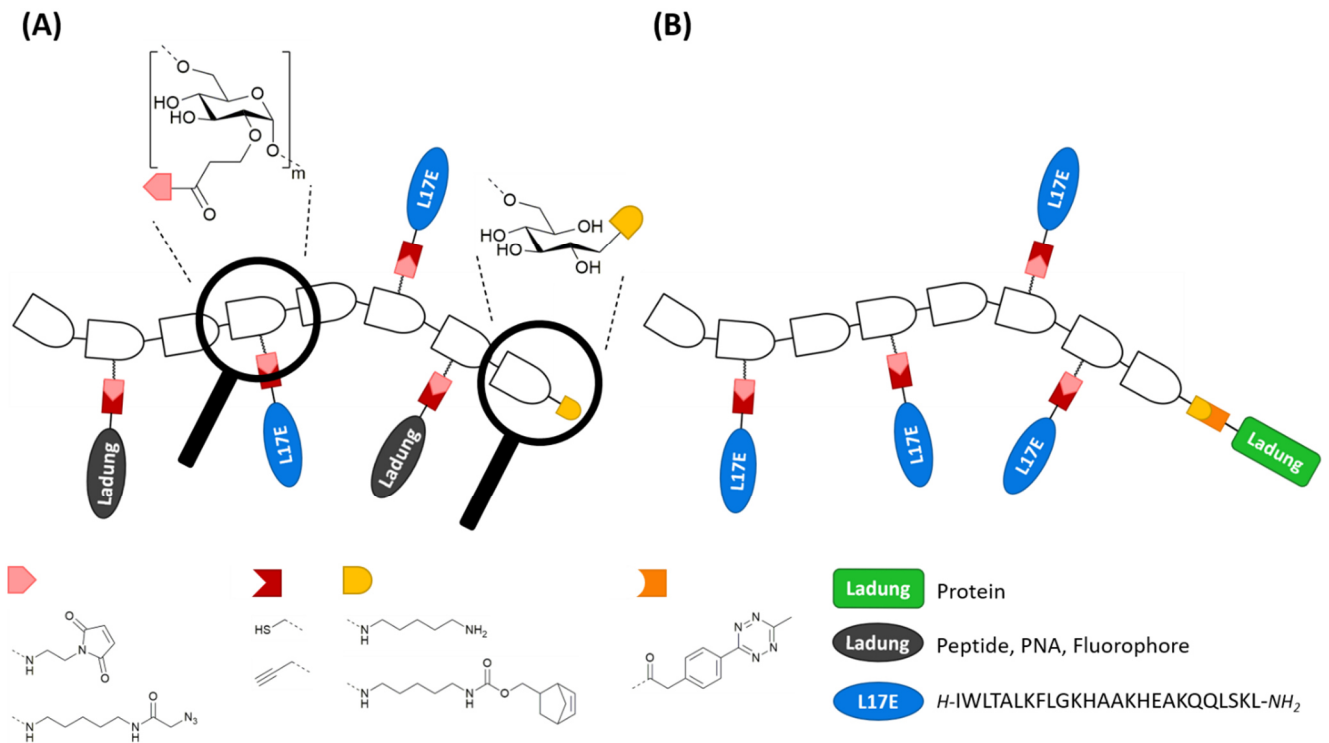


**Figure 60:** Schematische Darstellung zweier Möglichkeiten des Einsatzes von L17E-Dextran als Transportmodul: **(A)** Dextran, ausgestattet mit mehreren Kopien von sowohl L17E als auch zu transportierendem Makromolekül an den Glukose-Wiederholungseinheiten und weiterer Konjugationsmöglichkeit am reduzierenden Ende des Polysaccharids. **(B)** Dextran, ausgestattet mit mehreren Kopien von L17E an den Glukose-Wiederholungseinheiten und kovalent an das reduzierende Ende gebundenes Protein.

Basierend auf den vielversprechenden Ergebnissen dieser Proof-of-Concept Studie verbleiben einzelne Punkte, die noch weiterführend betrachtet werden sollten. So wurde für die durch L17E Koinkubation vermittelte zytoplasmatische Aufnahme von Makromolekülen ein Aufnahmemechanismus vorgeschlagen, der auf einer vorübergehenden Membranpermeabilisierung beruht. Es wurde angenommen, dass L17E durch Wechselwirkung mit der Zellmembran eine Aktinumlagerung induziert, die zu Membranrüschen und schließlich Makropinosyotose führt. Bevor die Bildung von Makropinosomen abgeschlossen ist, durchbricht L17E vermutlich die gekräuselte Membran und ermöglicht so den direkten Eintritt von L17E und Makromolekül in das Zytoplasma.<sup>[70]</sup> Es bleibt zu überprüfen, ob ein ähnlicher Mechanismus auch für L17E zutreffend ist, das in mehrfacher Ausfertigung kovalent an Dextran gebunden ist.

Darüber hinaus sollte hinsichtlich der L17E-Dextran vermittelten zytoplasmatischen Aufnahme von kovalent konjugiertem Protein das eGFP Modellprotein durch ein geeignetes funktionelles Biomolekül ersetzt werden. Es existiert eine Vielzahl an intrazellulären Zielen, deren spezifische Bindung oder funktionelle Blockierung in einem therapeutischen Kontext von Interesse sein könnten. Deshalb könnten beispielsweise Einzeldomänenantikörper, auch Nanobodies genannt, ideale Kandidaten für die Adressierung intrazellulärer therapeutischer Ziele darstellen. Zu diesem Zweck wäre der Transport dieser Makromoleküle ins Zytoplasma der jeweiligen Zielzelle von großer Bedeutung und könnte in

Zukunft eventuell durch ortsspezifische Konjugation an das L17E-Dextran Transportmodul realisiert werden.

## 7 Experimental Part

### 7.1 General

#### 7.1.1 Solvents

Solvents were obtained from *Acros Organics* (Fair Lawn, NJ, USA), *Carl Roth GmbH + Co. KG* (Karlsruhe, Germany), *Fisher Scientific GmbH* (Schwerte, Germany) or *Merck KGaA* (Darmstadt, Germany) and used without further purification except when mentioned specifically.

#### 7.1.2 Reagents

All reagents were purchased from *Agilent Technologies* (Santa Clara, CA, USA), *Carbolution Chemicals GmbH* (St. Ingbert, Germany), *Carl Roth GmbH + Co. KG* (Karlsruhe, Germany), *Fisher Scientific GmbH* (Schwerte, Germany), *Iris Biotech GmbH* (Marktredwitz, Germany), *Jena Bioscience* (Jena, Germany), *Merck KGaA* (Darmstadt, Germany) or *Sigma Aldrich* (*Merck KGaA*, Darmstadt, Germany) and used without further purification, unless stated otherwise.

#### 7.1.3 Buffers and solutions

**Table 6:** Composition of applied buffers and solutions.

Buffer / solution	Ingredients
10 × PBS	1.37 M NaCl 27 mM KCl 100 mM Na <sub>2</sub> HPO <sub>4</sub> 18 mM KH <sub>2</sub> PO <sub>4</sub>
4% paraformaldehyde solution (PFA)	4% (w/v) paraformaldehyde in PBS
Cathepsin B activation buffer	30 mM DTT 15 mM EDTA
Cathepsin B reaction buffer	25 mM acetate pH 5.0 1 mM EDTA
Coomassie destaining solution 1	10% (v/v) Acetic acid 25% (v/v) Isopropanol
Coomassie destaining solution 2	10% (v/v) Acetic acid
Coomassie staining solution	0.2% (w/v) Coomassie Brilliant Blue R-250 0.2% (w/v) Coomassie Brilliant Blue G-250 30% (v/v) Isopropanol 7.5% (v/v) Acetic acid
Eluent A (HPLC)	0.1% (v/v) aq. TFA
Eluent A (LC-MS)	0.1% (v/v) aq. FA
Eluent B (HPLC)	90% (v/v) aq. MeCN with 0.1% (v/v) TFA
Eluent B (LC-MS)	MeCN with 0.1% (v/v) FA
HIC buffer A	25 mM Tris-HCl pH 7.5 1.5 M (NH <sub>4</sub> ) <sub>2</sub> SO <sub>2</sub>
HIC buffer B	25 mM Tris-HCl pH 7.5

<b>IMAC A (running) Lysis buffer</b>	50 mM Tris-HCl pH 7.5 600 mM NaCl 20 mM Imidazole
<b>IMAC B (elution)</b>	50 mM Tris-HCl pH 7.5 600 mM NaCl 500 mM Imidazole
<b>Phosphate-buffered saline (PBS)</b>	137 mM NaCl 2.7 mM KCl 10 mM Na <sub>2</sub> HPO <sub>4</sub> 1.8 mM KH <sub>2</sub> PO <sub>4</sub> pH 7.4
<b>Protein A elution buffer</b>	0.1 M Citric acid pH 3.0
<b>Protein A neutralizing buffer</b>	1 M Tris-HCl pH 9.0
<b>Protein A running buffer</b>	20 mM Sodium phosphate pH 7.0
<b>SDS-PAGE 4 × running gel buffer</b>	3 M Tris-HCl pH 8.85 4 mg/mL SDS
<b>SDS-PAGE 4 × stacking gel buffer</b>	0.5 M Tris-HCl pH 6.8 4 mg/mL SDS
<b>SDS-PAGE 5 × sample buffer</b>	0.25 M Tris-HCl pH 8 7.5% (w/v) SDS 25% (v/v) Glycerin 0.25 mg/ml Bromphenol blue 12.5% (v/v) 2-mercaptoethanol
<b>SDS-PAGE running buffer</b>	50 mM Tris-HCl pH 8.8 190 mM Glycine 1 mg/mL SDS

#### 7.1.4 Lyophilization

Removal of aqueous solvents was performed with a Christ Alpha 2-4 LSC freeze dryer (*Martin Christ Gefriertrocknungsanlagen GmbH, Osterode, Germany*) equipped with an Ilmvac Typ 109012 high vacuum pump from Ilmvac (Now: *Welch by Gardner Denver, Fürstfeldbruck, Germany*).

#### 7.1.5 Removal of organic solvents

Organic solvents were evaporated under reduced pressure using a rotary evaporator Rotavapor R-300 (*BÜCHI Labortechnik AG, Flawil, Switzerland*).

### 7.2 Characterization

#### 7.2.1 High performance liquid chromatography (HPLC)

Analytical HPLC analysis was performed using either an *Agilent 1100* device equipped with an *Agilent Eclipse Plus* RP column (C18, 100×4.6 mm, 3.5 μm, 95 Å) or an *Agilent Infinity 1260* device equipped with an *Interchim* (Montluçon, France) *Uptisphere Strategy* RP column (C18-HQ, 3 μm, 100×4.6 mm) at a flow rate of 0.6 mL/min. Eluent system consisted of 0.1% (v/v) aq. Trifluoroacetic acid (TFA) (eluent A) and 90% (v/v) aq. acetonitrile containing 0.1% (v/v) TFA (LC-MS grade, *Fisher Scientific GmbH Schwerte, Germany*) (eluent B).

Isolation of peptides or water-soluble compounds was performed on a semi-preparative *Interchim PuriFlash 4250* (Montluçon, France) equipped with a semi-preparative C18 RP column (*Interchim Uptisphere Strategy* (C18-HQ, 5 μm, 250×21.2 mm)). At a flow rate of 18 mL/min, 5 min of isocratic flow

---

(starting concentration of eluent B) was followed by 20 min of gradient flow. Eluent system consisted of 0.1% (v/v) aq. trifluoroacetic acid (TFA) (eluent A) and 90% (v/v) aq. acetonitrile with 0.1% (v/v) TFA (eluent B). Absorption was detected at 220 nm and 280 nm.

### 7.2.2 Size exclusion chromatography (SEC)

SEC analysis was performed on a *Phenomenex BioSep SEC-s2000* column (Aschaffenburg, Germany) using an *Agilent 1100* device at a flow rate of 0.6 mL/min. Either same eluents as for RP-HPLC were used and samples were eluted at an isocratic flow of 30 % respectively 40% eluent B, or alternatively PBS was used as eluent for protein compounds. Absorption was detected at 220 nm or 280 nm.

### 7.2.3 Hydrophobic interaction chromatography (HIC)

HIC analysis was performed on a *TSKgel® Butyl-NPR* column (TOSHO Inc.) using an *Agilent 1100* device applying a linear gradient from 0 to 100% HIC buffer B over 35 minutes at a flow rate of 0.9 mL/min. Eluent system consisted of 25 mM Tris-HCl pH 7.5, 1.5 M (NH<sub>4</sub>)<sub>2</sub>SO<sub>2</sub> (HIC buffer A, high salt) and 25 mM Tris-HCl pH 7.5 (HIC buffer B). Absorption was detected at 220 nm or 280 nm.

### 7.2.4 Mass spectrometry (MS)

Electrospray ionization mass spectrometry (ESI-MS) spectra were obtained using a *Shimadzu* (Kyoto, Japan) *LCMS-2020* mass spectrometer equipped with a *Phenomenex Synergy 4 u Fusion-RP 80* (C-18, 250×4.6 mm, 2 μm, 80 Å). Eluent system consisted of 0.1% (v/v) aq. formic acid (FA) (LC-MS grade, Fisher Scientific (Hampton, NH, USA) (eluent A) and acetonitrile containing 0.1% (v/v) FA (LC-MS grade) (eluent B).

### 7.2.5 Nuclear magnetic resonance spectroscopy (NMR)

<sup>1</sup>H and <sup>13</sup>C NMR measurements were recorded on an *Avance III* or an *Avance II* NMR Spectrometer at 300 MHz (*Bruker BioSpin GmbH*, Rheinstetten, Germany) or on a *DRX 500* NMR Spectrometer at 500 MHz (*Bruker BioSpin GmbH*, Rheinstetten, Germany). All samples were dissolved in deuterium oxide, CDCl<sub>3</sub> or DMSO-d<sub>6</sub> from *Sigma Aldrich* (*Merck KGaA*, Darmstadt, Germany).

### 7.2.6 Infrared spectroscopy (IR)

IR measurements were performed using homogenous potassium bromide pellet or by attenuated total reflection (ATR)-IR on a FTIR-Spectrometer *Spectrum Two* (*PerkinElmer*, Rodgau, Germany). Spectra were obtained by *PerkinElmer Spectrum* following instructions of manufacturer. Wave number area: 8.300-350 cm<sup>-1</sup>, spectral resolution 0.5 cm<sup>-1</sup>; wave number accuracy better than 0,01 cm<sup>-1</sup> at 3.000 cm<sup>-1</sup>; wave number correctness: 0,1 cm<sup>-1</sup> at 3.000 cm<sup>-1</sup>; signal-to-noise-ratio: 9.300 : 1 Peak to Peak, 5 s and 32.000 : 1 Peak to Peak, 1 min.

### 7.2.7 UV/Vis spectroscopy

UV/Vis-spectroscopy was performed on a *Shimadzu UVmini 1240* device using *Hellma* (Müllheim, Germany) Quartz *SUPRASIL®* cuvettes.

### 7.2.8 Microscopy

Fluorescence microscopy was performed on a *Zeiss Axio Vert A1 FL* (*Carl Zeiss AG*, Jena, Germany) equipped with *Axio Cam ICM1*. GFP and fluorescein was detected with a λ = 470 nm laser, TAMRA was excited at λ = 540-580 nm. Confocal laser scanning microscopy was performed on a *Leica TSC SP8* confocal microscope (*Leica Microsystems CMS GmbH*, Wetzlar, Germany).

## 7.2.9 Fluorescence-activated cell sorting (FACS)

Cell sorting was performed using the *Influx*<sup>™</sup> (BD Bioscience, Heidelberg, Germany) cell sorter.

## 7.3 Biological materials and methods

### 7.3.1 Bacterial strains

*Escherichia coli* BL21 (DE3) F<sup>-</sup> *ompT hsdSB(rB<sup>-</sup>, mB<sup>-</sup>) gal dcm* (DE3)

### 7.3.2 Mammalian cell lines

SK-BR-3 Mammary gland adenocarcinoma

HeLa Human cervix adenocarcinoma cells (Henrietta Lacks)

HeLa-eGFP654 stably transfected with eGFP (interrupted by inserted mutant intron 2 of human  $\beta$ -globin (IVS2-654))

### 7.3.3 Sodium dodecyl sulfate polyacrylamide gel electrophoresis (SDS-PAGE)

SDS-PAGE was performed under reducing conditions for analysis of protein samples depending on size. Therefore, polyacrylamide gels consisting of 15% (w/v) polyacrylamide separation gel and 4% (w/v) polyacrylamide stacking gel (composition stated in **Table 7**) were prepared via radical polymerization.

**Table 7:** Composition of separation and stacking gel solutions for preparation of polyacrylamide gels applied in SDS-PAGE.

	Separation gel (15%)	Stacking gel (4%)
ROTIPHORESE30% acrylamide-bisacrylamide solution	13.0 mL	2.4 mL
ddH <sub>2</sub> O	6.5 mL	8.4 mL
SDS-PAGE 4 × running gel buffer	6.5 mL	-
SDS-PAGE 4 × stacking gel buffer	-	3.6 mL
10 % APS	195 $\mu$ L	130 $\mu$ L
TEMED	9.8 $\mu$ L	10.8 $\mu$ L

For sample preparation 5 x sample buffer was added to the protein samples and denaturation was realized by boiling at 98 °C for 10 minutes. In a gel chamber, the polyacrylamide gel was prepared by covering with running buffer and after loading with samples and prestained protein marker, the gel was run at 45 mA and 300 V for approximately 30 minutes. Protein bands were stained with Coomassie staining solution under microwave heating for 1 minute followed by incubation with destaining solutions 1 and 2 for removal of background staining.

### 7.3.4 eGFP-L17E fusion protein production

L17E sequence was fused to the eGFP C-terminus, connected with a glycine-serine linker. L17E-fusion gene was produced via OE-PCR applying primer stated in **Table 8** and inserted into pEGFP-E172-LAP vector (**Figure 61**) using *NotI* and *XbaI*. Following sequencing the plasmid was transformed into *E. coli* BL21 for expression.

**Table 8:** Primer used for production of L17E-fusion genes.

Primer	Sequence 5' → 3'
eGFP L17E up	AAAAAATCTAGAAATAATTTTGTTTAA CTTTAAGAAGGAGGATATACCATGGG
eGFP Gly-Ser lo	AAATTTTCAGCGCGGTCAGCCAAATAG AACCACCACCACCAGAACCACCACCA CCAGGAACCACCACCACCCTTGTACA GCTCGTCCATGCC
eGFP L17E NotI lo	AAAAAAGCGGCCGCTTACAGTTTGCT CAGCTGCTGTTTCGCTTCATGTTTCG CCGCATGTTTGCCAGAAATTCAGC GCGGTCAGCC

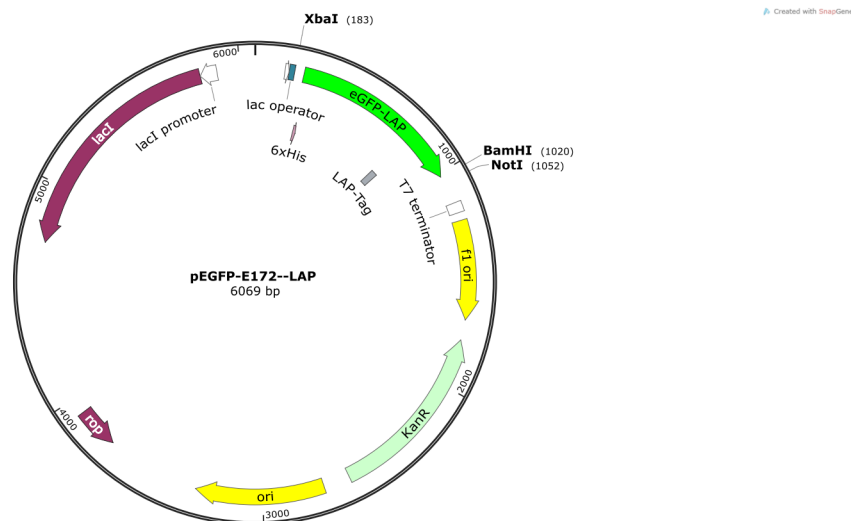


**Figure 61:** Vector map of pEGFP-E172-LAP encoding eGFP-LAP.

### 7.3.5 Transformation of *E. coli* by electroporation

Competent *E. Coli* cells (50  $\mu$ L) were electroporated with 2500 V, 25  $\mu$ F and 200  $\Omega$ . Following regeneration with 1 ml dYT-medium at 37°C for 1 h cells were plated out on antibiotic containing dYT-agar and incubated at 37°C.

### 7.3.6 Protein expression in *Escherichia coli*

In this work, eGFP-L17E fusion and LplA<sup>W37V</sup> were produced in *E. coli* BL21 (DE3). Following transformation of the corresponding expression plasmid into *E. coli* by electroporation, cells were plated on antibiotic containing dYT-plates and incubated at 37 °C overnight. A single colony was suspended in antibiotic containing dYT medium (50 mL) and incubated at 37 °C overnight. From the overnight culture, antibiotic containing dYT medium (1 L) was inoculated to an OD<sub>600nm</sub> of 0.1. At OD<sub>600nm</sub> of 0.5 protein production was induced by addition of IPTG (1 mM) and the culture was incubated at 30 °C (eGFP) or 18 °C (LplA) overnight. Cells were harvested by centrifugation and resuspended in lysis buffer, sonicated, centrifuged, and the supernatant was filtrated finally (0.45  $\mu$ m). The protein was isolated via Äkta (GE Healthcare) purification using a linear gradient of imidazole on a *HisTrap HP* column (1 ml, GE Healthcare). Product fractions were combined and dialyzed (MW cut-off 3.5 kDa) against PBS overnight.

### 7.3.7 Protein concentration measurement

Protein concentrations and L17E-dextran-eGFP conjugate concentrations were determined by absorption measurement via UV/Vis spectroscopy at a wavelength of 280 nm or 488 nm on a *Shimadzu BiosSpec-nano* or *Shimadzu UVmini 1240* device. Concentrations were calculated using known molar extinction coefficients and Lambert-Beer law:

$$A = \varepsilon * c * d$$

A = absorption

$\varepsilon$  = molar extinction coefficient [ $L * mol^{-1} * cm^{-1}$ ]

c = concentration [ $mol * L^{-1}$ ]

d = path length [cm]

### 7.3.8 Data of proteins applied in this work

#### 7.3.8.1 eGFP-L17E fusion protein

eGFP-L17E fusion protein (**Figure 62**) was generated as described in section 7.3.4 and yielded following overnight production in *E. coli* BL21 and IMAC purification (**Figure 168**).

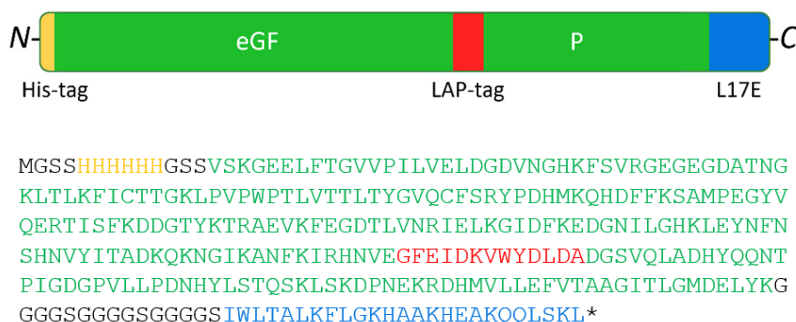


**Figure 62:** Schema and sequence of eGFP-L17E fusion protein with eGFP marked in green, hexa His tag marked in orange, LAP marked in red and L17E marked in blue.

Molecular weight: 33484 g/mol

Molar extinction coefficients:  $\varepsilon(280 \text{ nm}) = 30110 \text{ M}^{-1} * \text{cm}^{-1}$ ;  $\varepsilon(488 \text{ nm}) = 55900 \text{ M}^{-1} * \text{cm}^{-1}$

#### 7.3.8.2 Enhanced green fluorescent protein

Except eGFP-L17E fusion protein, entire enhanced green fluorescent protein applied in this work was a variant (**Figure 63**), established in the working group. In addition to a *N*-terminal hexa histidine tag, the eGFP variant was equipped with a second affinity tag towards *Strep-Tactin*<sup>®</sup> (strep-tagII) at the *C*-terminus. Furthermore, an internal 13 amino acid recognition sequence towards lipoic acid protein ligase A (LplA), lipoic acid acceptor peptide (LAP), was embedded in the sequence. As initially reported in the literature<sup>[114b]</sup> and further applied in LplA based protein-protein conjugation development in the Wombacher working group,<sup>[114a]</sup> the LAP-tag was located at a loop of the  $\beta$ -barrel structure between E172 and D173 of eGFP.



MGSSHHHHHHGSSSVSKGEELFTGVVPIIVELDGDVNGHKFSVRGEGEGDATNG  
 KLTLKFICTTGKLPVPWPTLVTTLTLYGVQCFSRYPDHMKQHDFFKSAMPEGYV  
 QERTISFKDDGYTKRAEVKFEQDTLVNR IELKGI DFKEDGNILGHKLEYNFN  
 SHNVIITADKQKNGIKANFKIRHNVEGFEIDKVVYDLDA DGSVQLADHYQQNT  
 PIGDGPVLLPDNHYLSTQSKLSKDPNEKRDMVLLLEFVTAAGITLGMDELYKG  
 SWSHPQFEK\*

**Figure 63:** Schema and sequence of eGFP variant applied in this work with eGFP marked in green, hexa His tag marked in orange, LAP marked in red and strep-tagII marked in blue.

Molecular weight: 30880 g/mol

Molar extinction coefficients:  $\epsilon(280 \text{ nm}) = 30110 \text{ M}^{-1} \cdot \text{cm}^{-1}$ ;  $\epsilon(488 \text{ nm}) = 55900 \text{ M}^{-1} \cdot \text{cm}^{-1}$

### 7.3.8.3 Lipoic acid protein ligase A

Lipoic acid protein ligase A applied in this work was the variant (**Figure 64**) including the W37V substitution. Three enzyme species were applied in this work. One was produced in the working group for prior experiments and applied in synthesis of eGFP-MeTet **54**. Two batches were yielded following overnight production in *E. coli* BL21 and IMAC purification (**Figure 169**) and applied in synthesis of eGFP-MeTet **54** and eGFP-MeTet **55**, respectively.

MKHHHHHHMSTLRLLLISDSYDPWFNLAVEECIFRQMPATQRVLFVLRNADTV  
 VIGRAQNPWKECNTRRMEEDNVLARRSSGGGAVFHD LGNTCFTFMAGKPEYD  
 KTISTSIVLNALNALGVSAEASGRNDLVVKTVEGDRKVS GSAYRETKDRGFHH  
 GTLLLNADLSRLANYLNPDKKLAAGITSVRSRVTNLTELLPGITHEQVCEA  
 ITEAFFAHYGERVEAEIISPNTPLDLPNFAET FARQSSWEWNFGQAPAFSHLL  
 DERFTWGGVELHFDVEKGHITRAQVFTDSLNPAPLEALAGRLQGCLYRADMLQ  
 QECEALLVDFPEQEKELELSAWMAGAVR\*

**Figure 64:** Sequence of LplA<sup>W37V</sup> applied in this work, hexa His tag marked in orange, W37V substitution marked in red.

Molecular weight: 39058 g/mol

Molar extinction coefficients:  $\epsilon(280 \text{ nm}) = 42540 \text{ M}^{-1} \cdot \text{cm}^{-1}$

### 7.3.9 Immobilized metal affinity chromatography (IMAC)

Proteins bearing a hexa-histidine-tag produced in *E. coli* were purified via IMAC purification using *Ni Sepharose High Performance prepacked HisTrap HP* (GE Healthcare) column on a *ÄKTA™ Explorer* (GE Healthcare) purifier platform. After loading of the column with 100 mM of Ni<sub>2</sub>Cl and equilibration with IMAC A buffer, the sterile filtered *E. coli* lysate in IMAC A buffer was loaded onto the column with a flow rate of 1 mL/min. The column was washed with IMAC A until the UV baseline was reached, and impurities were removed by washing with 5% of IMAC B. The bound protein of interest was eluted with a linear gradient 5 to 100% IMAC B over 10 minutes. The eluted protein fractions were analyzed with SDS-Page, combined, dialyzed against the respective buffer, and concentrated in *Amicon Ultra* centrifugal filters.

For purification of dextran-to-protein conjugates, gravity flow columns packed with *His-Pur™ Ni-NTA* (Thermo Scientific) were used. After loading the product onto the resin (30 min, ambient temperature) and washing with IMAC A buffer, the protein-to-dextran conjugates were eluted with IMAC B buffer and buffer was exchanged using *Amicon Ultra* centrifugal filters.

---

### 7.3.10 Protein A affinity chromatography

After chemical or enzymatic modification of antibodies, the conjugates were purified by protein A affinity chromatography using *Protein A HP SpinTrap*<sup>TM</sup> columns (GE Healthcare). After equilibration of the column with Protein A running buffer, the sample was load onto the column by incubation at ambient temperature for 5 minutes. After washing with running buffer, antibodies were eluted with 2 x 400  $\mu$ L Protein A elution buffer into reaction vessels each containing 30  $\mu$ L neutralization buffer. Purified antibody-conjugates were directly rebuffed and concentrated using *Amicon Ultra* centrifugal filters. *Protein A HP SpinTrap*<sup>TM</sup> columns were also used for immobilization of the antibody followed by chemically modification of the antibody bound to the solid phase. After modification unconsumed reagents were washed away and the respective antibody-conjugate eluted following the protocol of the supplier.

### 7.3.11 Cell culture

HeLa, HeLa-eGFP654, and SK-BR-3 cell lines were incubated under standard conditions at 37 °C in a humidified incubator with 5 % CO<sub>2</sub>. Cells were grown in Dulbecco's Modified Eagle's Medium (DMEM) with 10 % fetal bovine serum (FBS) and 1 $\times$  penicillin/streptomycin (pen/strep). HeLa-eGFP654 cells were ordered from the UNC Tissue Culture facility.

### 7.3.12 Cellular uptake assay

HeLa cells were seeded in 8- or 18-well microscopy slides in a density according to manufacturer protocol and incubated for 24 h under standard conditions at 37 °C in a humidified incubator with 5 % CO<sub>2</sub> in a volume DMEM (+10 % FBS) corresponding to the applied slide size. Cells were treated with the constructs in DMEM (w/o FBS) for 1 h under standard conditions at 37 °C in a humidified incubator with 5 % CO<sub>2</sub>, washed with PBS twice and incubated further 3 h in DMEM (+10 % FBS) at 37 °C and 5 % CO<sub>2</sub>. After washing with PBS, cells were fixed in 4 % PFA (15 min, ambient temperature). Alternatively, cells were washed with cold PBS prior to incubation with construct at 4 °C in DMEM (w/o FBS) for 1 h, washed with cold PBS twice and incubated further 3 h in DMEM (+10 % FBS) at 4 °C, followed by fixation.

### 7.3.13 Cell viability assay

The respective cells were seeded in a 96-well plate in a density of 1.5 $\times$ 10<sup>4</sup> cells/well in a volume of 90  $\mu$ L serum free DMEM. Cells were incubated for 24 h under standard conditions at 37 °C in a humidified incubator with 5 % CO<sub>2</sub>. Subsequently a serial dilution of the respective construct in 10  $\mu$ L PBS were added and cells incubated for a) 1 h at 37 °C and 5 % CO<sub>2</sub> plus further 3 h incubation in DMEM (+ 10 % FBS) at 37 °C and 5 % CO<sub>2</sub>, b) 1 h at 37 °C and 5 % CO<sub>2</sub> plus further 24 h incubation in DMEM (+ 10 % FBS) at 37 °C and 5 % CO<sub>2</sub>, or c) 72 h at 37 °C and 5 % CO<sub>2</sub>. After addition of 20  $\mu$ L MTS solution using *CellTiter96*<sup>®</sup> *AQueous One Solution Cell Proliferation Assay*, cell viability was measured with a *Tecan*<sup>®</sup> *Infinite F200 Pro* at 485 nm. As reference cell viability of untreated cells was set to 100%.

### 7.3.14 PNA mis-splicing correction assay

3 $\times$ 10<sup>4</sup> HeLa-eGFP654 cells/well in DMEM with 10% FBS were seeded in a 48-well plate and incubated at 37 °C in a humidified incubator with 5% CO<sub>2</sub> overnight. Cells were treated with the constructs in DMEM without l-glutamine, l-cystine, and l-methionine for 30 min under standard conditions at 37 °C in a humidified incubator with 5 % CO<sub>2</sub>. After removal of the supernatant, the cells were washed with PBS and subsequently with low-pH glycine buffer (cooled to 4 °C). After an additional washing step with PBS, the cells were treated with DMEM (+ 10 % FBS) and incubated at 37 °C in a humidified incubator with 5% CO<sub>2</sub> for 24 hours. After aspiration of the medium, cells were washed with PBS and trypsinized for 10 min, where after DMEM (+ 10 % FBS) was added. Cell suspensions were transferred to a 96-well

round bottom plate and centrifuged. The supernatant was discarded, the cells were resuspended in PBS and transferred to FACS tubes.

## 7.4 Enzymatic conjugation methods

### 7.4.1 Microbial transglutaminase (mTG) mediated conjugation

Amide bond formation between a reactive amine-donor and a protein bearing the amine-acceptor counterpart was catalyzed by mTG. 50-120 eq. amine-donor were incubated with 1 eq. protein bearing amine-acceptor and 0.25 eq. mTG in a suitable, primary amine free buffer at 37 °C for 12-24 h. Analysis of the reaction product was performed with SDS-PAGE or HIC.

### 7.4.2 Lipoic acid protein ligase A (LplA<sup>W37V</sup>) mediated conjugation

Site-specific introduction of click-chemistry substrates into proteins of interest, bearing LAP recognition sequence, was performed via lipoic acid protein ligase A (LplA<sup>W37V</sup>) mediated ligation. To this end, a solution was prepared according to **Table 9** and incubated at 37 °C for 1 h. Excessive substrate was removed using centrifugal filters.

**Table 9:** Components and final concentrations for LplA<sup>W37V</sup>-catalyzed ligation.

Component	Final concentration
POI-LAP	20 $\mu$ M
LplA <sup>W37V</sup>	2 $\mu$ M
Substrate	500 $\mu$ M
Mg(COO <sup>-</sup> ) <sub>2</sub>	5 mM
Sodium phosphate, pH 7.0	25 mM
ATP	5 mM
ddH <sub>2</sub> O	Filled up to final volume

## 7.5 General peptide synthesis

All peptides were synthesized using Fmoc-based solid-phase peptide synthesis on *AmphiSpheres 40* RAM resin (0.34 mmol/g) from *Agilent Technologies* (Waldbronn, Germany) or on 2-chlorotrityl chloride resin (1.6 mmol/g) from *Iris Biotech* (Marktredwitz, Germany). Amino acids from *Carbolution Chemicals GmbH* (St. Ingbert, Germany), *Carl Roth GmbH + Co. KG* (Karlsruhe, Germany) or *Iris Biotech GmbH* (Marktredwitz, Germany) were protected according to standard Fmoc/tert-butyl strategy, unless stated otherwise.

### 7.5.1 Automated peptide synthesis on CEM Liberty blue<sup>®</sup>

For fully automated microwave-assisted synthesis, a *CEM* (Kamp-Lintfort, Germany) *Liberty blue*<sup>®</sup> platform was applied in a 0.1 or 0.25 mmol scale. Coupling of amino acids was based on the *N,N*-diisopropylcarbodiimide (DIC, *Iris Biotech*)/ethyl-2-cyano-2-(hydroxyimino)acetate (Oxyma, *Iris-Biotech*) activation system, and *N*-terminal Fmoc was removed using 20% (v/v) piperidine and 0.1 M Oxyma in *N,N*-dimethylformamide (DMF).

### 7.5.2 General procedure for manual SPPS steps

#### 7.5.2.1 Loading onto 2-chlorotrityl chloride (2-ctc) resin

In a syringe equipped with a frit, 2-CTC resin (1.6 mmol/g) was swollen in dry dichloromethane (DCM) and gently agitated for 30 min, followed by washing with DCM (3 × 10 mL). The respective protected

---

amino acid (4 eq.) was dissolved in dry DCM and DIEA (8 eq.) was added. If necessary, DMF was added dropwise until the amino acid was dissolved totally. The solution was given into the syringe containing the swollen resin, and gently agitated at ambient temperature for 1 h. After removal of the reaction mixture and subsequent washing of the resin with DCM (5 × 10 mL) and DMF (5 × 10 mL), the loaded resin was ready for following Fmoc-deprotection and amino acid coupling steps.

### 7.5.2.2 Loading onto Rink amide (RAM) resin

In a syringe equipped with a frit, *AmphiSpheres 40* RAM resin (0.34 mmol/g) was swollen in DCM for 20 min, followed by swelling in DMF for further 20 min. After washing with DMF (3 × 10 mL) and removal of the Fmoc protecting group, the resin was ready for loading with the respective protected amino acid. The Fmoc amino acid (4 eq. respectively 2 eq. in case of non-standard amino acids) was dissolved in DMF and DIEA (8 eq. respectively 4 eq.) as well as coupling reagent 1-[bis(dimethylamino)methylene]-1H-1,2,3-triazolo[4,5-b]pyridinium 3-oxide hexafluorophosphate (HATU) or 3-[bis(dimethylamino)methylumyl]-3H-benzotriazol-1-oxid-hexafluorophosphat (HBTU) (3.96 eq. respectively 1.98 eq.) were added. After 5 minutes pre-activation, the mixture was given into the syringe containing the prepared RAM resin, and gently agitated at ambient temperature for 1 h. After removal of the reaction mixture and subsequent washing of the resin with DMF (5 × 10 mL), the loaded resin was ready for following Fmoc-deprotection and amino acid coupling steps.

### 7.5.2.3 Fmoc-deprotection

For removal of the Fmoc protecting group a deprotection solution of 20% (v/v) piperidine in DMF was added to the resin and gently agitated at ambient temperature for 5 minutes. The procedure was repeated with fresh deprotection solution for further 10 minutes and after thoroughly washing of the resin with DMF (5 × 10 mL), the resin was ready for coupling of the next Fmoc amino acid, additional modifications of the *N*-terminus or cleavage of the solid support.

### 7.5.2.4 Coupling step

The protected amino acid building block (4 eq. respectively 2 eq. in case of non-standard amino acids) was dissolved in DMF and DIEA (8 eq. respectively 4 eq.) or collidine (8 eq. respectively 4 eq.) in case of cysteine or histidine, which are prone to racemization, as well as coupling reagent HATU or HBTU (3.96 eq. respectively 1.98 eq.) were added. After 5 minutes pre-activation, the mixture was given into the syringe containing the *N*- $\alpha$ -Fmoc deprotected peptidyl resin, and gently agitated at ambient temperature for 1 h in case of single coupling (SC) steps. In case of double coupling (DC), the procedure was repeated with fresh reagents and the reaction mixture was gently agitated at ambient temperature for overall 2 × 45 min. After removal of the solution, the peptidyl resin was thoroughly washed with DMF (5 × 10 mL).

In case of microwave assisted manual SPPS, for acceleration of the reaction rate, the pre-activated amino acid solution was added to the reaction vessel, which contained the prepared resin. The vessel was microwave heated (30 W) to 50 °C for 10 minutes, allowing the solution to stand without heating for further 10 minutes before washing the resin with DMF.

### 7.5.2.5 Acetylation of the *N*-terminus

For acetylation of the *N*-terminus the *N*- $\alpha$ -Fmoc deprotected peptidyl resin was treated with a solution of acetic anhydride (8 eq.) and DIEA (16 eq.) in DMF at ambient temperature for 1 h followed by washing with DMF (5 × 10 mL).

### 7.5.3 Cleavage from solid support

The peptidyl resin was washed with DMF (5 × 10 mL), DCM (5 × 10 mL) and diethyl ether (DEE) (2 × 5 mL). For side chain deprotection as well as cleavage of the solid support, the tried resin was treated with the respective cleavage cocktail (10 mL per gram resin) and after gently agitation at ambient temperature for 2-3 h, the peptide was precipitated in ice-cold DEE (65 mL per 0.1 mmol).

Unless otherwise stated, the standard mixture for cleavage from RAM and 2-ctc resin consisted of TFA:TES:H<sub>2</sub>O (48:1:1, v:v:v) with addition of 2% (v/v) anisole and/or 2% (w/v) dithiothreitol (DTT), if the peptide sequence contained aromatic amino acids and/or cysteine.

### 7.5.4 Post-cleavage work-up

The precipitated peptides were isolated by centrifugation and washed with ice-cold DEE (3 × 40 mL). The crude peptides were dried, dissolved in a water/MeCN mixture and freeze-dried, resulting in white powder. Peptides were analyzed by RP-HPLC and LC-MS, and if necessary, purified via semi-preparative HPLC.

Peptides which did not precipitate in cold DEE were obtained after removal of the solvent under reduced pressure. The residue was redissolved in a water/MeCN mixture and analyzed via RP-HPLC and LC-MS after lyophilization, and if necessary, purified via semi-preparative HPLC.

## 7.6 Synthesis of aurein1.2 based peptides

### 7.6.1 Synthesis of Ac-Orn(N<sub>3</sub>)-VC-aurein1.2-Lys(maleimide)-NH<sub>2</sub> 3

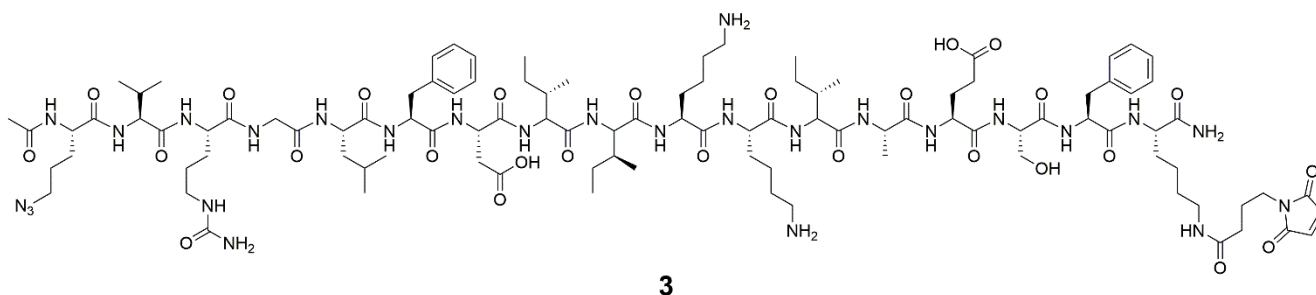


**Figure 65:** Structure of Ac-Orn(N<sub>3</sub>)-VC-aurein1.2-Lys(maleimide)-NH<sub>2</sub> 3, comprising azide-modification for azide-alkyne cycloaddition, enzyme cleavage-site, aurein1.2 sequence, and maleimide-modification for thiol-maleimide conjugation.

Sequence: Ac-Orn(N<sub>3</sub>)-Val-Cit-GLFDIHKKIAESF-Lys(maleimide)-NH<sub>2</sub>

Chemical Formula: C<sub>103</sub>H<sub>163</sub>N<sub>27</sub>O<sub>27</sub>

M<sub>w</sub>: 2211.60 g/mol

Peptide synthesis was carried out on 285 mg *AmphiSpheres 40* RAM resin (0.37 mmol/g) in 0.1 mmol scale. According to the general procedure, the resin was loaded with Fmoc-Lys(dde)-OH (2 eq.) using HATU/DIEA (1.96 eq./4 eq.) activation. The Fmoc-Lys(dde) loaded resin was applied in automated peptide synthesis of the following GLFDIHKKIAESF sequence on *CEM Liberty blue*<sup>®</sup> platform, according to the general procedure. Subsequently, Fmoc-Cit-OH (4 eq.) and Fmoc-Val-OH (4 eq.) were coupled (DC, 2 × 45 min) manually applying HBTU/DIEA (3.96 eq./8 eq.) activation as well as Fmoc-Orn(N<sub>3</sub>)-OH (2 eq.) (SC, 120 min) using HATU/DIEA (1.96 eq./4 eq.) activation. Next to *N*-α-Fmoc deprotection, the *N*-terminus was acetylated as described in the general procedure. For removal of the *N*-ε-dde lysine side chain protecting group, the tried peptidyl resin was treated with 2% (v/v) hydrazine in dry DMF (4 × 4 min). After thoroughly washing, a solution of 4-maleimidobutyric acid (4 eq.), HATU (3.96 eq.) and DIEA (8 eq.) in DMF was added to the resin and gently agitated at ambient temperature for 2 h. Following side chain deprotection and cleavage of the solid support, the crude peptide was precipitated

and washed in ice-cold DEE. The peptide **3** was isolated by semi-preparative HPLC, obtained as white powder after lyophilization, and analyzed via LC-MS and analytical RP-HPLC.

Yield: 36 mg (32.5%; only half amount of final peptidyl resin was applied in cleavage).

RP-HPLC (30to100% B): RT = 18.996 min.

MS (ESI) calculated:  $[M+H]^+ = 2211.60$ ;  $[M+2H]^{2+} = 1106.80$ ;  $[M+3H]^{3+} = 738.20$ ; observed:  $[M+2H]^{2+} = 1106.97$ ;  $[M+3H]^{3+} = 738.36$ .

## 7.6.2 Synthesis of Ac-Orn(N<sub>3</sub>)-VC-GS-Lys(maleimide)-NH<sub>2</sub> **6**

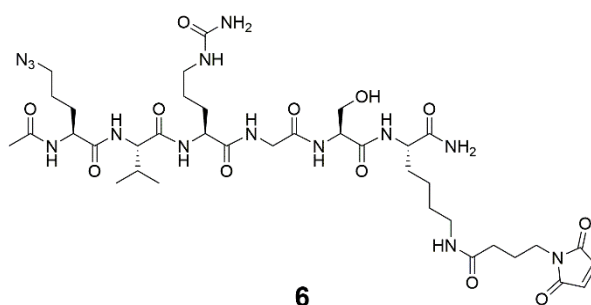


**Figure 66:** Structure of Ac-Orn(N<sub>3</sub>)-VC-GS-Lys(maleimide)-NH<sub>2</sub> **3**, comprising azide-modification for azide-alkyne cycloaddition, enzyme cleavage-site, and maleimide-modification for thiol-maleimide conjugation, lacking aurein1.2 sequence.

Sequence: Ac-Orn(N<sub>3</sub>)-Val-Cit-Gly-Ser-Lys(maleimide)-NH<sub>2</sub>

Chemical Formula: C<sub>37</sub>H<sub>60</sub>N<sub>14</sub>O<sub>12</sub>

M<sub>w</sub>: 892.97 g/mol

Peptide synthesis was carried out on 670 mg *AmphiSpheres 40* RAM resin (0.32 mmol/g) in 0.2 mmol scale. According to the general procedure, the resin was loaded with Fmoc-Lys(dde)-OH (2 eq.) using HATU/DIEA (1.96 eq./4 eq.) activation. Following amino acid building blocks Fmoc-Ser(*t*Bu)-OH (4 eq.), Fmoc-Gly-OH (4 eq.), Fmoc-Cit-OH (4 eq.) and Fmoc-Val-OH (4 eq.) were coupled (DC, 2 × 45 min) manually applying HATU/DIEA (3.96 eq./8 eq.) activation as well as Fmoc-Orn(N<sub>3</sub>)-OH (2 eq.) (SC, 120 min) using HATU/DIEA (1.96 eq./4 eq.) activation. Next to *N*-α-Fmoc deprotection, the *N*-terminus was acetylated as described in the general procedure. For removal of the *N*-ε-dde lysine side chain protecting group, the tried peptidyl resin was treated with 2% (v/v) hydrazine in dry DMF (4 × 4 min). After thoroughly washing, a solution of 4-maleimidobutyric acid (4 eq.), HATU (3.96 eq.) and DIEA (8 eq.) in DMF was added to the resin and gently agitated at ambient temperature for 1.5 h. Following side chain deprotection and cleavage of the solid support, the crude peptide was precipitated and washed in ice-cold DEE. The peptide **6** was isolated by semi-preparative HPLC, obtained as white powder after lyophilization, and analyzed via LC-MS and analytical RP-HPLC.

Yield: 9 mg (5%)

LC (10to100% B): RT = 10.25 min.

MS (ESI) calculated:  $[M+H]^+ = 893.97$ ;  $[M+2H]^{2+} = 447.49$ ; observed:  $[M+H]^+ = 893.69$ ;  $[M+2H]^{2+} = 447.56$ .

### 7.6.3 Synthesis of aurein1.2-Cys 33

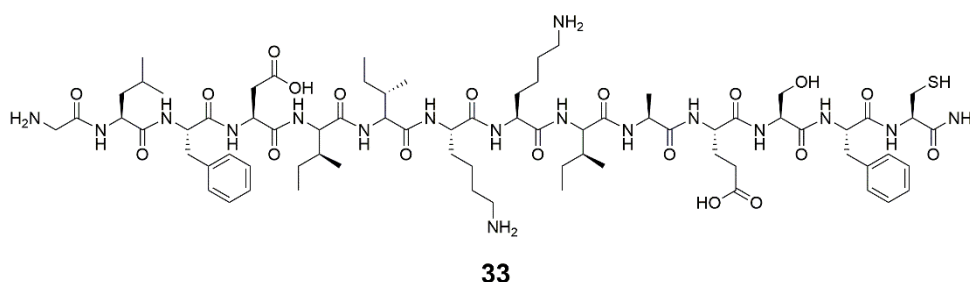


Figure 67: Structure of thiol modified aurein1.2-Cys 33.

Sequence: GLFDIIKKIAESFC-NH<sub>2</sub>  
Chemical Formula: C<sub>74</sub>H<sub>119</sub>N<sub>17</sub>O<sub>19</sub>S  
M<sub>w</sub>: 1582.93 g/mol

Peptide synthesis was performed according to the general procedure for automated peptide synthesis on *CEM Liberty blue*<sup>®</sup> platform. Synthesis was carried out on 833 mg *AmphiSpheres 40* RAM resin (0.34 mmol/g) in 0.25 mmol scale, applying double coupling and final *N*- $\alpha$ -Fmoc deprotection. Following side chain deprotection and cleavage of the solid support, the crude peptide was precipitated and washed in ice-cold DEE. The peptide **33** was isolated by semi-preparative HPLC, obtained as white powder after lyophilization, and analyzed via LC-MS and analytical RP-HPLC.

Yield: 70 mg (35.4%; only half amount of final peptidyl resin was applied in cleavage).  
RP-HPLC (20to100% B): RT = 15.824 min.  
MS (ESI) calculated: [M+H]<sup>+</sup> = 1583.93; [M+2H]<sup>2+</sup> = 792.47; [M+3H]<sup>3+</sup> = 528.64; observed:  
[M+2H]<sup>2+</sup> = 792.46; [M+3H]<sup>3+</sup> = 528.75.

## 7.7 Synthesis of M-Lycotoxin derived L17E peptides

### 7.7.1 Synthesis of L17E 12

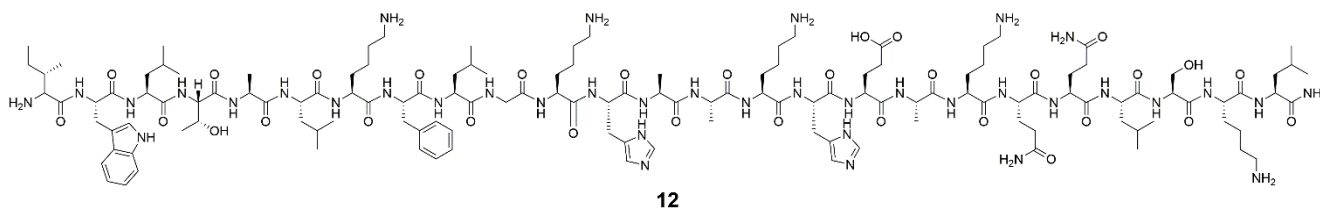


Figure 68: Structure of L17E peptide 12.

Sequence: IWLTKFLGKHA AKHEAKQQLSKL-NH<sub>2</sub>  
Chemical Formula: C<sub>134</sub>H<sub>220</sub>N<sub>38</sub>O<sub>31</sub>  
M<sub>w</sub>: 2859.47 g/mol

Peptide synthesis was performed according to the general procedure for automated peptide synthesis on *CEM Liberty blue*<sup>®</sup> platform. Synthesis was carried out on 833 mg *AmphiSpheres 40* RAM resin (0.34 mmol/g) in 0.25 mmol scale, applying double coupling and final *N*- $\alpha$ -Fmoc deprotection. Following side chain deprotection and cleavage of the solid support, the crude peptide was precipitated and washed in ice-cold DEE. The peptide **12** was isolated by semi-preparative HPLC, obtained as white powder after lyophilization, and analyzed via LC-MS and analytical RP-HPLC.



precipitated and washed in ice-cold DEE. The peptide **41** was isolated by semi-preparative HPLC, obtained as white powder after lyophilization, and analyzed via LC-MS and analytical RP-HPLC.

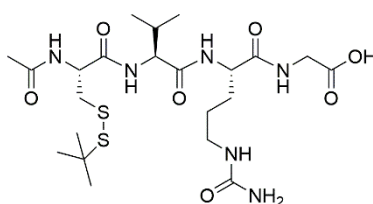
Yield: 90 mg (24.4%; only 50% of final peptidyl resin was cleaved).

RP-HPLC (20to100% B): RT = 11.849 min.

MS (ESI) calculated:  $[M+H]^+ = 2955.57$ ;  $[M+2H]^{2+} = 1478.29$ ;  $[M+3H]^{3+} = 985.86$ ;  $[M+4H]^{4+} = 739.64$ ;  $[M+5H]^{5+} = 591.91$ ;  $[M+6H]^{6+} = 493.43$ ; observed:  $[M+2H]^{2+} = 1478.18$ ;  $[M+3H]^{3+} = 985.77$ ;  $[M+4H]^{4+} = 739.56$ ;  $[M+5H]^{5+} = 591.86$ ;  $[M+6H]^{6+} = 493.45$ .

## 7.8 Synthesis of constituent C: Ac-Cys-VC-Gly-Dox 4

### 7.8.1 Synthesis of Ac-Cys(StBu)-VC-Gly 7: SPPS



**7**

**Figure 71:** Structure of CatB cleavable peptide linker Ac-Cys(StBu)-VC-Gly 7.

Sequence: Ac-Cys(StBu)-Val-Cit-Gly-OH

Chemical Formula:  $C_{22}H_{40}N_6O_7S_2$

$M_w$ : 564.72 g/mol

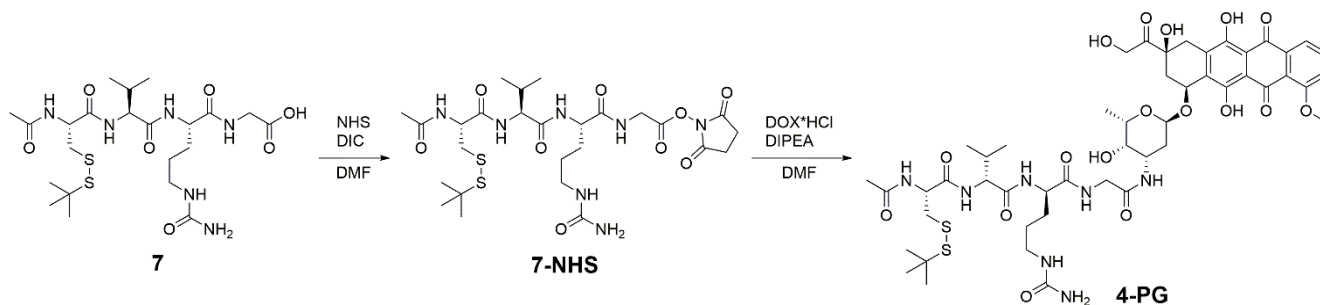
Peptide synthesis was performed according to the general procedure for manual peptide synthesis. Synthesis was carried out on 130 mg 2-CTC resin (1.6 mmol/g) in 0.20 mmol scale, applying single coupling of amino acid building blocks (4 eq.) using HBTU/DIEA (3.96 eq./8 eq.) activation and 20% (v/v) piperidine in DMF *N*- $\alpha$ -Fmoc deprotection. After final acetylation of the *N*-terminus, the crude peptide was cleaved of the solid support, precipitated, and washed in ice-cold DEE. The peptide **7** was isolated by semi-preparative HPLC, obtained as white powder after lyophilization, and analyzed via LC-MS and analytical RP-HPLC.

Yield: 61 mg (55.0%).

LC (10to100% B): RT = 11.53 min.

MS (ESI) calculated:  $[M+H]^+ = 565.72$ ; observed:  $[M+H]^+ = 565.38$ .

### 7.8.2 Synthesis of Ac-Cys(StBu)-VC-Gly-Dox 4-PG: Doxorubicin conjugation

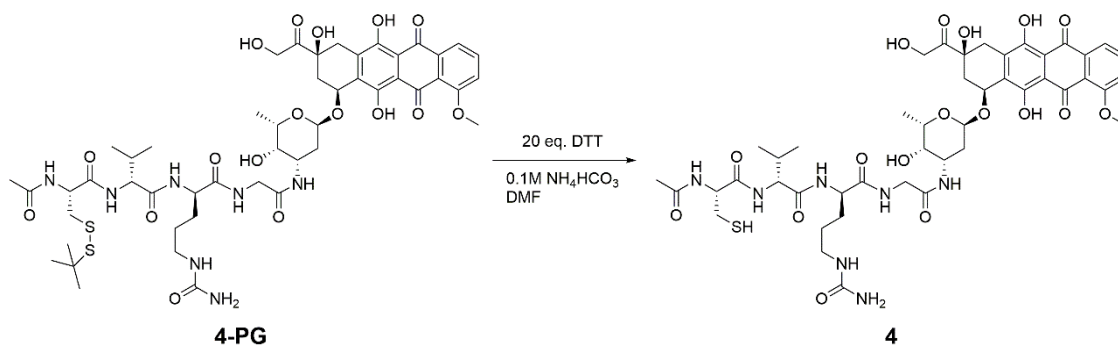


**Scheme 22:** C-terminal NHS-activation of Ac-Cys(StBu)-VC-Gly **7** and subsequent amide bond formation with doxorubicin.

18 mg Ac-Cys(*StBu*)-VC-Gly-OH **7** (0.032 mmol; 1 eq.) were dissolved in dry DMF, 9.9  $\mu$ L *N,N*-diisopropylcarbodiimide (DIC) (8.0 mg; 0.064 mmol; 2 eq.) and 7.3 mg NHS (0.064 mmol; 2 eq.) were added and stirred at ambient temperature for 2 h. Subsequently, 18.5 mg doxorubicin hydrochloride (0.032 mmol; 1 eq.) and 22.2  $\mu$ L DIEA (16.5 mg; 0.128 mmol; 4 eq.) were dissolved in minimal amount dry DMF and added to the reaction mixture. The red solution was stirred at ambient temperature overnight and product formation was controlled via analytical RP-HPLC. Solvent was removed under reduced pressure, the 64 mg crude product **4-PG** were obtained as red solid and directly used for the following deprotection without further analysis or purification.

RP-HPLC (0to100% B): RT = 17.869 min.

### 7.8.3 Synthesis of Ac-Cys-VC-Gly-Dox **4**: Thiol deprotection



**Scheme 23:** Removal of cysteine protecting group for generation of accessible thiol moiety in Ac-Cys-VC-Gly-Dox **4**.

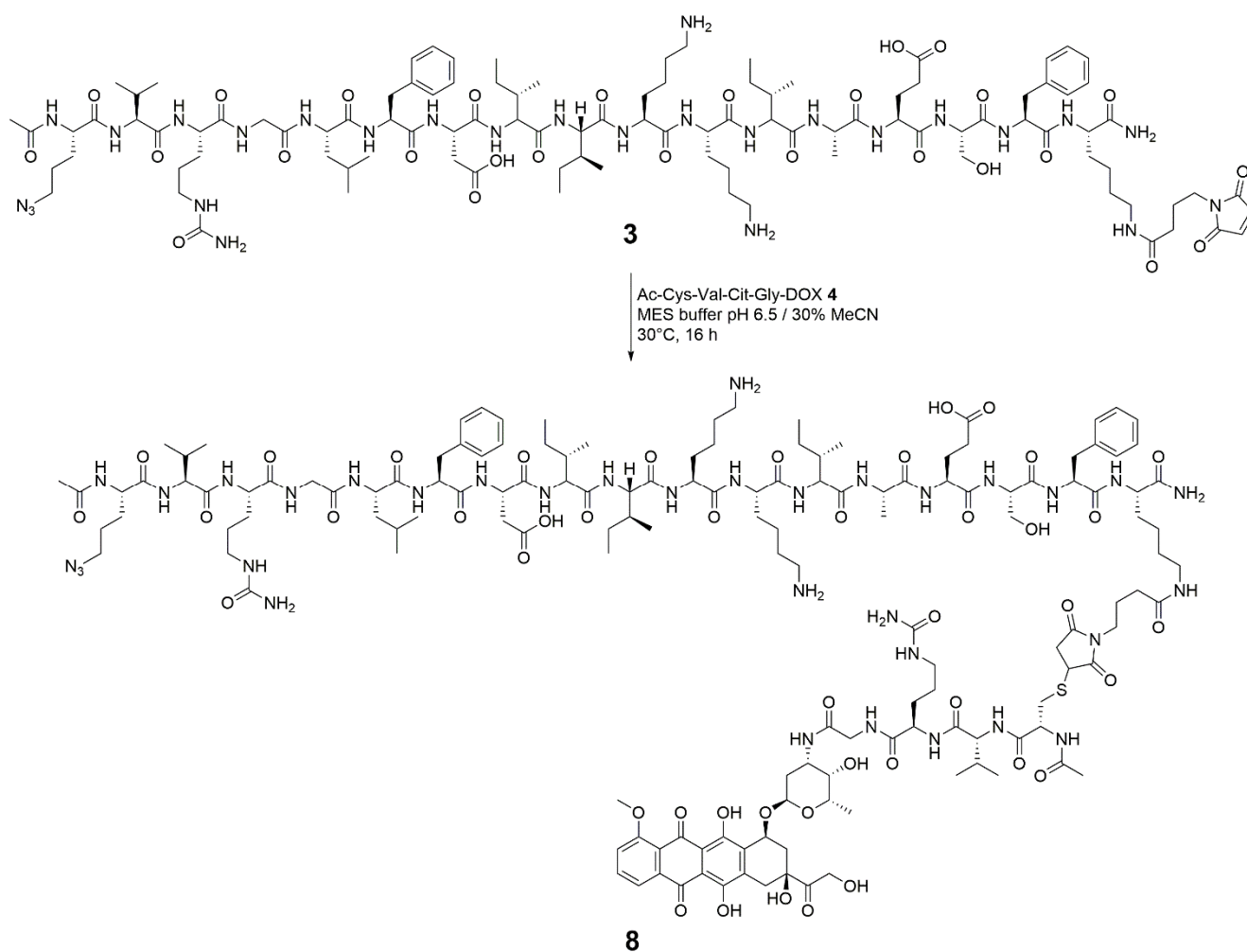
The crude Ac-Cys(*StBu*)-VC-Gly-Dox **4-PG** reaction mixture was dissolved in a degassed 50/50 mixture 0.1 M  $\text{NH}_4\text{HCO}_3$  buffer / DMF and flushed with Ar. 98 mg DTT (0.640 mmol; 20 eq.), dissolved in minimal amount degassed 0.1 M  $\text{NH}_4\text{HCO}_3$  buffer were added, and the mixture stirred at ambient temperature for 2 h. Reaction progress was monitored via analytical RP-HPLC. Solvents were removed under reduced pressure, the red residue was redissolved in 50% aq. MeCN and purified via semi-preparative RP-HPLC. After freeze-drying, 14 mg (44.1% related to starting material Ac-Cys(*StBu*)-VC-Gly-OH **7**) Ac-Cys-VC-Gly-Dox **4** were obtained as red powder and analyzed via LC-MS.

RP-HPLC (0to100% B): RT = 16.137 min.

LC (10to100% B): RT = 12.16 min.

MS (ESI) calculated:  $[\text{M}+\text{H}]^+ = 1003.06$ ;  $[3\text{M}+2\text{H}]^{2+} = 1504.09$ ;  $[\text{M}-\text{H}]^- = 1001.06$ ;  $[\text{M}-\text{H}+\text{TFA}]^- = 1115.06$ ; observed:  $[\text{M}+\text{H}]^+ = 1002.77$ ;  $[3\text{M}+2\text{H}]^{2+} = 1504.28$ ;  $[\text{M}-\text{H}]^- = 1001.06$ ;  $[\text{M}-\text{H}+\text{TFA}]^- = 1114.47$ .

## 7.9 Synthesis of azide-aurein1.2-doxorubicin conjugate **8**



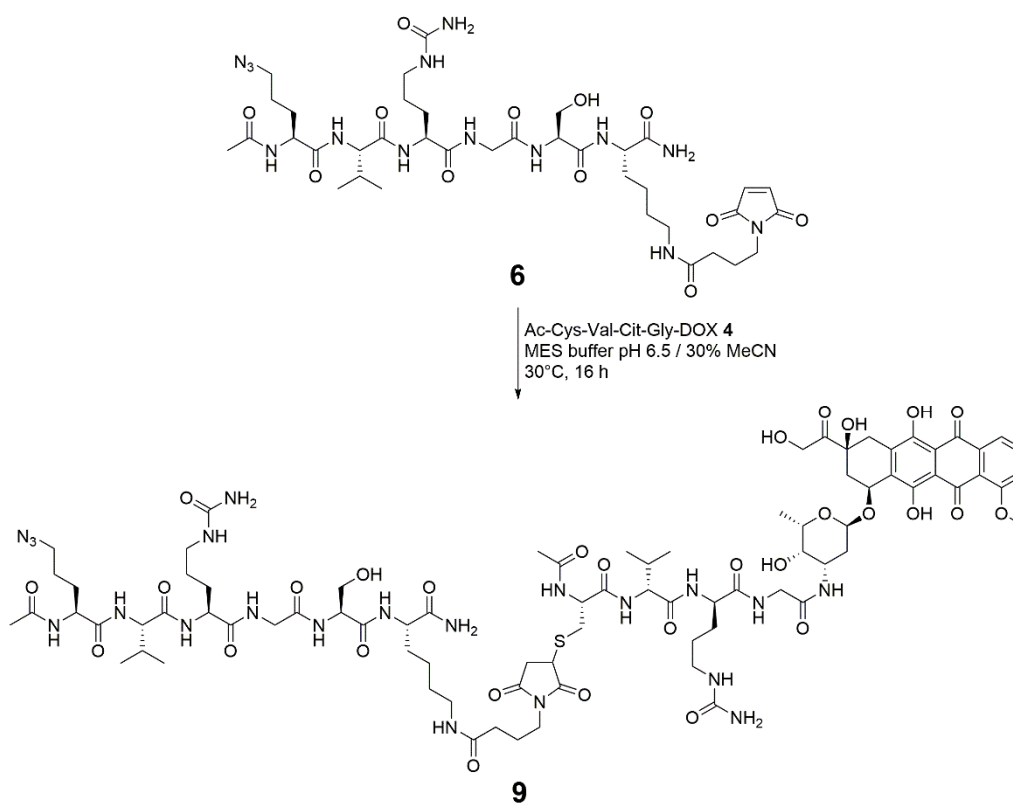
**Scheme 24:** Maleimide-thiol conjugation of Ac-Orn(N<sub>3</sub>)-VC-aurein1.2-Lys(maleimide)-NH<sub>2</sub> **3** and Ac-Cys-VC-Gly-Dox **4** yielded azide-aurein1.2-doxorubicin **8**.

11 mg Ac-Orn(N<sub>3</sub>)-VC-aurein1.2-Lys(maleimide)-NH<sub>2</sub> **3** (0.005 mmol; 1 eq.) were dissolved in degassed MES buffer pH 6.5 containing 33% MeCN and 7 mg modified doxorubicin compound Ac-Cys-VC-Gly-Dox **4** (0.007 mmol; 1.4 eq.) were added. The mixture was stirred at ambient temperature overnight, reaction process was monitored with LC-MS. The product was isolated by semi-preparative HPLC. After lyophilization, 15 mg (94.0%) conjugate **8** were obtained as red powder, and analyzed via LC-MS.

LC (10to100% B): RT = 16.16 min.

MS (ESI) calculated: [M+H]<sup>+</sup> = 3214.66; [M+2H]<sup>2+</sup> = 1607.83; [M+3H]<sup>3+</sup> = 1072.22; [M+4H]<sup>4+</sup> = 804.42; observed: [M+2H]<sup>2+</sup> = 1608.19; [M+3H]<sup>3+</sup> = 1072.37; [M+4H]<sup>4+</sup> = 804.56.

## 7.10 Synthesis of azide-doxorubicin conjugate 9 w/o aurein1.2



**Scheme 25:** Maleimide-thiol conjugation of Ac-Orn(N<sub>3</sub>)-VC-GS-Lys(maleimide)-NH<sub>2</sub> **6** and Ac-Cys-VC-Gly-Dox **4** yielded azide-doxorubicin **9**.

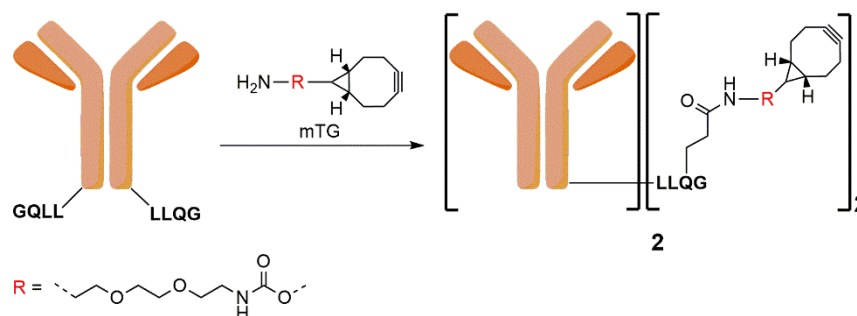
4.5 mg Ac-Orn(N<sub>3</sub>)-VC-GS-Lys(maleimide)-NH<sub>2</sub> **6** (0.005 mmol; 1 eq.) were dissolved in degassed MES buffer pH 6.5 containing 30% MeCN and 6 mg modified doxorubicin compound Ac-Cys-VC-Gly-Dox **4** (0.006 mmol; 1.2 eq.) were added. The mixture was stirred at ambient temperature overnight, reaction process was monitored with LC-MS. The product was isolated by semi-preparative HPLC. After lyophilization, 7 mg (73.0%) conjugate **9** were obtained as red powder, and analyzed via LC-MS.

LC (10to100% B): RT = 11.77 min.

MS (ESI) calculated: [M+H]<sup>+</sup> = 1896.03; [M+2H]<sup>2+</sup> = 948.52; [M+3H]<sup>3+</sup> = 632.67; [2M+3H]<sup>3+</sup> = 1264.35; [3M+4H]<sup>4+</sup> = 1422.27; observed: [M+H]<sup>+</sup> = 1896.30; [M+2H]<sup>2+</sup> = 948.67; [M+3H]<sup>3+</sup> = 632.86; [2M+3H]<sup>3+</sup> = 1264.58; [3M+4H]<sup>4+</sup> = 1422.58;

## 7.11 Assembly of Trastuzumab-conjugates

### 7.11.1 mTG mediated BCN-modification of Trastuzumab-LLQG



Scheme 26: mTG mediated BCN-modification of Trastuzumab-LLQG.

Trastuzumab bearing mTG addressable C-terminal LLQG tag at the heavy chains was modified via mTG catalyzed amide bond formation with *N*-[(1*R*,8*S*,9*S*)-Bicyclo[6.1.0]non-4-yn-9-ylmethoxycarbonyl]-1,8-diamino-3,6-dioxaoctane (BCN-amine). A solution of Trastuzumab-LLQG (1 eq.), mTG (0.25 eq.) and BCN-Peg-amine (120 eq.) in 25 mM Tris, 150 mM NaCl pH 8 was prepared resulting in final concentrations stated in **Table 10**, and incubated at 37 °C for 18 h.

Table 10: Final concentrations for mTG mediated BCN-modification of Trastuzumab-LLQG.

Component	Final concentration
Trastuzumab-LLQG (1 eq.)	33.3 $\mu$ M
mTG (0.25 eq.)	8.3 $\mu$ M
BCN-Peg-amine (120 eq.)	4 mM

Purification was performed either via protein A affinity chromatography or via simply removal of excessive amine-substrate using centrifugal filters. Alternatively, the product **2** was loaded onto protein A spin column, washed and the following reaction was performed with the protein bound to the solid support.

### 7.11.2 SPAAC test conjugation: Trastuzumab-aurein1.2-doxorubicin 1a-d

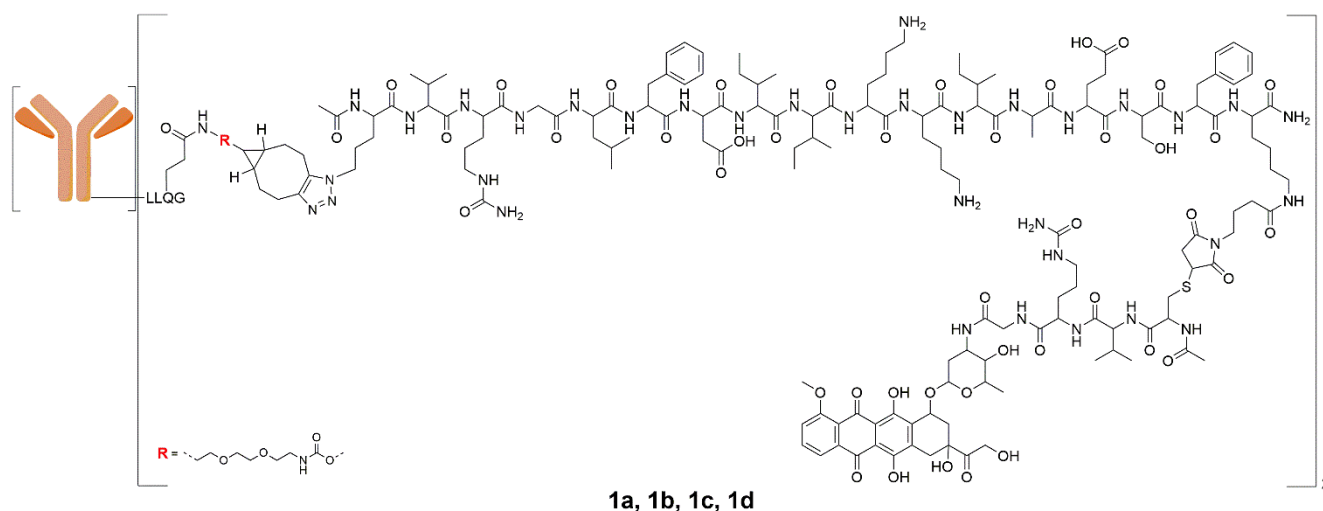


Figure 72: Structure of the SPAAC product: Trastuzumab-aurein1.2-Dox conjugate 1a-d.

Two reaction mixtures were prepared (30  $\mu\text{L}$  each) composed of 34  $\mu\text{M}$  Trastuzumab-BCN **2** (1 nmol; 1 eq.) and 102  $\mu\text{M}$  azide-aurein1.2-doxorubicin conjugate **8** (3 nmol; 3 eq.) in 25 mM Tris, 150 mM NaCl pH 8.0 and incubated at 20  $^{\circ}\text{C}$  for 16 h and 48 h, respectively.

The procedure was repeated using 340  $\mu\text{M}$  azide-aurein1.2-doxorubicin conjugate **8** (10 nmol; 10 eq.).

Products were analyzed via SDS-PAGE (**1a-d**) and HIC (**1a,b**).

### 7.11.3 SPAAC conjugation: Synthesis of Trastuzumab-aurein1.2-doxorubicin **1e**

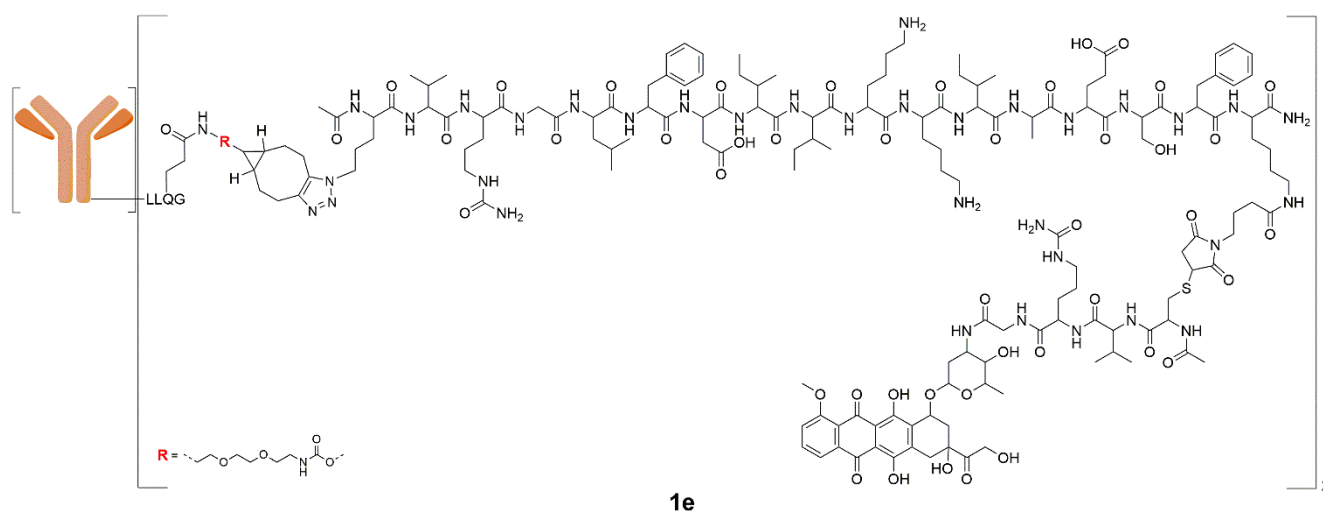


Figure 73: Structure of the final SPAAC product: Trastuzumab-aurein1.2-Dox conjugate **1e**.

300  $\mu\text{L}$  of a 100  $\mu\text{M}$  solution of azide-aurein1.2-doxorubicin conjugate **8** (0.03  $\mu\text{mol}$ ; 3 eq.) in 25 mM Tris, 150 mM NaCl pH 8.0 were added to protein A spin column, loaded with 1500  $\mu\text{g}$  Trastuzumab-BCN **2** (0.01  $\mu\text{mol}$ ; 1 eq.). The spin column was gently agitated at 20 $^{\circ}\text{C}$  for 16 h. After washing with 5% DMSO/PBS and PBS two times each, the modified protein was eluted with 2  $\times$  400  $\mu\text{L}$  elution buffer into reaction vessels containing 30  $\mu\text{L}$  neutralization buffer each. After buffer exchange to PBS and concentration using *Amicon Ultra* centrifugal filters 150  $\mu\text{L}$  solution of Trastuzumab-aurein1.2-doxorubicin conjugate **1e** in PBS with a protein concentration of 3.69 mg/mL was yielded. The protein was analyzed with SDS-PAGE.

### 7.11.4 SPAAC conjugation: Synthesis of Trastuzumab-doxorubicin **10**

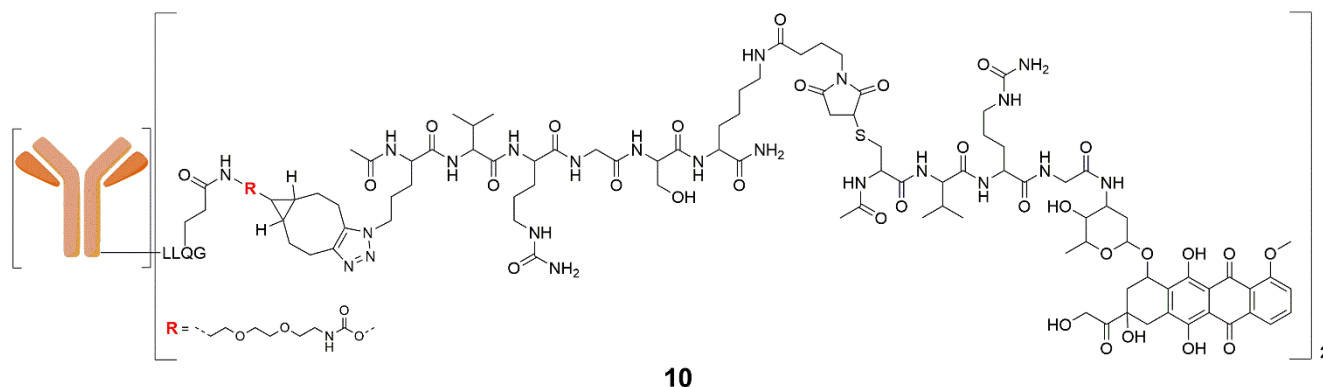
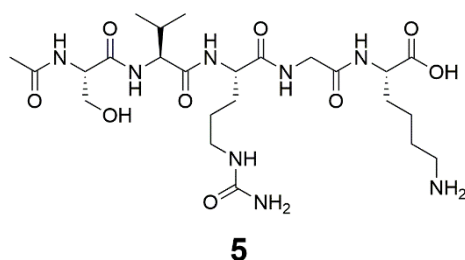


Figure 74: Structure of the final SPAAC product: Trastuzumab-Dox conjugate **10**.

300  $\mu\text{L}$  of a 100  $\mu\text{M}$  solution of azide-doxorubicin conjugate **9** w/o aurein1.2 (0.03  $\mu\text{mol}$ ; 3 eq.) in 25 mM Tris, 150 mM NaCl pH 8.0 were added to protein A spin column, loaded with 1500  $\mu\text{g}$  Trastuzumab-BCN **2** (0.01  $\mu\text{mol}$ ; 1 eq.). The spin column was gently agitated at 20°C for 16 h. After washing with 5% DMSO/PBS and PBS two times each, the modified protein was eluted with 2  $\times$  400  $\mu\text{L}$  elution buffer into reaction vessels containing 30  $\mu\text{L}$  neutralization buffer each. After buffer exchange to PBS and concentration using *Amicon Ultra* centrifugal filters 150  $\mu\text{L}$  solution of Trastuzumab-doxorubicin conjugate **10** in PBS with a protein concentration of 4.38 mg/mL was yielded. The protein was analyzed with SDS-PAGE.

## 7.12 Cathepsin B test cleavage

### 7.12.1 Synthesis of cathepsin B test peptide **5**



**Figure 75:** Structure of peptide **5** for cathepsin B test cleavage.

Sequence: Ac-Ser-Val-Cit-Gly-Lys-OH

Chemical Formula:  $\text{C}_{24}\text{H}_{44}\text{N}_8\text{O}_9$

$M_w$ : 588.66 g/mol

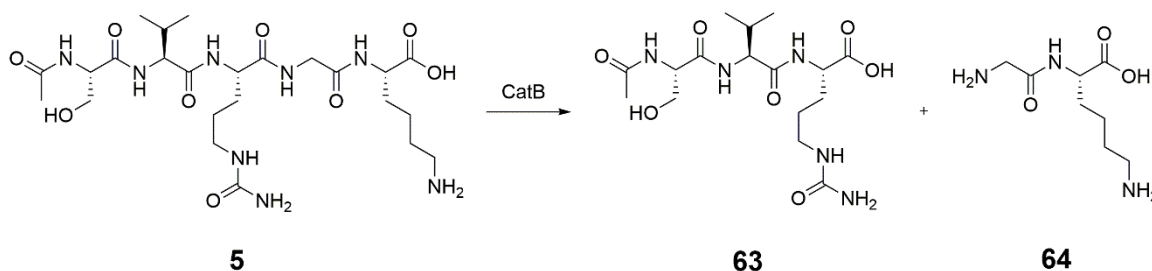
Peptide synthesis was performed according to the general procedure for manual peptide synthesis. Synthesis was carried out on 130 mg 2-CTC resin (1.6 mmol/g) in 0.20 mmol scale, applying single coupling of amino acid building blocks (4 eq.) using HBTU/DIEA (3.96 eq./8 eq.) activation, with exception of Fmoc-Cit-OH (2.5 eq.) using HBTU/DIEA (2.48 eq./5 eq.) activation and 20% (v/v) piperidine in DMF *N*- $\alpha$ -Fmoc deprotection. After final acetylation of the *N*-terminus, half amount of the crude peptide was cleaved of the solid support, precipitated, and washed in ice-cold DEE. The peptide **5** was isolated by semi-preparative HPLC, obtained as white powder after lyophilization, and analyzed via LC-MS and analytical RP-HPLC.

Yield: 53 mg (91.0%).

RP-HPLC (0to100% B): RT = 9.788 min.

MS (ESI) calculated:  $[\text{M}+\text{H}]^+ = 589.66$ ;  $[\text{M}+2\text{H}]^{2+} = 295.33$ ; observed:  $[\text{M}+\text{H}]^+ = 589.49$ ;  $[\text{M}+2\text{H}]^{2+} = 295.55$ .

### 7.12.2 Cathepsin B cleavage of test peptide **5**



**Scheme 27:** Cathepsin B mediated cleavage of test peptide **5**.

According to the literature,<sup>[110b]</sup> 4  $\mu\text{L}$  human liver cathepsin B stock solution (0.441 mg/mL in 50 mM sodium acetate buffer, 1 mM EDTA, pH 5.0) were given to 12  $\mu\text{L}$  activation buffer (30 mM DTT, 15 mM EDTA) and incubated at ambient temperature for 15 min. Following dilution with 2 mL reaction buffer (25 mM acetate, 1 mM EDTA, pH 5.0, 37  $^{\circ}\text{C}$ ), 8  $\mu\text{L}$  of a 10 mM peptide **5** solution was added, and the reaction mixture incubated at 37  $^{\circ}\text{C}$ . After 2 h the cleavage was analyzed via analytical HPLC and LC-MS.

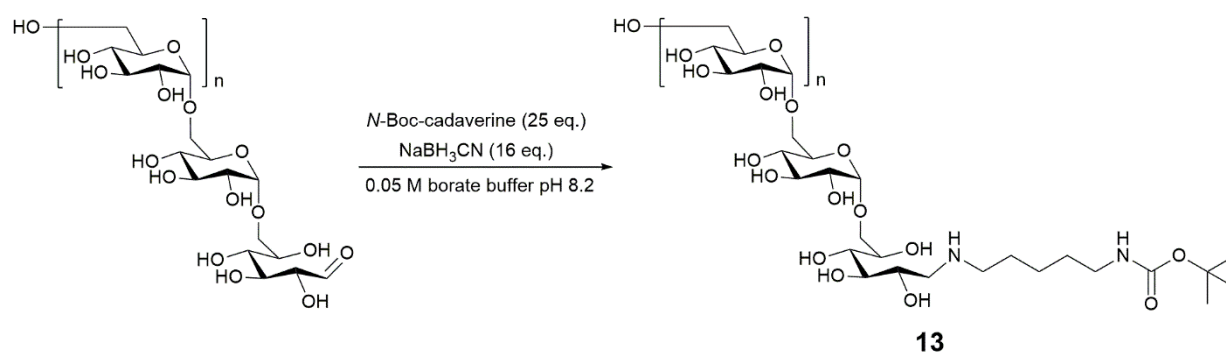
RP-HPLC (0to100% B): peptide **5** RT = 9.925 min.

RP-HPLC (0to100% B): cleavage product **63** RT = 9.460 min.

MS (ESI) calculated:  $[\text{M}+\text{H}]^+ = 403.44$ ; observed:  $[\text{M}+\text{H}]^+ = 404.46$ .

## 7.13 Dextran modification

### 7.13.1 Synthesis of dextran-*N*-Boc-cadaverine **13**



**Scheme 28:** Synthesis of dextran-*N*-Boc-cadaverine **13** via reductive amination.

For reductive amination, 5.0 g dextran (10 kDa from *Leuconostoc mesenteroides*) (0.5 mmol; 1.0 eq.), 2.6 mL *N*-Boc-cadaverine (2.5 g; 12.5 mmol; 25 eq.) and 0.5 g  $\text{NaBH}_3\text{CN}$  (8 mmol; 16 eq.) were dissolved in 0.05 M borate buffer pH 8.2 and the reaction mixture was stirred at 30  $^{\circ}\text{C}$  for 72 h. The product was precipitated and washed three times in cold methanol, dried and purified using PD 10 desalting column following the instructions of the manufacturer. 4.75 g (95 %) dextran-*N*-Boc-cadaverine **13** were obtained as white powder after lyophilization. Successful conversion was determined by  $^1\text{H}$  NMR spectroscopy as previously described in the literature.<sup>[76]</sup>

$^1\text{H}$  NMR (300 MHz, deuterium oxide)  $\delta = 5.48 - 4.88$  (m, 62 H, C(1)H), 4.10 - 3.40 (m, C(2-6)H (glucose units)), 3.16 - 3.05 (m, 4 H,  $\text{CH}_2-(\text{CH}_2)_3-\text{CH}_2-\text{NH}-\text{Boc}$ ), 1.80 - 1.40 (overlapped m, 15 H,  $(\text{CH}_2)_2-\text{CH}_2-(\text{CH}_2)_2-\text{NH}-\text{Boc}$ ,  $\text{CH}_2-\text{CH}_2-\text{CH}_2-\text{CH}_2-\text{CH}_2-\text{NH}-\text{Boc}$ , 3  $\text{CH}_3$  (Boc)) ppm.

## 7.13.2 General procedure for dextran modifications

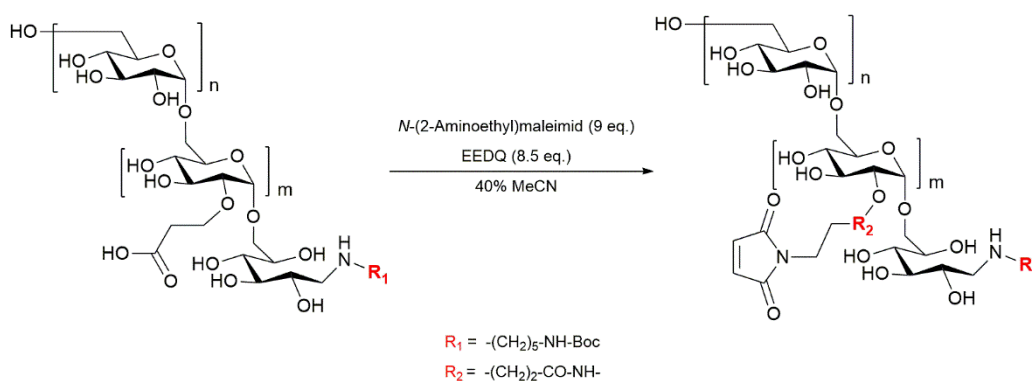
### 7.13.2.1 Carboxyethylation: Synthesis of 2-CE-dextran-*N*-Boc-cadaverine



**Scheme 29:** General synthesis of 2-CE-dextran-*N*-Boc-cadaverine via carboxyethylation.

Dextran-*N*-Boc-cadaverine (1 eq.) was dissolved in 1 M NaOH and acrylamide (2.5 eq. per desired 2-CE-group) was added. The reaction mixture was stirred at 30 °C for 24 h and further 24 h at 50 °C. After neutralization with 0.1 M HCl, the product was isolated using PD 10 desalting column and obtained as white powder after lyophilization. Successful conversion and quantification of carboxyethyl groups per dextran was determined by <sup>1</sup>H NMR spectroscopy as previously described in the literature.<sup>[61, 76]</sup>

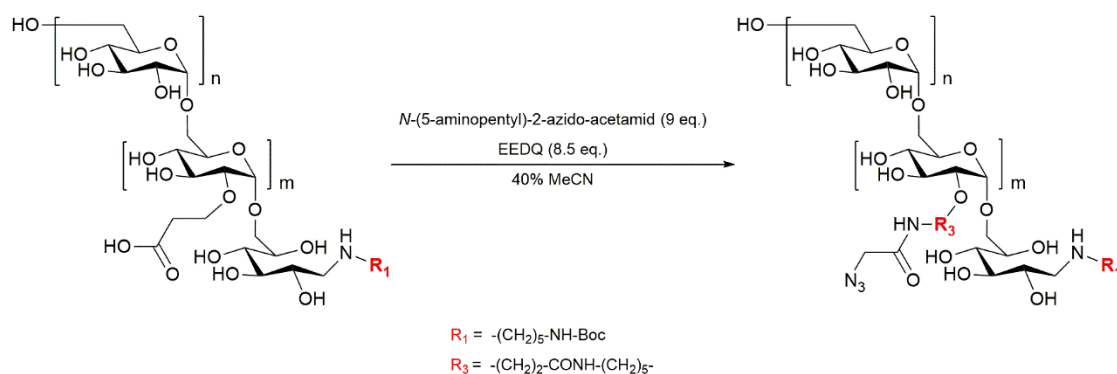
### 7.13.2.2 Maleimide conjugation: Synthesis of maleimide-dextran-*N*-Boc-cadaverine



**Scheme 30:** General synthesis of maleimide-dextran-*N*-Boc-cadaverine via EEDQ activated conjugation of maleimide and amine bifunctionalized linker. Stated equivalents refer to 2-CE groups per dextran.

Synthesis of maleimide-dextran-*N*-Boc-cadaverine was performed analogously to *N*<sub>3</sub>-dextran-*N*-Boc-cadaverine synthesis, previously reported in the literature.<sup>[76]</sup> Therefore, 2-CE-dextran-*N*-Boc-cadaverine (1.0 eq.), bearing the respective number of 2-CE-groups per dextran, was dissolved in 40 % aq. MeCN and EEDQ (8.5 eq. per CE-group), dissolved in 40 % aq. MeCN was added. After stirring at 30 °C for 1 h, *N*-(2-aminoethyl)maleimide **14** (9 eq. per CE-group) was added and the reaction mixture stirred at 30 °C for 4 h. The product was isolated using PD 10 desalting column and obtained as white powder after lyophilization. Successful conversion and quantification of maleimide groups per dextran was determined by <sup>1</sup>H NMR spectroscopy as previously described in the literature.<sup>[61, 76]</sup>

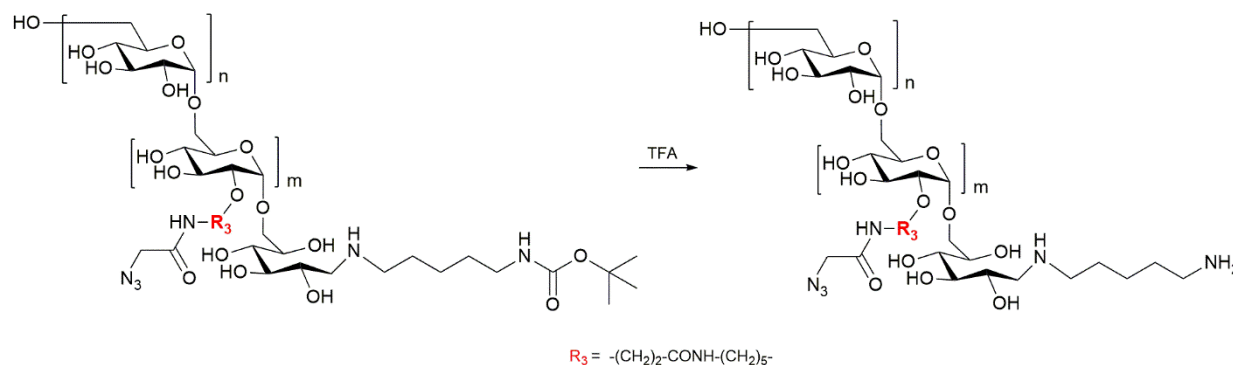
### 7.13.2.3 Azide conjugation: Synthesis of N<sub>3</sub>-dextran-*N*-Boc-cadaverine



**Scheme 31:** General synthesis of N<sub>3</sub>-dextran-*N*-Boc-cadaverine via EEDQ activated conjugation of azide and amine bifunctionalized linker. Stated equivalents refer to 2-CE groups per dextran.

Synthesis of N<sub>3</sub>-dextran-*N*-Boc-cadaverine was performed as previously reported in the literature.<sup>[76]</sup> Therefore, 2-CE-dextran-*N*-Boc-cadaverine (1.0 eq.), bearing the respective number of 2-CE-groups per dextran, was dissolved in 40 % aq. MeCN and EEDQ (8.5 eq. per CE-group), dissolved in 40 % aq MeCN was added. After stirring at 30 °C for 1 h, *N*-(5-aminopentyl)-2-azidoacetamide **21** (9 eq. per CE-group) was added and the reaction mixture stirred at 30 °C for 4 h. The product was isolated using PD 10 desalting column and obtained as white powder after lyophilization. Successful conversion and quantification of N<sub>3</sub>-groups per dextran was determined by <sup>1</sup>H NMR spectroscopy and IR-spectroscopy as previously described in the literature.<sup>[61, 76]</sup>

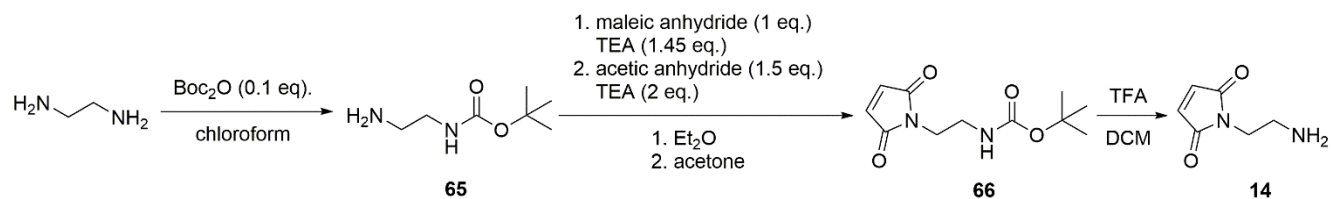
### 7.13.2.4 Removal of the Boc-protecting group



**Scheme 32:** Acidic removal of the Boc protecting group, resulting in accessible amine at the polysaccharide reducing end.

For Boc-deprotection, N<sub>3</sub>-dextran-*N*-Boc-cadaverine was dissolved in TFA and stirred at ambient temperature for 30 minutes. The product was evaporated, redissolved in water, and obtained as white powder after lyophilization. Deprotection was verified by <sup>1</sup>H NMR spectroscopy, as previously described in the literature.<sup>[76]</sup>

### 7.13.3 Synthesis of *N*-(2-aminoethyl)maleimide **14**



**Scheme 33:** Synthesis of maleimide and amine bifunctionalized linker *N*-(2-aminoethyl)maleimide **14**.

The synthesis of *N*-(2-aminoethyl)maleimide **14** was performed by colleagues of the working group, according to the literature.<sup>[119]</sup> Briefly: 1,2-ethylenediamine (1.0 eq.) was dissolved in chloroform and cooled down to 0 °C. A solution of Boc-anhydride (0.1 eq.) in chloroform was added dropwise over 3 h, where after the reaction mixture was allowed to warm to room temperature overnight. The solvent was removed under reduced pressure and the oily residue was dissolved in 2 M Na<sub>2</sub>CO<sub>3</sub>. The aqueous solution was extracted twice with DCM and the organic phase was dried over MgSO<sub>4</sub> and evaporated, yielding 5.13 g (81 %) *N*-Boc-ethylenediamine **65** as colourless oil.

<sup>1</sup>H NMR (300 MHz, chloroform-*d*) δ = 4.89 (s, 1H), 3.26 – 3.06 (m, 2H), 2.88 – 2.70 (m, 2H), 1.43 (s, 9H).

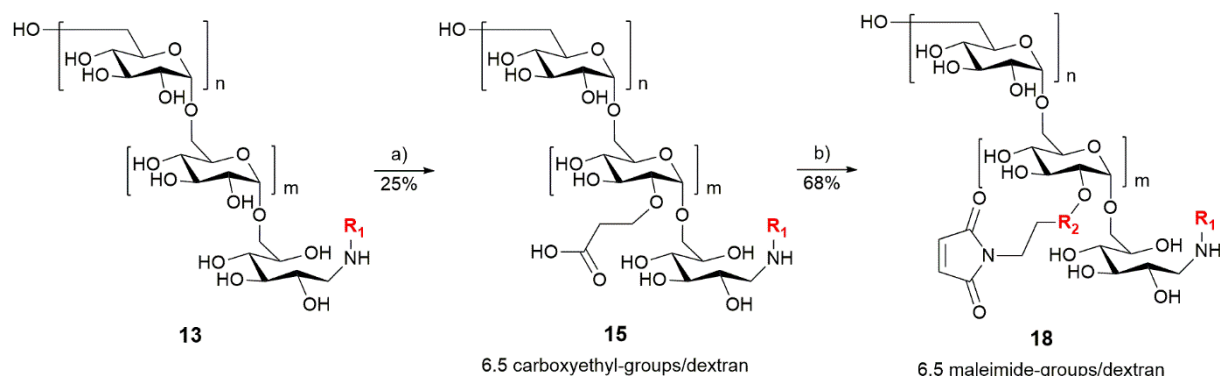
*N*-Boc-ethylenediamine **65** (1.0 eq.) and triethylamine (TEA) (1.45 eq.) were dissolved in diethyl ether and cooled down to 0 °C. Maleic anhydride (1 eq.) dissolved in diethyl ether was added dropwise, where after the cooling bath was removed and the reaction was stirred for further 4 h. The formed brown precipitate was filtered and dissolved in acetone. TEA (2 eq.) was added, and the reaction was heated to reflux, followed by addition of acetic anhydride (1.5 eq.). The reaction was refluxed for 20 h, where after the solvent was removed by evaporation. The brown residue was purified by column chromatography (silica gel, *n*-hexane:ethyl acetate 1:1) to yield 4.02 g (52 %) 1-((*N*-Boc)-2-aminoethyl)maleimide **66** as colourless solid.

<sup>1</sup>H NMR (300 MHz, chloroform-*d*) δ = 6.70 (s, 1H), 4.77 (s, 0H), 3.76 – 3.53 (m, 1H), 3.43 – 3.20 (m, 1H), 1.39 (s, 4H).

1-((*N*-Boc)-2-aminoethyl)maleimide **66** was dissolved in DCM and cooled down to 0 °C. TFA was added and the reaction was stirred for 1 h while being allowed to reach room temperature. Afterwards, the mixture was concentrated in vacuo and the residue was precipitated in cold diethyl ether. The suspension was filtrated, and the residue washed with diethyl ether (4 x) and dried in a desiccator. Purification by semi-preparative HPLC yielded 2.02 g (84 %) *N*-(2-aminoethyl)maleimide **14** as colorless solid.

<sup>1</sup>H NMR (300 MHz, deuterium oxide) δ = 6.92 (s, 1H), 3.93 – 3.78 (m, 1H), 3.24 (t, *J* = 5.8 Hz, 1H). MS (ESI) calculated: [M+H]<sup>+</sup> = 141.14; observed: [M+H]<sup>+</sup> = 141.43.

### 7.13.4 Synthesis of maleimide(6.5)-dextran-*N*-Boc-cadaverine **18**



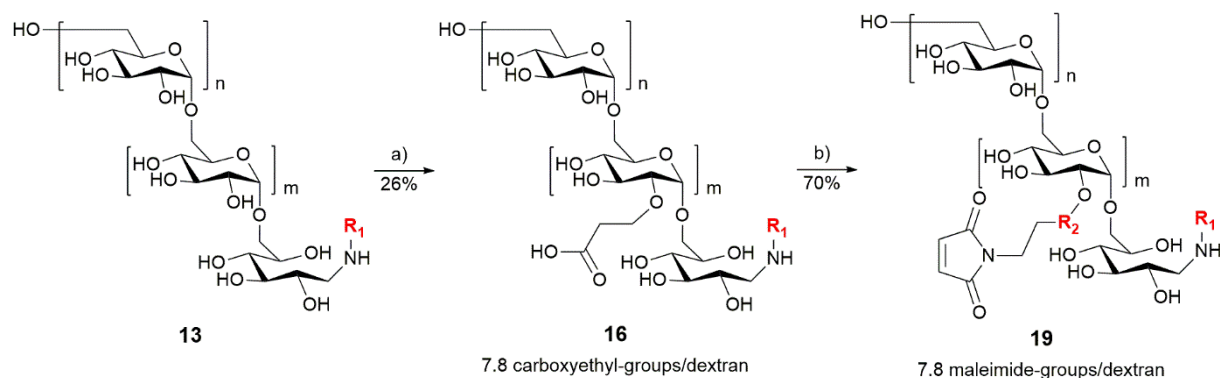
$R_1 = -(CH_2)_5-NH-Boc$  a) acrylamide (13.5 eq.), 1M NaOH  
 $R_2 = -(CH_2)_2-CO-NH-$  b) *N*-(2-Aminoethyl)maleimid **14** (9 eq.), EEDQ (8.5 eq.), 40% MeCN

**Scheme 34:** Synthesis of maleimide(6.5)-dextran-*N*-Boc-cadaverine **18**: Dextran-*N*-Boc-cadaverine **13** modification via carboxyethylation followed by EEDQ activated conjugation of *N*-(2-aminoethyl)maleimide **14**.

According to the general procedure of carboxyethylation a 2-CE-dextran-*N*-Boc-cadaverine bearing on average 6.5 2-CE groups per dextran was synthesized, followed by EEDQ activated introduction of maleimide moieties, according to the general procedure of maleimide conjugation. After lyophilization, 32 mg (17%) maleimide(6.5)-dextran-*N*-Boc-cadaverine **18** were obtained as white powder. For analysis and quantification of the number of maleimide groups per dextran  $^1H$  NMR spectroscopy was performed.

$^1H$  NMR (300 MHz, deuterium oxide)  $\delta = 7.03 - 6.86$  (s, 11 H,  $-CH=CH-$  (maleimide)),  $5.50 - 4.93$  (m, 62 H, C(1)H),  $4.16 - 3.32$  (m, C(2-6)H (glucose units)),  $2.66 - 2.40$  (m, 13 H,  $CH_2-CH_2-COOH$ ) ppm.

### 7.13.5 Synthesis of maleimide(7.8)-dextran-*N*-Boc-cadaverine **19**



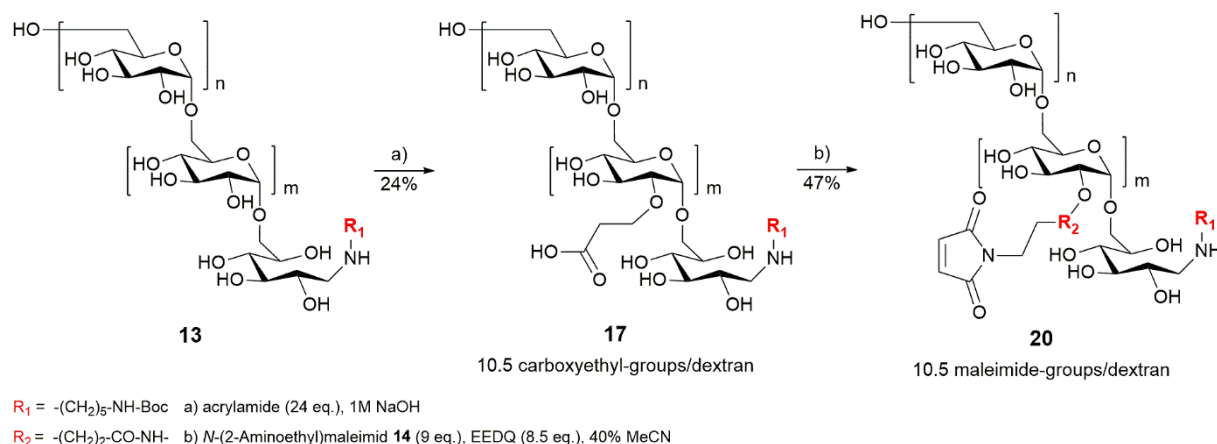
$R_1 = -(CH_2)_5-NH-Boc$  a) acrylamide (19 eq.), 1M NaOH  
 $R_2 = -(CH_2)_2-CO-NH-$  b) *N*-(2-Aminoethyl)maleimid **14** (9 eq.), EEDQ (8.5 eq.), 40% MeCN

**Scheme 35:** Synthesis of maleimide(7.8)-dextran-*N*-Boc-cadaverine **19**: Dextran-*N*-Boc-cadaverine **13** modification via carboxyethylation followed by EEDQ activated conjugation of *N*-(2-aminoethyl)maleimide **14**.

According to the general procedure of carboxyethylation a 2-CE-dextran-*N*-Boc-cadaverine bearing on average 7.8 2-CE groups per dextran was synthesized, followed by EEDQ activated introduction of maleimide moieties, according to the general procedure of maleimide conjugation. After lyophilization, 31 mg (18%) maleimide(7.8)-dextran-*N*-Boc-cadaverine **19** were obtained as white powder. For analysis and quantification of the number of maleimide groups per dextran  $^1H$  NMR spectroscopy was performed.

$^1\text{H}$  NMR (300 MHz, deuterium oxide)  $\delta = 7.01 - 6.84$  (s, 15 H,  $-\text{CH}=\text{CH}-$  (maleimide)), 5.43 – 4.92 (m, 62 H, C(1)H), 4.20 – 3.32 (m, C(2-6)H (glucose units)), 2.65 – 2.37 (m, 16 H,  $\text{CH}_2-\text{CH}_2-\text{COOH}$ ) ppm.

### 7.13.6 Synthesis of maleimide(10.5)-dextran-*N*-Boc-cadaverine 20



**Scheme 36:** Synthesis of maleimide(10.5)-dextran-*N*-Boc-cadaverine **20**: Dextran-*N*-Boc-cadaverine **13** modification via carboxyethylation followed by EEDQ activated conjugation of *N*-(2-aminoethyl)maleimide **14**.

According to the general procedure of carboxyethylation a 2-CE-dextran-*N*-Boc-cadaverine bearing on average 10.5 2-CE groups per dextran was synthesized, followed by EEDQ activated introduction of maleimide moieties, according to the general procedure of maleimide conjugation. After lyophilization, 21 mg (11%) maleimide(10.5)-dextran-*N*-Boc-cadaverine **20** were obtained as white powder. For analysis and quantification of the number of maleimide groups per dextran  $^1\text{H}$  NMR spectroscopy was performed.

$^1\text{H}$  NMR (300 MHz, deuterium oxide)  $\delta = 7.05 - 6.84$  (s, 20 H,  $-\text{CH}=\text{CH}-$  (maleimide)), 5.55 – 4.88 (m, 62 H, C(1)H), 4.14 – 3.33 (m, C(2-6)H (glucose units)), 2.61 – 2.43 (m, 21 H,  $\text{CH}_2-\text{CH}_2-\text{COOH}$ ) ppm.

### 7.13.7 Synthesis of *N*-(5-aminopentyl)-2-azidoacetamide 21

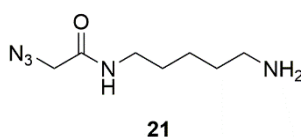


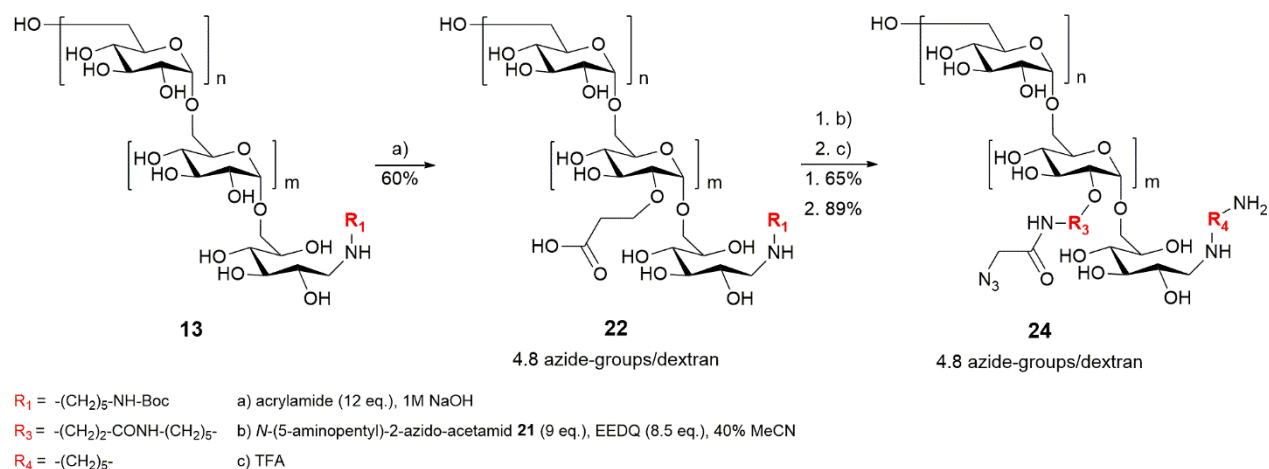
**Figure 76:** Structure of the *N*-(5-aminopentyl)-2-azidoacetamide **21** azide linker.

According to the literature<sup>[76]</sup>, the synthesis was performed on solid support. In a syringe equipped with a frit 1.25 g 2-chlorotriethyl chloride resin (1.6 mmol/g; scale 2.0 mmol) was swollen in DCM for 20 min and washed three times with (DCM) (10 mL). A solution of 2.34 mL cadaverine (2.04 g; 20.0 mmol; 10 eq.) and 6.97 mL DIEA (5.17 g; 40.0 mmol; 20 eq.) in DCM (5 mL) was added, and the reaction mixture was gently agitated at ambient temperature for 2 h. After washing with DCM (6 × 10 mL), a mixture of 299  $\mu\text{L}$  azidoacetic acid (0.40 g; 4.0 mmol; 2 eq.), 0.938 g Oxyma (6.6 mmol; 3.3 eq.) and 1.022 mL DIC (0.833 g, 6.6 mmol, 3.3 eq.) in DCM (10 mL) was added. The reaction mixture was gently agitated at ambient temperature for 18 h. After washing with DCM (6 × 10 mL) and diethyl ether (10 mL), the dried resin was treated with the cleavage cocktail trifluoroacetic acid:triethylsilane:anisole:H<sub>2</sub>O 23:1:1:1 (5 mL) at ambient temperature for 3 h. The product **21** was precipitated and washed in cold diethyl ether, and isolated via semi-preparative RP-HPLC, yielding 390 mg (65%) yellowish oil.

RP-HPLC (0to80% B): RT = 3.319 min.

MS (ESI) calculated:  $[M+H]^+ = 186.23$ ; observed:  $[M+H]^+ = 186.48$ .

### 7.13.8 Synthesis of N<sub>3</sub>(4.8)-dextran-cadaverine 24

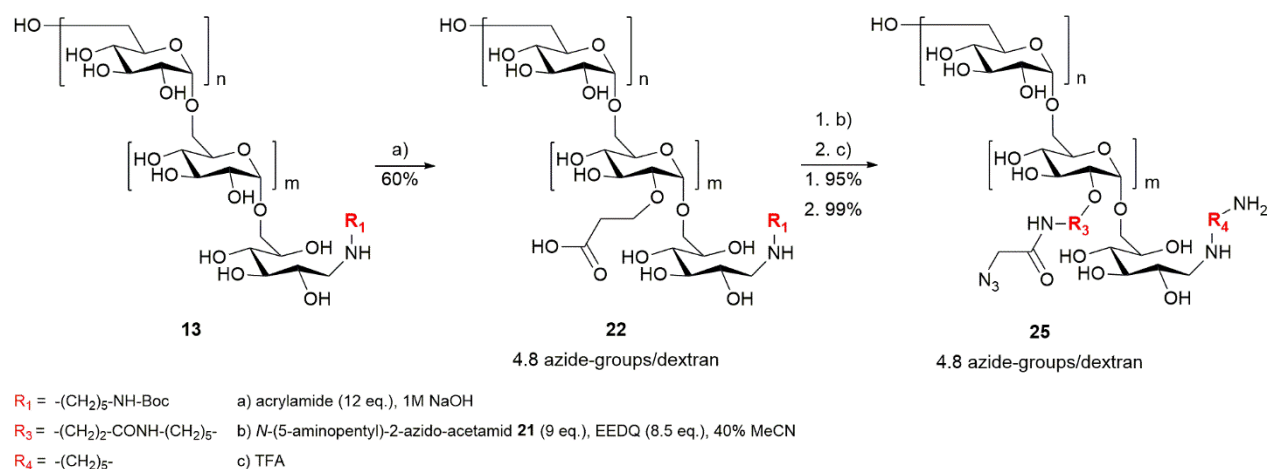


**Scheme 37:** Synthesis of N<sub>3</sub>(4.8)-dextran-cadaverine **24**: Dextran-*N*-Boc-cadaverine **13** modification via carboxyethylation followed by EEDQ activated conjugation of *N*-(5-aminopentyl)-2-azidoacetamide **21** and final removal of the Boc protecting group.

According to the general procedure of carboxyethylation a 2-CE-dextran-*N*-Boc-cadaverine bearing on average 4.8 2-CE groups per dextran was synthesized, followed by EEDQ activated introduction of azide moieties, according to the general procedure of azide conjugation. After removal of the Boc protecting group and purification as described in the general procedure, 22 mg (35%) N<sub>3</sub>(4.8)-dextran-cadaverine **24** were obtained as white powder. For analysis and quantification of the number of azide groups per dextran <sup>1</sup>H NMR spectroscopy and IR spectroscopy were performed.

<sup>1</sup>H NMR (300 MHz, deuterium oxide)  $\delta = 5.46 - 4.92$  (m, 62 H, C(1)H), 4.22 – 3.44 (m, C(2-6)H (glucose units)), 3.39 – 3.21 (m, 23 H, CH<sub>2</sub>-(CH<sub>2</sub>)<sub>3</sub>-CH<sub>2</sub>-NH-), 2.73 – 2.49 (m, 9 H, CH<sub>2</sub>-CH<sub>2</sub>-CONH), 1.69 – 1.52 (m, 23 H, CH<sub>2</sub>-CH<sub>2</sub>-CH<sub>2</sub>-CH<sub>2</sub>-CH<sub>2</sub>-NH-), 1.48 – 1.34 (m, 12 H, (CH<sub>2</sub>)<sub>2</sub>-CH<sub>2</sub>-(CH<sub>2</sub>)<sub>2</sub>-NH-) ppm.

### 7.13.9 Synthesis of N<sub>3</sub>(4.8)-dextran-cadaverine 25

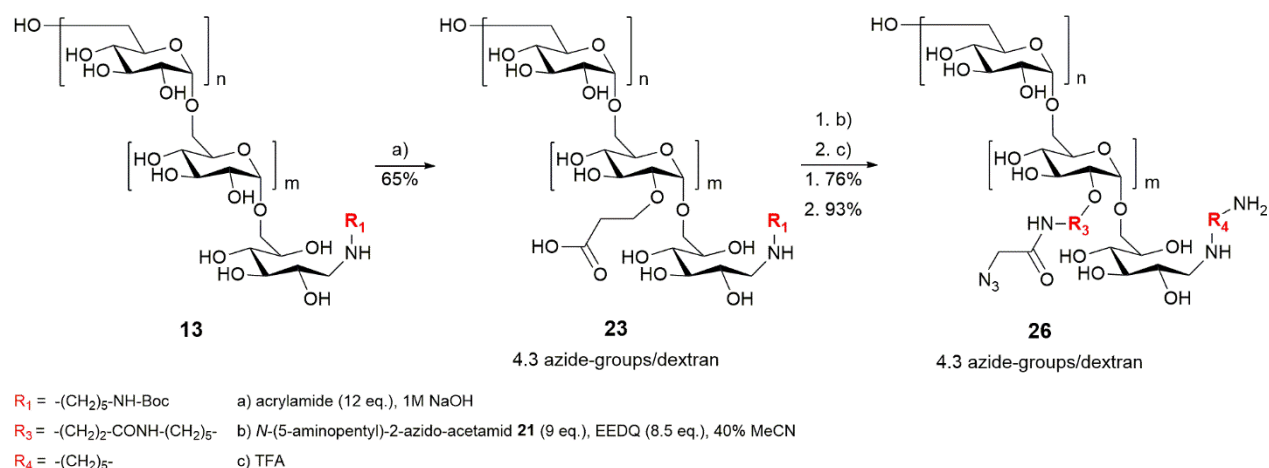


**Scheme 38:** Synthesis of N<sub>3</sub>(4.8)-dextran-cadaverine **25**: Dextran-*N*-Boc-cadaverine **13** modification via carboxyethylation followed by EEDQ activated conjugation of *N*-(5-aminopentyl)-2-azidoacetamide **21** and final removal of the Boc protecting group.

According to the general procedure of carboxyethylation a 2-CE-dextran-*N*-Boc-cadaverine bearing on average 4.8 2-CE groups per dextran was synthesized, followed by EEDQ activated introduction of azide moieties, according to the general procedure of azide conjugation. After removal of the Boc protecting group and purification as described in the general procedure, 141 mg (56%) N<sub>3</sub>(4.8)-dextran-cadaverine **25** were obtained as white powder. For analysis and quantification of the number of azide groups per dextran <sup>1</sup>H NMR spectroscopy and IR spectroscopy were performed.

<sup>1</sup>H NMR (300 MHz, deuterium oxide)  $\delta$  = 5.48 – 4.95 (m, 62 H, C(1)H), 4.20 – 3.43 (m, C(2-6)H (glucose units)), 3.38 – 3.18 (m, 23 H, CH<sub>2</sub>-(CH<sub>2</sub>)<sub>3</sub>-CH<sub>2</sub>-NH-), 2.71 – 2.48 (m, 9 H, CH<sub>2</sub>-CH<sub>2</sub>-CONH), 1.70 – 1.50 (m, 23 H, CH<sub>2</sub>-CH<sub>2</sub>-CH<sub>2</sub>-CH<sub>2</sub>-CH<sub>2</sub>-NH-), 1.47 – 1.34 (m, 13 H, (CH<sub>2</sub>)<sub>2</sub>-CH<sub>2</sub>-(CH<sub>2</sub>)<sub>2</sub>-NH-) ppm.

### 7.13.10 Synthesis of N<sub>3</sub>(4.3)-dextran-cadaverine **26**

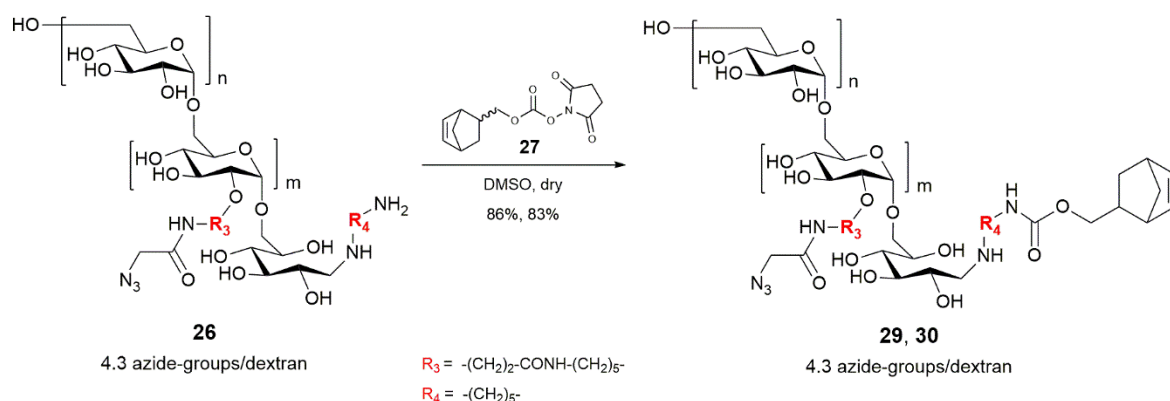


**Scheme 39:** Synthesis of N<sub>3</sub>(4.3)-dextran-cadaverine **26**: Dextran-*N*-Boc-cadaverine **13** modification via carboxyethylation followed by EEDQ activated conjugation of *N*-(5-aminopentyl)-2-azidoacetamide **21** and final removal of the Boc protecting group.

According to the general procedure of carboxyethylation a 2-CE-dextran-*N*-Boc-cadaverine bearing on average 4.8 2-CE groups per dextran was synthesized, followed by EEDQ activated introduction of azide moieties, according to the general procedure of azide conjugation. After removal of the Boc protecting group and purification as described in the general procedure, 37 mg (46%) N<sub>3</sub>(4.3)-dextran-cadaverine **26** were obtained as white powder. For analysis and quantification of the number of azide groups per dextran <sup>1</sup>H NMR spectroscopy was performed.

<sup>1</sup>H NMR (300 MHz, deuterium oxide)  $\delta$  = 5.41 – 4.78 (m, 62 H, C(1)H), 4.05 – 3.27 (m, C(2-6)H (glucose units)), 3.25 – 3.03 (m, 20 H, CH<sub>2</sub>-(CH<sub>2</sub>)<sub>3</sub>-CH<sub>2</sub>-NH-), 2.54 – 2.39 (m, 9 H, CH<sub>2</sub>-CH<sub>2</sub>-CONH), 1.54 – 1.36 (m, 21 H, CH<sub>2</sub>-CH<sub>2</sub>-CH<sub>2</sub>-CH<sub>2</sub>-CH<sub>2</sub>-NH-), 1.32 – 1.19 (m, 11 H, (CH<sub>2</sub>)<sub>2</sub>-CH<sub>2</sub>-(CH<sub>2</sub>)<sub>2</sub>-NH-) ppm.

### 7.13.11 Synthesis of N<sub>3</sub>(4.3)-dextran-norbornene 29, 30



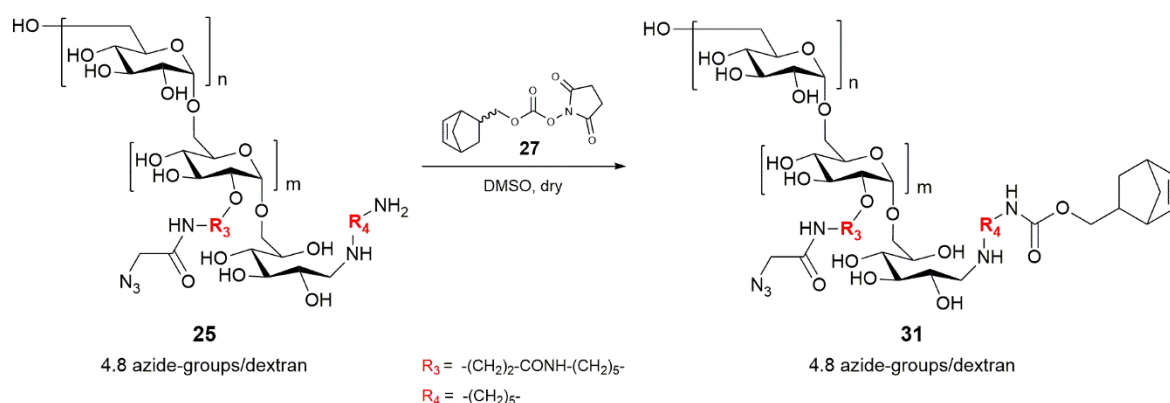
**Scheme 40:** Synthesis of N<sub>3</sub>-dextran-norbornene derivative **29** and **30** bearing 4.3 azide groups per dextran and a norbornene functionality at the polysaccharide reducing end.

15 mg N<sub>3</sub>(4.3)-dextran-cadaverine **26** (1.3 μmol; 1.0 eq.) were dissolved in dry DMSO, 1.7 mg (Norbornene-2-yl)-N-hydroxysuccinimidylcarbonate **27** (6.5 μmol; 5 eq.) and 4.5 μL DIEA (3.4 mg; 26 μmol; 20 eq.) were added and the mixture stirred at ambient temperature overnight. The product was precipitated and washed in cold MeCN, redissolved in water, and purified using PD 10 desalting column. The product **29** was obtained as white powder after lyophilization (13 mg, 86%). Introduction of the norbornene moiety was determined qualitatively by <sup>1</sup>H NMR spectroscopy.

Synthesis was repeated using 20 mg N<sub>3</sub>(4.3)-dextran-cadaverine **26** (1.7 μmol; 1.0 eq.), 2.3 mg (Norbornene-2-yl)-N-hydroxysuccinimidylcarbonate **27** (8.6 μmol; 5 eq.) and 6.0 μL DIEA (4.5 mg; 35 μmol; 20 eq.) yielding 16 mg (83%) product **30**.

<sup>1</sup>H NMR (300 MHz, deuterium oxide) δ = 6.35 – 6.29 (m, -CH=CH- (norbornene)), 6.28 – 6.20 (m, -CH=CH- (norbornene)), 6.11 – 6.03 (m, -CH=CH- (norbornene)), 5.52 – 4.89 (m, 62 H, C(1)H), 4.20 – 3.46 (m, C(2-6)H (glucose units)), 3.41 – 3.20 (m, 20 H, CH<sub>2</sub>-(CH<sub>2</sub>)<sub>3</sub>-CH<sub>2</sub>-NH-), 2.69 – 2.53 (m, 9 H, CH<sub>2</sub>-CH<sub>2</sub>-CONH), 1.75 – 1.55 (m, 20 H, CH<sub>2</sub>-CH<sub>2</sub>-CH<sub>2</sub>-CH<sub>2</sub>-CH<sub>2</sub>-NH-), 1.48 – 1.35 (m, 11 H, (CH<sub>2</sub>)<sub>2</sub>-CH<sub>2</sub>-(CH<sub>2</sub>)<sub>2</sub>-NH-) ppm.

### 7.13.12 Synthesis of N<sub>3</sub>(4.8)-dextran-norbornene 31



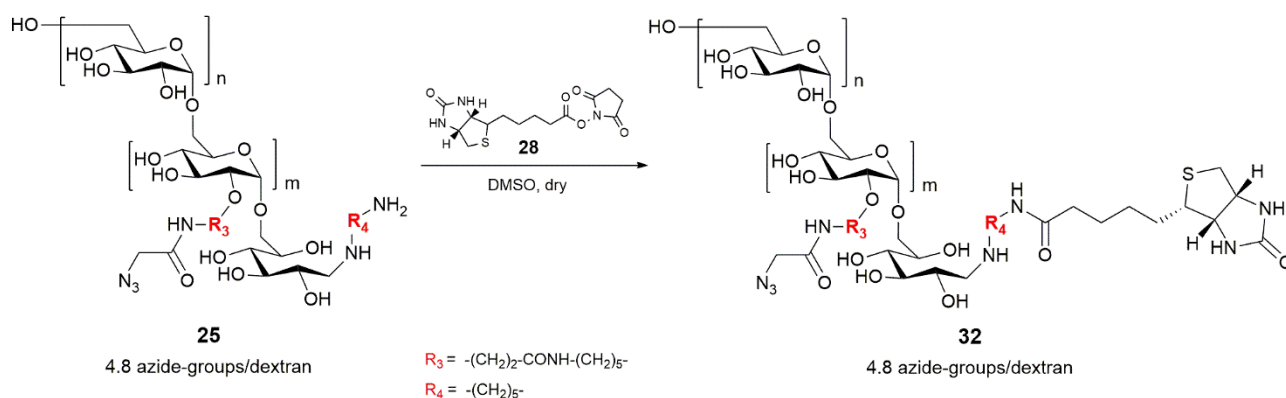
**Scheme 41:** Synthesis of N<sub>3</sub>-dextran-norbornene derivative **31** bearing 4.8 azide groups per dextran and a norbornene functionality at the polysaccharide reducing end.

63 mg N<sub>3</sub>(4.8)-dextran-cadaverine **25** (5.6 μmol; 1.0 eq.) were dissolved in dry DMSO, 7.4 mg (Norbornene-2-yl)-N-hydroxysuccinimidylcarbonate **27** (28.0 μmol; 5 eq.) and 19.5 μL DIEA (14.5 mg;

112  $\mu\text{mol}$ ; 20 eq.) were added and the mixture stirred at ambient temperature overnight. The product was precipitated and washed in cold MeCN, redissolved in water, and purified using PD 10 desalting column. The product **31** was obtained as white powder after lyophilization (49 mg, 76%). Introduction of the norbornene moiety was determined qualitatively by  $^1\text{H}$  NMR spectroscopy.

$^1\text{H}$  NMR (300 MHz, deuterium oxide)  $\delta$  = 6.35 – 6.30 (m, -CH=CH- (norbornene)), 6.26 – 6.22 (m, -CH=CH- (norbornene)), 6.10 – 6.05 (m, -CH=CH- (norbornene)), 5.50 – 4.95 (m, 62 H, C(1)H), 4.30 – 3.45 (m, C(2-6)H (glucose units)), 3.42 – 3.15 (m, 23 H,  $\text{CH}_2\text{-(CH}_2\text{)}_3\text{-CH}_2\text{-NH-}$ ), 2.70 – 2.52 (m, 10 H,  $\text{CH}_2\text{-CH}_2\text{-CONH}$ ), 1.73 – 1.51 (m, 22 H,  $\text{CH}_2\text{-CH}_2\text{-CH}_2\text{-CH}_2\text{-CH}_2\text{-NH-}$ ), 1.49 – 1.34 (m, 14 H,  $(\text{CH}_2)_2\text{-CH}_2\text{-(CH}_2\text{)}_2\text{-NH-}$ ) ppm.

### 7.13.13 Synthesis of $\text{N}_3(4.8)\text{-dextran-biotin 32}$



**Scheme 42:** Synthesis of  $\text{N}_3$ -dextran-biotin derivative **32** bearing 4.8 azide groups per dextran and a biotin functionality at the polysaccharide reducing end.

13 mg  $\text{N}_3(4.8)\text{-dextran-cadaverine 25}$  (2.7  $\mu\text{mol}$ ; 1.0 eq.) were dissolved in dry DMSO, 7.3 mg biotin-NHS **28** (21.5  $\mu\text{mol}$ ; 8 eq.) and 14  $\mu\text{L}$  DIEA (10.4 mg; 80.6  $\mu\text{mol}$ ; 30 eq.) were added and the mixture stirred at 30  $^\circ\text{C}$  overnight. The product was precipitated and washed in cold MeCN, redissolved in water, and purified using PD 10 desalting column. The product **32** was obtained as white powder after lyophilization (29 mg, 95%). Introduction of the biotin moiety was determined qualitatively by  $^1\text{H}$  NMR spectroscopy.

$^1\text{H}$  NMR (300 MHz, deuterium oxide)  $\delta$  = 5.49 – 4.97 (m, 62 H, C(1)H), 4.57 – 4.45 (m, 1 H, -S- $\text{CHR}_a\text{-CHR}_b\text{-NH-}$  (biotin)), 4.35 – 3.40 (m, C(2-6)H (glucose units)), 3.38 – 3.20 (m, 21 H,  $\text{CH}_2\text{-(CH}_2\text{)}_3\text{-CH}_2\text{-NH-}$ ), 3.12 – 3.01 (m, 1 H, -S- $\text{CHR}_a\text{-CHR}_b\text{-NH-}$  (biotin)), 2.92 – 2.82 (d, 2 H, -S- $\text{CH}_2\text{-CHR-NH-}$  (biotin)), 2.70 – 2.50 (m, 9 H,  $\text{CH}_2\text{-CH}_2\text{-CONH}$ ), 2.38 – 2.27 (t, 2 H, -NH-( $\text{CH}_2$ )<sub>5</sub>-NH-CO- $\text{CH}_2\text{-(CH}_2$ )<sub>3</sub>-(biotin)), 1.73 – 1.53 (m, 23 H,  $\text{CH}_2\text{-CH}_2\text{-CH}_2\text{-CH}_2\text{-CH}_2\text{-NH-}$ ), 1.50 – 1.30 (m, 14 H,  $(\text{CH}_2)_2\text{-CH}_2\text{-(CH}_2$ )<sub>2</sub>-NH-) ppm.

## 7.14 Thiol-maleimide addition of maleimide-functionalized dextran and thiol-modified cargo

### 7.14.1 Synthesis of TAMRA-thiol 35



Figure 77: Structure of TAMRA-thiol 35.

Sequence: TAMRA-O2Oc-Cys-OH

Chemical Formula: C<sub>34</sub>H<sub>38</sub>N<sub>4</sub>O<sub>9</sub>S

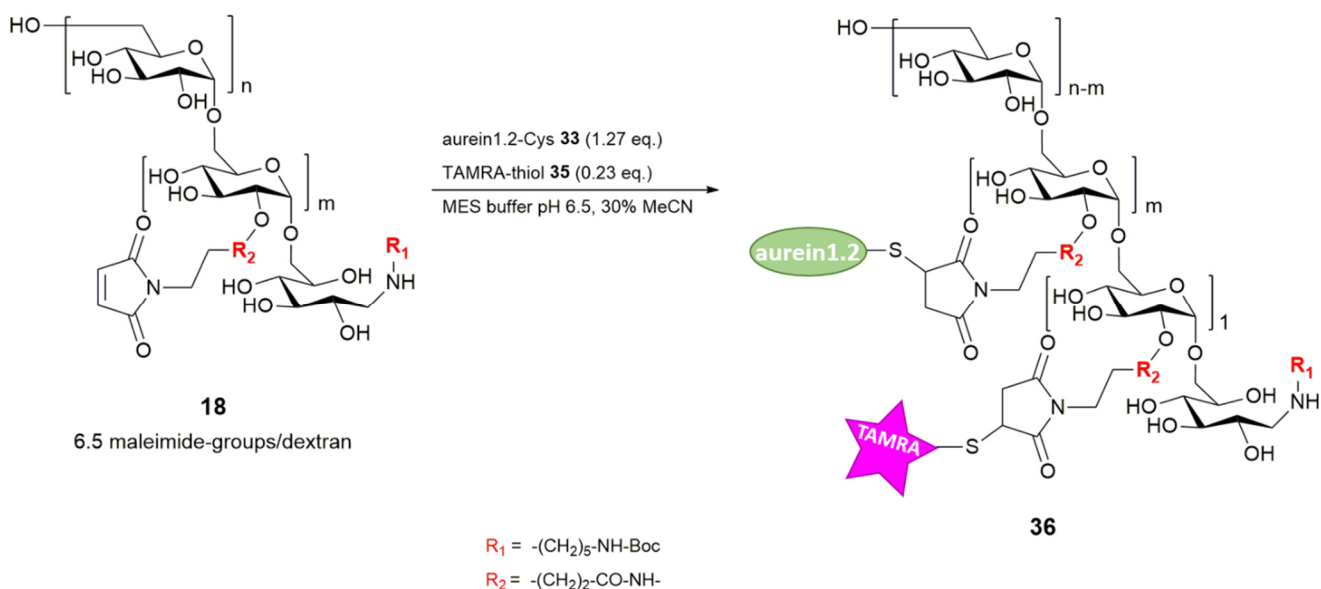
M<sub>w</sub>: 678.24 g/mol

TAMRA-thiol 35 synthesis was performed in the working group for prior experiments. Briefly: Synthesis was carried out on 2-ctc resin (1.6 mmol/g), applying single coupling of Fmoc-Cys(Trt)-OH (4 eq.), Fmoc-O2Oc-OH (1.5 eq) using HBTU/DIEA (1.4 eq./3 eq.), TAMRA-NHS (1.2 eq) / DIEA (4 eq.), and 20% (v/v) piperidine in DMF *N*-α-Fmoc deprotection. The peptide was cleaved of the solid support, precipitated, and washed in ice-cold DEE. TAMRA-thiol 35 was analyzed via LC-MS and analytical RP-HPLC.

RP-HPLC (20to100% B): RT = 18.778 min; 19.753 min.

MS (ESI) calculated: [M+H]<sup>+</sup> = 679.24; [M+2H]<sup>2+</sup> = 340.12; observed: [M+H]<sup>+</sup> = 679.38; [M+2H]<sup>2+</sup> = 340.46.

### 7.14.2 Synthesis of TAMRA-aurein1.2(4.5)-dextran-*N*-Boc-cadaverine 36



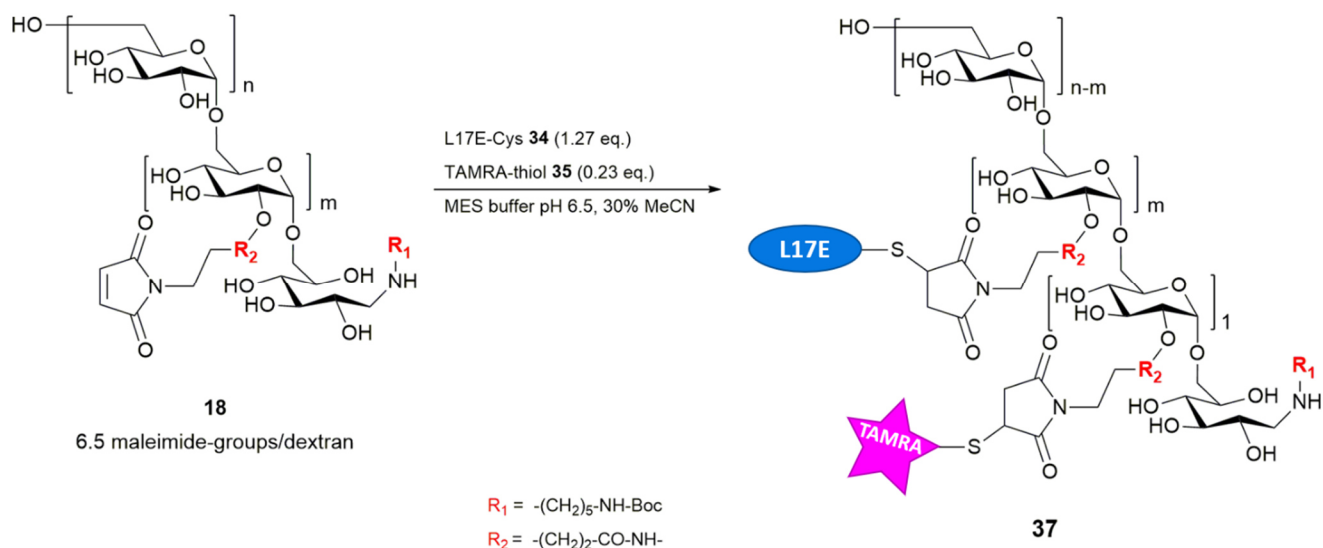
Scheme 43: Thiol-maleimide addition of maleimide(6.5)-dextran-*N*-Boc-cadaverine 18 with aurein1.2-Cys 33 and TAMRA-thiol 35. Stated equivalents related to maleimide groups per dextran.

13.1 mg aurein1.2-thiol 33 (8.25 μmol; 1.27 eq. per maleimide group) and 1.0 mg TAMRA-thiol 35 (1.50 μmol; 0.23 eq. per maleimide group) were dissolved in 2.5 mL degassed 0.1 M MES buffer pH 6.5, 30 % (v/v) MeCN and 10 mg maleimide(6.5)-dextran-*N*-Boc-cadaverine 18 (1.00 μmol; 1.0 eq.) were added. The reaction mixture was stirred at 30 °C overnight and subsequently purified using disposable

PD 10 desalting columns following the instructions of the supplier. 14 mg (75%) product **36** were obtained as pink powder after freeze-drying. For analysis and quantification  $^1\text{H}$  NMR spectroscopy was performed.

$^1\text{H}$  NMR (300 MHz, deuterium oxide)  $\delta$  = 7.70 – 6.98 (m, 55 aromatic H, Phe + TAMRA), 5.43 – 4.92 (m, 62 H, C(1)H), 4.40 – 0.50 (m, C(2-6)H (glucose units), peptide backbone + aliphatic residues) ppm.

### 7.14.3 Synthesis of TAMRA-L17E(3.8)-dextran-*N*-Boc-cadaverine **37**



**Scheme 44:** Thiol-maleimide addition of maleimide(6.5)-dextran-*N*-Boc-cadaverine **18** with L17E-Cys **34** and TAMRA-thiol **35**. Stated equivalents related to maleimide groups per dextran.

24.4 mg L17E-thiol **34** (8.25  $\mu\text{mol}$ ; 1.27 eq. per maleimide group) and 1.0 mg TAMRA-thiol **35** (1.50  $\mu\text{mol}$ ; 0.23 eq. per maleimide group) were dissolved in 2.5 mL degassed 0.1 M MES buffer pH 6.5, 30 % (v/v) MeCN and 10 mg maleimide(6.5)-dextran-*N*-Boc-cadaverine **18** (1.00  $\mu\text{mol}$ ; 1.0 eq.) were added. The reaction mixture was stirred at 30  $^\circ\text{C}$  overnight and subsequently purified using disposable PD 10 desalting columns following the instructions of the supplier. 20 mg (86%) product **37** were obtained as pink powder after freeze-drying. For analysis and quantification  $^1\text{H}$  NMR spectroscopy was performed.

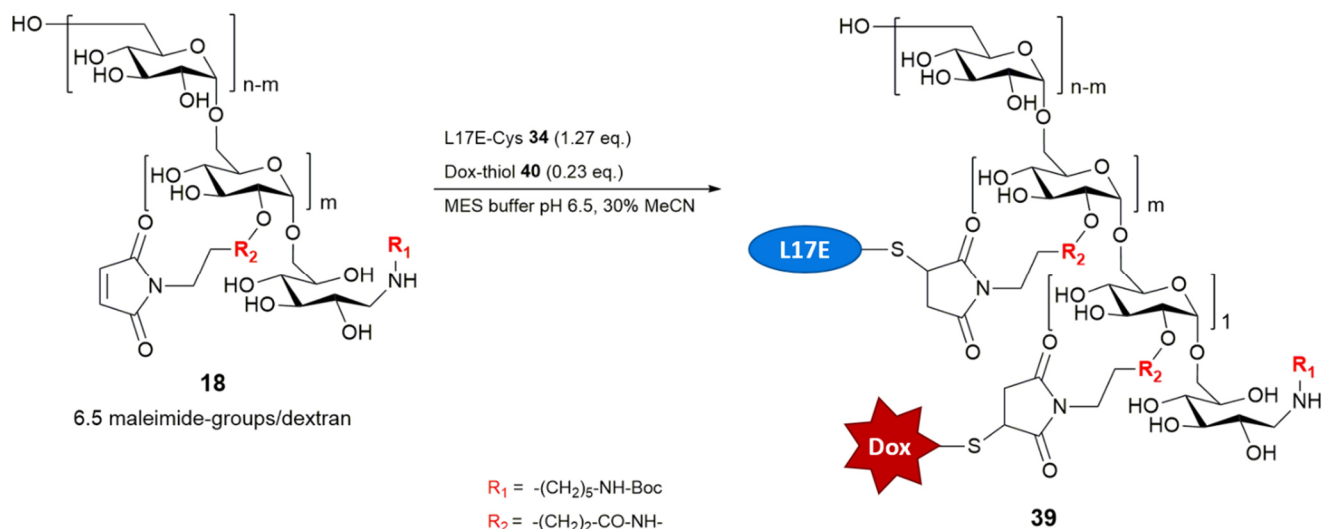
$^1\text{H}$  NMR (300 MHz, deuterium oxide)  $\delta$  = 7.96 – 6.88 (m, 62 aromatic H, His, Trp, Phe + TAMRA), 5.59 – 4.89 (m, 62 H, C(1)H), 4.71 – 0.80 (m, C(2-6)H (glucose units), peptide backbone + aliphatic residues) ppm.



LC (10to100% B): RT = 11.31 min.

MS (ESI) calculated:  $[M-H]^- = 687.70$ ; observed:  $[M-H]^- = 687.08$ .

### 7.14.5 Synthesis of doxorubicin-L17E(5.2)-dextran-*N*-Boc-cadaverine **39**

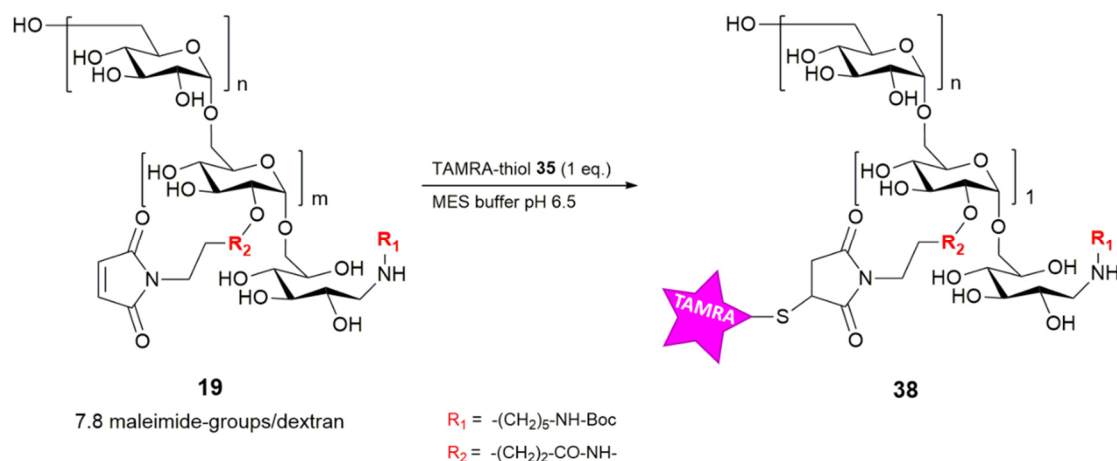


**Scheme 46:** Thiol-maleimide addition of maleimide(6.5)-dextran-*N*-Boc-cadaverine **18** with L17E-Cys **34** and Dox-thiol **40**. Stated equivalents related to maleimide groups per dextran.

24.0 mg L17E-Cys **34** ( $8.25 \mu\text{mol}$ ; 1.27 eq. per maleimide group) and 1.0 mg doxorubicin-thiol **40** ( $1.50 \mu\text{mol}$ ; 0.23 eq. per maleimide group) were dissolved in 2.5 mL degassed 0.1 M MES buffer pH 6.5, 30 % (v/v) MeCN and 10 mg maleimide(6.5)-dextran-*N*-Boc-cadaverine **18** ( $1.00 \mu\text{mol}$ ; 1.0 eq.) were added. The reaction mixture was stirred at 30 °C overnight and subsequently purified using disposable PD 10 desalting columns following the instructions of the supplier. 17 mg (64%) product **49** were obtained as red powder after freeze-drying. For analysis and quantification  $^1\text{H}$  NMR spectroscopy was performed.

$^1\text{H}$  NMR (300 MHz, deuterium oxide)  $\delta = 7.89 - 6.89$  (m, 76 aromatic H, His, Trp, Phe + Dox), 5.45 - 4.94 (m, 62 H, C(1)H), 4.55 - 0.80 (m, C(2-6)H (glucose units), peptide backbone + aliphatic residues) ppm.

### 7.14.6 Synthesis of TAMRA-dextran-*N*-Boc-cadaverine **38**

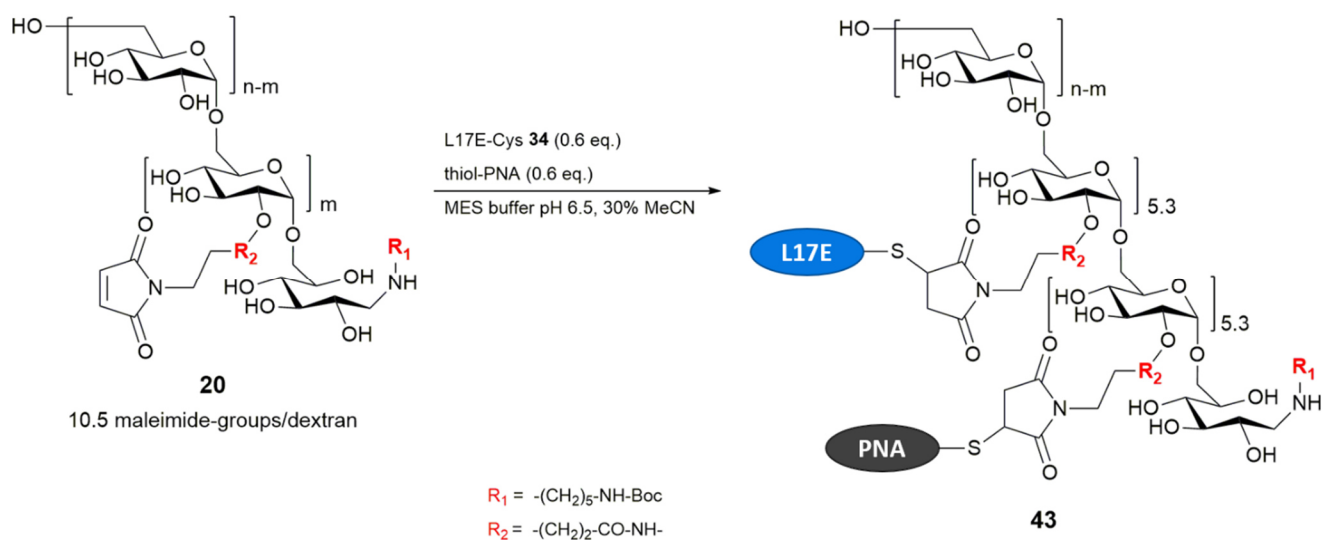


**Scheme 47:** Thiol-maleimide addition of maleimide(7.8)-dextran-*N*-Boc-cadaverine **19** with 1 eq. TAMRA-thiol **35** for generation of TAMRA labeled dextran **38**.

10 mg maleimide(7.8)-dextran-*N*-Boc-cadaverine **19** ( $1\ \mu\text{mol}$ ; 1.0 eq.) were dissolved in 2.5 mL degassed 0.1 M MES buffer pH 6.5 and 0.7 mg TAMRA-thiol **35** ( $1\ \mu\text{mol}$ ; 1.0 eq.) were added. The reaction mixture was stirred at 30 °C overnight and subsequently purified using disposable PD 10 desalting columns following the instructions of the supplier. 8 mg (64%) product **38** were obtained as pink powder after freeze-drying. For analysis  $^1\text{H}$  NMR spectroscopy was performed.

$^1\text{H}$  NMR (300 MHz, deuterium oxide)  $\delta$  = 8.33 – 7.22 (m, aromatic H, TAMRA), 6.96 – 6.87 ((s, 10 H, -CH=CH- (maleimide)), 6.40 – 6.36 (d, 2 H, -CH=CH- (maleimide, hydrolysed)), 6.02 – 5.98 (d, 2 H, -CH=CH- (maleimide, hydrolysed)), 5.43 – 4.91 (m, 62 H, C(1)H), 4.25 – 2.57 (m, C(2-6)H (glucose units + TAMRA-thiol)), 2.57 – 2.45 (m, 21 H, CH<sub>2</sub>-CH<sub>2</sub>-COOH) ppm.

### 7.14.7 Synthesis of L17E-PNA-dextran-*N*-Boc-cadaverine **43**



**Scheme 48:** Thiol-maleimide addition of maleimide(10.5)-dextran-*N*-Boc-cadaverine **20** with thiol-PNA and L17E-Cys **34**. Stated equivalents related to maleimide groups per dextran.

13.3 mg L17E-Cys **34** ( $4.5\ \mu\text{mol}$ ; 0.6 eq. per maleimide group) and 22.7 mg thiol-PNA ( $4.5\ \mu\text{mol}$ ; 0.6 eq. per maleimide group) were dissolved in 2.5 mL degassed 0.1 M MES buffer pH 6.5, 30 % (v/v) MeCN and 10 mg maleimide(10.5)-dextran-*N*-Boc-cadaverine **20** ( $1.00\ \mu\text{mol}$ ; 1.0 eq.) were added. The reaction mixture was stirred at 30 °C overnight and subsequently purified using disposable PD 10 desalting columns following the instructions of the supplier. 28 mg (56%) product **43** were obtained as white powder after freeze-drying.

The employed 18mer thiol-PNA was synthesized by Simon Englert via Fmoc SPPS:

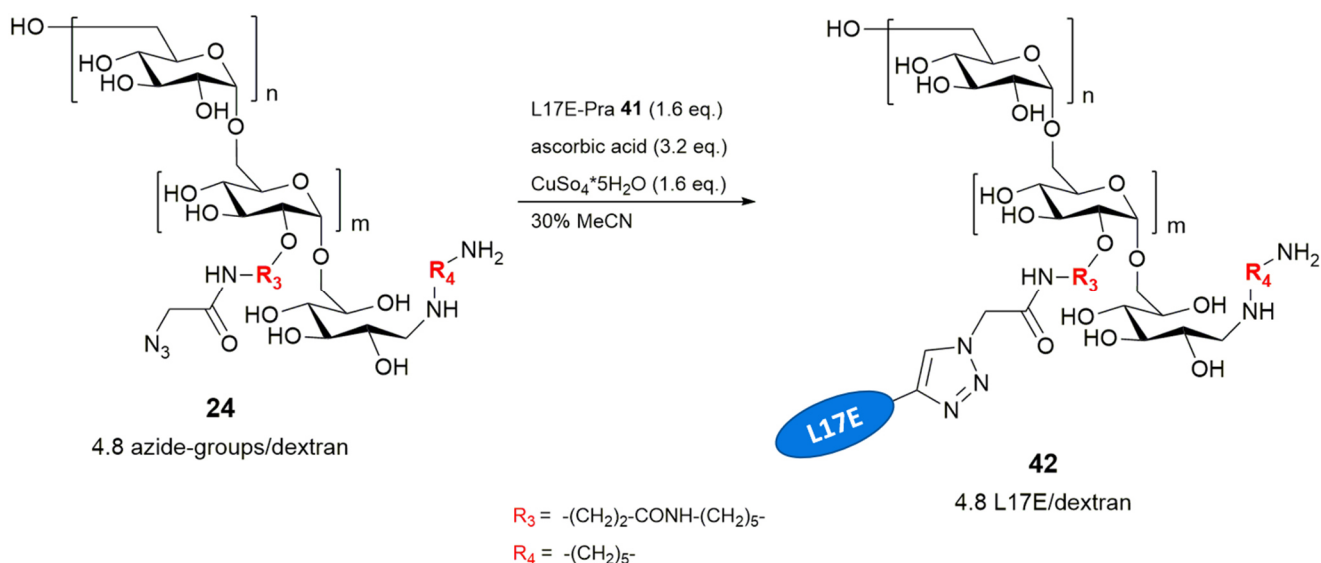
Sequence: 3-mercaptopropionic acid-gct-att-acc-tta-acc-cag-K-NH<sub>2</sub>

Chemical Formula: C<sub>201</sub>H<sub>258</sub>N<sub>102</sub>O<sub>56</sub>S

M<sub>w</sub>: 5030.91 g/mol

## 7.15 CuAAC conjugation of azide-functionalized dextran and alkyne-modified cargo

### 7.15.1 Synthesis of L17E(4.8)-dextran-cadaverine **42**

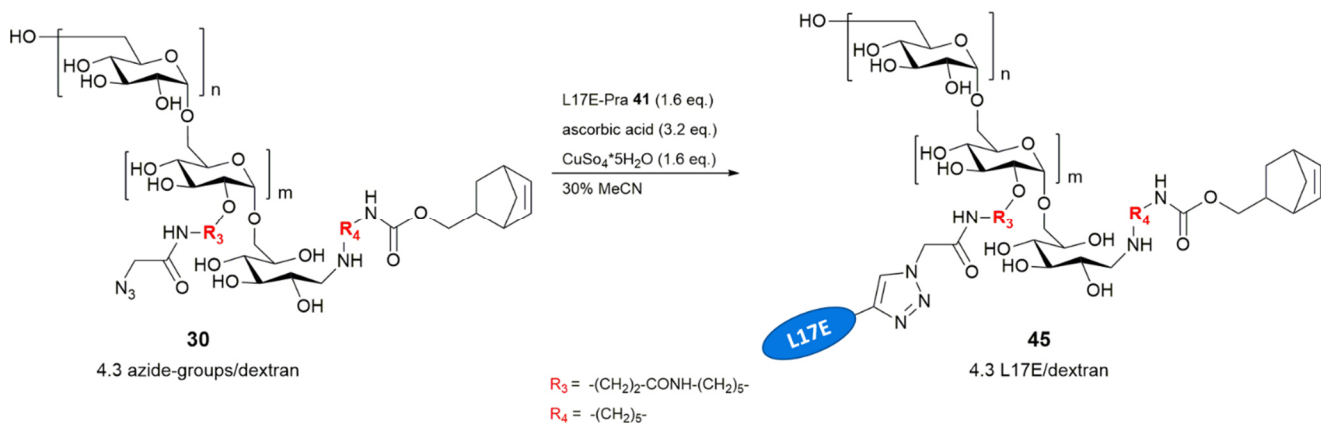


**Scheme 49:** Addressing N<sub>3</sub>(4.8)-dextran-cadaverine **24** with L17E-Pra **41** in Cu(I)-catalyzed azide-alkyne-cycloaddition. Stated equivalents related to azide groups per dextran.

For copper catalyzed azide-alkyne cycloaddition a freshly prepared aqueous solution containing 0.45 mg ascorbic acid (2.5 μmol; 3.2 eq. per N<sub>3</sub>-group) was added to a freshly prepared aqueous solution containing 0.32 mg CuSO<sub>4</sub>·5H<sub>2</sub>O (1.3 μmol; 1.6 eq. per N<sub>3</sub>-group). After color change from blue to green, 3.76 mg L17E-Pra **41** (1.3 μmol; 1.6 eq. per N<sub>3</sub>-group), dissolved in 30% MeCN aq. were added and the mixture was given to an aqueous solution containing 2 mg N<sub>3</sub>(4.8)-dextran-cadaverine **24** (0.18 μmol; 1 eq.) resulting in a total volume of 130 μL. The reaction mixture was agitated at 30 °C for 3 h. The product was isolated using PD MidiTrap™ G-25 and SEC. 2.3 mg (53%) L17E(4.8)-dextran-cadaverine **42** were obtained as white powder after lyophilization and analyzed using SEC as well as UV/Vis (quantitative analysis) and IR spectroscopy (qualitative analysis).

SEC (40% B, isocratic flow): RT = 9.800 min.

### 7.15.2 Synthesis of L17E(4.3)-dextran-norbornene **45**

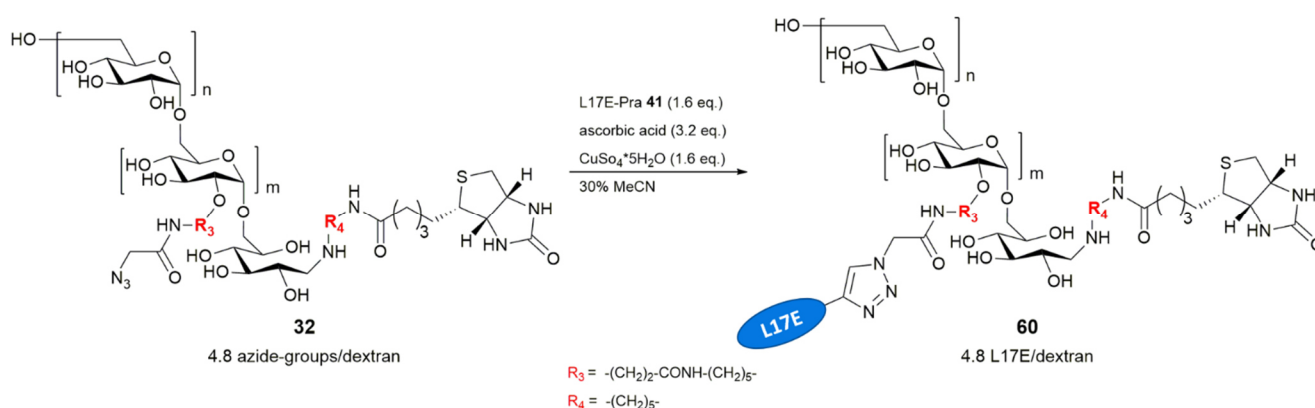


**Scheme 50:** Addressing N<sub>3</sub>(4.3)-dextran-norbornene **30** with L17E-Pra **41** in Cu(I)-catalyzed azide-alkyne-cycloaddition. Stated equivalents related to azide groups per dextran.

For copper catalyzed azide-alkyne cycloaddition a freshly prepared aqueous solution containing 4.9 mg ascorbic acid (28.2  $\mu\text{mol}$ ; 3.2 eq. per  $\text{N}_3$ -group) was added to a freshly prepared aqueous solution containing 3.5 mg  $\text{CuSO}_4 \cdot 5\text{H}_2\text{O}$  (14.1  $\mu\text{mol}$ ; 1.6 eq. per  $\text{N}_3$ -group). After color change from blue to green, 41.6 mg L17E-Pra **41** (14.1  $\mu\text{mol}$ ; 1.6 eq. per  $\text{N}_3$ -group), dissolved in 30% MeCN aq. were added and the mixture was given to an aqueous solution containing 19 mg  $\text{N}_3(4.3)$ -dextran-norbornene **30** (1.6  $\mu\text{mol}$ ; 1 eq.). The reaction mixture was agitated at 30 °C for 3 h. The product was isolated using PD 10 desalting column. 31 mg (70%) L17E(4.3)-dextran-norbornene **45** were obtained as white powder after lyophilization and analyzed via  $^1\text{H}$  NMR and IR spectroscopy.

$^1\text{H}$  NMR (300 MHz, deuterium oxide)  $\delta$  = 8.69 – 7.10 (m, 48 aromatic H, His, Trp, Phe), 5.57 – 4.95 (m, 62 H, C(1)H), 4.61 – 0.80 (m, C(2-6)H (glucose units), peptide backbone + aliphatic residues) ppm.

### 7.15.3 Synthesis of L17E(4.8)-dextran-biotin **60**



**Scheme 51:** Addressing  $\text{N}_3(4.8)$ -dextran-biotin **32** with L17E-Pra **41** in Cu(I)-catalyzed azide-alkyne-cycloaddition. Stated equivalents relating to azide groups per dextran.

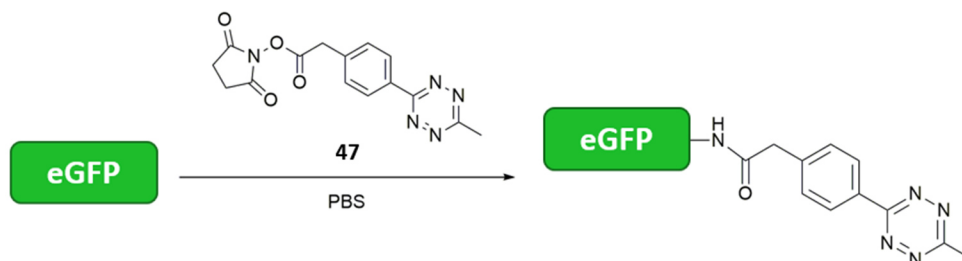
For copper catalyzed azide-alkyne cycloaddition a freshly prepared aqueous solution containing 1.4 mg ascorbic acid (7.8  $\mu\text{mol}$ ; 3.2 eq. per  $\text{N}_3$ -group) was added to a freshly prepared aqueous solution containing 1.0 mg  $\text{CuSO}_4 \cdot 5\text{H}_2\text{O}$  (3.9  $\mu\text{mol}$ ; 1.6 eq. per  $\text{N}_3$ -group). After color change from blue to green, 11.6 mg L17E-Pra **41** (3.9  $\mu\text{mol}$ ; 1.6 eq. per  $\text{N}_3$ -group), dissolved in 30% MeCN aq. were added and the mixture was given to an aqueous solution containing 6.2 mg  $\text{N}_3(4.8)$ -dextran-biotin **32** (0.54  $\mu\text{mol}$ ; 1 eq.). The reaction mixture was agitated at 30 °C for 3 h. The product was isolated using PD 10 desalting column, 11 mg (82%) L17E(4.8)-dextran-biotin **60** were obtained as white powder after lyophilization and analyzed via  $^1\text{H}$  NMR spectroscopy.

$^1\text{H}$  NMR (300 MHz, deuterium oxide)  $\delta$  = 8.39 – 6.81 (m, 47 aromatic H, His, Trp, Phe), 5.46 – 4.95 (m, 62 H, C(1)H), 4.71 – 0.80 (m, C(2-6)H (glucose units), peptide backbone + aliphatic residues) ppm.

## 7.16 General synthesis of L17E-dextran-protein conjugates

### 7.16.1 General modification of eGFP with methyltetrazine functionality

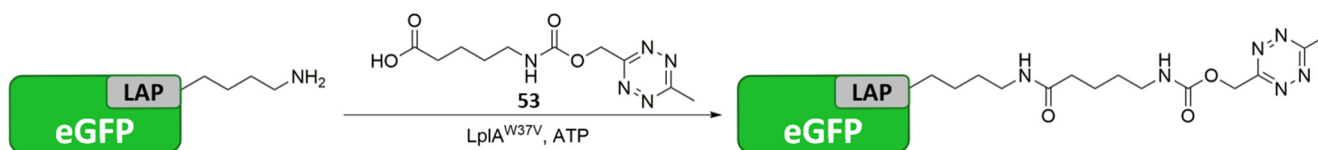
#### 7.16.1.1 eGFP modification with NHS-activated methyltetrazine derivative



**Scheme 52:** eGFP functionalization with methyltetrazine via NHS-activated methyltetrazine derivative **47**.

A reaction solution containing  $200\ \mu\text{M}$  eGFP and  $1000\ \mu\text{M}$  methyltetrazine-phenylacetyl succinimidyl ester **47** in PBS was prepared and incubated at ambient temperature for 1 h. Afterwards, excessive methyltetrazine-phenylacetyl succinimidyl ester was removed by *Amicon Ultra* ( $M_w$  cut-off 3 kDa) centrifugation.

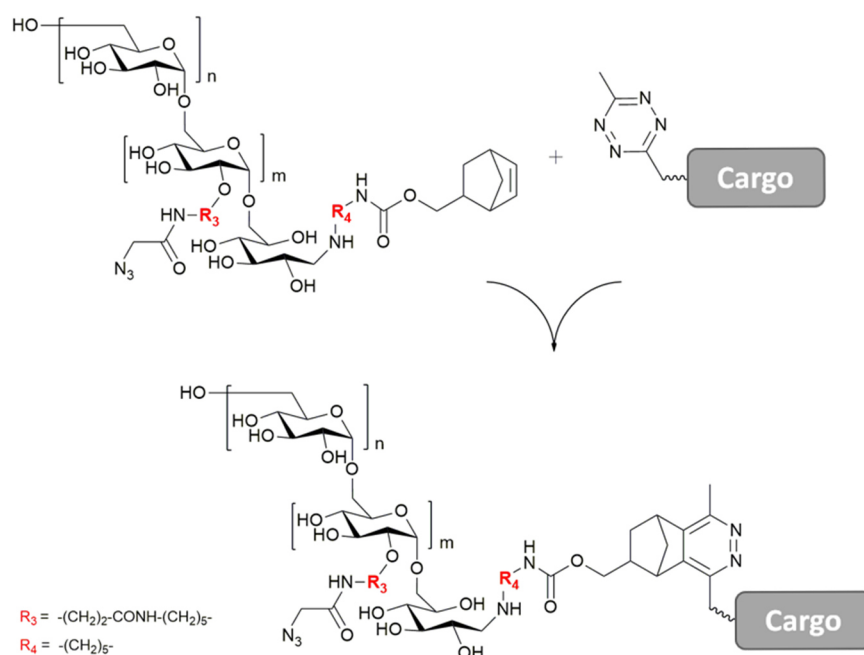
#### 7.16.1.2 Site-specific eGFP modification with methyltetrazine mediated by LplA<sup>W37V</sup>



**Scheme 53:** LplA<sup>W37V</sup> mediated amide bond formation between lysine  $\epsilon$ -amine of the LAP-tagged eGFP and a methyl tetrazine substrate derivative derived of lipoic acid.

According to the general protocol for LplA<sup>W37V</sup> mediated ligation, eGFP-LAP was modified with methyltetrazine substrate. The reaction mixture (composition stated in **Table 9**) was incubated at  $37\ ^\circ\text{C}$  for 1 h and subsequently excessive substrate was removed using *Amicon Ultra* centrifugal filters.

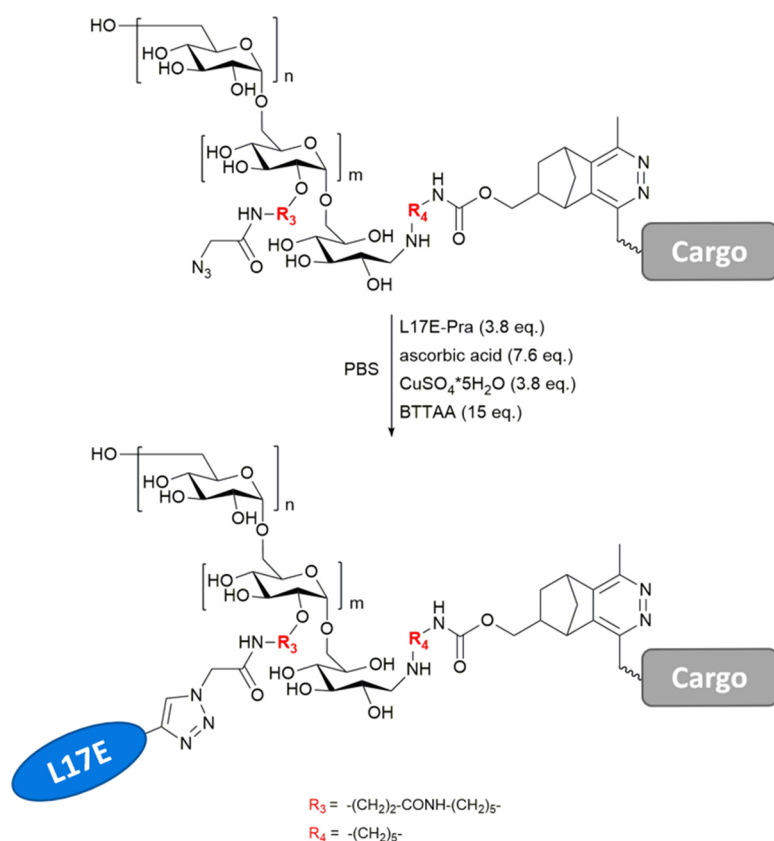
## 7.16.2 General iEDDA dextran-to-protein conjugation



**Scheme 54:** iEDDA dextran-to-protein conjugation of norbornene functionalized N<sub>3</sub>-dextran with MeTet modified cargo protein.

An aqueous solution of N<sub>3</sub>-dextran-norbornene (10 mM; 20 eq.) was added to methyltetrazine modified cargo protein (1 eq.) in PBS and the reaction mixture was incubated at 4° C overnight. For removal of excessive N<sub>3</sub>-dextran-norbornene IMAC purification was performed utilizing the His-tag of the cargo protein. In a syringe equipped with a frit, a gravity flow column using *His-Pur<sup>TM</sup> Ni-NTA* resin was packed. After equilibration with IMAC A buffer, the product was diluted with equal amount IMAC A buffer and bound to the resin at ambient temperature for 30 min. The loaded resin was thoroughly washed with IMAC A buffer and subsequently the N<sub>3</sub>-dextran-protein conjugate was eluted with 3 × 250 μL IMAC B buffer. The protein samples were combined and rebuffered to PBS. The product was analyzed with SDS-PAGE.

### 7.16.3 General biocompatible CuAAC



**Scheme 55:** Addressing N<sub>3</sub>-dextran-protein with L17E-Pra **41** in biocompatible Cu(I)-catalyzed azide-alkyne-cycloaddition. Stated equivalents related to number of azide groups per dextran.

For biocompatible copper(I) catalyzed azide-alkyne cycloaddition a freshly prepared aqueous solution of CuSO<sub>4</sub>·5H<sub>2</sub>O (3.8 eq. per N<sub>3</sub>-group) was added to a freshly prepared aqueous solution of 2-(4-((bis((1-(*tert*-butyl)-1H-1,2,3-triazol-4-yl)methyl)amino)methyl)-1H-1,2,3-triazol-1-yl)acetic acid (BTAA) (15 eq. per N<sub>3</sub>-group), whereupon the light blue solution turned dark blue. A freshly prepared aqueous solution of ascorbic acid (7.4 eq. per N<sub>3</sub>-group) was added, and the dark blue solution turned colorless. Aqueous solution of L17E-Pra **41** (3.8 eq. per N<sub>3</sub>-group) as well as the respective amount 10xPBS were added and the mixture given to N<sub>3</sub>-dextran-protein (1 eq.) in PBS. After 3 h incubation at ambient temperature the L17E-dextran-protein cycloaddition product was isolated via *Microcon Ultracel-10* (M<sub>w</sub> cutoff 10 kDa) centrifugation

### 7.16.4 Alternative strategy: Dextran-to-protein conjugation applying pre-assembled L17E-dextran-norbornene **45**

#### 7.16.4.1 Synthesis of eGFP-MeTet **69**

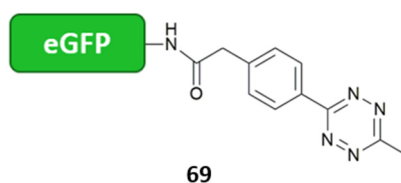
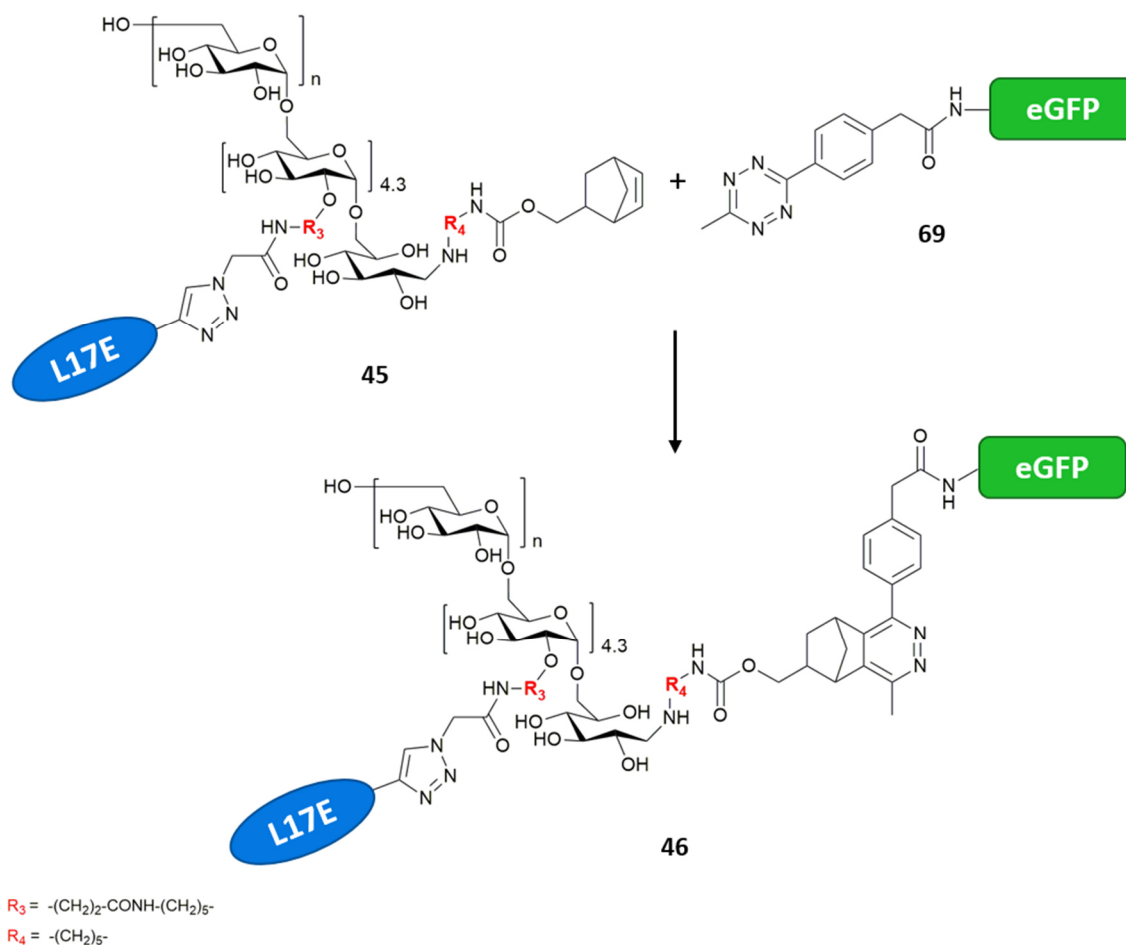


**Figure 79:** Structure of MeTet modified eGFP **69**.

According to the general procedure for eGFP modification with NHS-activated methyltetrazine derivative, 1.2  $\mu\text{L}$  of a methyltetrazine-phenylacetyl succinimidyl ester **47** stock solution in DMSO (75 mM) were added to 50.8  $\mu\text{L}$  eGFP stock solution in PBS (354  $\mu\text{M}$ ) and diluted with PBS, resulting in final concentrations of 200  $\mu\text{M}$  eGFP (0.0179  $\mu\text{mol}$ ; 1 eq.) and 1000  $\mu\text{M}$  methyltetrazine-phenylacetyl succinimidyl ester **47** (0.090  $\mu\text{mol}$ ; 5 eq.). The mixture was incubated at ambient temperature for 1 h. Excessive methyltetrazine-phenylacetyl succinimidyl ester was removed by *Amicon Ultra* ( $M_w$  cut-off 3 kDa) centrifugation. For following iEDDA conjugation no loss of protein and 100% turnover was assumed.

#### 7.16.4.2 Alternative strategy: Synthesis of L17E(4.3)-dextran-eGFP **46**



**Scheme 56:** Alternative iEDDA dextran-to-protein conjugation applying pre-assembled L17E(4.3)-dextran-norbornene **45** and eGFP-MeTet **69**.

95.5  $\mu\text{L}$  aqueous stock solution of L17E(4.3)-dextran-norbornene **45** (2.81 mM; 0.268  $\mu\text{mol}$ ; 15 eq.) were added to 40  $\mu\text{L}$  eGFP-MeTet **69** in PBS (0.0179  $\mu\text{mol}$ ; 1 eq.) and the reaction mixture was incubated at 4° C overnight. For removal of excessive L17E(4.3)-dextran-norbornene **45** IMAC purification was performed as described in the general procedure for iEDDA dextran-to-protein conjugation. The L17E(4.3)-dextran-eGFP dextran-to-protein conjugation product **46** was analyzed with SDS-PAGE.

## 7.17 Synthesis of L17E(4.3)-dextran-eGFP 44

### 7.17.1 Synthesis of eGFP-MeTet 48

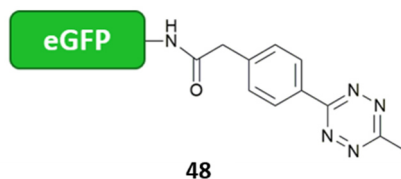


Figure 80: Structure of MeTet modified eGFP 48.

According to the general procedure for eGFP modification with NHS-activated methyltetrazine derivative, 1.2  $\mu\text{L}$  of a methyltetrazine-phenylacetyl succinimidyl ester 47 stock solution in DMSO (75 mM) were added to 50.8  $\mu\text{L}$  eGFP stock solution in PBS (354  $\mu\text{M}$ ) and diluted with PBS, resulting in final concentrations of 200  $\mu\text{M}$  eGFP (0.0179  $\mu\text{mol}$ ; 1 eq.) and 1000  $\mu\text{M}$  methyltetrazine-phenylacetyl succinimidyl ester 47 (0.090  $\mu\text{mol}$ ; 5 eq.). The mixture was incubated at ambient temperature for 1 h. Excessive methyltetrazine-phenylacetyl succinimidyl ester was removed by *Amicon Ultra* ( $M_w$  cut-off 3 kDa) centrifugation. For following iEDDA dextran-to-protein conjugation, no loss of protein and 100% turnover were assumed.

### 7.17.2 Synthesis of N<sub>3</sub>(4.3)-dextran-eGFP 49

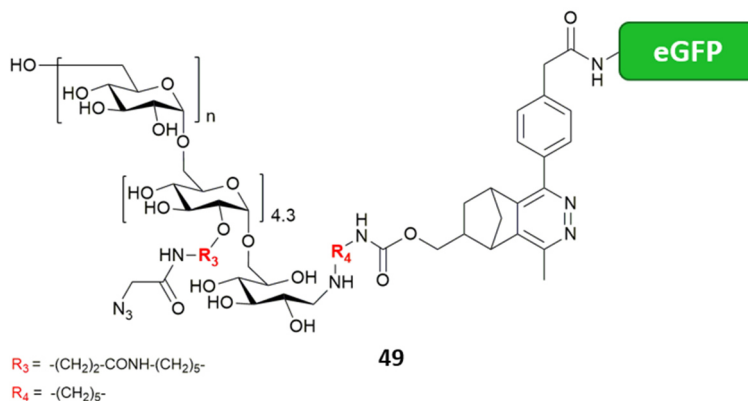
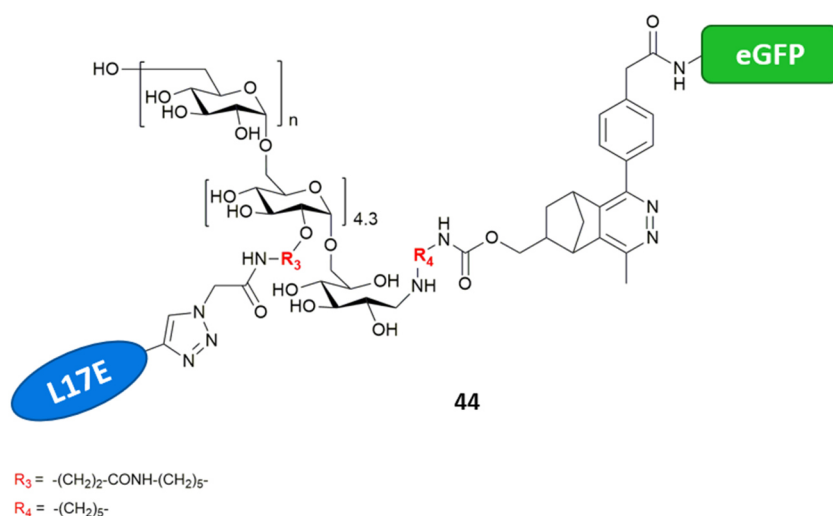


Figure 81: Structure of dextran-to-protein conjugate N<sub>3</sub>(4.3)-dextran-eGFP 49.

According to the general procedure for iEDDA dextran-to-protein conjugation, 35.8  $\mu\text{L}$  aqueous stock solution of N<sub>3</sub>(4.3)-dextran-norbornene 29 (10 mM; 0.3574  $\mu\text{mol}$ ; 20 eq.) were added to 40  $\mu\text{L}$  eGFP-MeTet 48 in PBS (0.0179  $\mu\text{mol}$ ; 1 eq.) and the reaction mixture was incubated at 4° C overnight. For removal of excessive N<sub>3</sub>(4.3)-dextran-norbornene 29, IMAC purification was performed as described in the general procedure. The dextran-to-protein conjugation product 49 was analyzed with SDS-PAGE. For following CuAAC conjugation, no loss of protein and 100% turnover were assumed.

### 7.17.3 Synthesis of L17E(4.3)-dextran-eGFP 44



**Figure 82:** Structure of final L17E(4.3)-dextran-eGFP conjugate **44** comprising dextran, decorated with on average 4.3 L17E at the glucose repeating units, and covalently bound eGFP at the polysaccharide reducing end.

According to the general procedure for biocompatibilized CuAAC, 2.4  $\mu\text{L}$  of a freshly prepared aqueous solution containing 0.09 mg  $\text{CuSO}_4 \cdot 5\text{H}_2\text{O}$  (0.36  $\mu\text{mol}$ ; 3.8 eq. per  $\text{N}_3$ -group) were added to 15.3  $\mu\text{L}$  of a freshly prepared aqueous solution containing 0.61 mg BTAA (1.42  $\mu\text{mol}$ ; 15 eq. per  $\text{N}_3$ -group), whereupon the light blue solution turned dark blue. 3.2  $\mu\text{L}$  of a freshly prepared aqueous solution containing 0.12 mg ascorbic acid (0.70  $\mu\text{mol}$ ; 7.4 eq. per  $\text{N}_3$ -group) were added and the dark blue solution turned colorless. 187  $\mu\text{L}$  aqueous solution containing 1.06 mg L17E-Pra **41** (0.36  $\mu\text{mol}$ ; 3.8 eq. per  $\text{N}_3$ -group) as well as 20  $\mu\text{L}$  10 $\times$  PBS were added and the mixture given to  $\text{N}_3$ (4.3)-dextran-eGFP **49** (0.0179  $\mu\text{mol}$ ; 1 eq.) in PBS. After 3 h incubation at ambient temperature, the L17E(4.3)-dextran-eGFP **44** product was isolated using *Microcon Ultracel-10* ( $M_w$  cutoff 10 kDa) centrifugation, yielding 69  $\mu\text{L}$  product solution. Product concentration of 37.1  $\mu\text{M}$  was determined via absorbance at 488 nm and the conjugate was analysed via SDS-PAGE.

### 7.18 Synthesis of L17E(4.8)-dextran-eGFP 52

#### 7.18.1 Synthesis of eGFP-MeTet 50

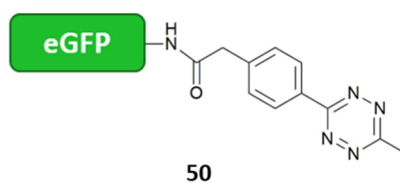


**Figure 83:** Structure of MeTet modified eGFP **50**.

According to the general procedure for eGFP modification with NHS-activated methyltetrazine derivative, 8.6  $\mu\text{L}$  of a methyltetrazine-phenylacetyl succinimidyl ester **47** stock solution in DMSO (75 mM) were added to 367.2  $\mu\text{L}$  eGFP stock solution in PBS (354  $\mu\text{M}$ ) and diluted with PBS resulting in final concentrations of 200  $\mu\text{M}$  eGFP (0.129  $\mu\text{mol}$ ; 1 eq.) and 1000  $\mu\text{M}$  methyltetrazine-phenylacetyl succinimidyl ester **47** (0.645  $\mu\text{mol}$ ; 5 eq.). The mixture was incubated at ambient temperature for 1 h. Excessive methyltetrazine-phenylacetyl succinimidyl ester was removed by *Amicon Ultra* ( $M_w$  cut-off

3 kDa) centrifugation. For following iEDDA dextran-to-protein conjugation, no loss of protein and 100% turnover were assumed.

### 7.18.2 Synthesis of N<sub>3</sub>(4.8)-dextran-eGFP 51

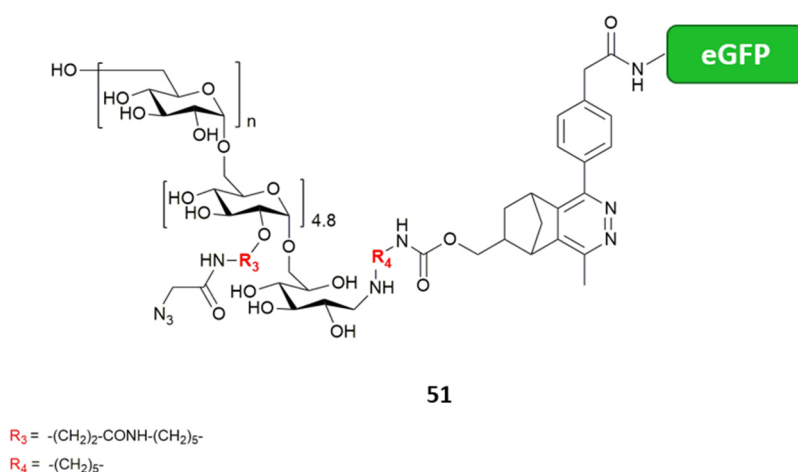


**Figure 84:** Structure of dextran-to-protein conjugate N<sub>3</sub>(4.8)-dextran-eGFP 51.

According to the general procedure for iEDDA dextran-to-protein conjugation, 105.4  $\mu\text{L}$  aqueous stock solution of N<sub>3</sub>(4.8)-dextran-norbornene **31** (10 mM; 1.05  $\mu\text{mol}$ ; 8.2 eq.) were added to 240  $\mu\text{L}$  eGFP-MeTet **50** in PBS (0.129  $\mu\text{mol}$ ; 1 eq.) and the reaction mixture was incubated at 4° C overnight. For removal of excessive N<sub>3</sub>(4.8)-dextran-norbornene **31**, IMAC purification was performed as described in the general procedure. The dextran-to-protein conjugation product **51** was analyzed with SDS-PAGE. For following CuAAC conjugation, no loss of protein and 100% turnover were assumed.

### 7.18.3 Synthesis of L17E(4.8)-dextran-eGFP 52

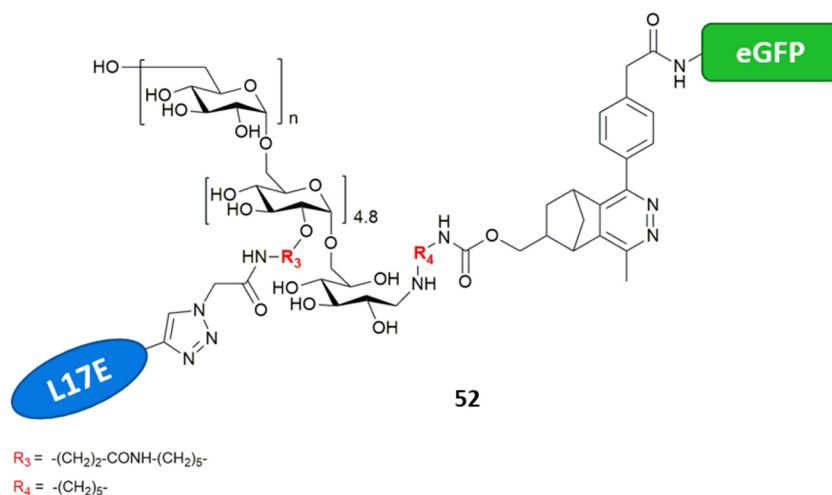


**Figure 85:** Structure of final L17E(4.8)-dextran-eGFP conjugate **52** comprising dextran, decorated with on average 4.8 L17E at the glucose repeating units, and covalently bound eGFP at the polysaccharide reducing end.

According to the general procedure for biocompatibilized CuAAC, 2.42  $\mu\text{L}$  of a freshly prepared aqueous solution containing 0.09 mg CuSO<sub>4</sub>·5H<sub>2</sub>O (0.368  $\mu\text{mol}$ ; 3.8 eq. per N<sub>3</sub>-group) were added to 15.6  $\mu\text{L}$  of a freshly prepared aqueous solution containing 0.63 mg BTAA (1.450  $\mu\text{mol}$ ; 15 eq. per N<sub>3</sub>-group), whereupon the light blue solution turned dark blue. 3.24  $\mu\text{L}$  of a freshly prepared aqueous solution containing 0.13 mg ascorbic acid (0.717  $\mu\text{mol}$ ; 7.4 eq. per N<sub>3</sub>-group) were added and the dark blue

solution turned colorless. 191  $\mu\text{L}$  aqueous solution containing 1.09 mg L17E-Pra **41** ( $0.368 \mu\text{mol}$ ; 3.8 eq. per  $\text{N}_3$ -group) as well as 21  $\mu\text{L}$  10 $\times$ PBS were added and the mixture given to  $\text{N}_3(4.8)$ -dextran-eGFP **51** ( $0.022 \mu\text{mol}$ ; 1 eq.) in PBS. After 3 h incubation at ambient temperature, the L17E(4.8)-dextran-eGFP **52** conjugation product was isolated using *Microcon Ultracel-10* ( $M_w$  cutoff 10 kDa) centrifugation, yielding 75  $\mu\text{L}$  product solution. Product concentration of  $33.1 \mu\text{M}$  was determined via absorbance at 488 nm and the conjugate was analysed via SDS-PAGE.

## 7.19 Synthesis of L17E(4.8)-dextran-eGFP **57** applying LplA<sup>W37V</sup>-mediated site-specific dextran-to-protein conjugation

### 7.19.1 LplA<sup>W37V</sup>-mediated synthesis of eGFP-MeTet **54**, **55**

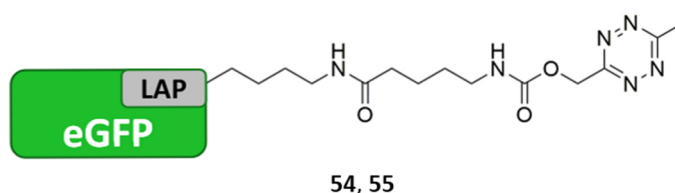


**Figure 86:** Structure of methyltetrazine modified eGFP **54**, **55**, yielded upon site-specific introduction of methyltetrazine substrate mediated by LplA<sup>W37V</sup>.

According to the general procedure for LplA<sup>W37V</sup>-mediated ligation, eGFP bearing LAP-tag was modified with methyltetrazine functionality. A reaction mixture was prepared according to the composition stated in

**Table 11**, containing  $0.018 \mu\text{mol}$  LAP-tagged eGFP. The solution was incubated at  $37^\circ\text{C}$  for 1 h and subsequently excessive substrate was removed using *Amicon Ultra* centrifugal filters. The ligation product eGFP-MeTet **54** was analyzed by HIC.

The ligation was repeated, under same conditions and composition, applying, LplA<sup>W37V</sup> (batch 1), which was yielded upon production in *E. coli* and IMAC purification. The ligation product eGFP-MeTet **55** was analyzed by HIC.

**Table 11:** Components and concentrations for LplA<sup>W37V</sup>-mediated ligation.

Component	Final concentration
POI-LAP	$20 \mu\text{M}$
LplA <sup>W37V</sup>	$2 \mu\text{M}$
Substrate	$500 \mu\text{M}$
$\text{Mg}(\text{COO}^-)_2$	5 mM
Sodium phosphate, pH 7.0	25 mM
ATP	5 mM
ddH <sub>2</sub> O	Filled up to final volume of $900 \mu\text{L}$

### 7.19.2 LplA<sup>W37V</sup>-mediated synthesis of eGFP-MeTet 56

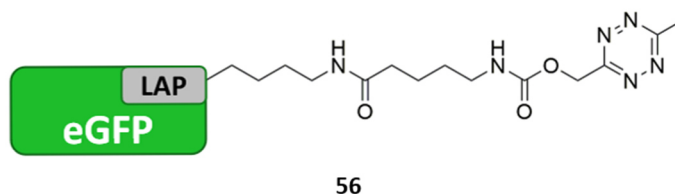


**Figure 87:** Structure of methyltetrazine modified eGFP **56**, yielded upon site-specific introduction of methyltetrazine substrate mediated by LplA<sup>W37V</sup>.

According to the general procedure for LplA<sup>W37V</sup>-mediated ligation, eGFP bearing LAP-tag was modified with methyltetrazine functionality, applying LplA<sup>W37V</sup> (batch 2), which was yielded upon production in *E. coli* and improved IMAC purification. A reaction mixture was prepared in a composition stated in **Table 12**, containing 0.018  $\mu\text{mol}$  LAP-tagged eGFP and reduced substrate concentration. The reaction mixture was incubated at 37 °C for 1 h and subsequently excessive substrate was removed using *Amicon Ultra* centrifugal filters.

**Table 12:** Components and concentrations for LplA<sup>W37V</sup>-mediated ligation.

Component	Final concentration
POI-LAP	20 $\mu\text{M}$
LplA <sup>W37V</sup>	2 $\mu\text{M}$
Substrate	300 $\mu\text{M}$
Mg(COO <sup>-</sup> ) <sub>2</sub>	5 mM
Sodium phosphate, pH 7.0	25 mM
ATP	5 mM
ddH <sub>2</sub> O	Filled up to final volume of 900 $\mu\text{L}$

### 7.19.3 Synthesis of N<sub>3</sub>(4.8)-dextran-eGFP 58

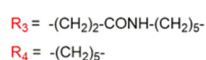
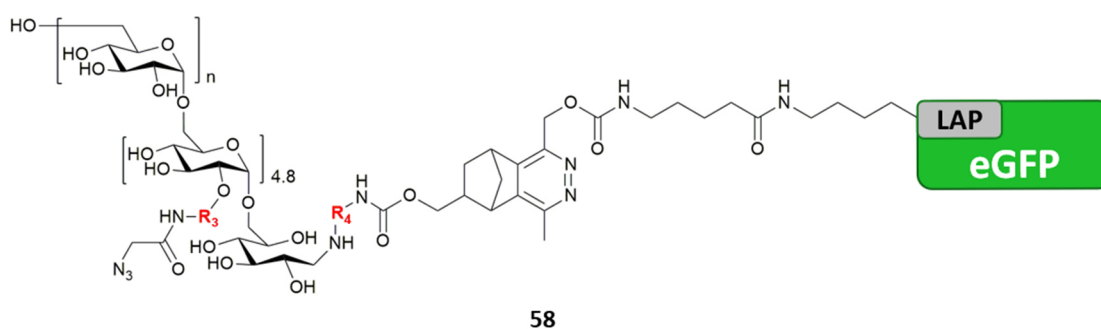


**Figure 88:** Structure of protein-to-dextran conjugate N<sub>3</sub>(4.8)-dextran-eGFP **58**.

According to the general procedure for iEDDA dextran-to-protein conjugation, 26.9  $\mu\text{L}$  aqueous stock solution of N<sub>3</sub>(4.8)-dextran-norbornene **31** (10 mM; 0.269  $\mu\text{mol}$ ; 15 eq.) were added to 40  $\mu\text{L}$  eGFP-MeTet **56** in PBS (0.018  $\mu\text{mol}$ ; 1 eq.) and the reaction mixture was incubated at 4 °C overnight. For removal of excessive N<sub>3</sub>(4.8)-dextran-norbornene **31**, IMAC purification was performed as described in the general procedure. The dextran-to-protein conjugation product **58** was analyzed with SDS-PAGE

(data not shown). For following CuAAC conjugation, no loss of protein and 100% turnover were assumed.

#### 7.19.4 Synthesis of L17E(4.8)-dextran-eGFP 57

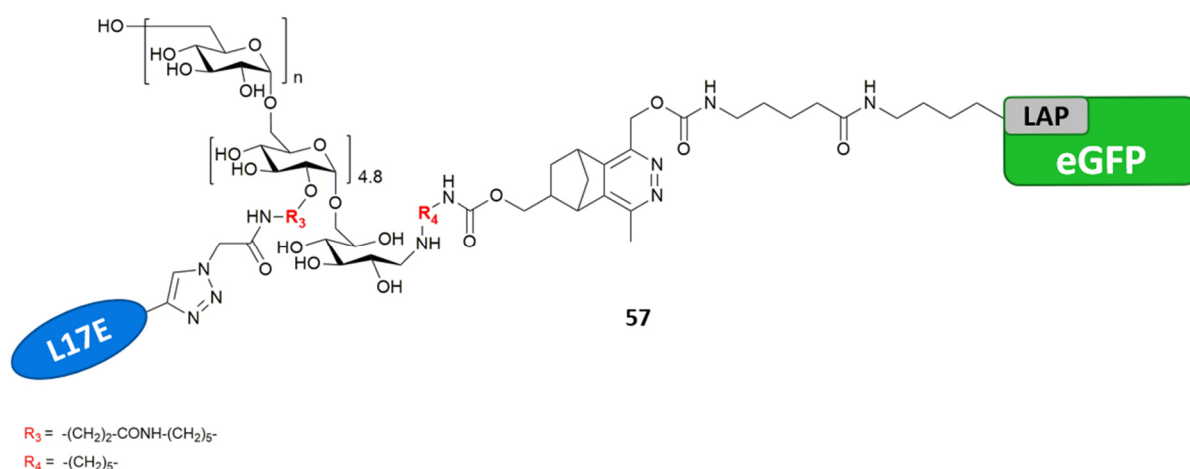


**Figure 89:** Structure of final L17E(4.8)-dextran-eGFP conjugate **57** comprising dextran, decorated with on average 4.8 L17E at the glucose repeating units, and covalently bound eGFP at the polysaccharide reducing end.

According to the general procedure for biocompatibilized CuAAC, 0.55  $\mu\text{L}$  of a freshly prepared aqueous solution containing 0.02 mg  $\text{CuSO}_4 \cdot 5\text{H}_2\text{O}$  (0.087  $\mu\text{mol}$ ; 3.8 eq. per  $\text{N}_3$ -group) were added to 3.72  $\mu\text{L}$  of a freshly prepared aqueous solution containing 0.15 mg BTAA (0.346  $\mu\text{mol}$ ; 15 eq. per  $\text{N}_3$ -group), whereupon the light blue solution turned dark blue. 0.75  $\mu\text{L}$  of a freshly prepared aqueous solution containing 0.03 mg ascorbic acid (0.171  $\mu\text{mol}$ ; 7.4 eq. per  $\text{N}_3$ -group) were added and the dark blue solution turned colorless. 45.5  $\mu\text{L}$  aqueous solution containing 0.26 mg L17E-Pra **41** (0.087  $\mu\text{mol}$ ; 3.8 eq. per  $\text{N}_3$ -group) as well as 5  $\mu\text{L}$  10  $\times$  PBS were added and the mixture given to  $\text{N}_3(4.8)$ -dextran-eGFP **58** (0.018  $\mu\text{mol}$ ; 1 eq.) in PBS. After 3 h incubation at ambient temperature the L17E(4.8)-dextran-eGFP **57** conjugation product was isolated using *Microcon Ultracel-10* ( $M_w$  cutoff 10 kDa) centrifugation, yielding 45  $\mu\text{L}$  product solution. Product concentration of 41  $\mu\text{M}$  was determined via absorbance at 488 nm.

---

## 8 Supporting information

---

### 8.1 Supplementary microscope images

#### 8.1.1 TAMRA-dextran-*N*-Boc-cadaverine **38**

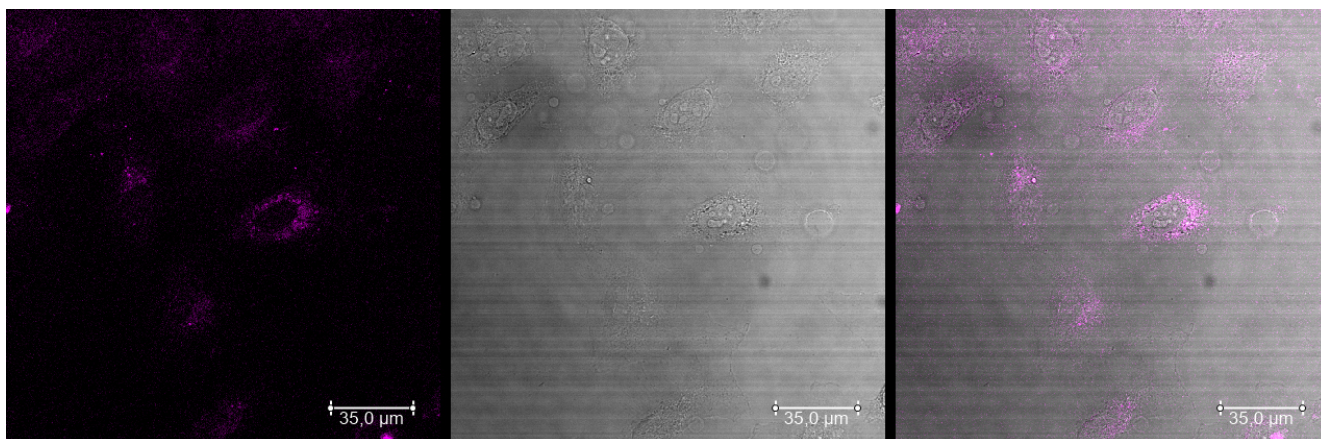


**Figure 90:** CLSM images (20×) of HeLa cells treated with 25 µM TAMRA-labeled dextran **38** (10 kDa). TAMRA-fluorescence channel (left), brightfield (middle) and merge (right).

#### 8.1.2 TAMRA-dextran-*N*-Boc-cadaverine **38** with L17E **12** coincubation

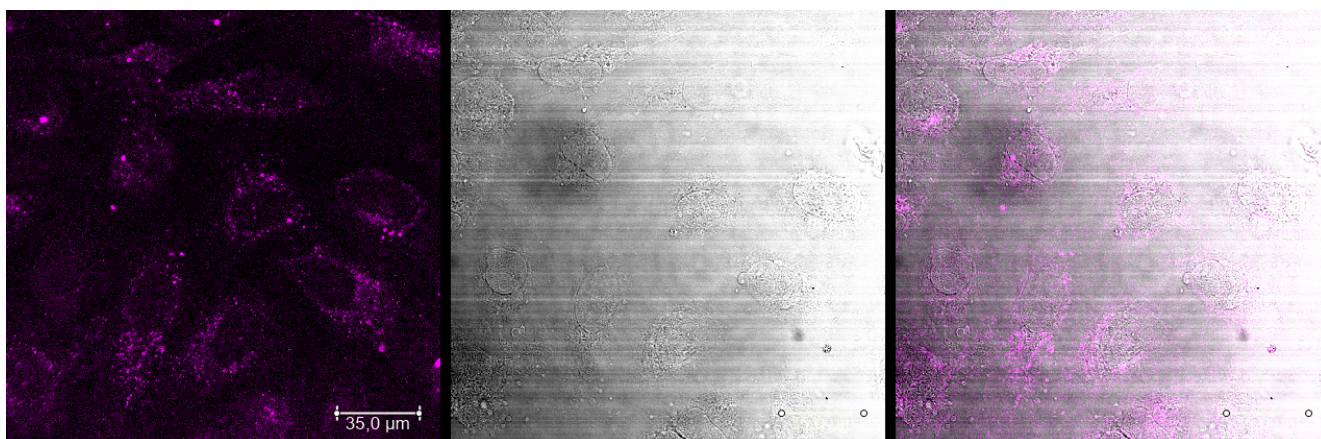


**Figure 91:** CLSM images (20×) of HeLa cells treated with 25 µM TAMRA-labeled dextran **38** (10 kDa) and coincubated with solitary L17E **12** 40 µM. TAMRA-fluorescence channel (left), brightfield (middle) and merge (right).

### 8.1.3 TAMRA-L17E(3.8)-dextran-*N*-Boc-cadaverine 37



**Figure 92:** CLSM images (20×) of HeLa cells treated with 3.13 µM construct **37**, TAMRA-labeled dextran (10 kDa) bearing 3.8 covalently conjugated L17E units per dextran on average. TAMRA-fluorescence channel (left), brightfield (middle) and merge (right).

### 8.1.4 TAMRA- aurein1.2(4.5)-dextran-*N*-Boc-cadaverine 36

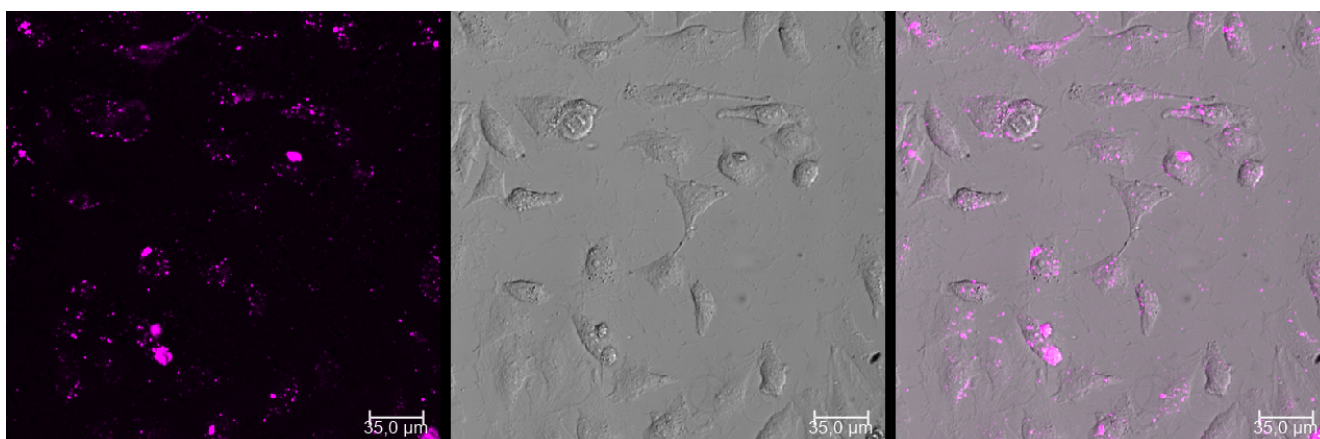


**Figure 93:** CLSM images (20×) of HeLa cells treated with 25 µM construct **36**, TAMRA-labeled dextran (10 kDa) bearing 4.5 covalently conjugated aurein1.2 units per dextran on average. TAMRA-fluorescence channel (left), brightfield (middle) and merge (right).

### 8.1.5 Dox-L17E(5.2)-dextran-N-Boc-cadaverine 39

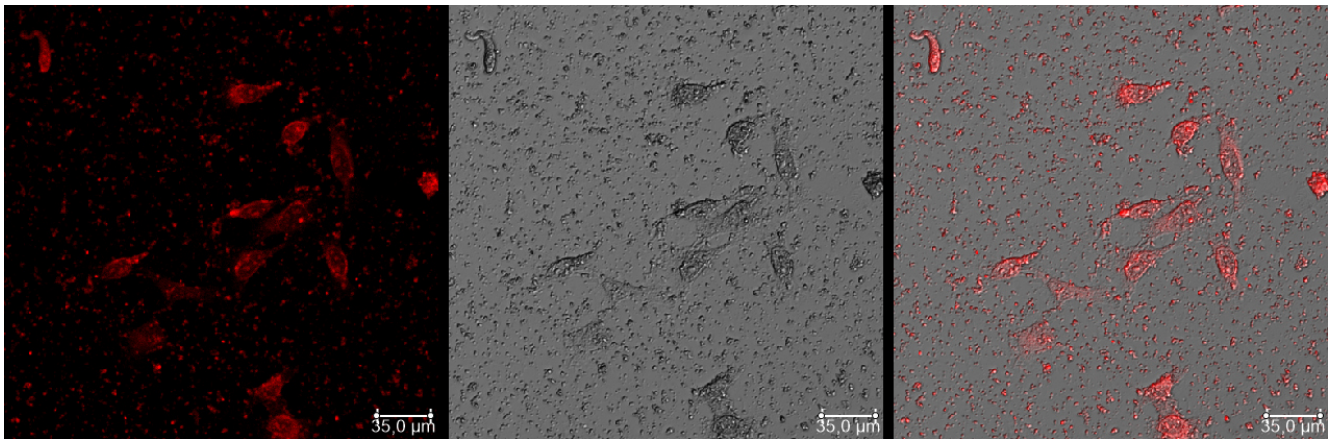


**Figure 94:** CLSM images (20 $\times$ ) of HeLa cells treated with 12.5  $\mu$ M construct **39**, doxorubicin-labeled dextran (10 kDa) bearing 5.2 covalently conjugated L17E units per dextran on average. Doxorubicin-fluorescence channel (left), brightfield (middle) and merge (right).

### 8.1.6 L17E(4.3)-dextran-eGFP X

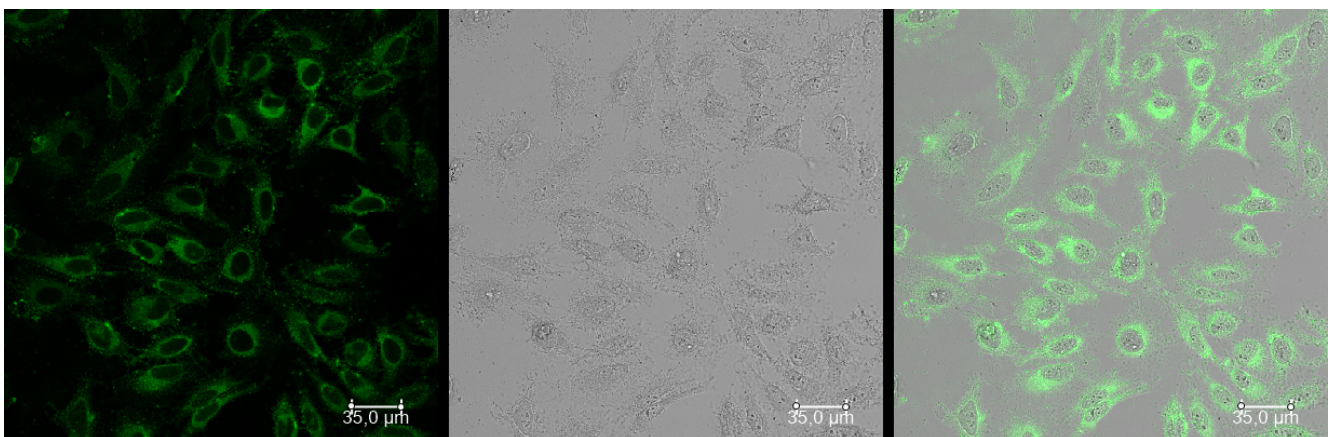


**Figure 95:** CLSM images (20 $\times$ ) of HeLa cells treated with 4  $\mu$ M L17E(4.3)-dextran-eGFP **44**. eGFP fluorescence channel (left), bright field (middle) and merge (right).

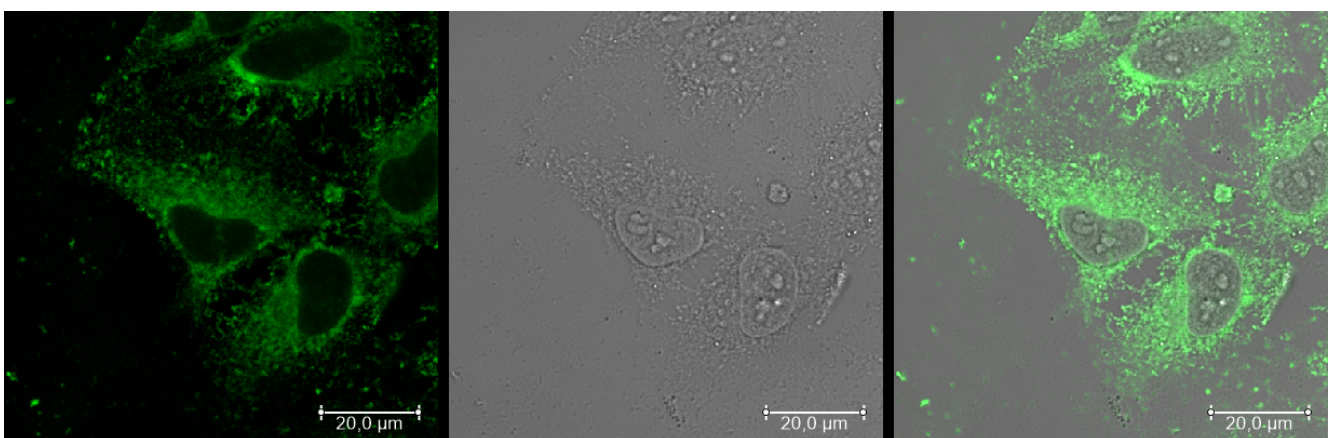


**Figure 96:** CLSM images (63 $\times$ ) of HeLa cells treated with 4  $\mu$ M L17E(4.3)-dextran-eGFP **44**. eGFP fluorescence channel (left), bright field (middle) and merge (right).

## 8.2 Analytical data of Ac-Orn(N<sub>3</sub>)-VC-aurein1.2-Lys(maleimide)-NH<sub>2</sub> 3

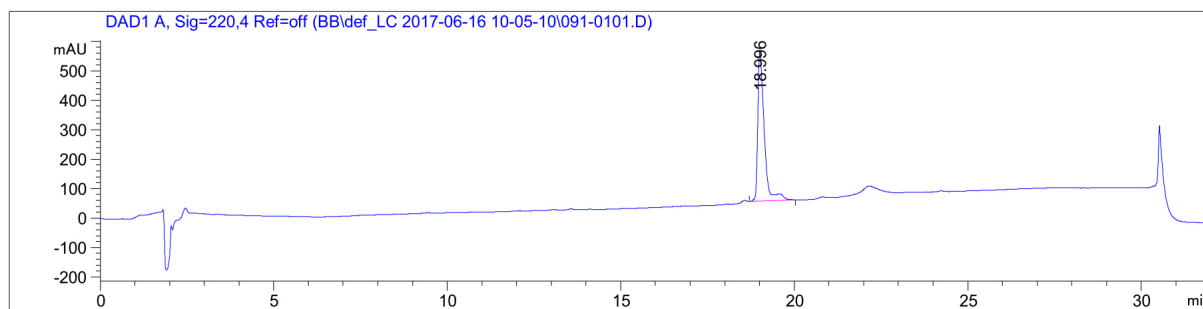


Figure 97: Analytical RP-HPLC chromatogram of Ac-Orn(N<sub>3</sub>)-VC-aurein1.2-Lys(maleimide)-NH<sub>2</sub> 3, 30 to 100% B (gradient 20 min), 220 nm, RT = 18.996 min.

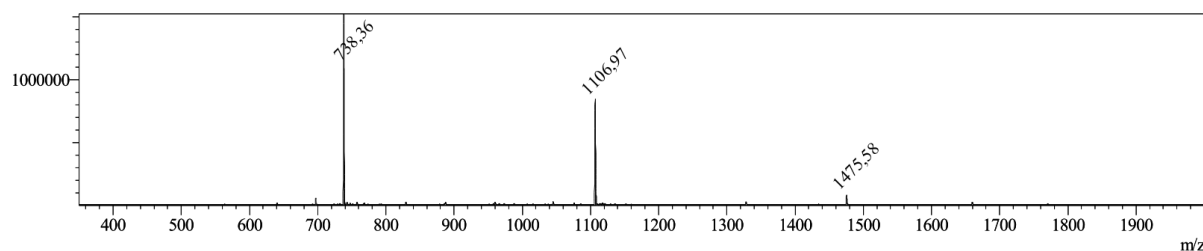


Figure 98: MS (ESI) of Ac-Orn(N<sub>3</sub>)-VC-aurein1.2-Lys(maleimide)-NH<sub>2</sub> 3, calculated:  $[M+H]^+ = 2211.60$ ;  $[M+2H]^{2+} = 1106.80$ ;  $[M+3H]^{3+} = 738.20$ ; observed:  $[M+2H]^{2+} = 1106.97$ ;  $[M+3H]^{3+} = 738.36$ .

## 8.3 Analytical data of Ac-Orn(N<sub>3</sub>)-VC-GS-Lys(maleimide)-NH<sub>2</sub> 6

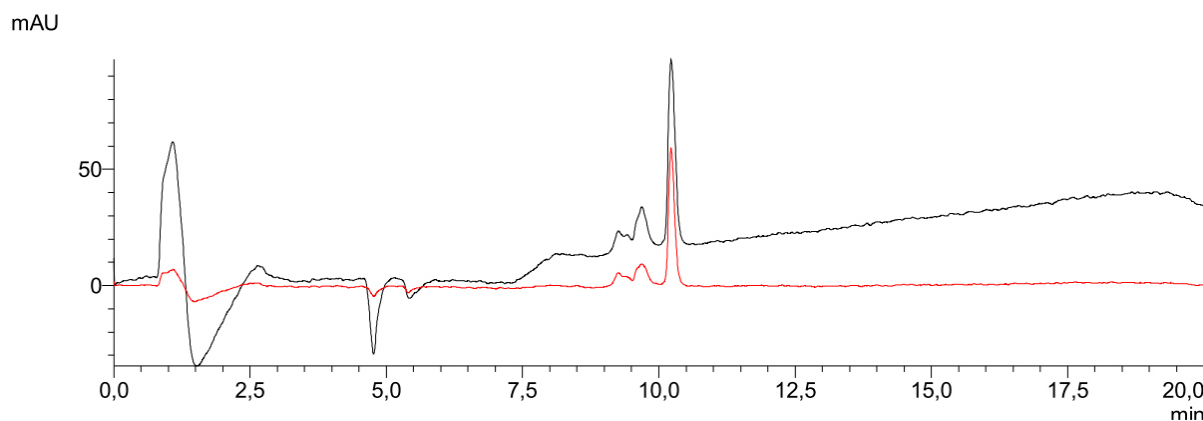


Figure 99: LC-chromatogram of Ac-Orn(N<sub>3</sub>)-VC-GS-Lys(maleimide)-NH<sub>2</sub> 6, 10 to 100% B (gradient 13.5 min), 220 nm (black), 280 nm (red), RT = 10.25 min.

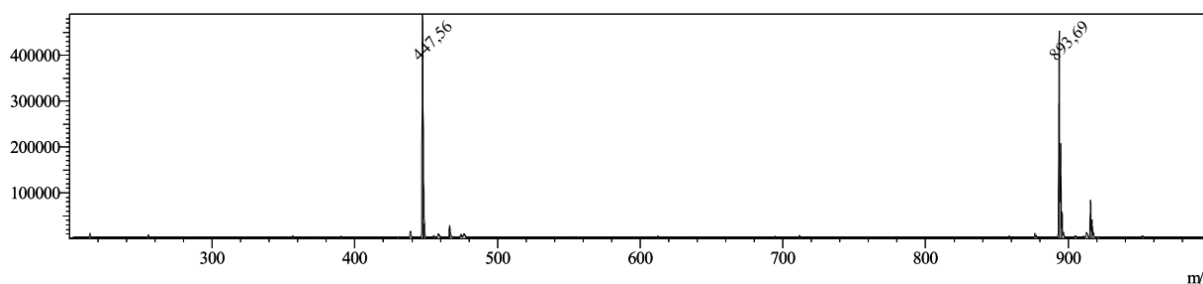


Figure 100: MS (ESI) of Ac-Orn(N<sub>3</sub>)-VC-GS-Lys(maleimide)-NH<sub>2</sub> 6, calculated:  $[M+H]^+ = 893.97$ ;  $[M+2H]^{2+} = 447.49$ ; observed:  $[M+H]^+ = 893.69$ ;  $[M+2H]^{2+} = 447.56$ .

## 8.4 Analytical data of aurein1.2-Cys 33

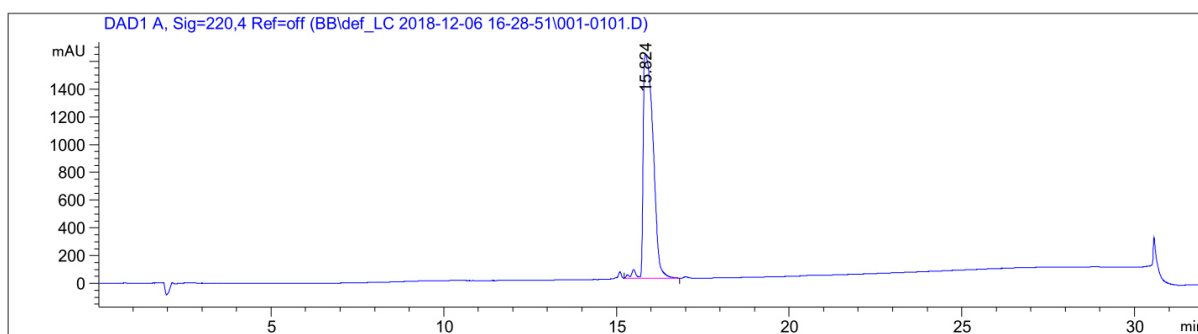


Figure 101: Analytical RP-HPLC chromatogram of Aurein1.2-Cys 33, 20 to 100% B (gradient 20 min), 220 nm, RT = 15.824 min.

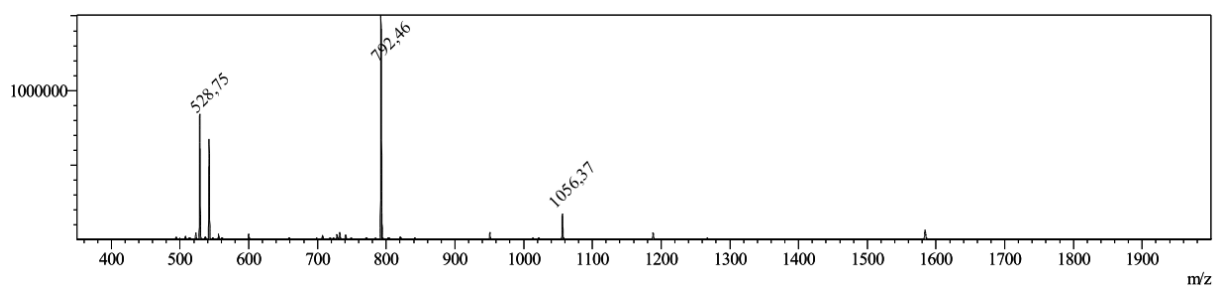


Figure 102: MS (ESI) of Aurein1.2-Cys 33, calculated:  $[M+H]^+ = 1583.93$ ;  $[M+2H]^{2+} = 792.47$ ;  $[M+3H]^{3+} = 528.64$ ; observed:  $[M+2H]^{2+} = 792.46$ ;  $[M+3H]^{3+} = 528.75$ .

## 8.5 Analytical data of L17E 12

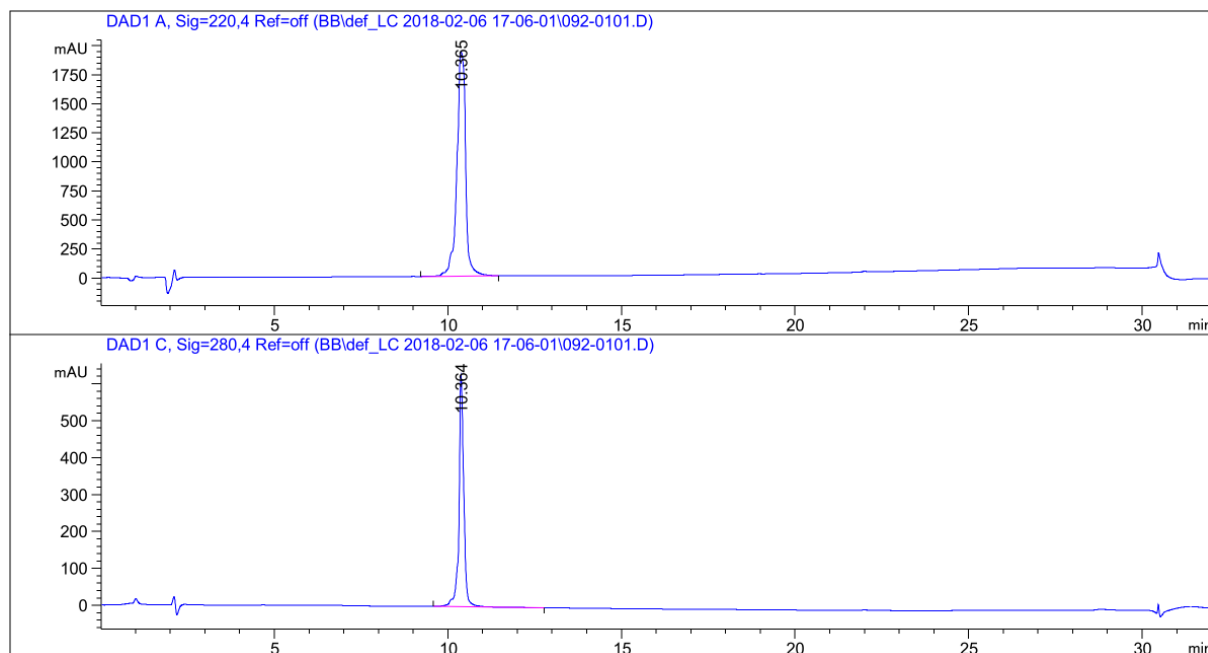
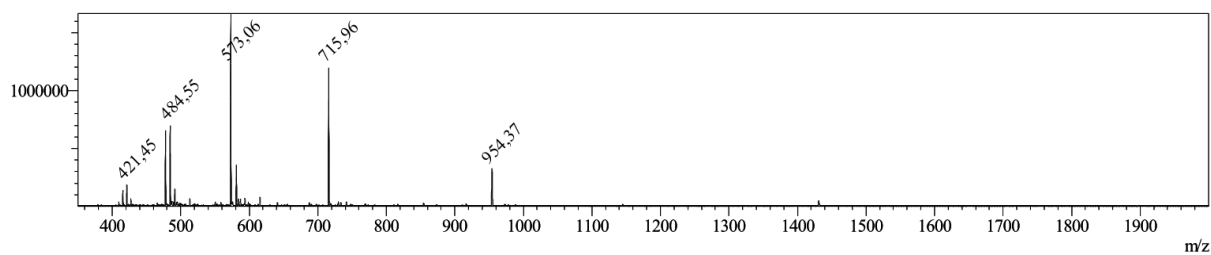
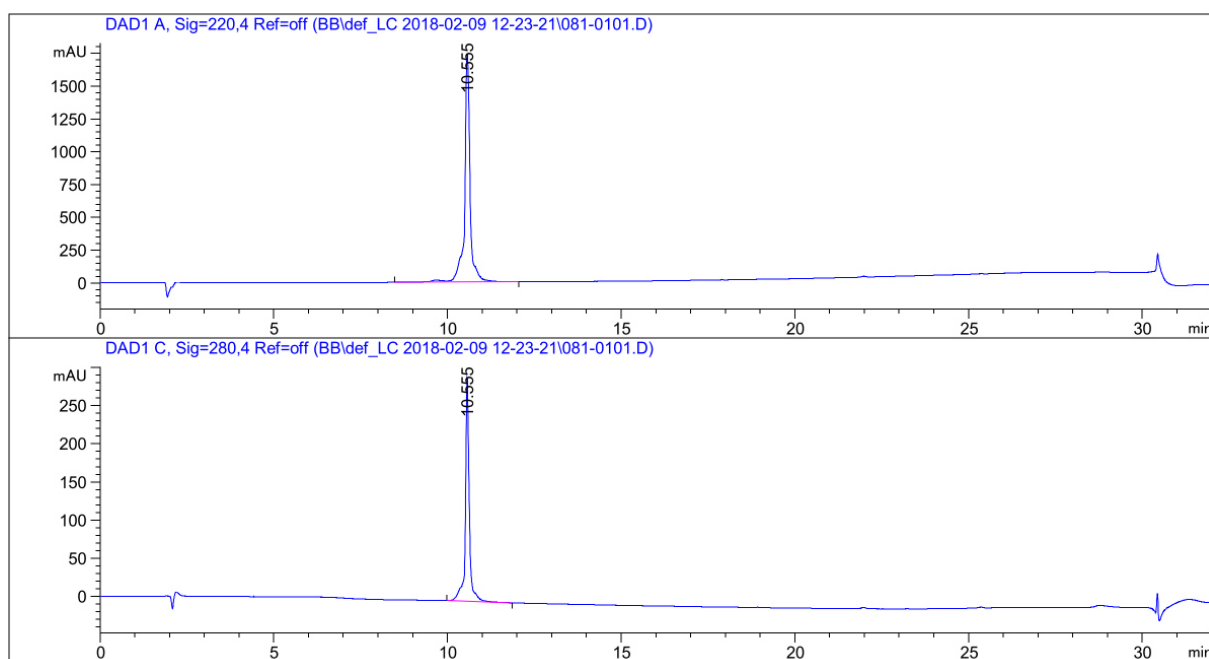


Figure 103: Analytical RP-HPLC chromatogram of L17E 12, 20 to 100% B (gradient 20 min), 220 nm (upper), 280 nm (lower), RT = 10.365 min.



**Figure 104:** MS (ESI) of L17E 12, calculated:  $[M+H]^+ = 2859.47$ ;  $[M+3H]^{3+} = 954.16$ ;  $[M+4H]^{4+} = 715.87$ ;  $[M+5H]^{5+} = 572.89$ ; observed:  $[M+3H]^{3+} = 954.37$ ;  $[M+4H]^{4+} = 715.96$ ;  $[M+5H]^{5+} = 573.06$ .

## 8.6 Analytical data of L17E-Cys 34



**Figure 105:** Analytical RP-HPLC chromatogram of L17E-Cys 34, 20 to 100% B (gradient 20 min), 220 nm (upper), 280 nm (lower), RT = 10.555 min.

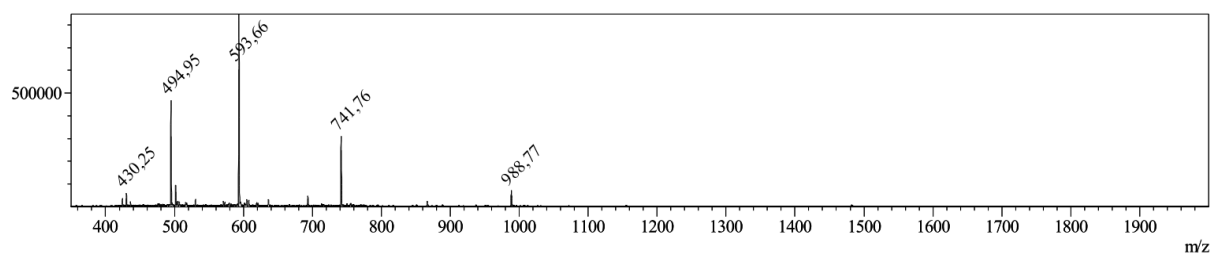


**Figure 106:** MS (ESI) of L17E-Cys 34, calculated:  $[M+H]^+ = 2962.61$ ;  $[M+3H]^{3+} = 988.53$ ;  $[M+4H]^{4+} = 741.65$ ;  $[M+5H]^{5+} = 593.52$ ;  $[M+6H]^{6+} = 494.76$ ; observed:  $[M+3H]^{3+} = 988.77$ ;  $[M+4H]^{4+} = 741.76$ ;  $[M+5H]^{5+} = 593.66$ ;  $[M+6H]^{6+} = 494.95$ .

## 8.7 Analytical data of L17E-Pra 41

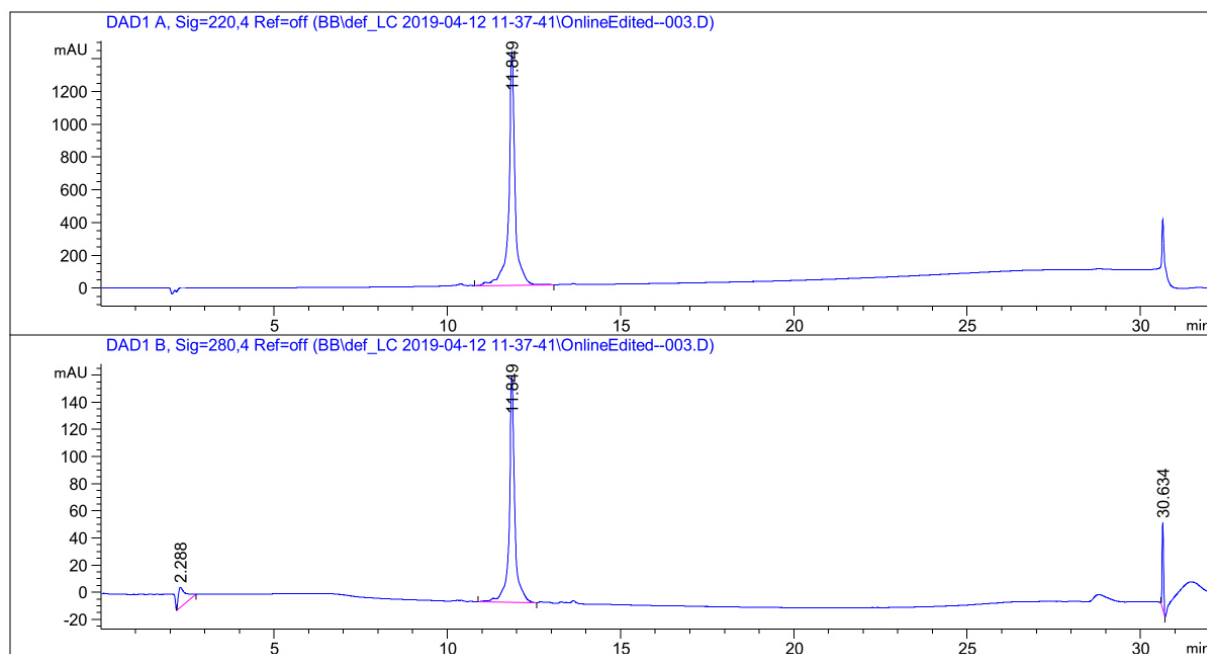


**Figure 107:** Analytical RP-HPLC chromatogram of L17E-Pra 41, 20 to 100% B (gradient 20 min), 220 nm (upper), 280 nm (lower), RT = 11.849 min.

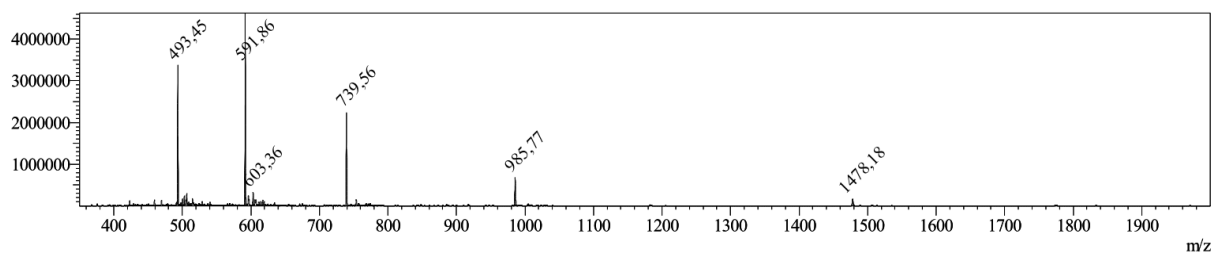


**Figure 108:** MS (ESI) of L17E-Pra 41, calculated:  $[M+H]^+ = 2955.57$ ;  $[M+2H]^{2+} = 1478.29$ ;  $[M+3H]^{3+} = 985.86$ ;  $[M+4H]^{4+} = 739.64$ ;  $[M+5H]^{5+} = 591.91$ ;  $[M+6H]^{6+} = 493.43$ ; observed:  $[M+2H]^{2+} = 1478.18$ ;  $[M+3H]^{3+} = 985.77$ ;  $[M+4H]^{4+} = 739.56$ ;  $[M+5H]^{5+} = 591.86$ ;  $[M+6H]^{6+} = 493.45$ .

## 8.8 Analytical data of Ac-Cys(*StBu*)-VC-Gly 7

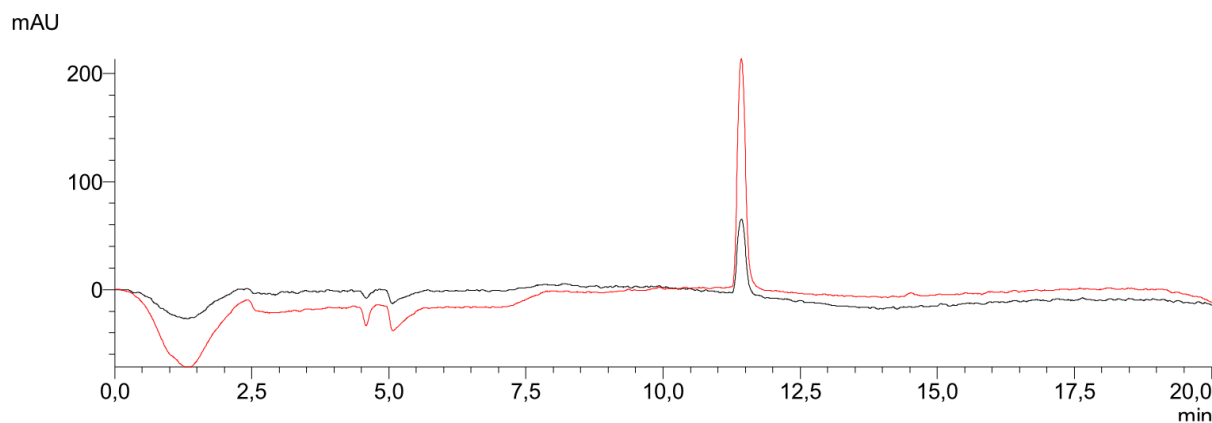


**Figure 109:** LC-chromatogram of Ac-Cys(*StBu*)-VC-Gly 7, 10 to 100% B (gradient 13.5 min), 220 nm (black), 280 nm (red), RT = 11.53 min.

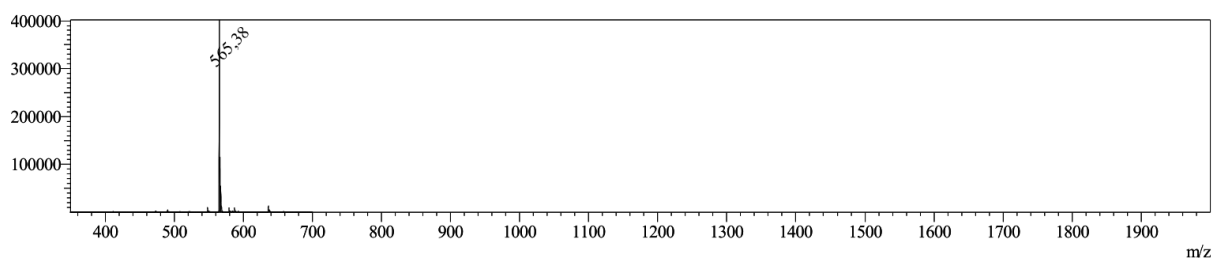


Figure 110: MS (ESI) of Ac-Cys(*StBu*)-VC-Gly **7**, calculated:  $[M+H]^+ = 565.72$ ; observed:  $[M+H]^+ = 565.38$ .

## 8.9 Analytical data of Ac-Cys(*StBu*)-VC-Gly-Dox 4-PG

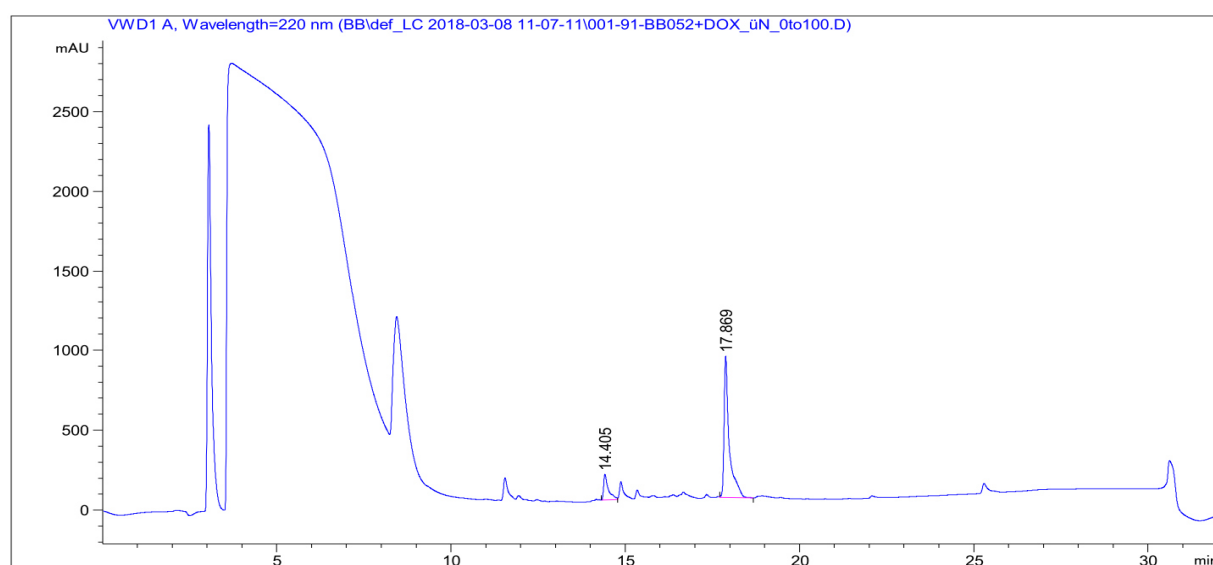


Figure 111: Analytical RP-HPLC chromatogram of Ac-Cys(*StBu*)-VC-Gly-Dox **4-PG**, 00 to 100% B (gradient 20 min), 220 nm, RT = 17.869 min, (RT = 14.405: Ac-Cys(*StBu*)-VC-Gly **7**).

## 8.10 Analytical data of Ac-Cys-VC-Gly-Dox 4

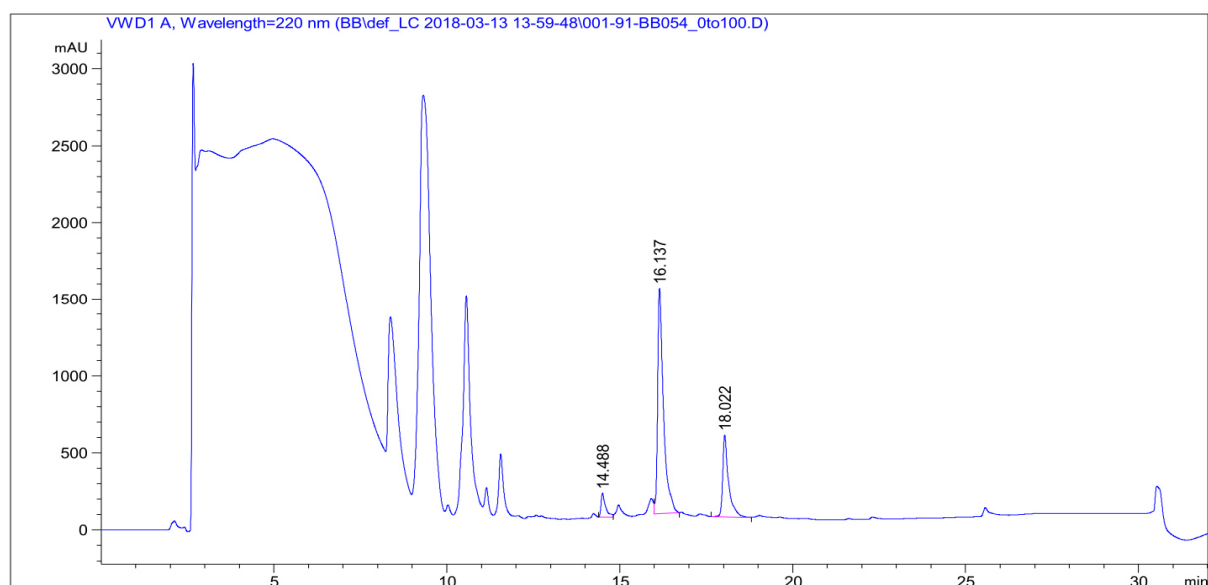
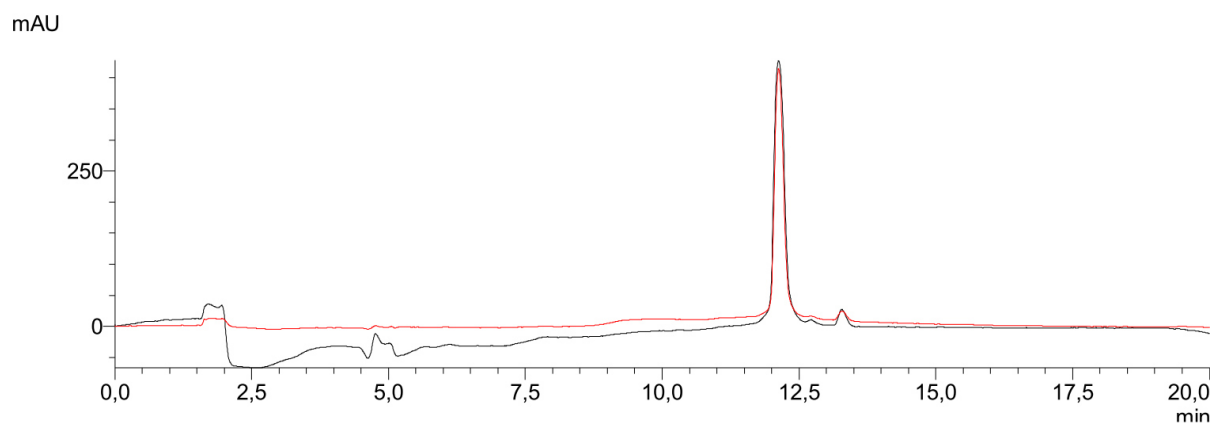
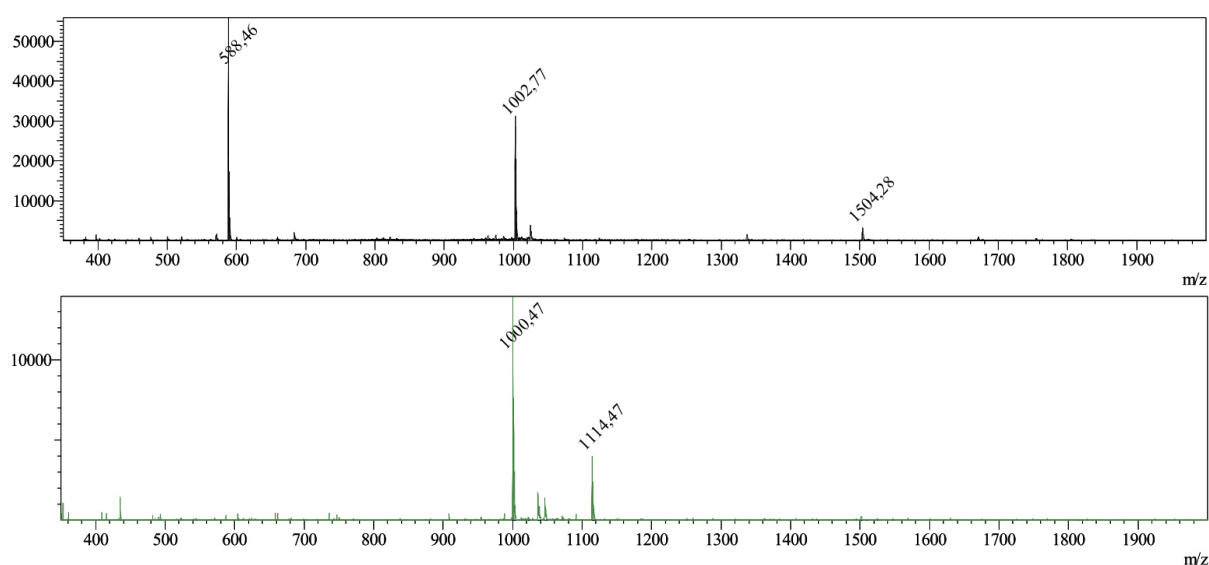


Figure 112: Analytical RP-HPLC monitoring of Ac-Cys-VC-Gly-Dox **4** synthesis, 00 to 100% B (gradient 20 min), 220 nm, RT = 16.137 min, (RT = 14.488: Ac-Cys(*StBu*)-VC-Gly **7**; RT = 18.022: Ac-Cys(*StBu*)-VC-Gly-Dox **4-PG**).



**Figure 113:** LC-chromatogram of Ac-Cys-VC-Gly-Dox **4**, 10 to 100% B (gradient 13.5 min), 220 nm (black), 280 nm (red), RT = 12.16 min.



**Figure 114:** MS (ESI) of Ac-Cys-VC-Dox **4**, calculated:  $[M+H]^+ = 1003.06$ ;  $[3M+2H]^{2+} = 1504.09$ ;  $[M-H]^- = 1001.06$ ;  $[M-H+TFA]^- = 1115.06$ ; observed:  $[M+H]^+ = 1002.77$ ;  $[3M+2H]^{2+} = 1504.28$ ;  $[M-H]^- = 1001.06$ ;  $[M-H+TFA]^- = 1114.47$ .

## 8.11 Analytical data of azide-aurein1.2-doxorubicin conjugate **8**

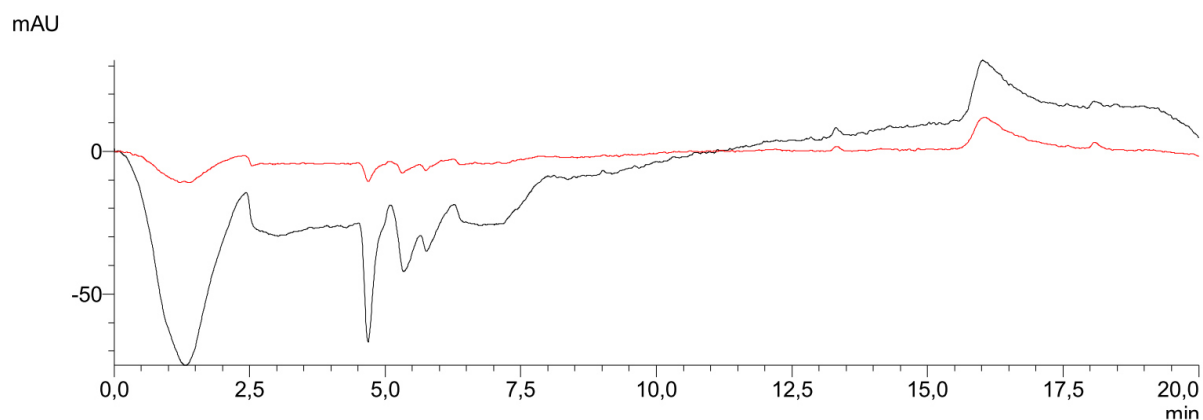


**Figure 115:** LC-chromatogram of azide equipped enzyme-cleavable aurein1.2-doxorubicin conjugate **8**, 10 to 100% B (gradient 13.5 min), 220 nm (black), 280 nm (red), RT = 16.16 min.

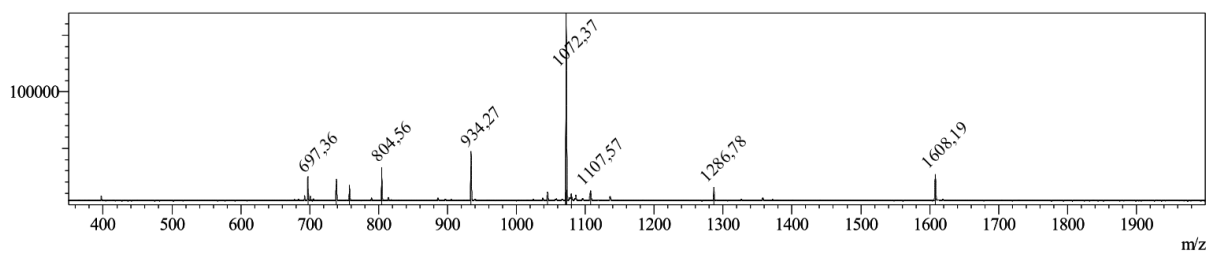


**Figure 116:** MS (ESI) of azide-aurein1.2-doxorubicin conjugate **8**, calculated:  $[M+H]^+ = 3214.66$ ;  $[M+2H]^{2+} = 1607.83$ ;  $[M+3H]^{3+} = 1072.22$ ;  $[M+4H]^{4+} = 804.42$ ;  $[2M+5H]^{5+} = 1286.46$ ; observed:  $[M+2H]^{2+} = 1608.19$ ;  $[M+3H]^{3+} = 1072.37$ ;  $[M+4H]^{4+} = 804.56$ ;  $[2M+5H]^{5+} = 1286.78$ .

## 8.12 Analytical data of azide-doxorubicin conjugate **9** w/o aurein1.2

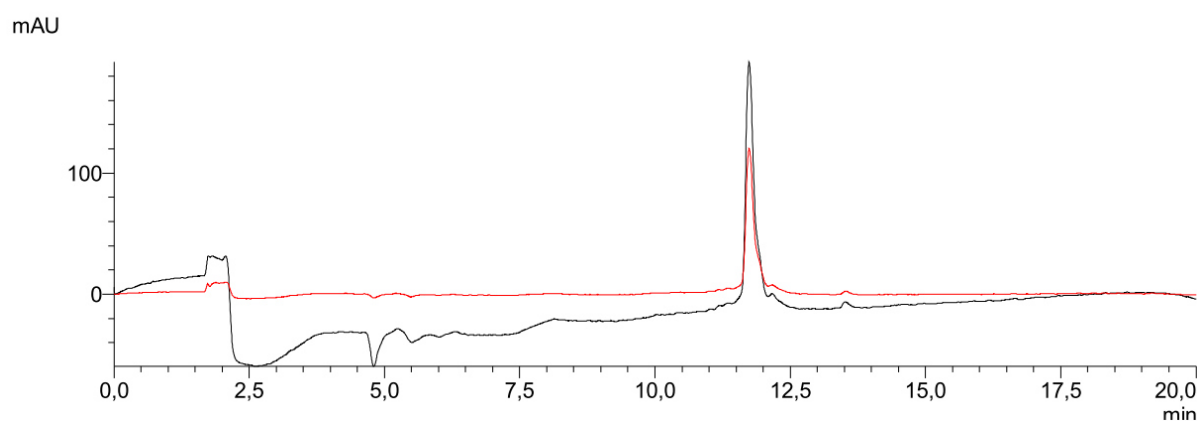


**Figure 117:** LC-chromatogram of azide-doxorubicin conjugate **9** w/o aurein1.2, 10 to 100% B (gradient 13.5 min), 220 nm (black), 280 nm (red), RT = 11.77 min.

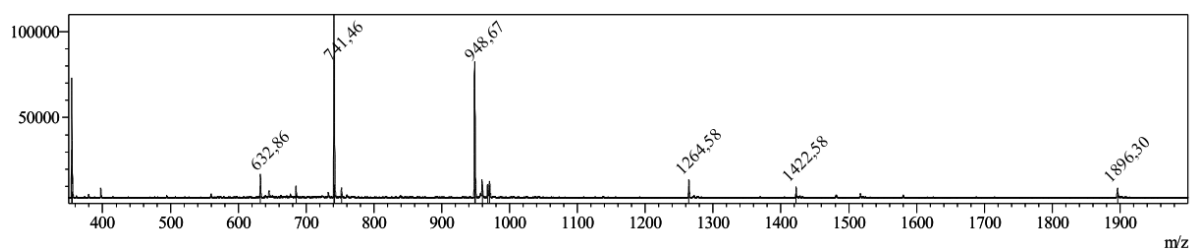


**Figure 118:** MS (ESI) of azide-doxorubicin conjugate **9** w/o aurein1.2, calculated:  $[M+H]^+ = 1896.03$ ;  $[M+2H]^{2+} = 948.52$ ;  $[M+3H]^{3+} = 632.67$ ;  $[2M+3H]^{3+} = 1264.35$ ;  $[3M+4H]^{4+} = 1422.27$ ; observed:  $[M+H]^+ = 1896.30$ ;  $[M+2H]^{2+} = 948.67$ ;  $[M+3H]^{3+} = 632.86$ ;  $[2M+3H]^{3+} = 1264.58$ ;  $[3M+4H]^{4+} = 1422.58$ .

### 8.13 Analytical data of SPAAC test conjugation 1a-d

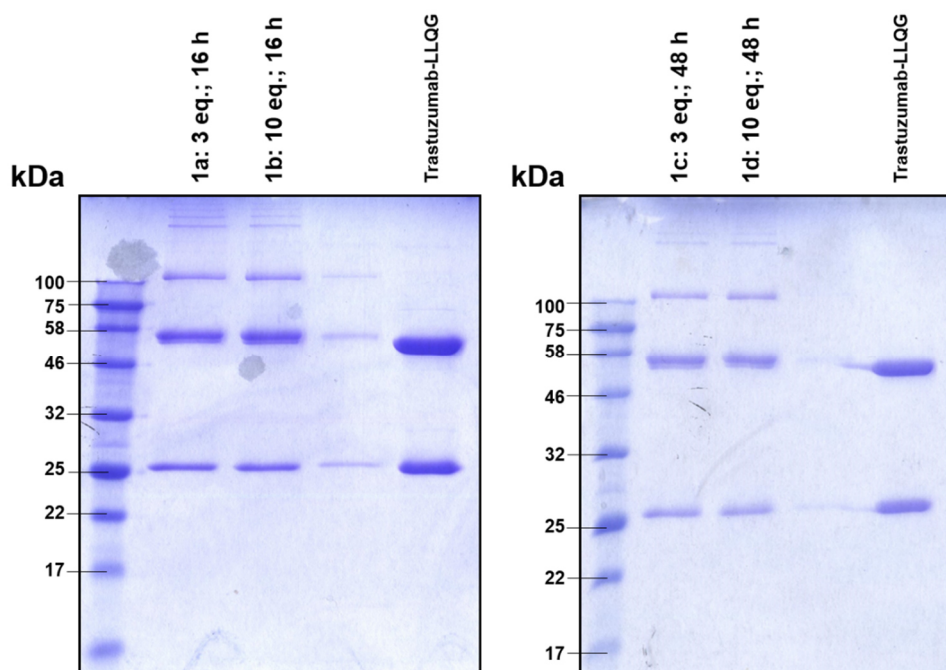


**Figure 119:** Coomassie stained SDS-PAGE analysis of Trastuzumab-aurein1.2-doxorubicin **1a-d** conjugation under different reaction conditions: Comparison of threefold and tenfold molar excess of azide-aurein1.2-doxorubicin **8** applying 16- or 48-hours reaction time.

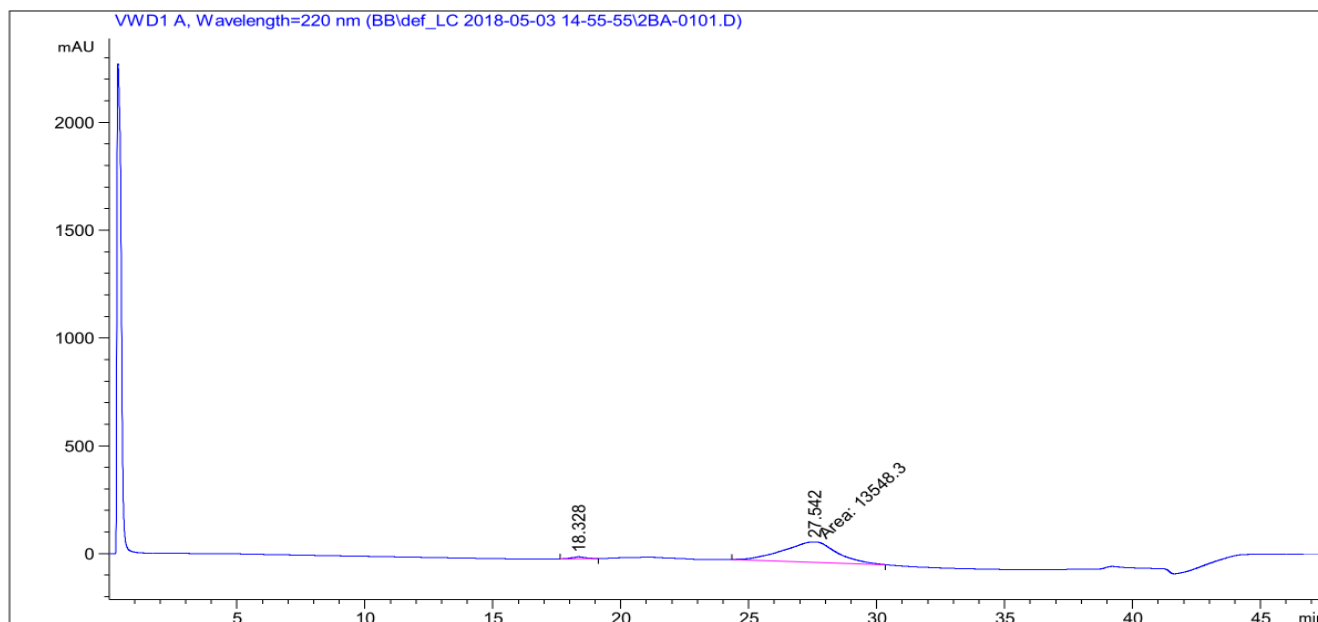


**Figure 120:** HIC chromatogram of Trastuzumab-aurein1.2-doxorubicin **1a** conjugation product applying threefold molar excess of azide-aurein1.2-doxorubicin **8** and 16-hours reaction time; 0to100%B, 35 min, 0.9 mL/min, 220 nm.

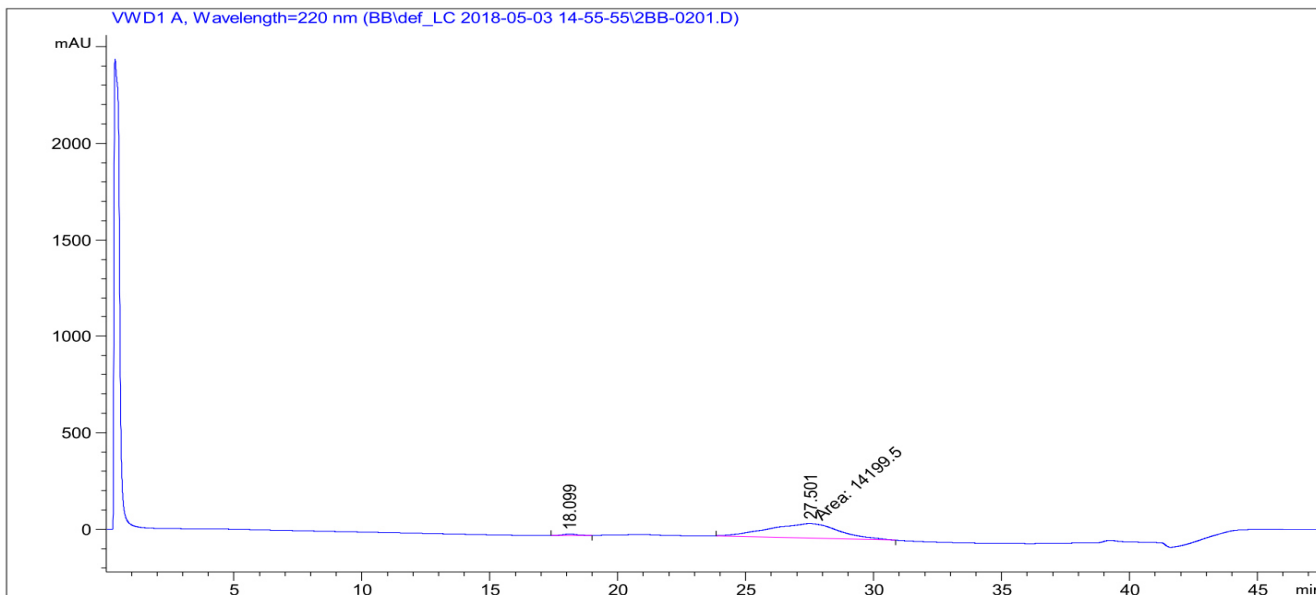


**Figure 121:** HIC chromatogram of Trastuzumab-aurein1.2-doxorubicin **1b** conjugation product applying tenfold molar excess of azide-aurein1.2-doxorubicin **8** and 16-hours reaction time; 0to100%B, 35 min, 0.9 mL/min, 220 nm.

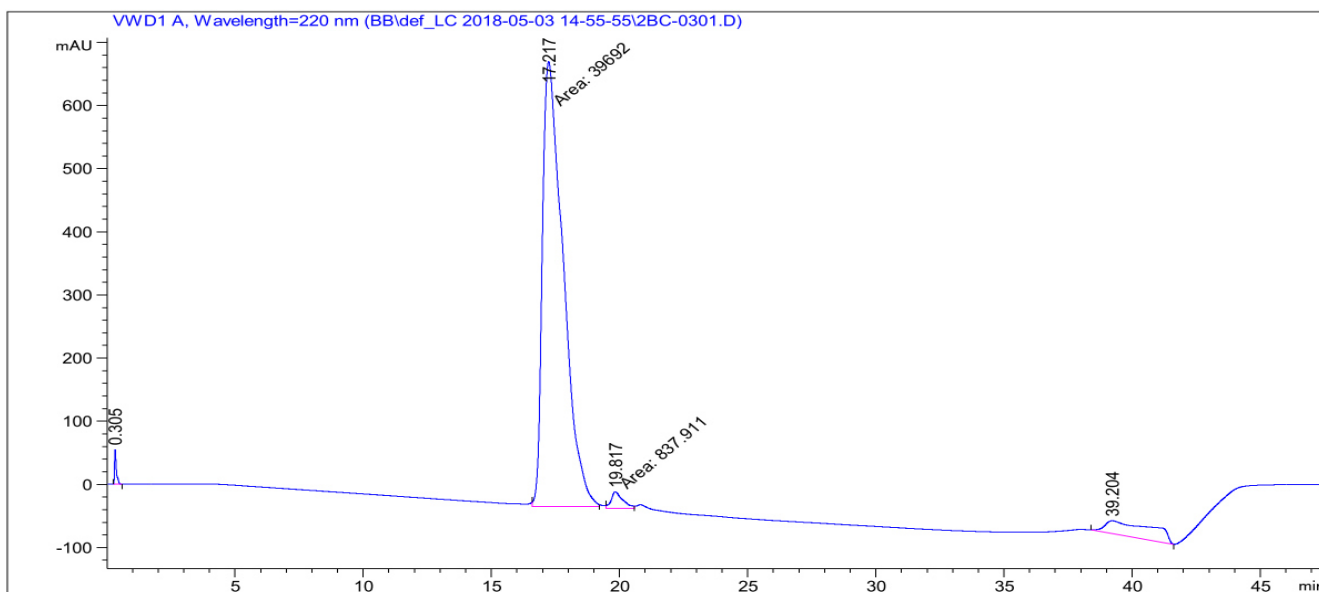


**Figure 122:** HIC chromatogram of Trastuzumab-LLQG; 0to100%B, 35 min, 0.9 mL/min, 220 nm.

## 8.14 Analytical data of Trastuzumab-aurein1.2-doxorubicin 1e and Trastuzumab-doxorubicin 10

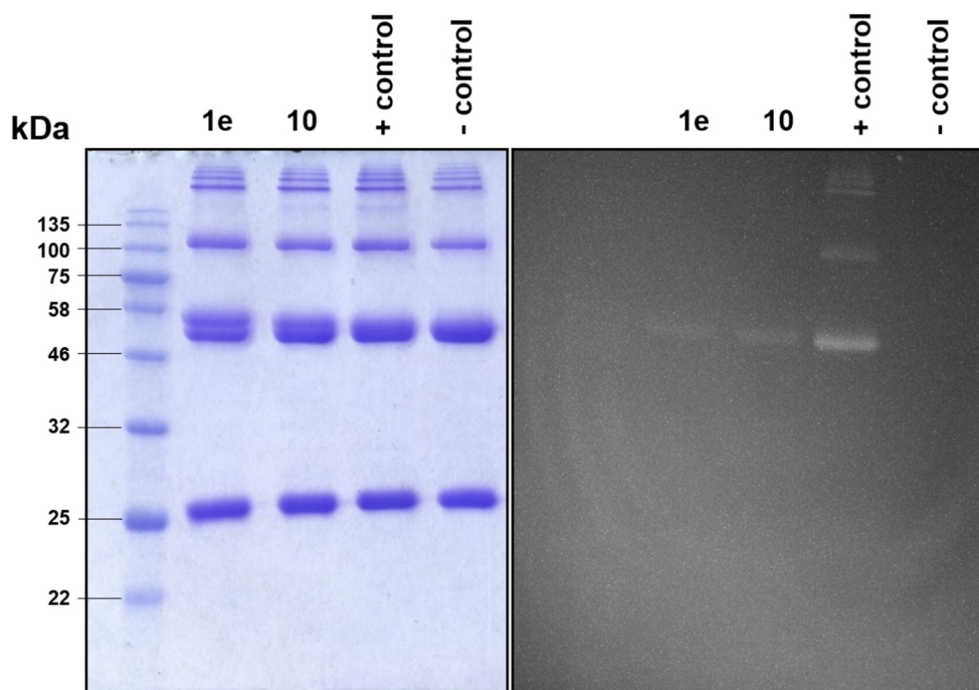


**Figure 123:** Left: Coomassie stained SDS-PAGE analysis of Trastuzumab-aurein1.2-Dox **1e**; Trastuzumab-Dox **10**; Trastuzumab-BCN + TAMRA-N<sub>3</sub> as positive control for previous Trastuzumab-LLQG-BCN formation; Trastuzumab-LLQG-BCN as negative control. Right: Irradiated SDS-PAGE before staining: Doxorubicin fluorescent Trastuzumab-aurein1.2-Dox **1e**; doxorubicin fluorescent Trastuzumab-Dox **10**; TAMRA fluorescent Trastuzumab-BCN + TAMRA-N<sub>3</sub> positive control; Trastuzumab-LLQG-BCN negative control.

## 8.15 Analytical data of cathepsin B test peptide 5

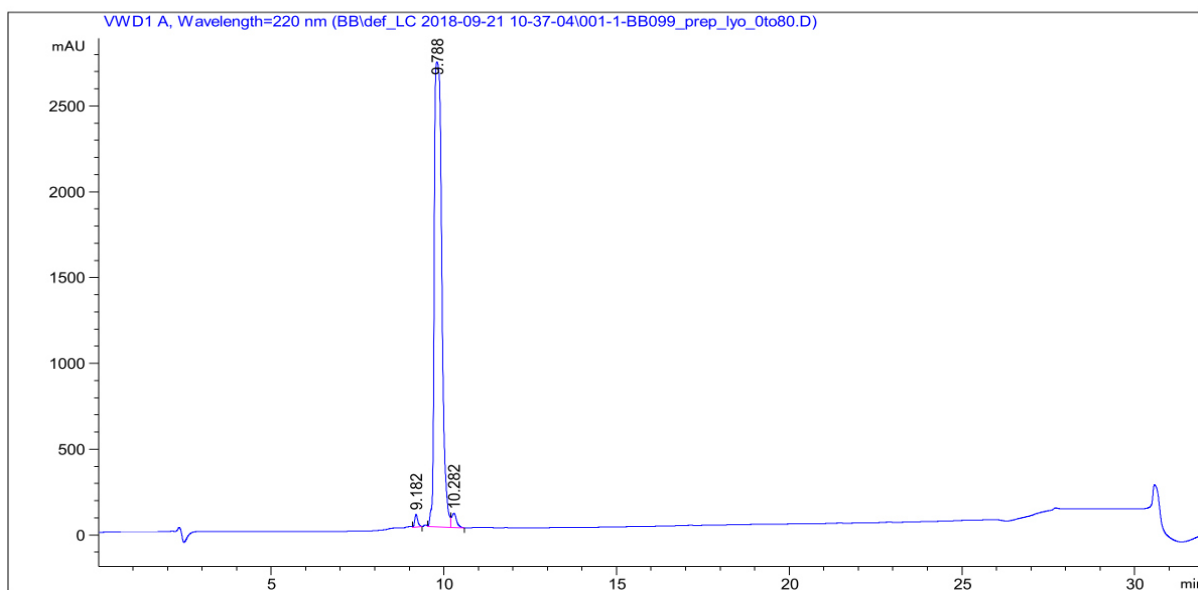


**Figure 124:** Analytical RP-HPLC chromatogram of Ac-Ser-Val-Cit-Gly-Lys-OH **5**, 0 to 80% B (gradient 20 min), 220 nm, RT = 9.788 min.

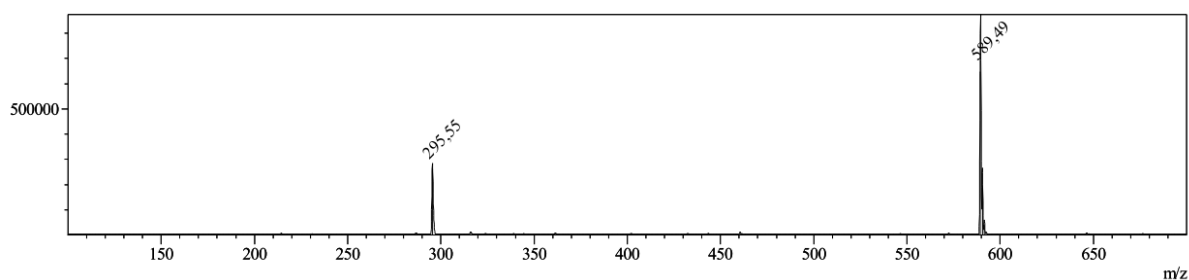


**Figure 125:** MS (ESI) of Ac-Ser-Val-Cit-Gly-Lys-OH **5**, calculated:  $[M+H]^+ = 589.66$ ;  $[M+2H]^{2+} = 295.33$ ; observed:  $[M+H]^+ = 589.49$ ;  $[M+2H]^{2+} = 295.55$ .

## 8.16 Analytical data of cathepsin B mediated cleavage of test peptide 5

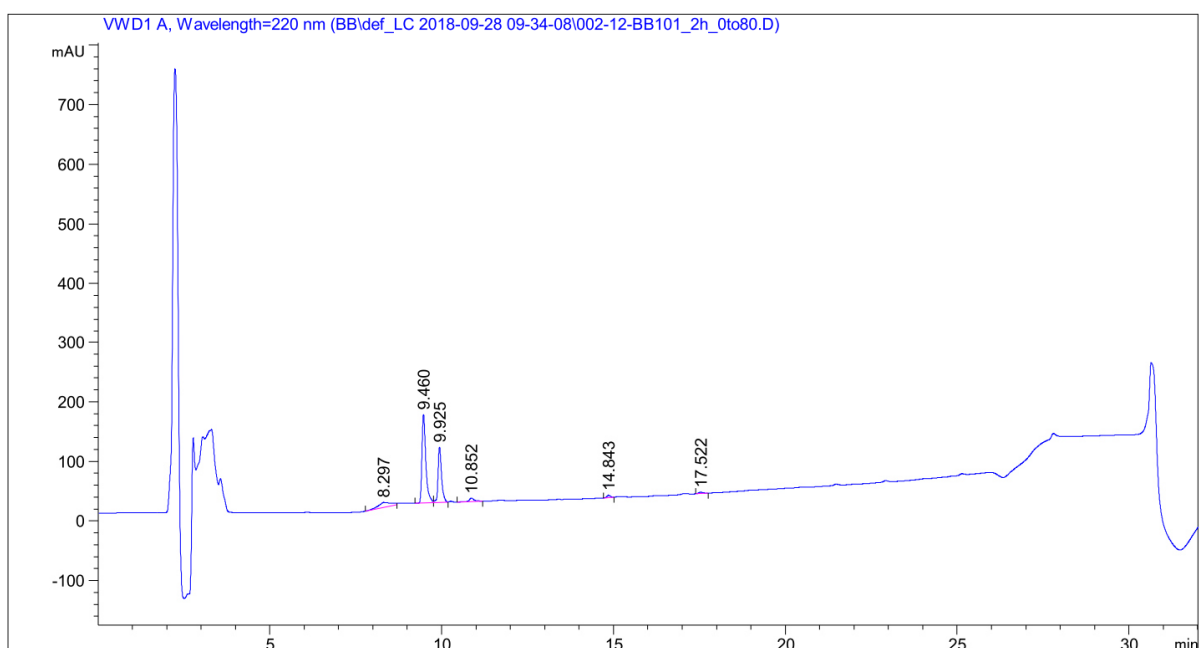


**Figure 126:** Analytical RP-HPLC chromatogram of cathepsin B mediated cleavage of test peptide **5** after 2 h incubation, 0 to 80% B (gradient 20 min), 220 nm, RT = 9.460 min (cleavage product **63**).

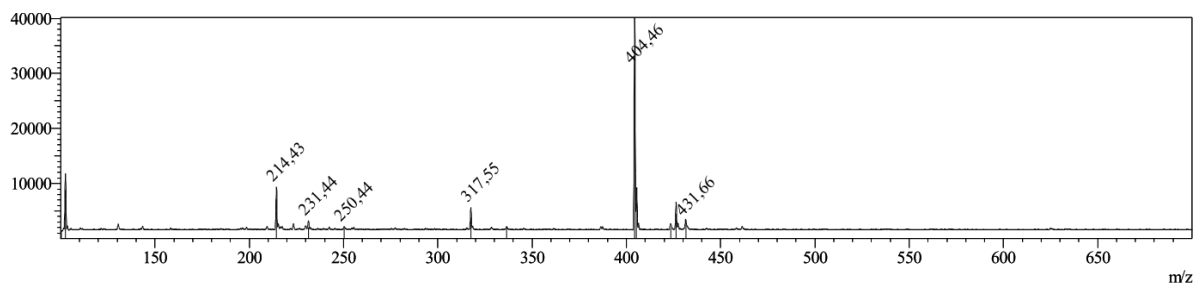


**Figure 127:** MS (ESI) of cathepsin B cleavage product **63**, calculated:  $[M+H]^+ = 403.44$ ; observed:  $[M+H]^+ = 404.46$ .

## 8.17 Analytical data of dextran-*N*-Boc-cadaverine 13

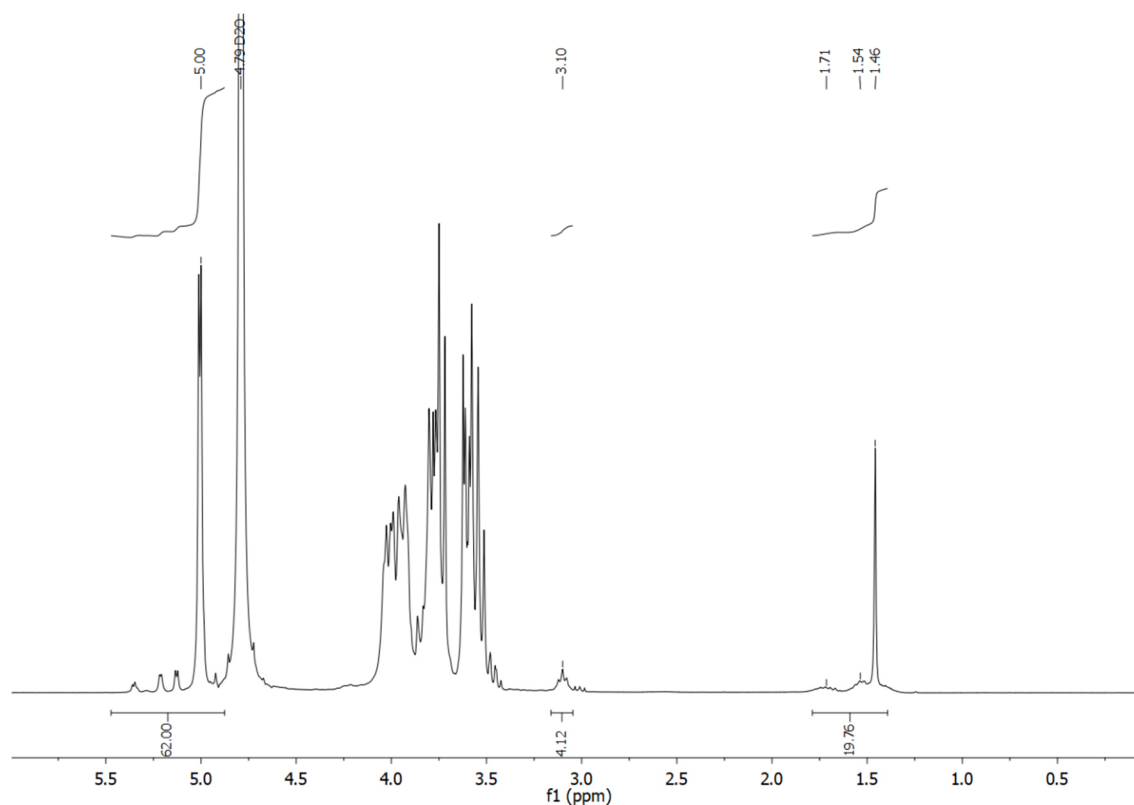


Figure 128: <sup>1</sup>H NMR spectrum of dextran-*N*-Boc-cadaverine 13.

## 8.18 Analytical data of *N*-(2-aminoethyl)maleimide 14 and intermediates 65, 66

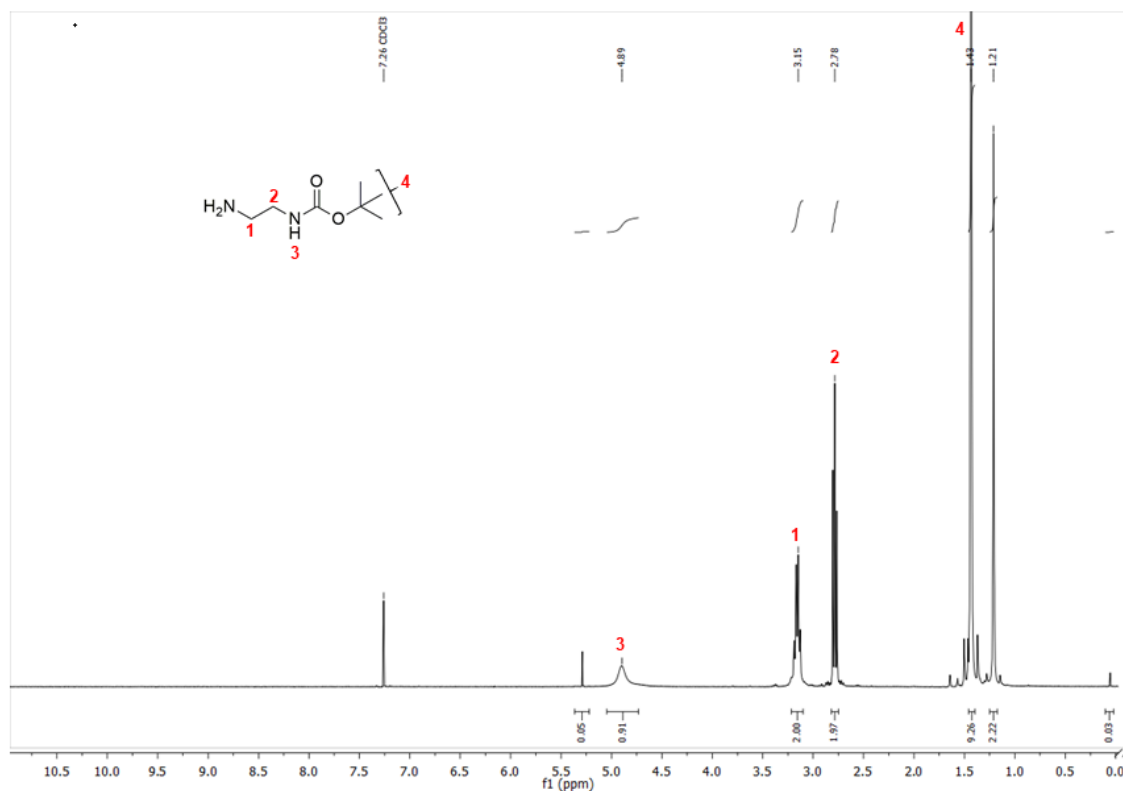


Figure 129: <sup>1</sup>H NMR spectrum of *N*-Boc-ethylendiamine 65.

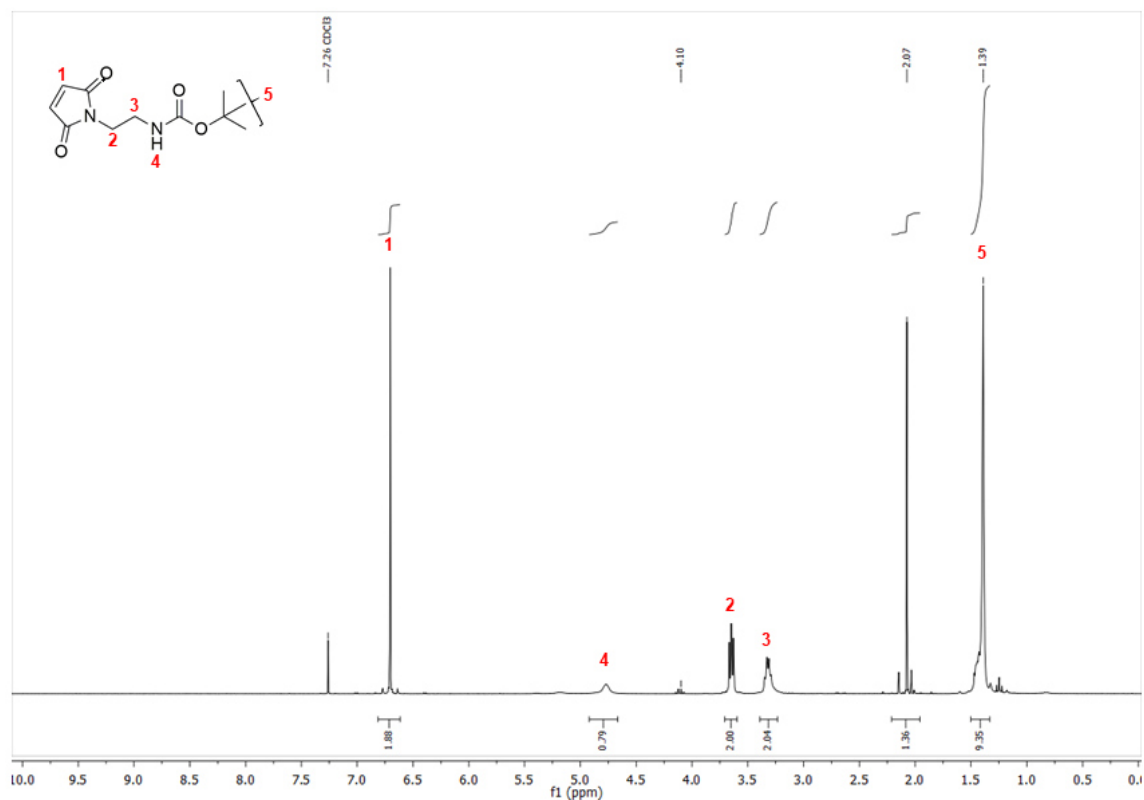


Figure 130: <sup>1</sup>H NMR spectrum of 1-(*N*-Boc)-*N*-(2-aminoethyl)maleimide **66**

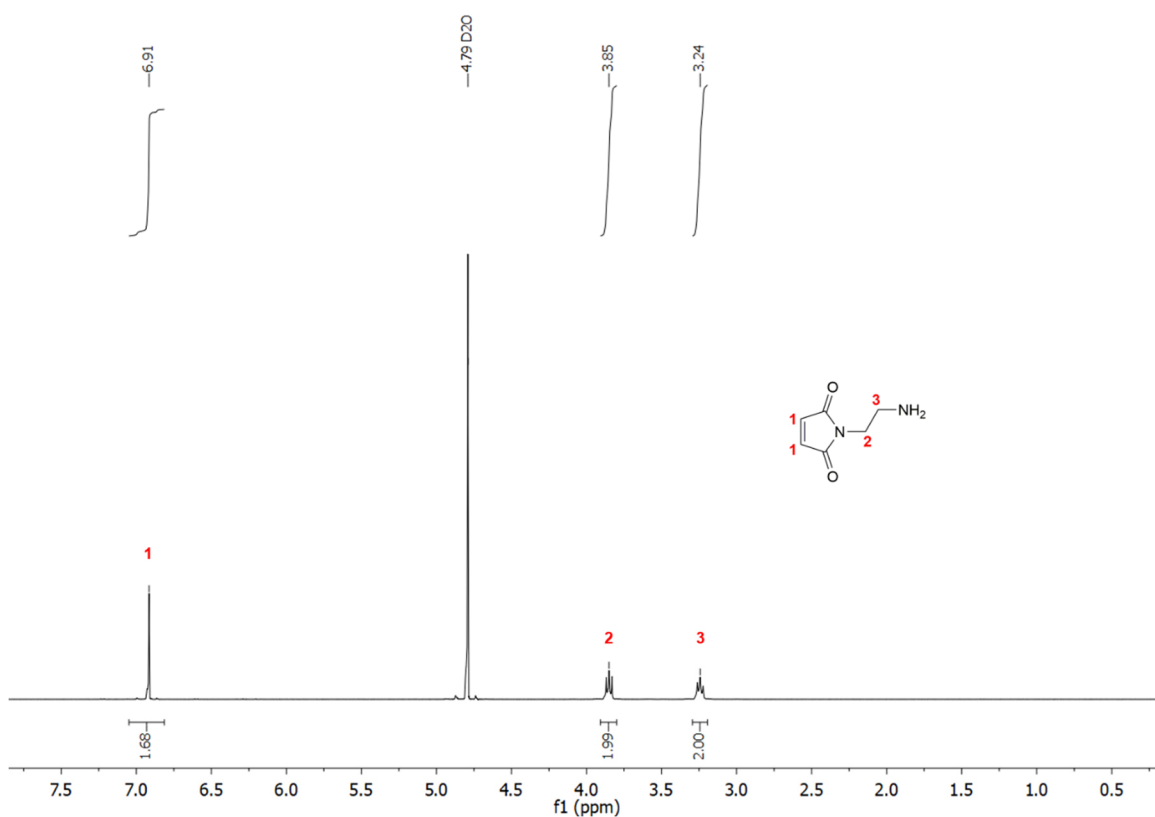


Figure 131: <sup>1</sup>H NMR spectrum of *N*-(2-aminoethyl)maleimide **14**.

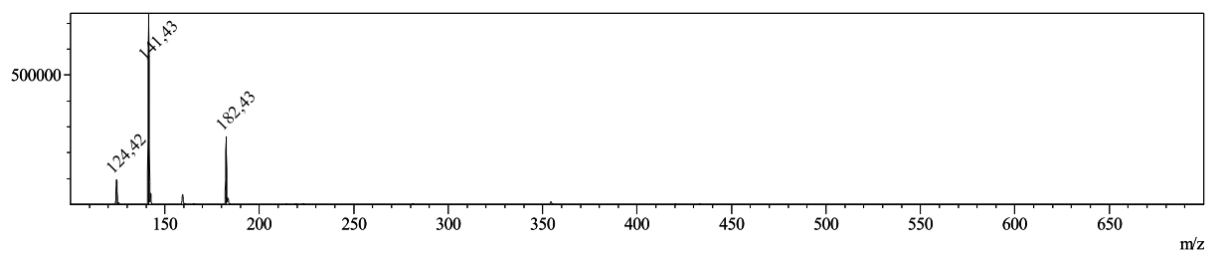


Figure 132: MS (ESI) of *N*-(2-aminoethyl)maleimide **14**, calculated:  $[M+H]^+ = 141.14$ ; observed:  $[M+H]^+ = 141.43$ .

### 8.19 Analytical data of maleimide(6.5)-dextran-*N*-Boc-cadaverine **18**

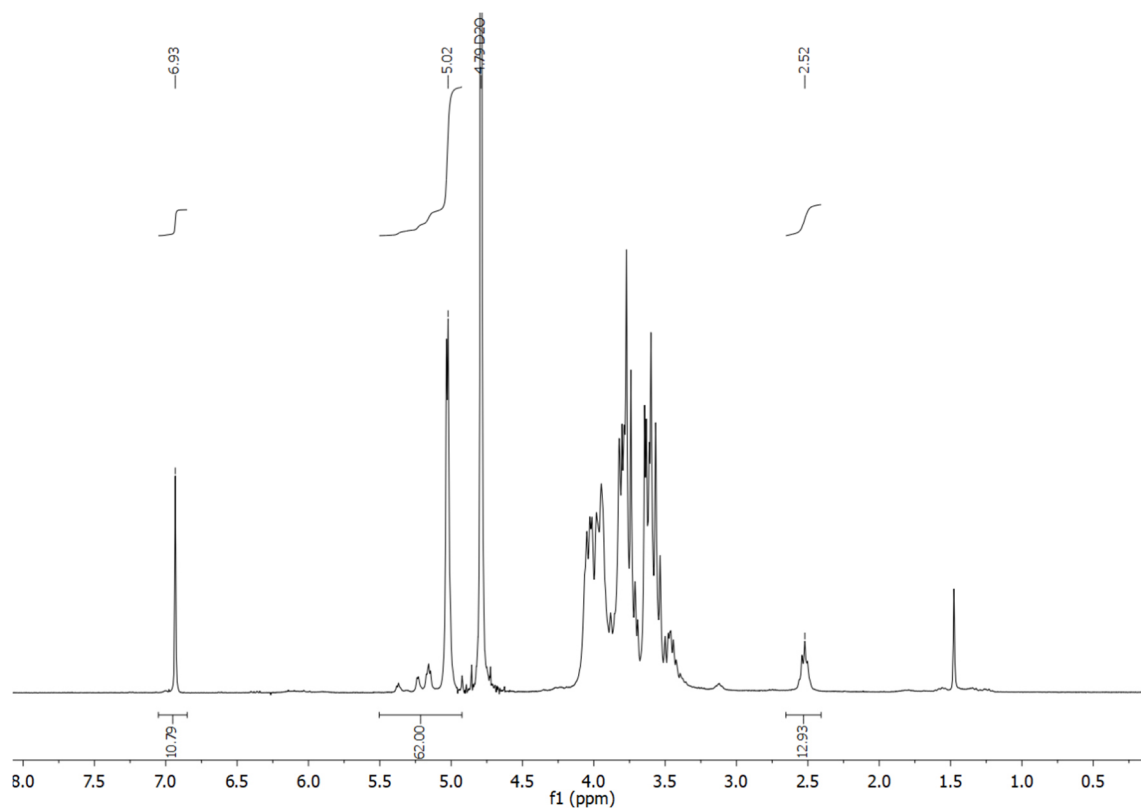


Figure 133:  $^1\text{H}$  NMR spectrum of maleimide(6.5)-dextran-*N*-Boc-cadaverine **18**.

## 8.20 Analytical of maleimide(7.8)-dextran-*N*-Boc-cadaverine 19

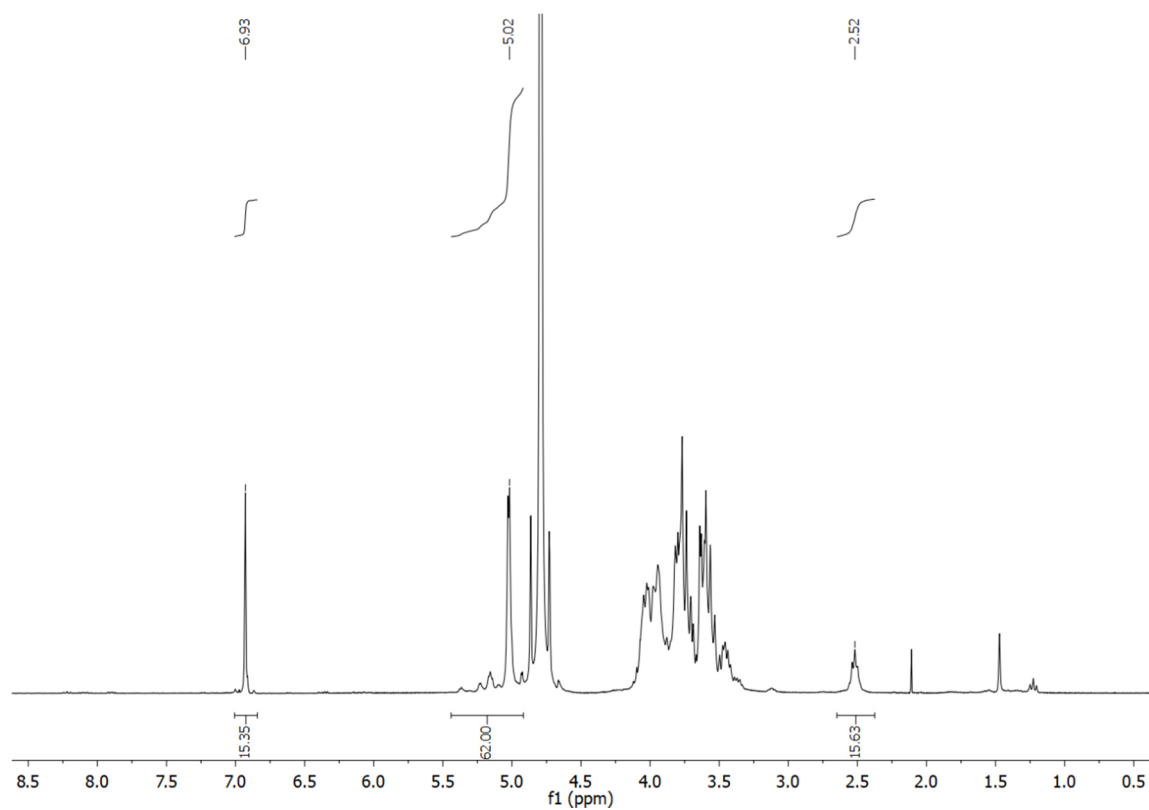


Figure 134:  $^1\text{H}$  NMR spectrum of maleimide(7.8)-dextran-*N*-Boc-cadaverine 19.

## 8.21 Analytical data of maleimide(10.5)-dextran-*N*-Boc-cadaverine 20

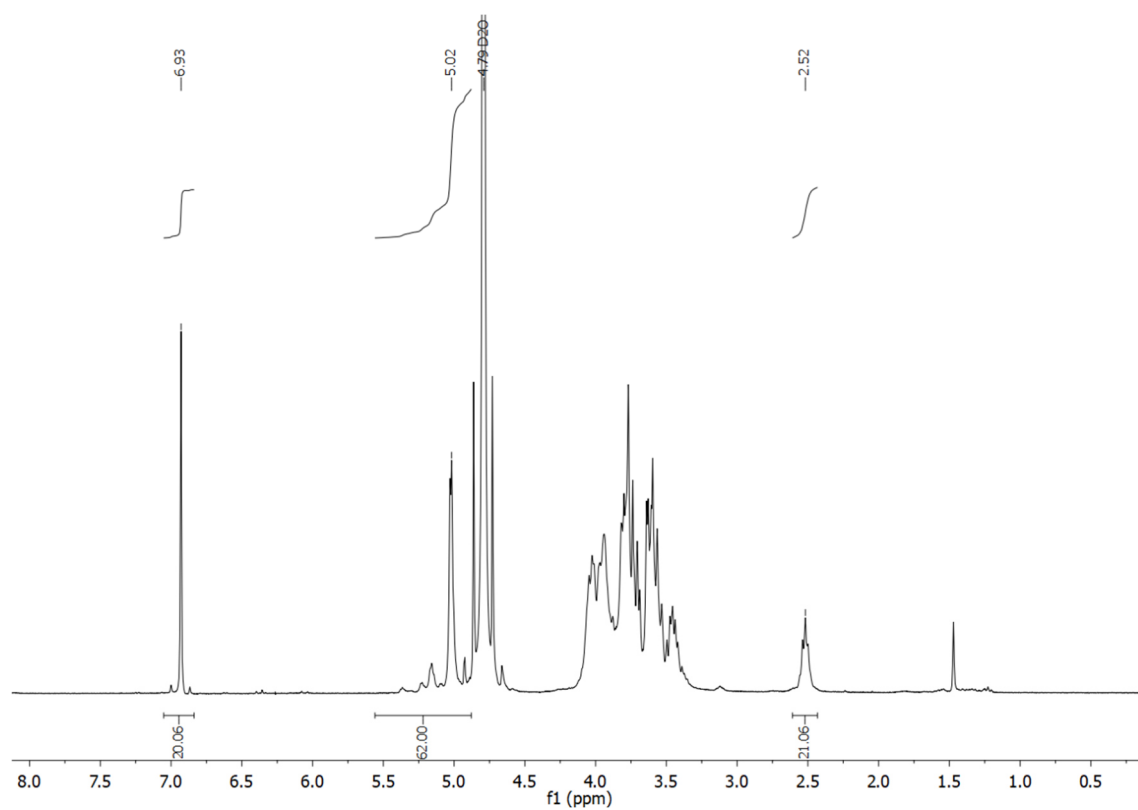


Figure 135:  $^1\text{H}$  NMR spectrum of maleimide(10.5)-dextran-*N*-Boc-cadaverine 20.

## 8.22 Analytical data of *N*-(5-aminopentyl)-2-azidoacetamide 21

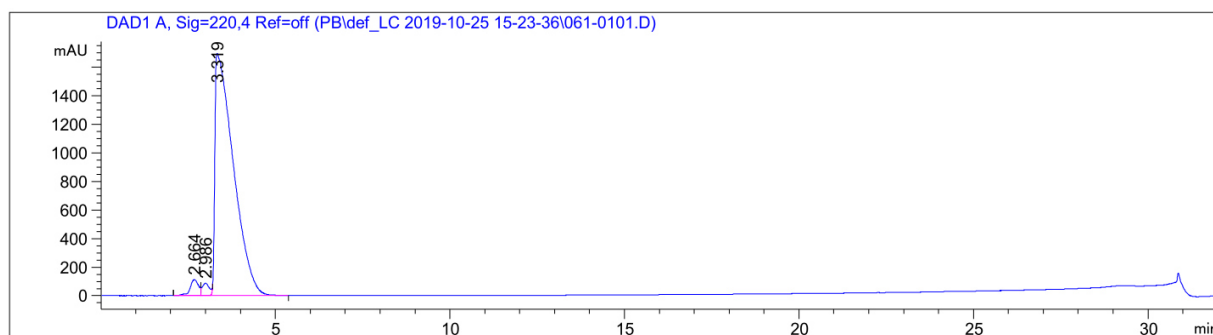


Figure 136: Analytical RP-HPLC chromatogram of *N*-(5-aminopentyl)-2-azidoacetamide 21, 00 to 80% B (gradient 20 min), 220 nm, RT = 3.319 min.

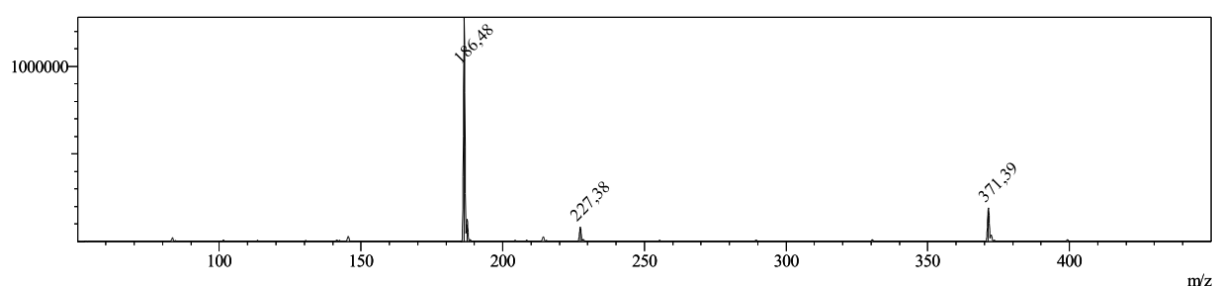


Figure 137: MS (ESI) of *N*-(5-aminopentyl)-2-azidoacetamide 21, calculated:  $[M+H]^+ = 186.23$ ; observed:  $[M+H]^+ = 186.48$ .

## 8.23 Analytical data of $N_3(4.8)$ -dextran-cadaverine 24

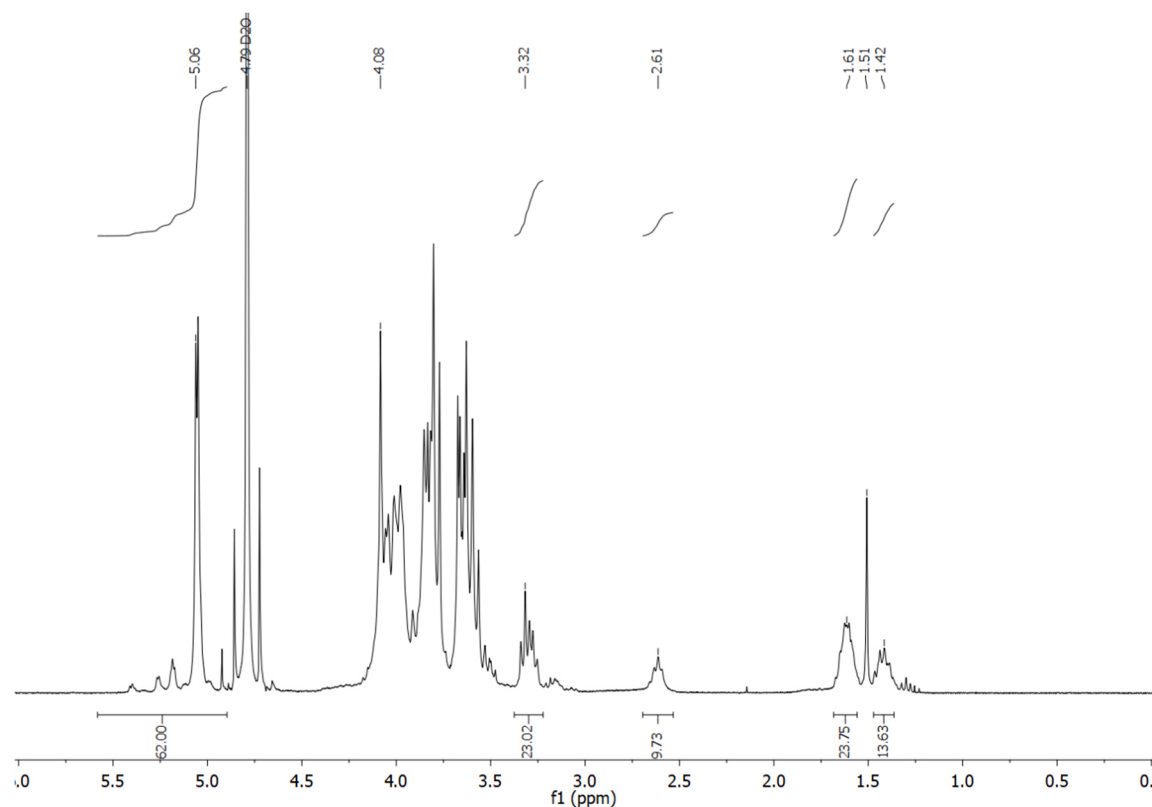


Figure 138:  $^1\text{H}$  NMR spectrum of unprotected  $N_3(4.8)$ -dextran-*N*-Boc-cadaverine before removal of Boc protecting group.

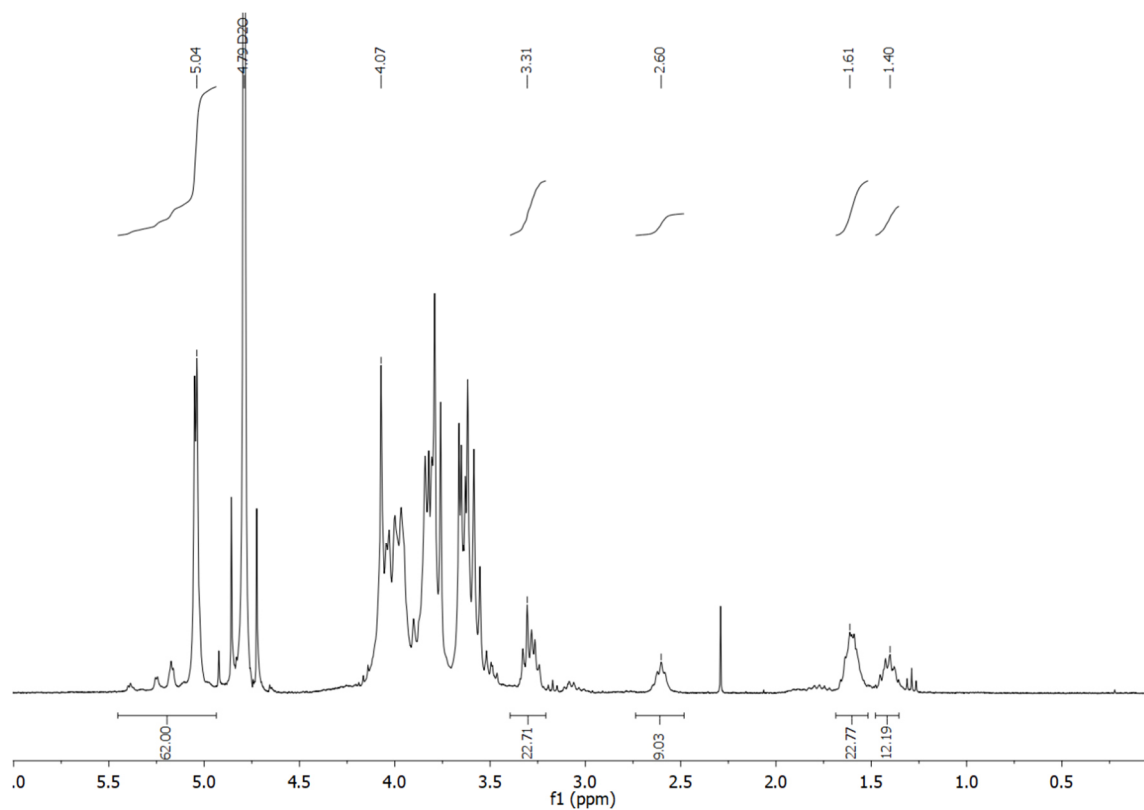


Figure 139:  $^1\text{H}$  NMR spectrum of  $\text{N}_3(4.8)$ -dextran-cadaverine **24**.

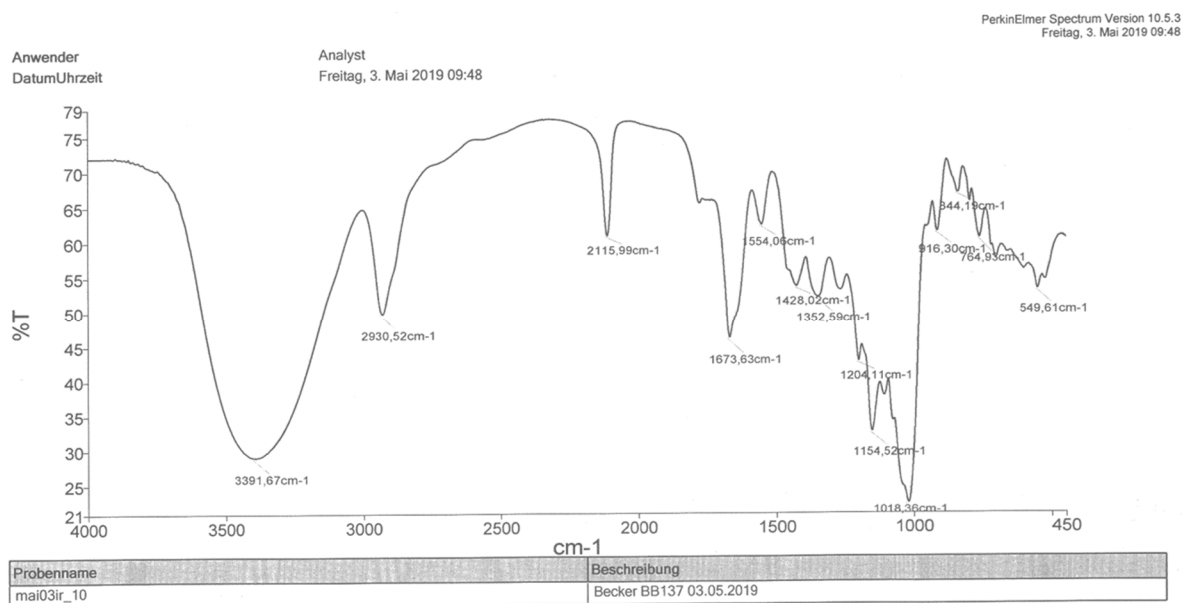


Figure 140: IR spectrum of azide modified dextran-cadaverine **24** showing the corresponding azide band at a wavenumber of approximately  $2116\text{ cm}^{-1}$ .

## 8.24 Analytical data of N<sub>3</sub>(4.8)-dextran-cadaverine 25

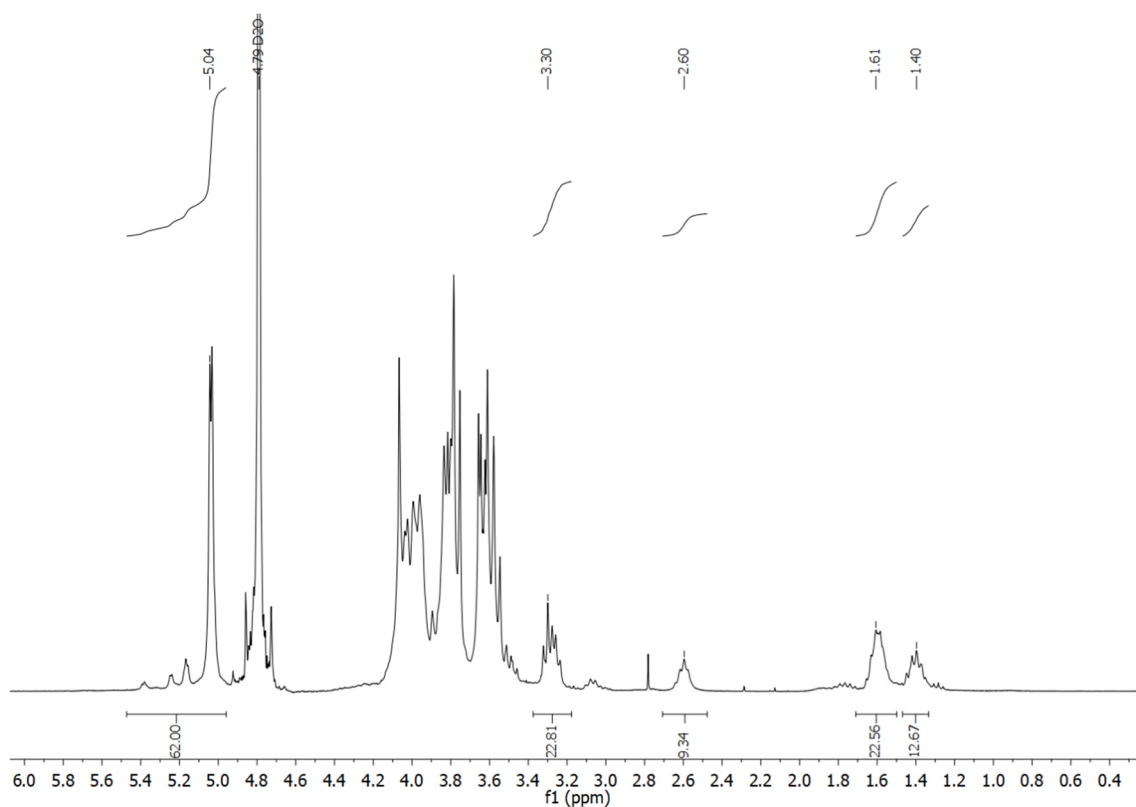


Figure 141: <sup>1</sup>H NMR spectrum of N<sub>3</sub>(4.8)-dextran-cadaverine 25.

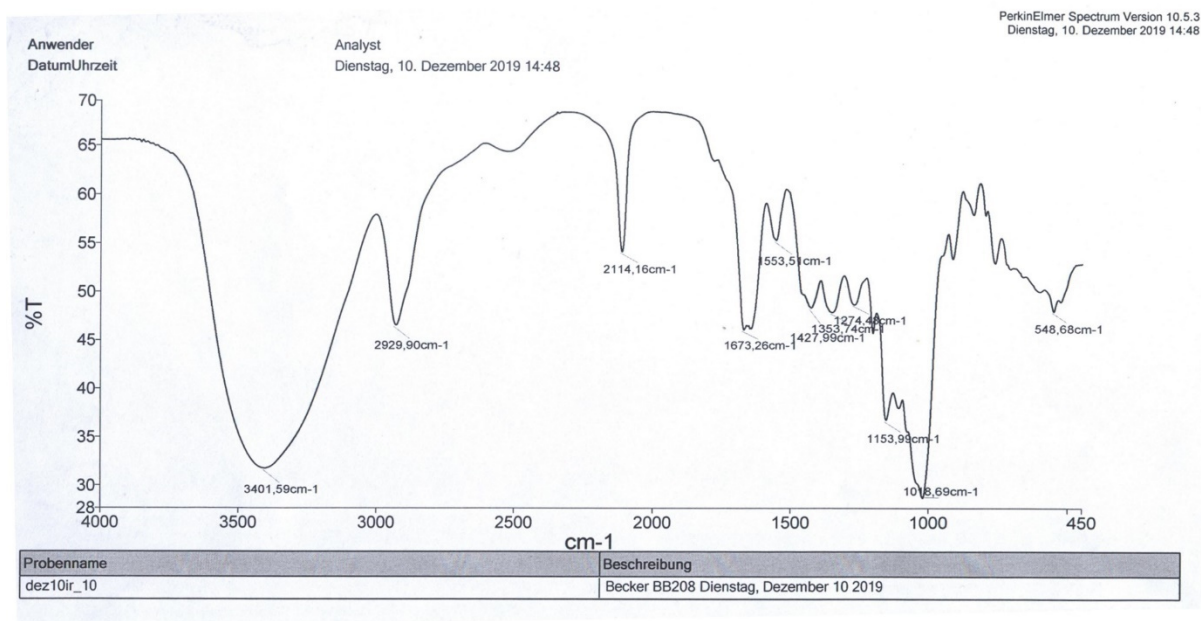


Figure 142: IR spectrum of azide modified dextran-cadaverine 25 showing the corresponding azide band at a wavenumber of approximately 2114 cm<sup>-1</sup>.

## 8.25 Analytical data of N<sub>3</sub>(4.3)-dextran-cadaverine 26

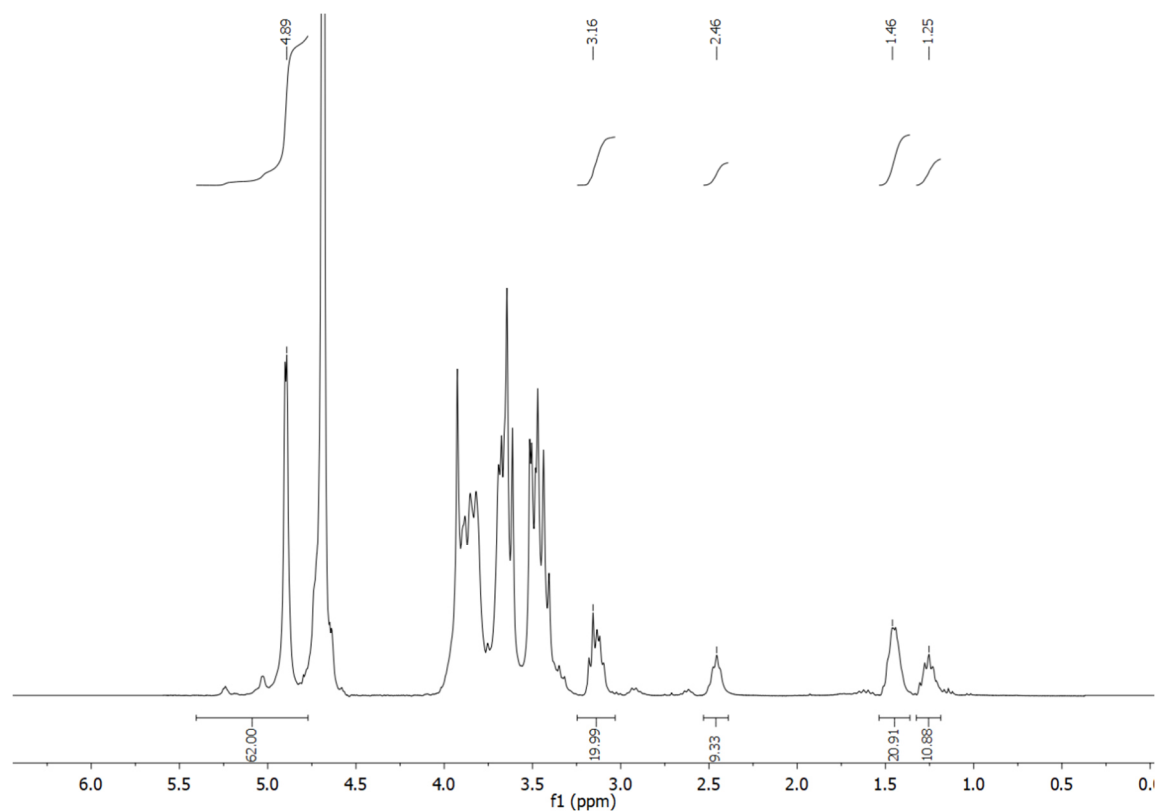


Figure 143: <sup>1</sup>H NMR spectrum of N<sub>3</sub>(4.3)-dextran-cadaverine 26.

## 8.26 Analytical data of N<sub>3</sub>(4.3)-dextran-norbornene 29

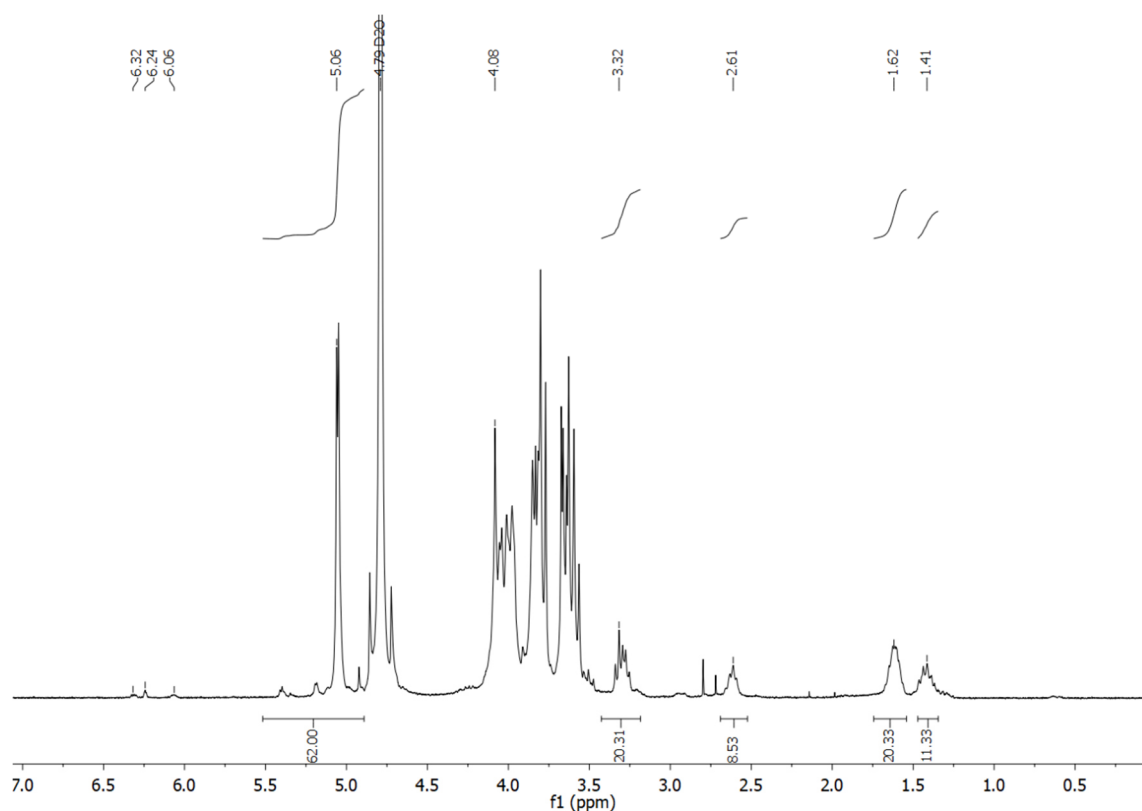


Figure 144: <sup>1</sup>H NMR spectrum of N<sub>3</sub>(4.3)-dextran-norbornene 29.

## 8.27 Analytical data of N<sub>3</sub>(4.8)-dextran-norbornene 31

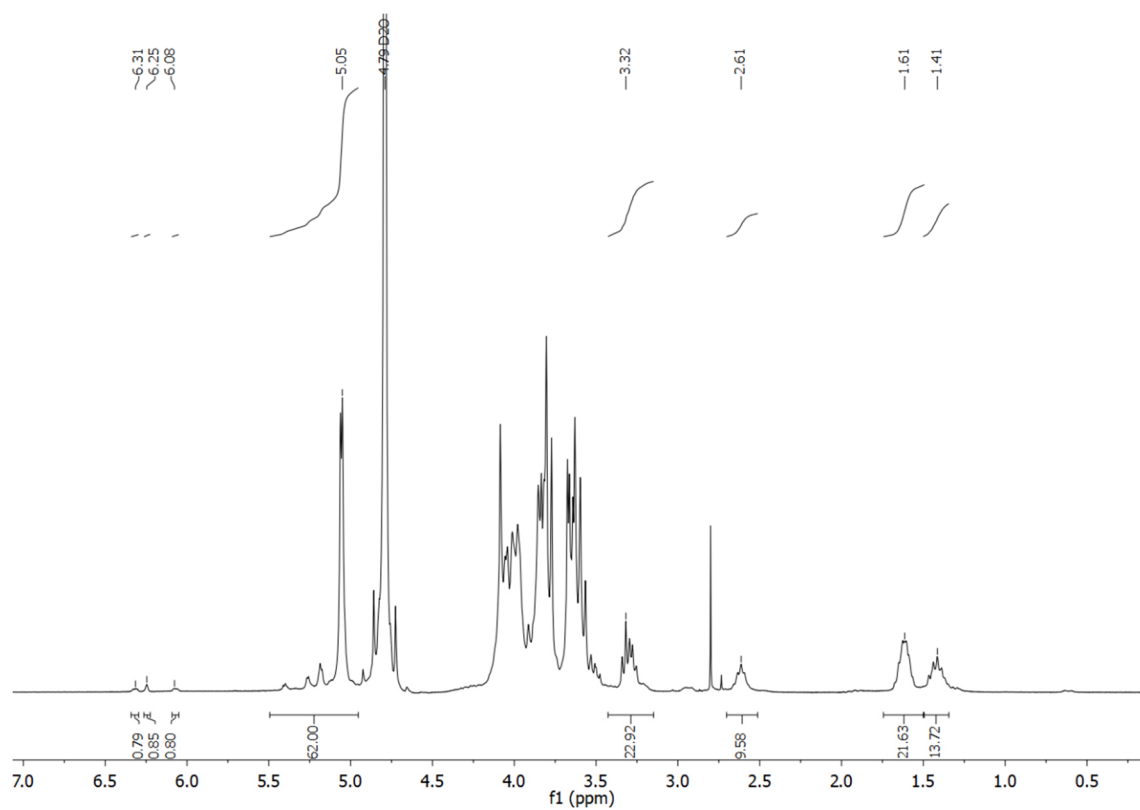


Figure 145: <sup>1</sup>H NMR spectrum of N<sub>3</sub>(4.8)-dextran-norbornene 31.

## 8.28 Analytical data of N<sub>3</sub>(4.8)-dextran-biotin 32

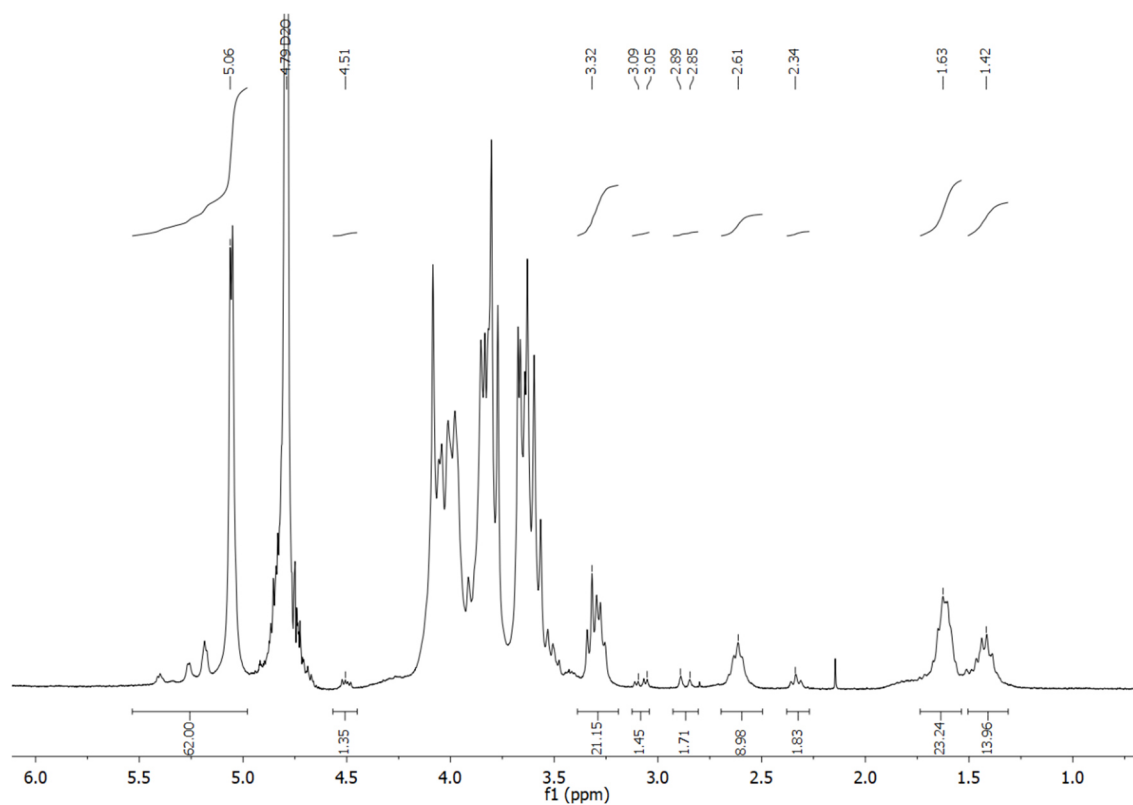
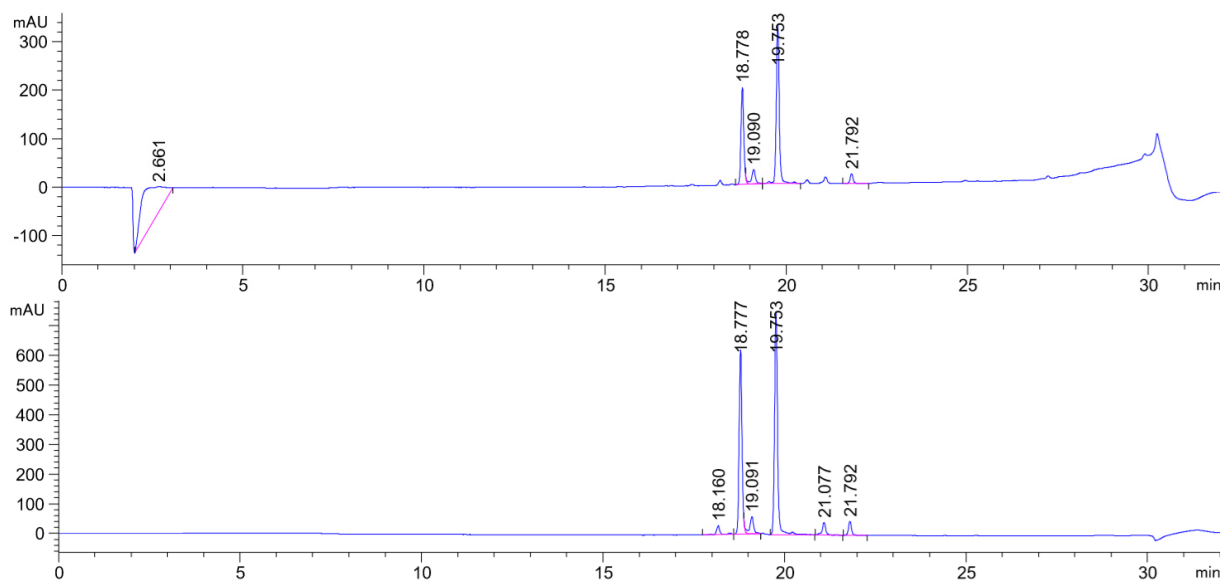
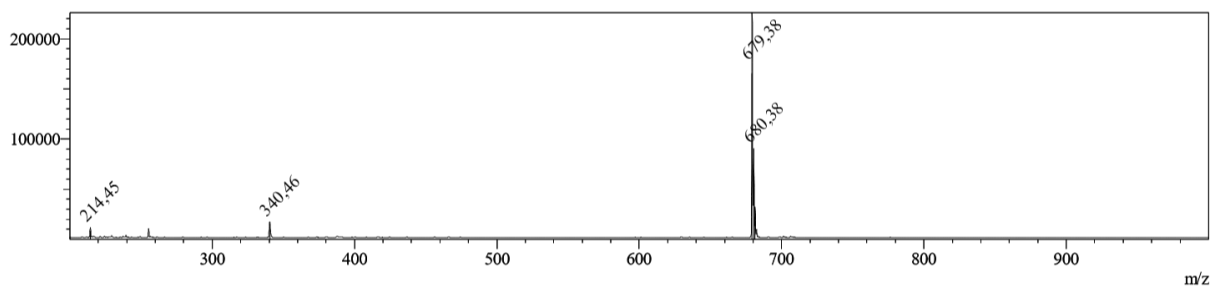


Figure 146: <sup>1</sup>H NMR spectrum of N<sub>3</sub>(4.8)-dextran-biotin 32.

## 8.29 Analytical data of TAMRA-thiol 35



**Figure 147:** Analytical RP-HPLC chromatogram of TAMRA-thiol **35** (both TAMRA isomers): 0 to 60% B (gradient 20 min), 220 nm (upper), 550 nm (lower), RT = 18.778 min; 19.753 min.



**Figure 148:** MS (ESI) of TAMRA-thiol **35**, calculated:  $[M+H]^+ = 679.24$ ;  $[M+2H]^{2+} = 340.12$ ; observed:  $[M+H]^+ = 679.38$ ;  $[M+2H]^{2+} = 340.46$ .

### 8.30 Analytical data of TAMRA-aurein1.2(4.5)-dextran-*N*-Boc-cadaverine 36

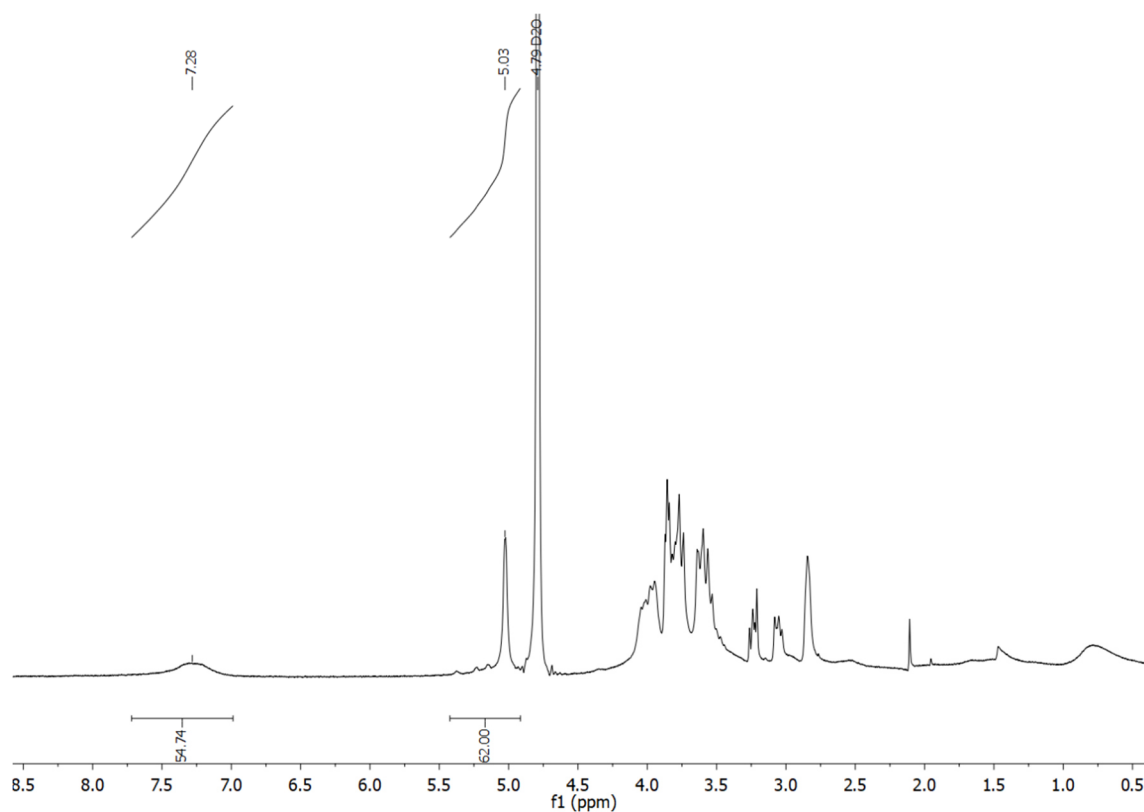


Figure 149:  $^1\text{H}$  NMR spectrum of TAMRA-aurein1.2(4.5)-dextran-*N*-Boc-cadaverine 36.

### 8.31 Analytical data of TAMRA-L17E(3.8)-dextran-*N*-Boc-cadaverine 37

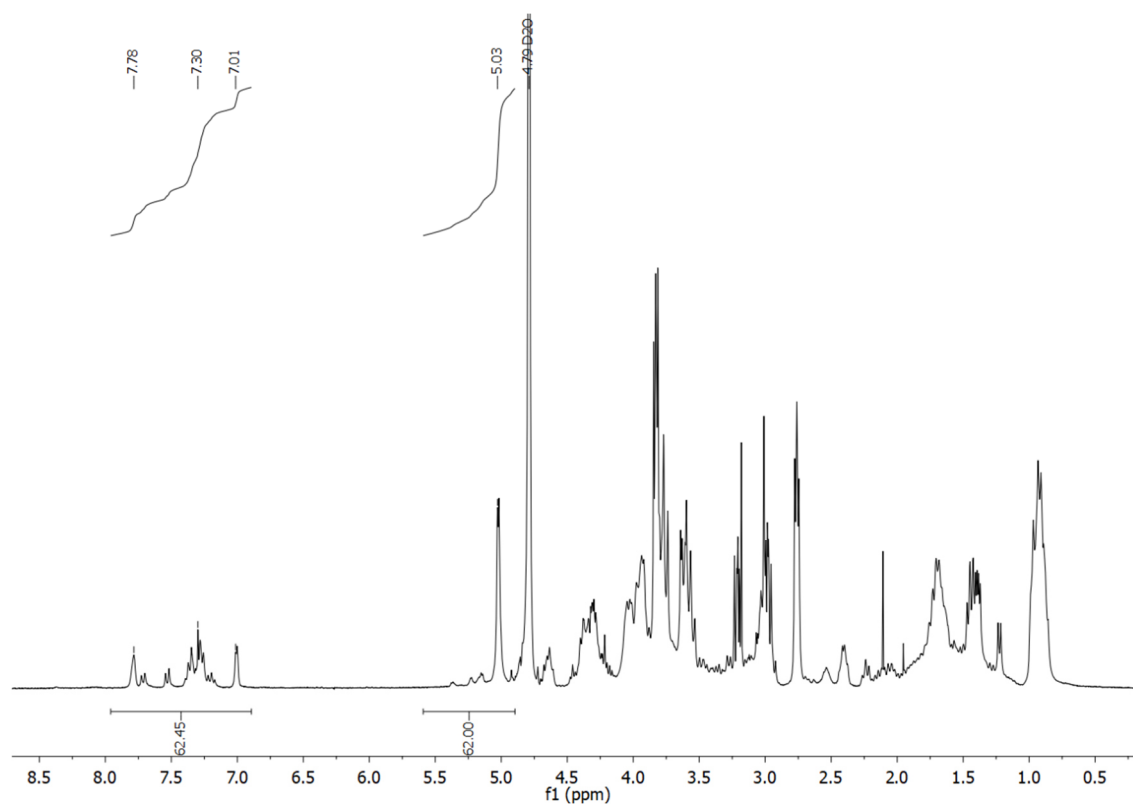


Figure 150:  $^1\text{H}$  NMR spectrum of TAMRA-L17E(3.8)-dextran-*N*-Boc-cadaverine 37.

### 8.32 Analytical data of Ac-Cys(S*t*Bu)-OH 67

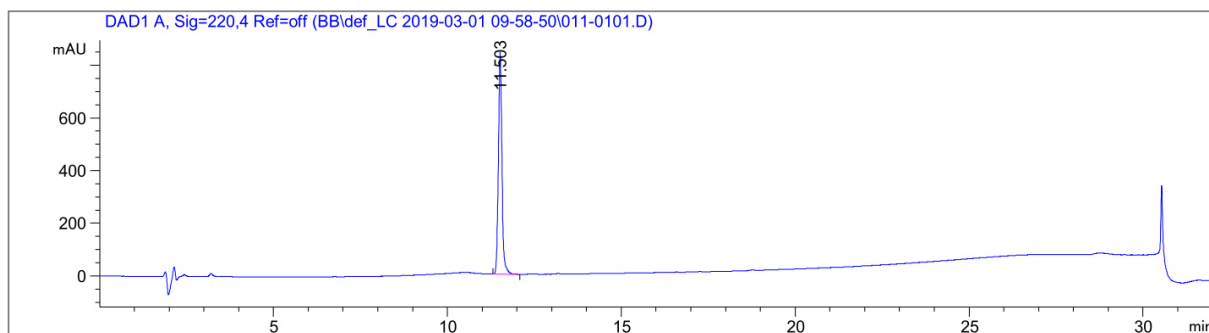


Figure 151: Analytical RP-HPLC chromatogram of Ac-Cys(S*t*Bu)-OH **67**, 10 to 100% B (gradient 20 min), 220 nm, RT = 11.503 min.

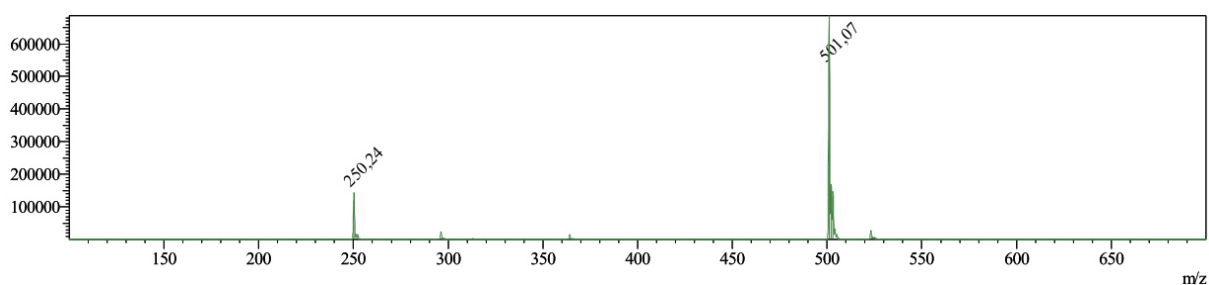


Figure 152: MS (ESI) of Ac-Cys(S*t*Bu)-OH **67**, calculated:  $[M-H]^- = 250.36$ ; observed:  $[M-H]^- = 250.24$ .

### 8.33 Analytical data of Dox-thiol (Ac-Cys-Dox) 40

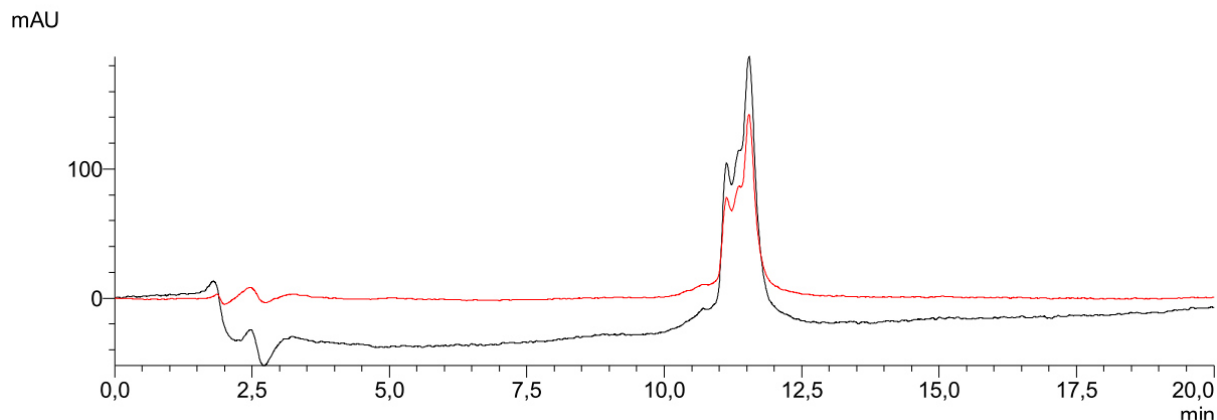


Figure 153: LC-chromatogram of Ac-Cys-Dox **40**, 10 to 100% B (gradient 13.5 min), 220 nm (black), 280 nm (red), RT = 11.31 min.

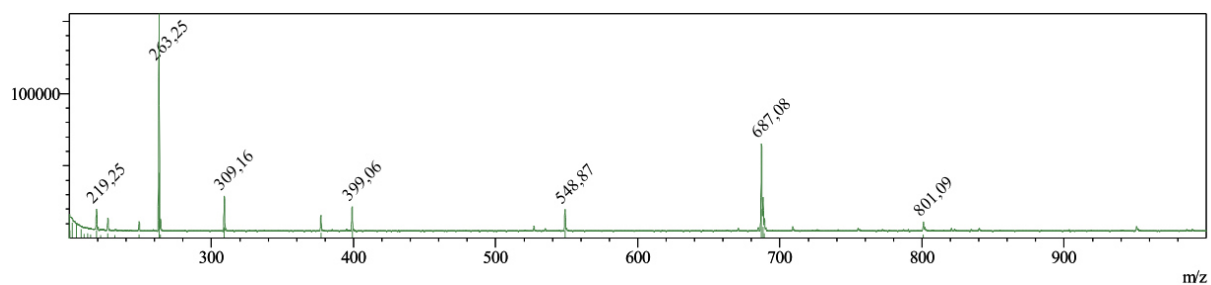


Figure 154: MS (ESI) of Ac-Cys-Dox **40**, calculated:  $[M-H]^- = 687.70$ ; observed:  $[M-H]^- = 687.08$ .

### 8.34 Analytical data of doxorubicin-L17E(5.2)-dextran-*N*-Boc-cadaverine 39

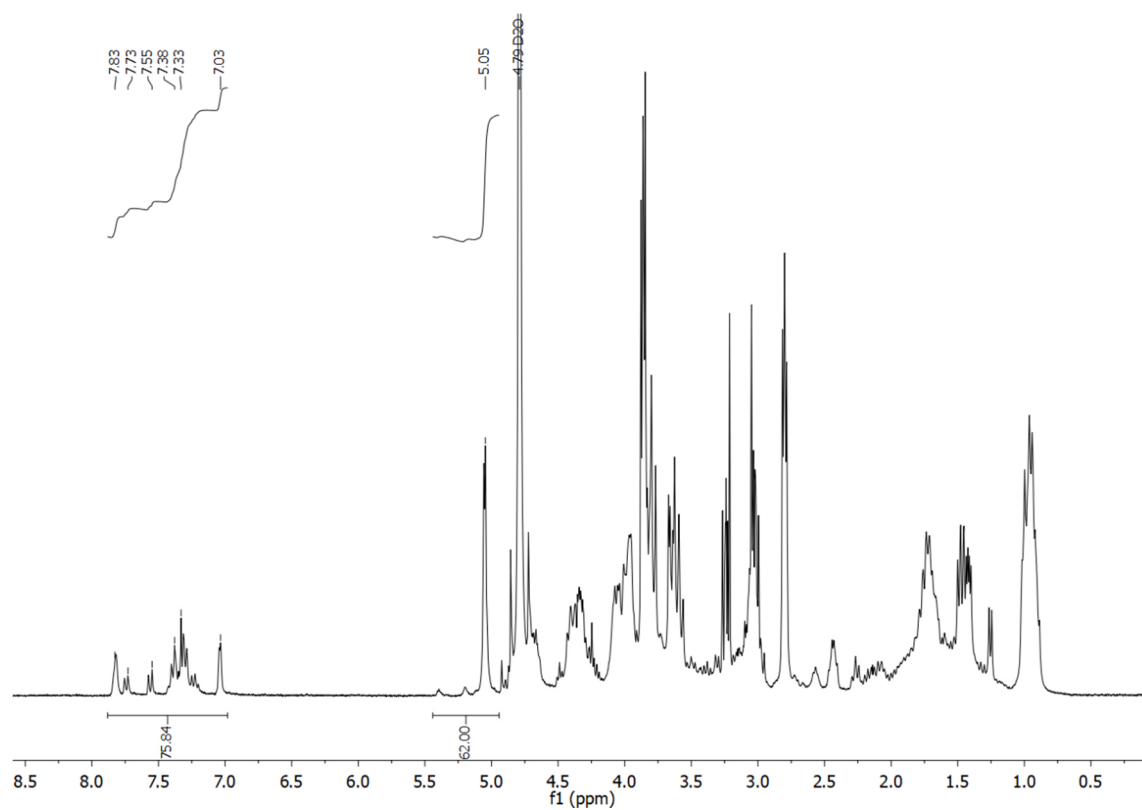


Figure 155: <sup>1</sup>H NMR spectrum of doxorubicin-L17E(5.2)-dextran-*N*-Boc-cadaverine 39.

### 8.35 Analytical data of TAMRA- dextran-*N*-Boc-cadaverine 38

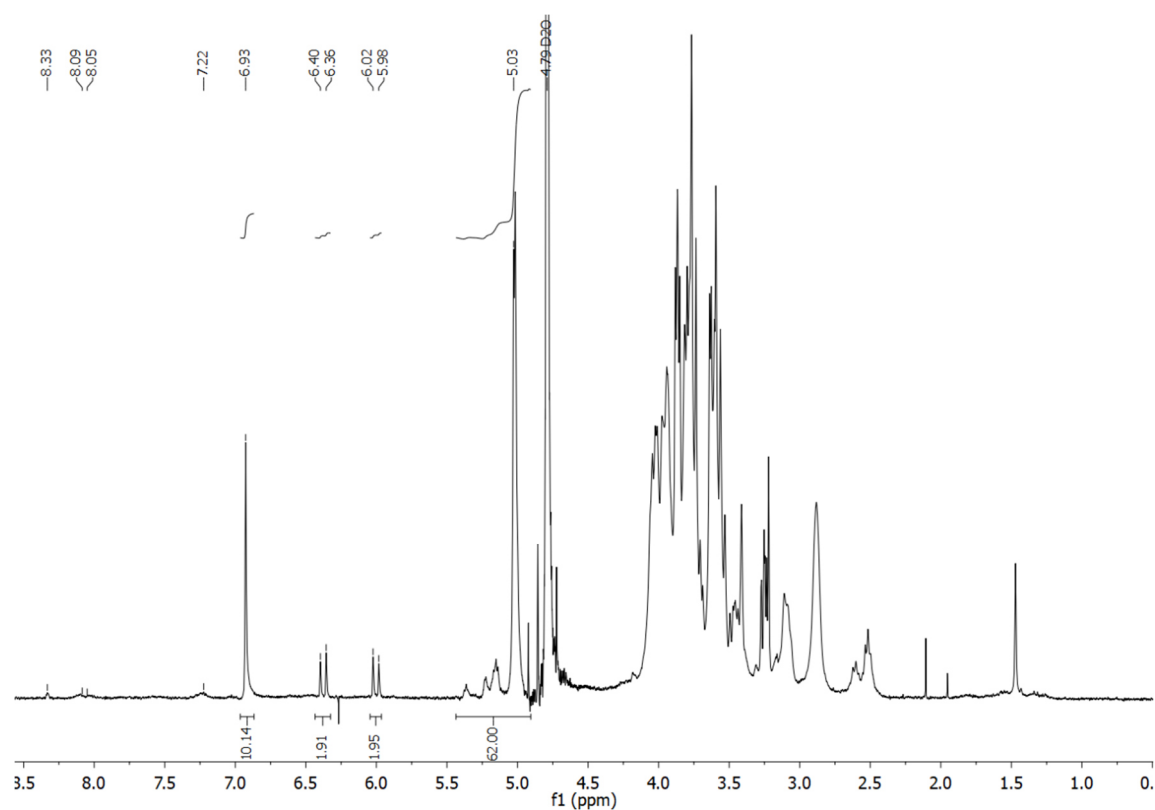
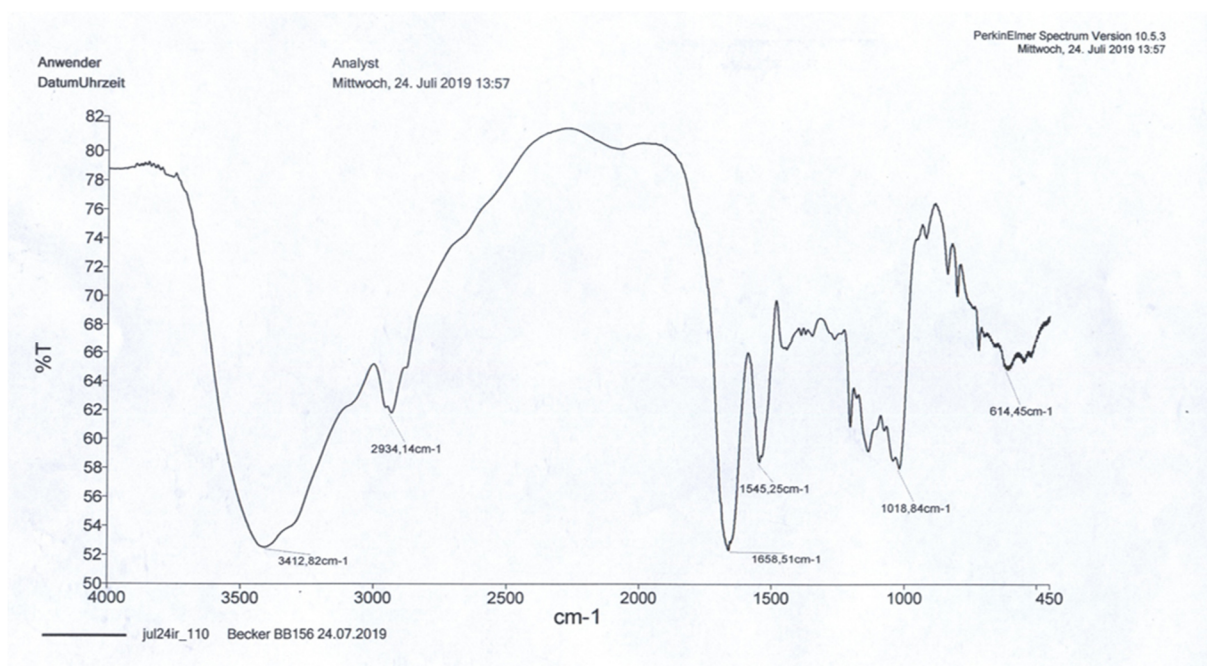
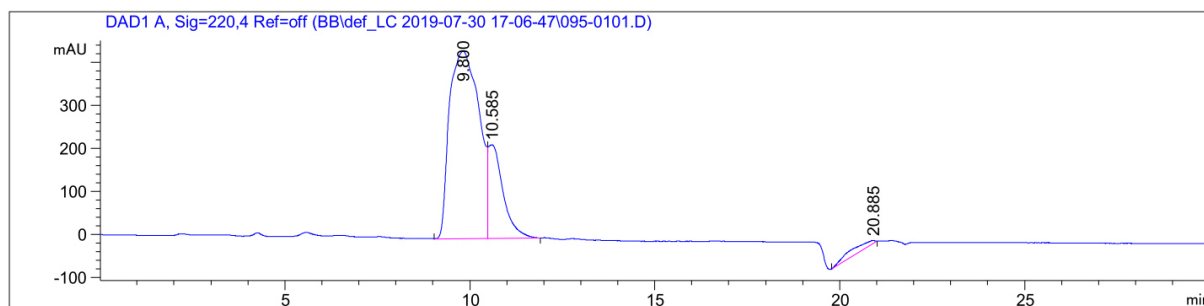


Figure 156: <sup>1</sup>H NMR spectrum of TAMRA-dextran-*N*-Boc-cadaverine 38.

## 8.36 Analytical data of L17E(4.8)-dextran-cadaverine 42



**Figure 157:** IR spectrum of L17E(4.8)-dextran-cadaverine **42**. The azide band of the starting material at a wavenumber of  $2116\text{ cm}^{-1}$  (**Figure 140**) disappeared after CuAAC.



**Figure 158:** SEC chromatogram of L17E(4.8)-dextran-cadaverine **42**, 40% B (isocratic flow, 30 min, 0.6 mL/min,), 220 nm, RT = 9.800 min.

### 8.37 Analytical data of L17E(4.3)-dextran-norbornene 45

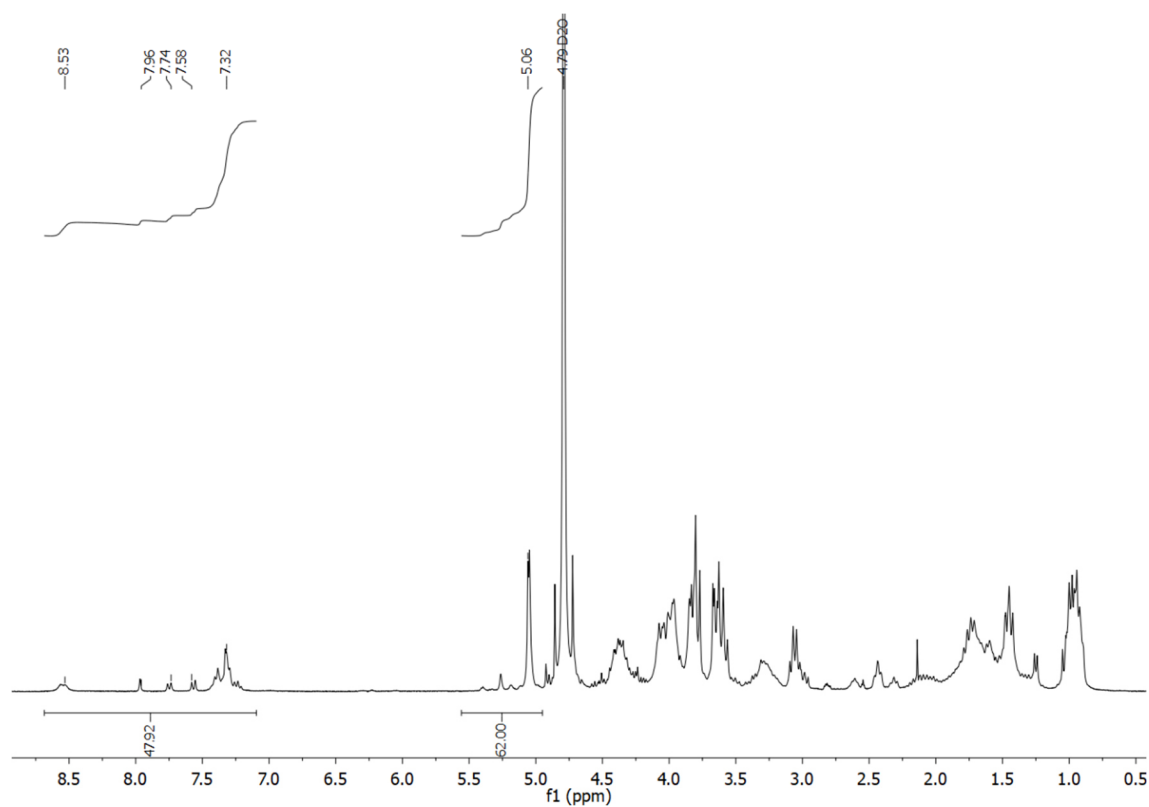


Figure 159: <sup>1</sup>H NMR spectrum of L17E(4.3)-dextran-norbornene 45.

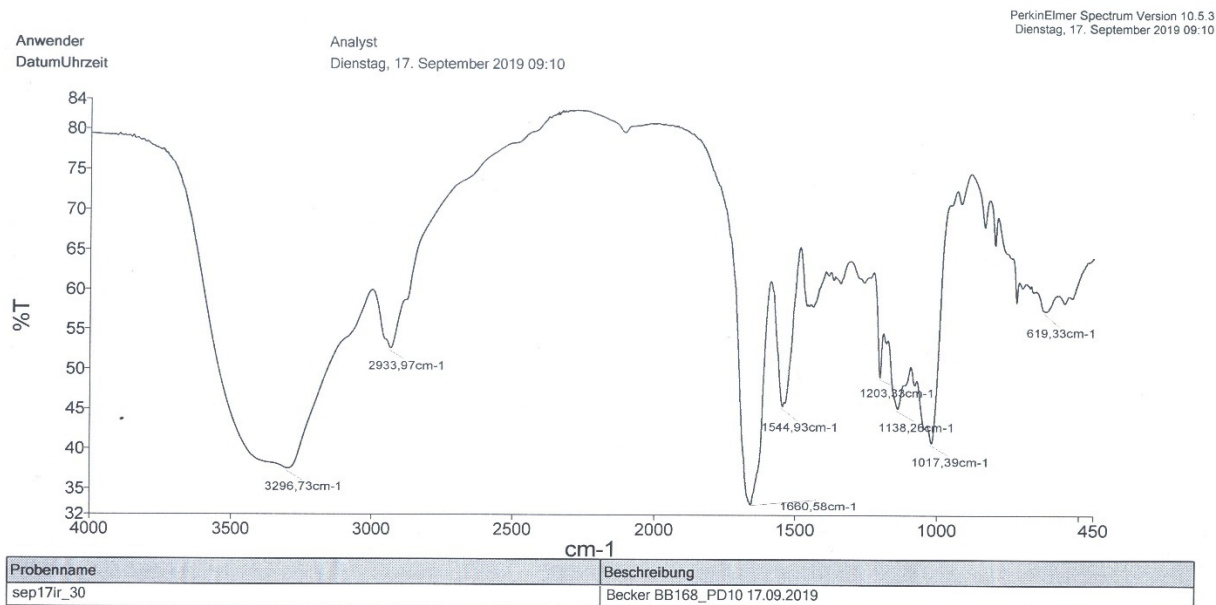


Figure 160: IR spectrum of L17E(4.3)-dextran-norbornene 45. Azide band no longer observable after CuAAC.

### 8.38 Analytical data of L17E(4.8)-dextran-biotin 60

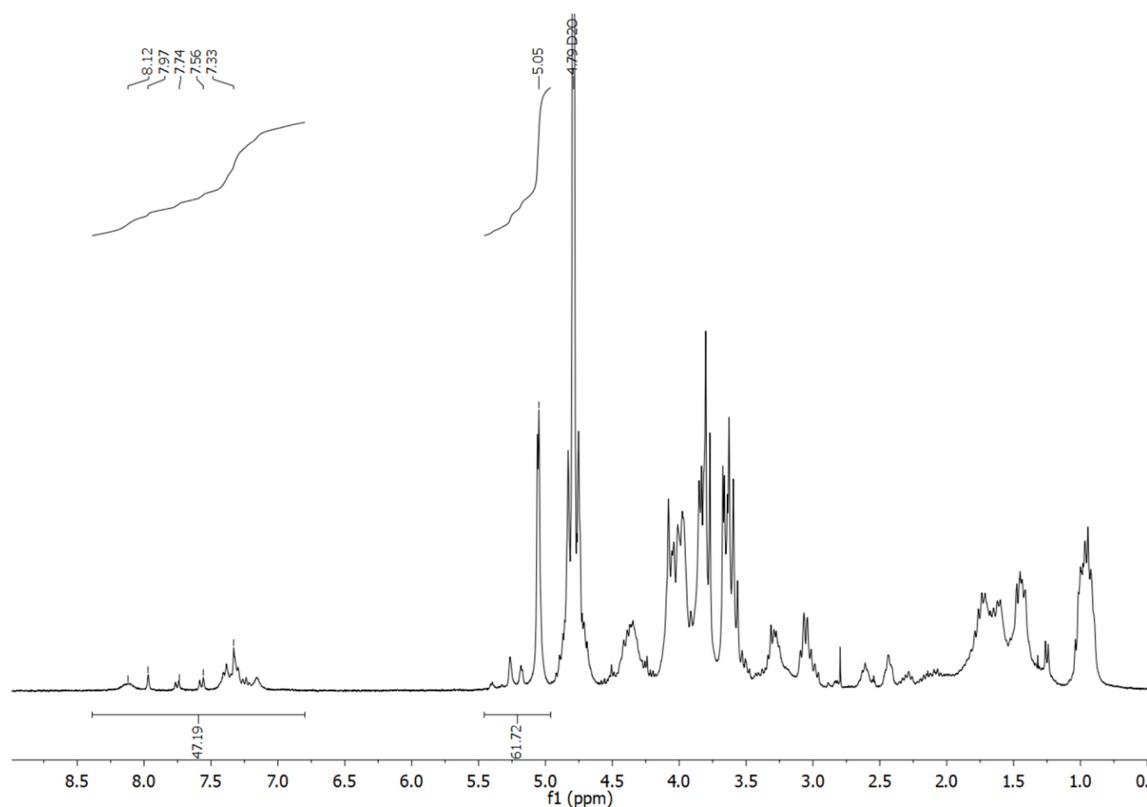


Figure 161: <sup>1</sup>H NMR spectrum of L17E(4.8)-dextran-biotin 60.

### 8.39 Analytical data of L17E(4.3)-dextran-eGFP 46, assembled via alternative strategy: Dextran-to-protein conjugation applying pre-assembled L17E(4.3)-dextran-norbornene 45

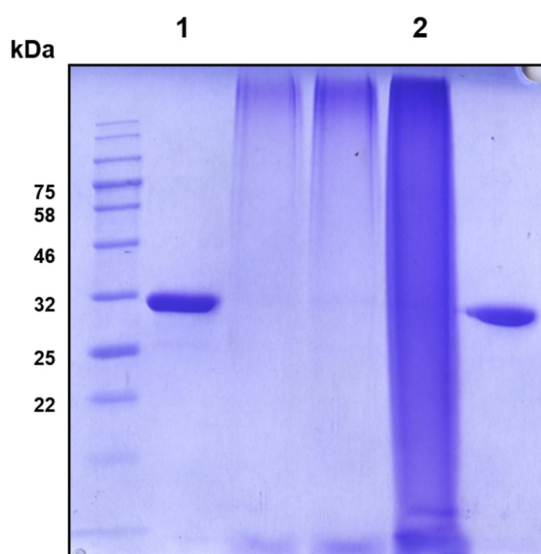
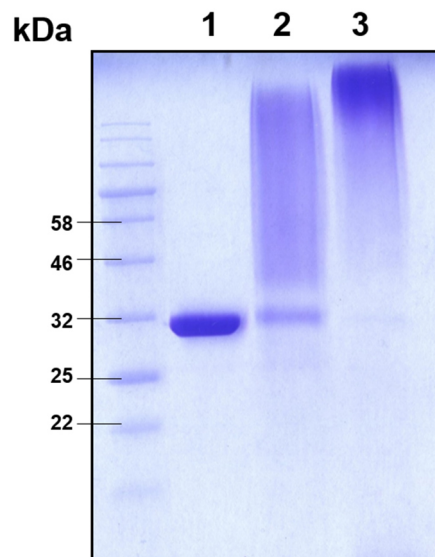


Figure 162: Coomassie stained SDS-PAGE analysis: (1) unmodified eGFP; (2) L17E(4.3)-dextran-eGFP 46 following ineffective IMAC purification.

#### 8.40 Analytical data of L17E(4.3)-dextran-eGFP 44



**Figure 163:** Coomassie stained SDS-PAGE of (1) unmodified eGFP, (2) N3(4.3)-dextran-eGFP 49 and (3) final L17E(4.3)-dextran-eGFP 44.

#### 8.41 Analytical data of L17E(4.8)-dextran-eGFP 52

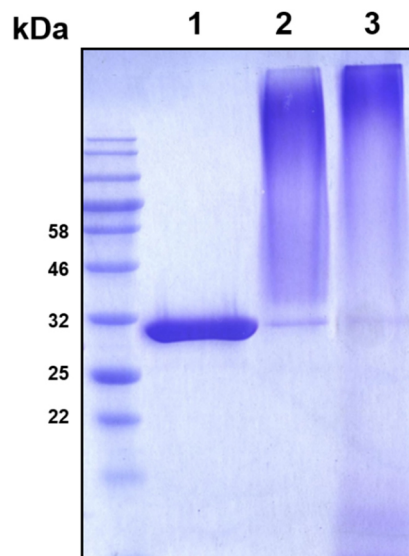


**Figure 164:** Coomassie stained SDS-PAGE of (1) unmodified eGFP, (2) N3(4.8)-dextran-eGFP 51 and (3) final L17E(4.8)-dextran-eGFP 52.

## 8.42 Analytical data of LplA<sup>W37V</sup>-mediated site-specific eGFP modification with methyltetrazine

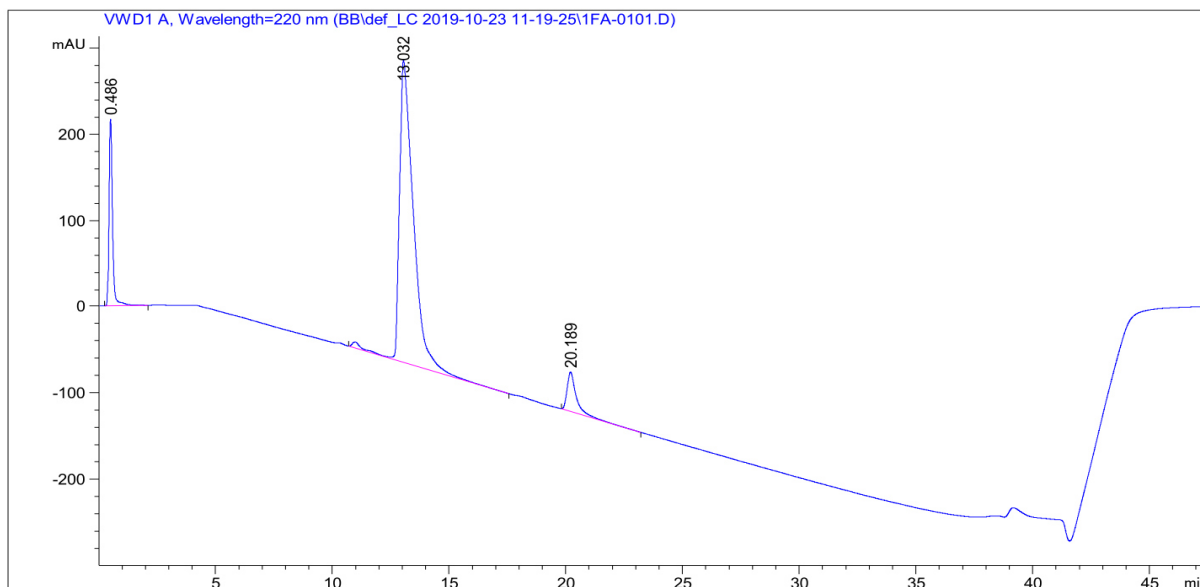


Figure 165: HIC chromatogram of unmodified eGFP; 0to100%B, 35 min, 0.9 mL/min, 220 nm.

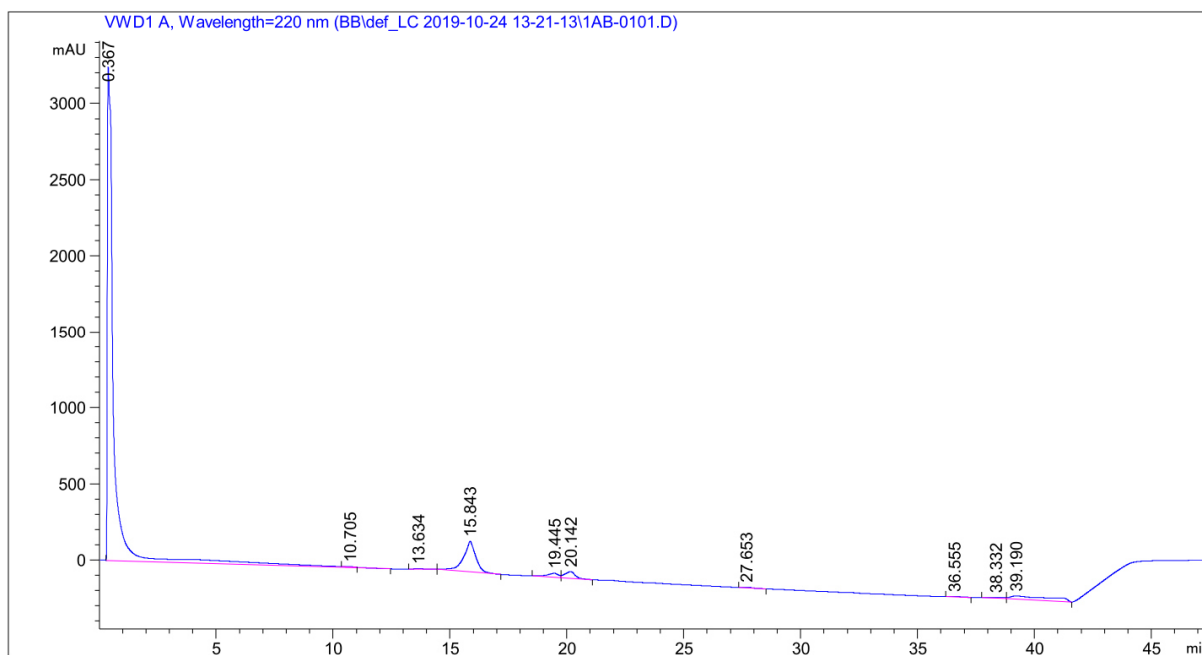
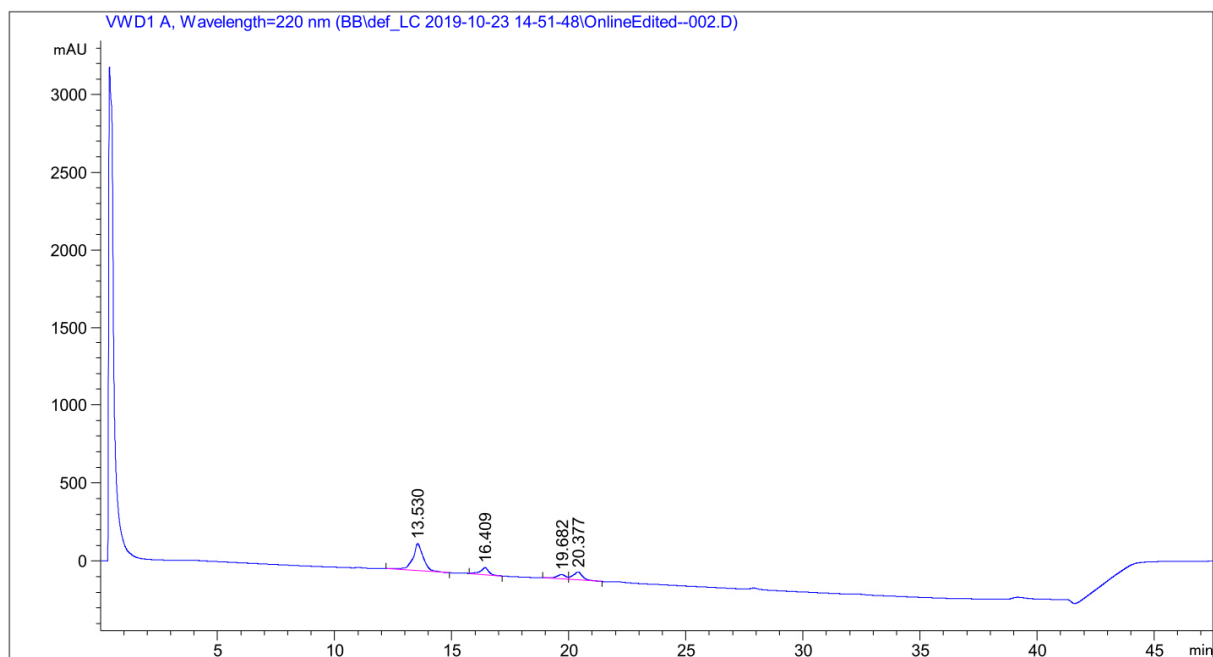


Figure 166: HIC chromatogram of eGFP-MeTet 54 conjugation product applying reference LplA<sup>W37V</sup>; 0to100%B, 35 min, 0.9 mL/min, 220 nm.



**Figure 167:** HIC chromatogram of eGFP-MeTet 55 conjugation product applying LpIA<sup>W37V</sup> (batch 1); 0to100%B, 35 min, 0.9 mL/min, 220 nm.

## 8.43 Protein productions: IMAC purification

### 8.43.1 eGFP-L17E 11 fusion

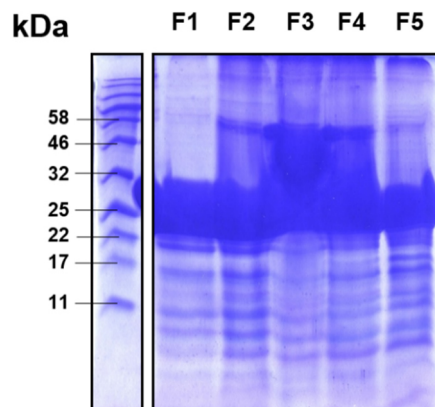


**Figure 168:** Coomassie stained SDS-PAGE analysis of elution fraction of IMAC purified eGFP-L17E 11.

### 8.43.2 LpLA<sup>W37V</sup> batch 1 and batch 2

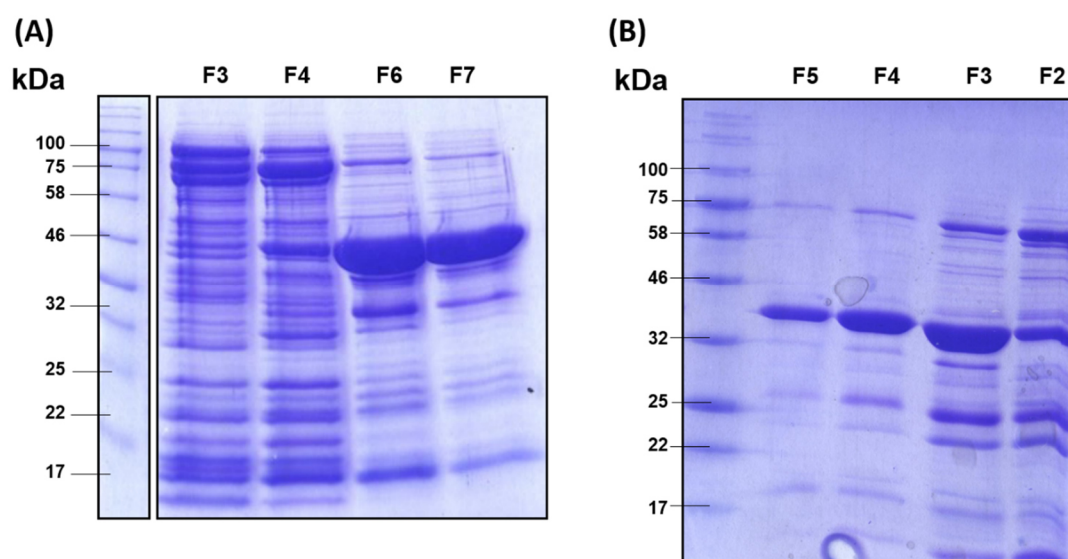


**Figure 169:** Coomassie stained SDS-PAGE analysis of elution fraction of (A) IMAC purified LpLA<sup>W37V</sup> (batch 1) first attempt and (B) IMAC purified LpLA<sup>W37V</sup> (batch 2) second attempt.

---

## References

---

- [1] B. Leader, Q. J. Baca, D. E. Golan, *Nature Reviews Drug Discovery* **2008**, *7*, 21-39.
- [2] A. S. Rathore, A. Bhargava, *Regulatory Toxicology and Pharmacology* **2020**, *110*, 104525.
- [3] V. J. Bruce, B. R. McNaughton, *Cell Chemical Biology* **2017**, *24*, 924-934.
- [4] S. Mitragotri, P. A. Burke, R. Langer, *Nature Reviews Drug Discovery* **2014**, *13*, 655-672.
- [5] D. Pei, M. Buyanova, *Bioconjugate Chemistry* **2019**, *30*, 273-283.
- [6] M. Uhlén, L. Fagerberg, B. M. Hallström, C. Lindskog, P. Oksvold, A. Mardinoglu, Å. Sivertsson, C. Kampf, E. Sjöstedt, A. Asplund, I. Olsson, K. Edlund, E. Lundberg, S. Navani, C. A.-K. Szigartyo, J. Odeberg, D. Djureinovic, J. O. Takanen, S. Hober, T. Alm, P.-H. Edqvist, H. Berling, H. Tegel, J. Mulder, J. Rockberg, P. Nilsson, J. M. Schwenk, M. Hamsten, K. von Feilitzen, M. Forsberg, L. Persson, F. Johansson, M. Zwahlen, G. von Heijne, J. Nielsen, F. Pontén, *Science* **2015**, *347*, 1260419.
- [7] N. J. Yang, M. J. Hinner, *Methods Mol Biol* **2015**, *1266*, 29-53.
- [8] R. Santos, O. Ursu, A. Gaulton, A. P. Bento, R. S. Donadi, C. G. Bologa, A. Karlsson, B. Al-Lazikani, A. Hersey, T. I. Oprea, J. P. Overington, *Nature reviews. Drug discovery* **2017**, *16*, 19-34.
- [9] C. V. Dang, E. P. Reddy, K. M. Shokat, L. Soucek, *Nature reviews. Cancer* **2017**, *17*, 502-508.
- [10] W. Müller-Esterl, *Biochemie: Eine Einführung für Mediziner und Naturwissenschaftler - Unter Mitarbeit von Ulrich Brandt, Oliver Anderka, Stefan Kieß, Katrin Ridinger und Michael Plenikowski, Vol. 1. Auflage*, Elsevier GmbH, München, **2004**.
- [11] G. van Meer, D. R. Voelker, G. W. Feigenson, *Nature Reviews Molecular Cell Biology* **2008**, *9*, 112-124.
- [12] J. C. M. Holthuis, A. K. Menon, *Nature* **2014**, *510*, 48-57.
- [13] K. Simons, J. L. Sampaio, *Cold Spring Harb Perspect Biol* **2011**, *3*, a004697-a004697.
- [14] F.-X. Contreras, A. M. Ernst, F. Wieland, B. Brügger, *Cold Spring Harb Perspect Biol* **2011**, *3*, a004705.
- [15] L. Di, P. Artursson, A. Avdeef, G. F. Ecker, B. Faller, H. Fischer, J. B. Houston, M. Kansy, E. H. Kerns, S. D. Krämer, H. Lennernäs, K. Sugano, *Drug Discovery Today* **2012**, *17*, 905-912.
- [16] K.-C. Chou, D. W. Elrod, *Proteins: Structure, Function, and Bioinformatics* **1999**, *34*, 137-153.
- [17] Z. Wang, *Int J Mol Sci* **2016**, *17*, 95.
- [18] S. J. Singer, G. L. Nicolson, *Science* **1972**, *175*, 720-731.
- [19] D. Lingwood, K. Simons, *Science* **2010**, *327*, 46.
- [20] S. D. Conner, S. L. Schmid, *Nature* **2003**, *422*, 37-44.
- [21] S. Mayor, R. E. Pagano, *Nature Reviews Molecular Cell Biology* **2007**, *8*, 603-612.
- [22] a) J. P. Lim, P. A. Gleeson, *Immunology & Cell Biology* **2011**, *89*, 836-843;  
b) I. Ruseska, A. Zimmer, *Beilstein J Nanotechnol* **2020**, *11*, 101-123.
- [23] R. G. Parton, K. Simons, *Nature Reviews Molecular Cell Biology* **2007**, *8*, 185-194.
- [24] S. R. Elkin, A. M. Lakoduk, S. L. Schmid, *Wiener Medizinische Wochenschrift* **2016**, *166*, 196-204.
- [25] a) J. M. Hogle, *Annu Rev Microbiol* **2002**, *56*, 677-702;  
b) O. Meier, U. F. Greber, *The Journal of Gene Medicine* **2003**, *5*, 451-462.
- [26] S. J. Kaczmarczyk, K. Sitaraman, H. A. Young, S. H. Hughes, D. K. Chatterjee, *Proc Natl Acad Sci U S A* **2011**, *108*, 16998-17003.
- [27] Y. Zhang, L.-C. Yu, *Current Opinion in Biotechnology* **2008**, *19*, 506-510.
- [28] S. R. Paliwal, R. Paliwal, S. P. Vyas, *Drug Delivery* **2015**, *22*, 231-242.
- [29] S. Kube, N. Hersch, E. Naumovska, T. Gensch, J. Hendriks, A. Franzen, L. Landvogt, J.-P. Siebrasse, U. Kubitscheck, B. Hoffmann, R. Merkel, A. Csiszár, *Langmuir* **2017**, *33*, 1051-1059.
- [30] I. Canton, M. Massignani, N. Patikarnmonthon, L. Chierico, J. Robertson, S. A. Renshaw, N. J. Warren, J. P. Madsen, S. P. Armes, A. L. Lewis, G. Battaglia, *The FASEB Journal* **2013**, *27*, 98-108.
- [31] O. S. Thomas, W. Weber, *Frontiers in Bioengineering and Biotechnology* **2019**, *7*, 415.
- [32] a) I. I. Slowing, B. G. Trewyn, V. S. Y. Lin, *Journal of the American Chemical Society* **2007**, *129*, 8845-8849;

- b) Y. Yang, Y. Niu, J. Zhang, A. K. Meka, H. Zhang, C. Xu, C. X. C. Lin, M. Yu, C. Yu, *Small* **2015**, *11*, 2743-2749.
- [33] K. Sandvig, B. van Deurs, *Gene Therapy* **2005**, *12*, 865-872.
- [34] G. L. Beilhartz, S. N. Sugiman-Marangos, R. A. Melnyk, *Biochemical Pharmacology* **2017**, *142*, 13-20.
- [35] P. D. R. Dyer, T. R. Shepherd, A. S. Gollings, S. A. Shorter, M. A. M. Gorringer-Patrick, C.-K. Tang, B. N. Cattoz, L. Baillie, P. C. Griffiths, S. C. W. Richardson, *Journal of Controlled Release* **2015**, *220*, 316-328.
- [36] a) X. Liao, A. E. Rabideau, B. L. Pentelute, *ChemBioChem* **2014**, *15*, 2458-2466;  
b) A. E. Rabideau, B. L. Pentelute, *ACS Chemical Biology* **2016**, *11*, 1490-1501.
- [37] P. Järver, Ü. Langel, *Biochimica et Biophysica Acta (BBA) - Biomembranes* **2006**, *1758*, 260-263.
- [38] A. D. Frankel, C. O. Pabo, *Cell* **1988**, *55*, 1189-1193.
- [39] M. Green, P. M. Loewenstein, *Cell* **1988**, *55*, 1179-1188.
- [40] E. Vivès, P. Brodin, B. Lebleu, *Journal of Biological Chemistry* **1997**, *272*, 16010-16017.
- [41] D. Derossi, A. H. Joliot, G. Chassaing, A. Prochiantz, *Journal of Biological Chemistry* **1994**, *269*, 10444-10450.
- [42] S. Futaki, T. Suzuki, W. Ohashi, T. Yagami, S. Tanaka, K. Ueda, Y. Sugiura, *Journal of Biological Chemistry* **2001**, *276*, 5836-5840.
- [43] F. Wang, Y. Wang, X. Zhang, W. Zhang, S. Guo, F. Jin, *Journal of Controlled Release* **2014**, *174*, 126-136.
- [44] S. Deshayes, M. C. Morris, G. Divita, F. Heitz, *Cellular and Molecular Life Sciences CMLS* **2005**, *62*, 1839-1849.
- [45] D. Derossi, S. Calvet, A. Trembleau, A. Brunissen, G. Chassaing, A. Prochiantz, *The Journal of biological chemistry* **1996**, *271*, 18188-18193.
- [46] A. K. Varkouhi, M. Scholte, G. Storm, H. J. Haisma, *Journal of Controlled Release* **2011**, *151*, 220-228.
- [47] Z. Qian, A. Martyna, R. L. Hard, J. Wang, G. Appiah-Kubi, C. Coss, M. A. Phelps, J. S. Rossman, D. Pei, *Biochemistry* **2016**, *55*, 2601-2612.
- [48] D. W. Pack, D. Putnam, R. Langer, *Biotechnology and Bioengineering* **2000**, *67*, 217-223.
- [49] C. Lin, J. F. J. Engbersen, *Journal of Controlled Release* **2008**, *132*, 267-272.
- [50] a) M. Horn, F. Reichart, S. Natividad-Tietz, D. Diaz, I. Neundorf, *Chemical Communications* **2016**, *52*, 2261-2264;  
b) G. Lättig-Tünnemann, M. Prinz, D. Hoffmann, J. Behlke, C. Palm-Apergi, I. Morano, H. D. Herce, M. C. Cardoso, *Nature Communications* **2011**, *2*, 453;  
c) J. Song, Z. Qian, A. Sahni, K. Chen, D. Pei, *ChemBioChem* **2019**, *20*, 2085-2088.
- [51] N. Nischan, H. D. Herce, F. Natale, N. Bohlke, N. Budisa, M. C. Cardoso, C. P. R. Hackenberger, *Angewandte Chemie International Edition* **2015**, *54*, 1950-1953.
- [52] H. D. Herce, D. Schumacher, A. F. L. Schneider, A. K. Ludwig, F. A. Mann, M. Fillies, M.-A. Kasper, S. Reinke, E. Krause, H. Leonhardt, M. C. Cardoso, C. P. R. Hackenberger, *Nature Chemistry* **2017**, *9*, 762-771.
- [53] A. F. L. Schneider, A. L. D. Wallabregue, L. Franz, C. P. R. Hackenberger, *Bioconjugate Chemistry* **2019**, *30*, 400-404.
- [54] M. Sauter, M. Strieker, C. Kleist, A. Wischnjow, V. Daniel, A. Altmann, U. Haberkorn, W. Mier, *Journal of Controlled Release* **2020**, *322*, 200-208.
- [55] W. Li, F. Nicol, F. C. Szoka, *Advanced Drug Delivery Reviews* **2004**, *56*, 967-985.
- [56] M. Akishiba, T. Takeuchi, Y. Kawaguchi, K. Sakamoto, H. H. Yu, I. Nakase, T. Takatani-Nakase, F. Madani, A. Graslund, S. Futaki, *Nat Chem* **2017**, *9*, 751-761.
- [57] N. Tamemoto, M. Akishiba, K. Sakamoto, K. Kawano, H. Noguchi, S. Futaki, *Molecular Pharmaceutics* **2020**, *17*, 2175-2185.
- [58] J. V. V. Arafiles, H. Hirose, M. Akishiba, S. Tsuji, M. Imanishi, S. Futaki, *Bioconjugate Chemistry* **2020**, *31*, 547-553.

- [59] S. G. Patel, E. J. Sayers, L. He, R. Narayan, T. L. Williams, E. M. Mills, R. K. Allemann, L. Y. P. Luk, A. T. Jones, Y.-H. Tsai, *Scientific Reports* **2019**, *9*, 6298.
- [60] G. A. Eggimann, S. Buschor, T. Darbre, J.-L. Reymond, *Organic & Biomolecular Chemistry* **2013**, *11*, 6717-6733.
- [61] M. Richter, A. Chakrabarti, I. R. Ruttekkolk, B. Wiesner, M. Beyermann, R. Brock, J. Rademann, *Chemistry – A European Journal* **2012**, *18*, 16708-16715.
- [62] A. Chakrabarti, J. J. Witsenburg, M. D. Sinzinger, M. Richter, R. Wallbrecher, J. C. Cluitmans, W. P. R. Verdurmen, S. Tanis, M. J. W. Adjobo-Hermans, J. Rademann, R. Brock, *Biochimica et Biophysica Acta (BBA) - Biomembranes* **2014**, *1838*, 3097-3106.
- [63] a) M. Zasloff, *Nature* **2002**, *415*, 389-395;  
b) L.-j. Zhang, R. L. Gallo, *Current Biology* **2016**, *26*, R14-R19.
- [64] G. Wang, X. Li, Z. Wang, *Nucleic Acids Res* **2016**, *44*, D1087-D1093.
- [65] T. Rozek, J. H. Bowie, J. C. Wallace, M. J. Tyler, *Rapid Communications in Mass Spectrometry* **2000**, *14*, 2002-2011.
- [66] T. Rozek, K. L. Wegener, J. H. Bowie, I. N. Olver, J. A. Carver, J. C. Wallace, M. J. Tyler, *European Journal of Biochemistry* **2000**, *267*, 5330-5341.
- [67] D. I. Fernandez, A. P. Le Brun, T. C. Whitwell, M.-A. Sani, M. James, F. Separovic, *Physical Chemistry Chemical Physics* **2012**, *14*, 15739-15751.
- [68] M. Li, Y. Tao, Y. Shu, J. R. LaRochelle, A. Steinauer, D. Thompson, A. Schepartz, Z.-Y. Chen, D. R. Liu, *Journal of the American Chemical Society* **2015**, *137*, 14084-14093.
- [69] L. Yan, M. E. Adams, *Journal of Biological Chemistry* **1998**, *273*, 2059-2066.
- [70] M. Akishiba, S. Futaki, *Molecular Pharmaceutics* **2019**, *16*, 2540-2548.
- [71] C. Larsen, *Advanced Drug Delivery Reviews* **1989**, *3*, 103-154.
- [72] R. Mehvar, *Journal of Controlled Release* **2000**, *69*, 1-25.
- [73] R. Fagnani, M. S. Hagan, R. Bartholomew, *Cancer Research* **1990**, *50*, 3638.
- [74] R. Fagnani, S. Halpern, M. Hagan, *Nucl Med Commun* **1995**, *16*, 362-369.
- [75] a) R. G. Melton, C. N. Wiblin, R. L. Foster, R. F. Sherwood, *Biochemical Pharmacology* **1987**, *36*, 105-112;  
b) S. B. van Witteloostuijn, S. L. Pedersen, K. J. Jensen, *ChemMedChem* **2016**, *11*, 2474-2495.
- [76] H. Schneider, L. Deweid, T. Pirzer, D. Yanakieva, S. Englert, B. Becker, O. Avrutina, H. Kolmar, *ChemistryOpen* **2019**, *8*, 354-357.
- [77] a) M. S. Verma, F. X. Gu, *Carbohydrate polymers*. **2012**, *87*, 2740-2744;  
b) M. Yalpani, D. E. Brooks, *Journal of Polymer Science: Polymer Chemistry Edition* **1985**, *23*, 1395-1405.
- [78] H. Schneider, D. Yanakieva, A. Macarrón, L. Deweid, B. Becker, S. Englert, O. Avrutina, H. Kolmar, *ChemBioChem* **2019**, *20*, 3006-3012.
- [79] H. C. Kolb, M. G. Finn, K. B. Sharpless, *Angewandte Chemie International Edition* **2001**, *40*, 2004-2021.
- [80] a) R. Huisgen, *Angewandte Chemie International Edition in English* **1963**, *2*, 633-645;  
b) R. Huisgen, *Angewandte Chemie International Edition in English* **1963**, *2*, 565-598.
- [81] a) V. V. Rostovtsev, L. G. Green, V. V. Fokin, K. B. Sharpless, *Angewandte Chemie International Edition* **2002**, *41*, 2596-2599;  
b) C. W. Tornøe, C. Christensen, M. Meldal, *The Journal of Organic Chemistry* **2002**, *67*, 3057-3064.
- [82] a) C. Besanceney-Webler, H. Jiang, T. Zheng, L. Feng, D. Soriano del Amo, W. Wang, L. M. Klivansky, F. L. Marlow, Y. Liu, P. Wu, *Angewandte Chemie International Edition* **2011**, *50*, 8051-8056;  
b) C. Uttamapinant, A. Tangpeerachaikul, S. Grecian, S. Clarke, U. Singh, P. Slade, K. R. Gee, A. Y. Ting, *Angew Chem Int Ed Engl* **2012**, *51*, 5852-5856.
- [83] a) J. Dommerholt, S. Schmidt, R. Temming, L. J. A. Hendriks, F. P. J. T. Rutjes, J. C. M. van Hest, D. J. Lefeber, P. Friedl, F. L. van Delft, *Angewandte Chemie International Edition* **2010**, *49*, 9422-9425;

- b) E. M. Sletten, C. R. Bertozzi, *Accounts of Chemical Research* **2011**, *44*, 666-676.
- [84] E. M. Sletten, C. R. Bertozzi, *Angewandte Chemie International Edition* **2009**, *48*, 6974-6998.
- [85] a) N. J. Agard, J. A. Prescher, C. R. Bertozzi, *Journal of the American Chemical Society* **2004**, *126*, 15046-15047;  
b) J. M. Baskin, J. A. Prescher, S. T. Laughlin, N. J. Agard, P. V. Chang, I. A. Miller, A. Lo, J. A. Codelli, C. R. Bertozzi, *Proc Natl Acad Sci U S A* **2007**, *104*, 16793-16797;  
c) N. E. Mbua, J. Guo, M. A. Wolfert, R. Steet, G.-J. Boons, *ChemBioChem* **2011**, *12*, 1912-1921.
- [86] J. M. J. M. Ravasco, H. Faustino, A. Trindade, P. M. P. Gois, *Chemistry – A European Journal* **2019**, *25*, 43-59.
- [87] A. Beck, L. Goetsch, C. Dumontet, N. Corvaia, *Nature Reviews Drug Discovery* **2017**, *16*, 315-337.
- [88] a) M. L. Blackman, M. Royzen, J. M. Fox, *Journal of the American Chemical Society* **2008**, *130*, 13518-13519;  
b) N. K. Devaraj, R. Weissleder, S. A. Hilderbrand, *Bioconjugate Chemistry* **2008**, *19*, 2297-2299;  
c) T. Plass, S. Milles, C. Koehler, J. Szymański, R. Mueller, M. Wießler, C. Schultz, E. A. Lemke, *Angewandte Chemie International Edition* **2012**, *51*, 4166-4170;  
d) J. Schoch, M. Staudt, A. Samanta, M. Wiessler, A. Jäschke, *Bioconjugate Chemistry* **2012**, *23*, 1382-1386.
- [89] R. A. Carboni, R. V. Lindsey, *Journal of the American Chemical Society* **1959**, *81*, 4342-4346.
- [90] K. Lang, L. Davis, J. Torres-Kolbus, C. Chou, A. Deiters, J. W. Chin, *Nature Chemistry* **2012**, *4*, 298-304.
- [91] a) M. Griffin, R. Casadio, C. M. Bergamini, *Biochemical Journal* **2002**, *368*, 377-396;  
b) P. Strop, *Bioconjugate Chemistry* **2014**, *25*, 855-862.
- [92] D. Lukas, A. Olga, K. Harald, *Biological Chemistry* **2019**, *400*, 257-274.
- [93] a) I. Plagmann, A. Chalaris, A. A. Kruglov, S. Nedospasov, P. Rosenstiel, S. Rose-John, J. Scheller, *Journal of Biotechnology* **2009**, *142*, 170-178;  
b) T. Takazawa, N. Kamiya, H. Ueda, T. Nagamune, *Biotechnology and Bioengineering* **2004**, *86*, 399-404.
- [94] a) M. Kitaoka, Y. Tsuruda, Y. Tanaka, M. Goto, M. Mitsumori, K. Hayashi, Y. Hiraishi, K. Miyawaki, S. Noji, N. Kamiya, *Chemistry – A European Journal* **2011**, *17*, 5387-5392;  
b) J. Tominaga, Y. Kemori, Y. Tanaka, T. Maruyama, N. Kamiya, M. Goto, *Chemical Communications* **2007**, 401-403.
- [95] a) J. Buchardt, H. Selvig, P. F. Nielsen, N. L. Johansen, *Peptide Science* **2010**, *94*, 229-235;  
b) S. Scaramuzza, G. Tonon, A. Olianias, I. Messana, R. Schrepfer, G. Orsini, P. Caliceti, *Journal of Controlled Release* **2012**, *164*, 355-363.
- [96] a) G. Falck, K. M. Müller, *Antibodies (Basel)* **2018**, *7*, 4;  
b) H. Schneider, L. Deweid, O. Avrutina, H. Kolmar, *Analytical Biochemistry* **2020**, *595*, 113615.
- [97] a) D. E. Green, T. W. Morris, J. Green, J. E. Cronan, Jr., J. R. Guest, *Biochemical Journal* **1995**, *309*, 853-862;  
b) S. Puthenveetil, D. S. Liu, K. A. White, S. Thompson, A. Y. Ting, *Journal of the American Chemical Society* **2009**, *131*, 16430-16438.
- [98] M. Fernández-Suárez, H. Baruah, L. Martínez-Hernández, K. T. Xie, J. M. Baskin, C. R. Bertozzi, A. Y. Ting, *Nature Biotechnology* **2007**, *25*, 1483-1487.
- [99] C. Uttamapinant, K. A. White, H. Baruah, S. Thompson, M. Fernández-Suárez, S. Puthenveetil, A. Y. Ting, *Proceedings of the National Academy of Sciences* **2010**, *107*, 10914.
- [100] M. Best, A. Degen, M. Baalman, T. T. Schmidt, R. Wombacher, *ChemBioChem* **2015**, *16*, 1158-1162.
- [101] D. S. Liu, A. Tangpeerachaikul, R. Selvaraj, M. T. Taylor, J. M. Fox, A. Y. Ting, *Journal of the American Chemical Society* **2012**, *134*, 792-795.
- [102] M. Baalman, M. J. Ziegler, P. Werther, J. Wilhelm, R. Wombacher, *Bioconjugate Chemistry* **2019**, *30*, 1405-1414.
- [103] P. E. Nielsen, M. Egholm, R. H. Berg, O. Buchardt, *Science* **1991**, *254*, 1497.
- [104] P. E. Nielsen, *Chemistry & Biodiversity* **2010**, *7*, 786-804.

- 
- [105] J. Saarbach, P. M. Sabale, N. Winssinger, *Current Opinion in Chemical Biology* **2019**, *52*, 112-124.
- [106] W. B. Kauffman, S. Guha, W. C. Wimley, *Nature Communications* **2018**, *9*, 2568.
- [107] P. Sazani, S.-H. Kang, M. A. Maier, C. Wei, J. Dillman, J. Summerton, M. Manoharan, R. Kole, *Nucleic Acids Res* **2001**, *29*, 3965-3974.
- [108] P. E. Nielsen, T. Shiraishi, *Artificial DNA: PNA & XNA* **2011**, *2*, 90-99.
- [109] E. L. Sievers, P. D. Senter, *Annual Review of Medicine* **2013**, *64*, 15-29.
- [110] a) G. M. Dubowchik, R. A. Firestone, *Bioorganic & Medicinal Chemistry Letters* **1998**, *8*, 3341-3346;  
b) G. M. Dubowchik, R. A. Firestone, L. Padilla, D. Willner, S. J. Hofstead, K. Mosure, J. O. Knipe, S. J. Lasch, P. A. Trail, *Bioconjugate Chemistry* **2002**, *13*, 855-869.
- [111] J. D. Bargh, A. Isidro-Llobet, J. S. Parker, D. R. Spring, *Chemical Society Reviews* **2019**, *48*, 4361-4374.
- [112] F. Kratz, A. Mansour, J. Soltau, A. Warnecke, I. Fichtner, C. Unger, J. Dreves, *Archiv der Pharmazie* **2005**, *338*, 462-472.
- [113] N. Dan, S. Setua, V. K. Kashyap, S. Khan, M. Jaggi, M. M. Yallapu, S. C. Chauhan, *Pharmaceuticals (Basel)* **2018**, *11*, 32.
- [114] a) M. Baalman, L. Neises, S. Bitsch, H. Schneider, L. Deweid, P. Werther, N. Ilkenhans, M. Wolfring, M. J. Ziegler, J. Wilhelm, H. Kolmar, R. Wombacher, *Angewandte Chemie International Edition* **2020**, *59*, 12885-12893;  
b) J. G. Plaks, R. Falatach, M. Kastantin, J. A. Berberich, J. L. Kaar, *Bioconjugate Chemistry* **2015**, *26*, 1104-1112.
- [115] Jmol: an open-source Java viewer for chemical structures in 3D. <http://www.jmol.org/>, March 2021
- [116] C. Pérez-Arnaiz, N. Busto, J. M. Leal, B. García, *The Journal of Physical Chemistry B* **2014**, *118*, 1288-1295.
- [117] D. Görlich, U. Kutay, *Annual Review of Cell and Developmental Biology* **1999**, *15*, 607-660.
- [118] S. F. Hedegaard, M. S. Derbas, T. K. Lind, M. R. Kasimova, M. V. Christensen, M. H. Michaelsen, R. A. Campbell, L. Jorgensen, H. Franzyk, M. Cárdenas, H. M. Nielsen, *Scientific Reports* **2018**, *8*, 6327.
- [119] M. Richter, A. Chakrabarti, I. R. Ruttekkolk, B. Wiesner, M. Beyermann, R. Brock, J. Rademann, *Chemistry* **2012**, *18*, 16708-16715.

---

## Abbreviations

---

2-CE	2-carboxyethyl
2-ctc	2-chlorotritylchloride
ADC	antibody-drug conjugate
AMP	antimicrobial peptide
BCN	bicyclo[6.1.0]nonyne
Boc	<i>tert</i> -butyloxycarbonyl
BTAA	2-(4-((bis((1-( <i>tert</i> -butyl)-1H-1,2,3-triazol-4-yl)methyl)amino)methyl)-1H-1,2,3-triazol-1-yl)acetic acid
CatB	cathepsin B
Cer	ceramide
Cit	citrulline
CLIC	clathrin- and dynamin-independent carrier
CLSM	confocal laser scanning microscopy
CuAAC	copper(I)-catalyzed azide-alkyne cycloaddition
DAG	diacylglycerol
DC	double coupling
DCC	<i>N,N</i> -dicyclohexylcarbodiimide
DCM	dichloromethane
dde	(1-(4,4-dimethyl-2,6-dioxocyclohexylidene)ethyl
ddH <sub>2</sub> O	double deionized water
DEE	diethylether
DIC	<i>N,N</i> -diisopropylcarbodiimide
DIEA	<i>N,N</i> -diisopropylethylamine
DMEM	Dulbecco's Modified Eagle's Medium
DMF	<i>N,N</i> -dimethylformamide
DMSO	dimethyl sulfoxide
Dox	doxorubicin
Dox-HCl	doxorubicin hydrochloride
DTT	dithiothreitol
EDTA	ethylenediaminetetraacetic acid
EEDQ	<i>N</i> -ethoxycarbonyl-2-ethoxy-1,2-dihydroquinoline
EEE	endosomal escape enhancer
eGFP	enhanced green fluorescent protein
EGFR	epidermal growth factor receptor
FACS	fluorescence-activated cell sorting
FBS	fetal bovine serum
FITC	fluorescein isothiocyanate
Fmoc	fluorenylmethoxycarbonyl
GEEC	GPI-anchored protein enriched early endosomal compartment
GFP	green fluorescent protein
Gly	glycine
GPCR	G-protein-coupled receptor
GPI	glycosylphosphatidylinositol
GSL	glycosphingolipid
HATU	1-[bis(dimethylamino)methylene]-1H-1,2,3-triazolo[4,5-b]pyridinium 3-oxide hexafluorophosphat
HBTU	3-[bis(dimethylamino)methylumyl]-3H-benzotriazol-1-oxid-hexafluorophosphat
HIC	Hydrophobic interaction chromatography
His	histidine
iEDDA	inverse electron-demand Diels–Alder reaction
IMAC	immobilized metal affinity chromatography

---

IR	infrared
LC-MS	liquid chromatography–mass spectrometry
LplA	lipoic acid protein ligase A
LplA <sup>W37V</sup>	lipoic acid protein ligase A with W37V mutation
Lys	lysine
mAb	monoclonal antibody
MeCN	acetonitrile
MES	2-( <i>N</i> -morpholino)ethanesulfonic acid
MeTet	methyl tetrazine
mTG	microbial transglutaminase
NHS	<i>N</i> -hydroxysuccinimide
Ni-NTA	nickel-charged nitrilotriacetic acid
NMR	nuclear magnetic resonance spectroscopy
Orn	ornithine
PBS	phosphate-buffered saline
Pen/strep	penicillin/streptomycin
PFA	4 % paraformaldehyde solution
Phe	phenylalanine
POI	protein of interest
PPI	protein-protein interaction
ppm	parts per million
PtdCho	phosphatidylcholine
PtdEtn	phosphatidylethanolamine
PtdIns	phosphatidylinositol
PtdSer	phosphatidylserine
RAM	rink amide
RP-HPLC	reversed phase high-performance liquid chromatography
RT	retention time
RTK	receptor tyrosine kinase
SC	single coupling
SDS-PAGE	sodium dodecyl sulfate–polyacrylamide gel electrophoresis
Ser	serine
SM	sphingomyelin
SPAAC	strain-promoted azide-alkyne 1,3-cycloaddition
<i>t</i> bu	<i>tert</i> -butyl
TES	triethylsilane
TFA	trifluoroacetic acid
Tris	tris(hydroxymethyl)aminomethane
Trp	tryptophan
UV/Vis	ultraviolet–visible
Val	valine
CPP	cell-penetrating peptide
TCO	<i>trans</i> -cyclooctene
LAP	lipoic acid acceptor peptide
δ	chemical shift

---

## List of figures

---

<b>Figure 1:</b> Three main classes of membrane lipids with most common prototypes in mammals. Glycerophospholipid (left): Phosphatidylcholine based on Glycerol (red) esterified with palmitic acid, oleic acid, and phosphocholine. Sphingolipid (middle): Sphingomyelin based on Sphingosine (red) esterified with palmitic acid and phosphocholine. Sterol (right): Cholesterol. Hydrophobic chains marked in blue and polar head units marked in yellow. ....	2
<b>Figure 2:</b> Schematic depiction of cell membrane architectures according to homogenous phase in fluid mosaic model (A) and subcompartmentalized domains in the lipid raft model (B), adapted from <sup>[18-19]</sup> .....	3
<b>Figure 3:</b> Schematic depiction of pinocytic pathways and following endocytosis, intracellular trafficking to the early endosome, adapted from. <sup>[21]</sup> .....	4
<b>Figure 4:</b> Schematic depiction of delivery strategies applying viral and nonviral systems. ....	5
<b>Figure 5:</b> Classification of CPPs according to either origin or properties of the peptide.....	7
<b>Figure 6:</b> Schematic depiction of the postulated mechanism for direct translocation across the cell membrane of cell-penetrating peptides. Adapted from <sup>[22b]</sup> .....	8
<b>Figure 7:</b> L17E-mediated cytoplasmic delivery of biomacromolecular cargoes via transient cell membrane permeabilization upon L17E-induced actin reorganization. Uptake mechanism introduced by and depiction adapted from Futaki and coworkers. <sup>[70]</sup> .....	12
<b>Figure 8:</b> Structure of dextran polysaccharide showing linear $\alpha$ -(1-6) glycosidic bonds of the D-glucose repeating units with little branching of $\alpha$ -(1-3) linkages. ....	12
<b>Figure 9:</b> Structure of methyl-tetrazine derivative as substrate for Lp1A <sup>W37V</sup> . <sup>[102]</sup> .....	17
<b>Figure 10:</b> Chemical structure of the <i>N</i> -(2-aminoethyl) glycine pseudopeptide backbone of PNA and the attached nucleobases. <sup>[103]</sup> .....	17
<b>Figure 11:</b> Schematic depiction of aberrant splicing and mis-splicing correction upon hybridization of antisense PNA. Adapted from <sup>[107]</sup> .....	18
<b>Figure 12:</b> Schematic depiction of the multicomponent model conjugate Trastutumab-aurein1.2-doxorubicin 1. ....	20
<b>Figure 13:</b> Depiction of major constituents of conjugate 1, and their schematic abbreviations in lower right corners: (A) Trastuzumab-LLQG, modified with BCN; (B) aurein1.2 peptide, <i>N</i> -terminally modified with azide functionality and enzymatic valine-citrulline cleavage site and <i>C</i> -terminally modified with maleimide functionality; (C) enzyme cleavable peptidic linker featuring <i>N</i> -terminal cysteine for maleimide-thiol conjugation and <i>C</i> -terminally attached doxorubicin; (D) conjugation methods applied for assembly of the multicomponent conjugate. ....	21
<b>Figure 14:</b> Depiction of constituent B-NC (Ac-Orn(N <sub>3</sub> )-VC-GS-Lys(maleimide)-NH <sub>2</sub> ) 6 for assembly of a negative control lacking aurein1.2. Schematic abbreviation in the upper right corner. ....	22
<b>Figure 15:</b> Structure of constituent B: Ac-Orn(N <sub>3</sub> )-VC-aurein1.2-Lys(maleimide)-NH <sub>2</sub> 3 and constituent B-NC: Ac-Orn(N <sub>3</sub> )-VCGS-Lys(maleimide)-NH <sub>2</sub> 6. ....	23
<b>Figure 16:</b> Structure of constituent C: Ac-Cys-VC-Gly-Dox 4. ....	24
<b>Figure 17:</b> Structure of azide-aurein1.2-doxorubicin 8, conjugation product of maleimide-thiol addition of constituent B + C. ....	24
<b>Figure 18:</b> Structure of azide-doxorubicin 9, conjugation product of maleimide-thiol addition of constituent B-NC + C. ....	25
<b>Figure 19:</b> LC-MS analysis of azide-aurein1.2-doxorubicin 8 (upper) and azide-doxorubicin 9 (lower). ....	25
<b>Figure 20:</b> Structures of final multicomponent conjugates Trastuzumab-aurein1.2-doxorubicin 1 and Trastuzumab-doxorubicin 10. ....	26
<b>Figure 21:</b> Coomassie stained SDS-PAGE analysis of Trastuzumab-aurein1.2-doxorubicin 1a-d conjugation under different reaction conditions: Comparison of threefold and tenfold molar excess of azide-aurein1.2-doxorubicin 8, applying 16- or 48-hours reaction time. ....	27
<b>Figure 22:</b> HIC-chromatogram of Trastuzumab-LLQG (orange) and conjugates Trastuzumab-aurein1.2-doxorubicin 1a and 1b, synthesized applying 3 eq. (red) respectively 10 eq. (black) molar excess azide-aurein1.2-doxorubicin 8 and 16 h reaction time. ....	27

<b>Figure 23:</b> Left: Coomassie stained SDS-PAGE analysis of Trastuzumab-aurein1.2-Dox <b>1e</b> ; Trastuzumab-Dox <b>10</b> ; Trastuzumab-BCN + TAMRA-N <sub>3</sub> as positive control for preceding Trastuzumab-LLQG-BCN formation; Trastuzumab-LLQG-BCN as negative control. Right: Irradiated SDS-PAGE before staining: Doxorubicin fluorescent Trastuzumab-aurein1.2-Dox <b>1e</b> ; doxorubicin fluorescent Trastuzumab-Dox <b>10</b> ; TAMRA fluorescent Trastuzumab-BCN + TAMRA-N <sub>3</sub> positive control; Trastuzumab-LLQG-BCN negative control.....	28
<b>Figure 24:</b> (A) Schematic depiction of Trastuzumab-aurein1.2-doxorubicin <b>1e</b> and Trastuzumab-doxorubicin <b>10</b> ; (B) Effect of both conjugates on cell viability of SK-BR-3 cell line. ....	29
<b>Figure 25:</b> Schematic depiction of eGFP-L17E fusion protein <b>11</b> with L17E sequence C-terminally fused to eGFP. Protein structure adapted from. <sup>[115]</sup> .....	30
<b>Figure 26:</b> Schematic depiction of dextran modification: Introduction of conjugation sites at the repeating units (red) and at the polysaccharide reducing end (orange). ....	32
<b>Figure 27:</b> <sup>1</sup> H NMR spectrum of dextran- <i>N</i> -Boc-cadaverine <b>13</b> : Depicted correlation of adequate protons and proton signals displayed successful introduction of <i>N</i> -Boc-cadaverine via reductive amination. ....	33
<b>Figure 28:</b> <sup>1</sup> H NMR spectrum of maleimide(6.5)-dextran- <i>N</i> -Boc-cadaverine <b>18</b> : Depicted correlation of adequate protons and proton signals used for quantification of introduced maleimide functionalities per dextran on average.....	34
<b>Figure 29:</b> IR-spectrum of azide modified dextran-cadaverine <b>24</b> showing the characteristic azide band (marked in red) at a wavenumber of 2116 cm <sup>-1</sup> . ....	36
<b>Figure 30:</b> Comparison of <sup>1</sup> H NMR spectra of N <sub>3</sub> (4.8)-dextran-cadaverine <b>24</b> (lower) and the N <sub>3</sub> -dextran- <i>N</i> -Boc-cadaverine intermediate (upper). Disappearance of the Boc signal (marked in red) upon deprotection. ....	37
<b>Figure 31:</b> <sup>1</sup> H NMR spectrum of N <sub>3</sub> (4.8)-dextran-cadaverine <b>24</b> : Depicted correlation of adequate protons and proton signals used for quantification of introduced azide functionalities per dextran on average. ....	38
<b>Figure 32:</b> <sup>1</sup> H NMR spectrum of N <sub>3</sub> (4.3)-dextran-norbornene <b>29</b> : Depicted correlation of unsaturated norbornene protons and proton signals (9) as qualitative validation of norbornene introduction. ....	40
<b>Figure 33:</b> <sup>1</sup> H NMR spectrum of N <sub>3</sub> (4.8)-dextran-biotin <b>32</b> : Depicted correlation of biotin protons and proton signals (15 + 13 + 14 + 9) as qualitative validation of biotin introduction.....	41
<b>Figure 34:</b> Schematic depiction of dextran decorated with TAMRA fluorophore and multiple copies of aurein1.2 <b>36</b> respectively L17E <b>37</b> as well as dextran decorated with TAMRA-label only <b>38</b> .....	42
<b>Figure 35:</b> <sup>1</sup> H NMR spectra of TAMRA-aurein1.2(4.5)-dextran- <i>N</i> -Boc-cadaverine <b>36</b> (upper) and TAMRA-L17E(3.8)-dextran- <i>N</i> -Boc-cadaverine <b>37</b> (lower) used for quantification of number of conjugated peptides per dextran on average.....	43
<b>Figure 36:</b> Schematic depiction of dextran <b>39</b> decorated with doxorubicin as fluorescent label and multiple copies of L17E. ....	44
<b>Figure 37:</b> CLSM images (20×) of HeLa cells treated with different fluorophore-labeled peptide-dextran hybrids. TAMRA-fluorescence channel: (A) HeLa cells incubated with 25 μM TAMRA-labeled dextran <b>38</b> ; (B) HeLa cells incubated with 25 μM TAMRA-labeled dextran <b>38</b> plus coincubation with 40 μM solitary L17E <b>12</b> ; (C) HeLa cells incubated with 3.13 μM TAMRA-L17E(3.8)-dextran <b>37</b> ; (D) HeLa cells incubated with 25 μM TAMRA-aurein1.2(4.5)-dextran <b>36</b> . Doxorubicin-fluorescence channel: (E) HeLa cells incubated with 12.5 μM Dox-L17E(5.2)-dextran <b>39</b> .....	46
<b>Figure 38:</b> Schematic depiction of L17E-dextran module <b>42</b> decorated with multiple copies of L17E. ....	48
<b>Figure 39:</b> IR spectra of N <sub>3</sub> (4.8)-dextran-cadaverine <b>24</b> starting material (left) and L17E(4.8)-dextran-cadaverine <b>42</b> product (right). The azide band at a wavenumber of 2116 cm <sup>-1</sup> disappeared after CuAAC. ....	49
<b>Figure 40:</b> Calibration curve based on data shown in <b>Table 4</b> . The molar extinction coefficient of L17E-Pra <b>41</b> at 280 nm was determined to be 3542.6 L/(mol*cm).....	50
<b>Figure 41:</b> (A) Schematic depiction of L17E-dextran conjugate <b>42</b> , bearing 4.8 L17E per dextran on average, employed in cell viability assay on HeLa cell line. (B) Cell viability assay: HeLa cells treated 1 h with construct <b>42</b> and solitary L17E <b>12</b> in medium and subsequently 3 h in medium only. (C):	

Cell viability assay: HeLa cells treated 1 h with construct <b>42</b> and solitary L17E <b>12</b> in medium and subsequently 24 h in medium only. ....	51
<b>Figure 42:</b> Depiction of two possible setups applying L17E-dextran module for intracellular delivery of cargo. <b>(A)</b> Dextran decorated with multiple copies of both L17E and cargo molecules at the glucose repeating units, offering a possible conjugation site for a second cargo at the reducing end. <b>(B)</b> Dextran decorated with multiple copies of L17E at the glucose repeating units and a conjugated cargo at the reducing end. ....	52
<b>Figure 43:</b> Schematic depiction of dextran <b>43</b> decorated with multiple copies of L17E and PNA. ....	52
<b>Figure 44:</b> Maleimide-thiol conjugation of maleimide functionalized dextran with equimolar mixture of L17E-Cys <b>34</b> and thiol-PNA, yielding L17E-PNA-dextran conjugate <b>43</b> . ....	53
<b>Figure 45:</b> <b>(A)</b> Schematic depiction of L17E-PNA-dextran conjugate <b>43</b> . <b>(B)</b> Flow cytometric analysis (GFP-fluorescence on the x-axis) of HeLa-eGFP654 cells treated with thiol PNA (20 $\mu$ M) (top left) and different concentrations of <b>43</b> (top middle to bottom right). Grey histograms represent cells treated with PBS only. ....	54
<b>Figure 46:</b> Schematic depiction of L17E-dextran module <b>44</b> decorated with multiple copies of L17E and covalently conjugated eGFP at the reducing end. ....	54
<b>Figure 47:</b> Synthesis strategy for assembly of L17E-dextran module, equipped with protein cargo at the reducing end. Dextran-to-protein conjugation via iEDDA applying N <sub>3</sub> -dextran-norbornene and MeTet modified protein followed by addressing the azide groups at the glucose repeating units with L17E-Pra via CuAAC. ....	55
<b>Figure 48:</b> <b>(A)</b> Alternative synthesis strategy applying pre-assembled L17E-dextran-norbornene in dextran-to-protein conjugation via iEDDA. <b>(B)</b> Coomassie stained SDS-PAGE analysis <b>1</b> : unmodified eGFP; <b>2</b> : IMAC purified L17E-dextran-to-protein conjugation product: removal of excessive L17E-dextran-norbornene was not possible. ....	56
<b>Figure 49:</b> SDS-PAGE of <b>1</b> : eGFP; <b>2</b> : N <sub>3</sub> (4.3)-dextran-eGFP <b>49</b> ; <b>3</b> : L17E(4.3)-dextran-eGFP <b>44</b> . ....	57
<b>Figure 50:</b> Fluorescence microscopy (20 $\times$ ) images of HeLa cells treated with eGFP (8 $\mu$ M) co-incubated with 40 $\mu$ M L17E <b>12</b> ( <b>(A)</b> : brightfield image; <b>(B)</b> : eGFP fluorescence channel). ....	58
<b>Figure 51:</b> Fluorescence microscopy (20 $\times$ ) images of HeLa cells treated with L17E(4.3)-dextran-eGFP <b>44</b> (4 $\mu$ M) ( <b>(C)</b> : brightfield image; <b>(D)</b> : eGFP fluorescence channel). ....	58
<b>Figure 52:</b> Cytosolic delivery of eGFP model protein mediated by covalently conjugated L17E-dextran delivery module. HeLa cells were treated with 4 $\mu$ M L17E(4.3)-dextran-eGFP <b>44</b> and analyzed via CLSM. <b>(A)</b> : treated HeLa cells, eGFP fluorescence channel (20 $\times$ ). <b>(B)</b> : Merge of eGFP fluorescence and brightfield image (20 $\times$ ). <b>(C)</b> : treated HeLa cells, eGFP fluorescence channel (63 $\times$ ). <b>(D)</b> : Merge of eGFP fluorescence and brightfield image (63 $\times$ ). ....	59
<b>Figure 53:</b> <b>(A)</b> Structure of L17E(4.8)-dextran-eGFP <b>52</b> ; <b>(B)</b> Schematic depiction of conjugate <b>52</b> ; <b>(C)</b> Coomassie stained SDS-PAGE analysis showing unmodified eGFP ( <b>1</b> ), N <sub>3</sub> (4.8)-dextran-eGFP <b>51</b> ( <b>2</b> ) and L17E(4.3)-dextran-eGFP <b>52</b> ( <b>3</b> ). ....	60
<b>Figure 54:</b> Fluorescence microscopy (20 $\times$ ) images of HeLa cells treated with L17E(4.8)-dextran-eGFP <b>52</b> (2 $\mu$ M) at 4 $^{\circ}$ C ( <b>(A)</b> : brightfield image; <b>(B)</b> : eGFP fluorescence channel). ....	61
<b>Figure 55:</b> HIC chromatograms of eGFP (green) and eGFP-MeTet <b>54</b> (blue). ....	62
<b>Figure 56:</b> Schematic depiction of L17E-dextran module <b>57</b> decorated with multiple copies of L17E and site-specific conjugated eGFP at the reducing end. ....	63
<b>Figure 57:</b> HIC chromatograms of eGFP (green) and eGFP-MeTet <b>55</b> (black). ....	63
<b>Figure 58:</b> Fluorescence microscopy (20 $\times$ ) images of HeLa cells treated with L17E(4.8)-dextran-eGFP <b>57</b> / unmodified eGFP mixture (4 $\mu$ M) ( <b>(A)</b> : brightfield image; <b>(B)</b> : eGFP fluorescence channel). ....	67
<b>Figure 59:</b> <b>(A)</b> Schematic depiction of L17E-dextran delivery module in the setup applying multiple copies of both L17E and cargo at the glucose repeating units and a possibility for conjugation of a second cargo at the polysaccharide reducing end. <b>(B)</b> L17E-dextran delivery module decorated with multiple copies of L17E at the glucose repeating units and protein cargo covalently conjugated to the reducing end. ....	71
<b>Figure 60:</b> Schematische Darstellung zweier Möglichkeiten des Einsatzes von L17E-Dextran als Transportmodul: <b>(A)</b> Dextran, ausgestattet mit mehreren Kopien von sowohl L17E als auch zu	

transportierendem Makromolekül an den Glukose-Wiederholungseinheiten und weiterer Konjugationsmöglichkeit am reduzierenden Ende des Polysaccharids. (B) Dextran, ausgestattet mit mehreren Kopien von L17E an den Glukose-Wiederholungseinheiten und kovalent an das reduzierende Ende gebundenes Protein. ....	74
<b>Figure 61:</b> Vector map of pEGFP-E172-LAP encoding eGFP-LAP. ....	79
<b>Figure 62:</b> Schema and sequence of eGFP-L17E fusion protein with eGFP marked in green, hexa His tag marked in orange, LAP marked in red and L17E marked in blue. ....	80
<b>Figure 63:</b> Schema and sequence of eGFP variant applied in this work with eGFP marked in green, hexa His tag marked in orange, LAP marked in red and strep-tagII marked in blue. ....	81
<b>Figure 64:</b> Sequence of LplA <sup>W37V</sup> applied in this work, hexa His tag marked in orange, W37V substitution marked in red. ....	81
<b>Figure 65:</b> Structure of Ac-Orn(N <sub>3</sub> )-VC-aurein1.2-Lys(maleimide)-NH <sub>2</sub> <b>3</b> , comprising azide-modification for azide-alkyne cycloaddition, enzyme cleavage-site, aurein1.2 sequence, and maleimide-modification for thiol-maleimide conjugation. ....	85
<b>Figure 66:</b> Structure of Ac-Orn(N <sub>3</sub> )-VC-GS-Lys(maleimide)-NH <sub>2</sub> <b>3</b> , comprising azide-modification for azide-alkyne cycloaddition, enzyme cleavage-site, and maleimide-modification for thiol-maleimide conjugation, lacking aurein1.2 sequence. ....	86
<b>Figure 67:</b> Structure of thiol modified aurein1.2-Cys <b>33</b> . ....	87
<b>Figure 68:</b> Structure of L17E peptide <b>12</b> . ....	87
<b>Figure 69:</b> Structure of thiol modified L17E-Cys peptide <b>34</b> . ....	88
<b>Figure 70:</b> Structure of alkyne modified L17E-Pra peptide <b>41</b> . ....	88
<b>Figure 71:</b> Structure of CatB cleavable peptide linker Ac-Cys( <i>StBu</i> )-VC-Gly <b>7</b> . ....	89
<b>Figure 72:</b> Structure of the SPAAC product: Trastuzumab-aurein1.2-Dox conjugate <b>1a-d</b> . ....	93
<b>Figure 73:</b> Structure of the final SPAAC product: Trastuzumab-aurein1.2-Dox conjugate <b>1e</b> . ....	94
<b>Figure 74:</b> Structure of the final SPAAC product: Trastuzumab-Dox conjugate <b>10</b> . ....	94
<b>Figure 75:</b> Structure of peptide <b>5</b> for cathepsin B test cleavage. ....	95
<b>Figure 76:</b> Structure of the <i>N</i> -(5-aminopentyl)-2-azidoacetamide <b>X</b> azide linker. ....	101
<b>Figure 77:</b> Structure of TAMRA-thiol <b>35</b> . ....	106
<b>Figure 78:</b> Structure of acetylated, <i>StBu</i> protected cysteine <b>67</b> . ....	108
<b>Figure 79:</b> Structure of MeTet modified eGFP <b>69</b> . ....	115
<b>Figure 80:</b> Structure of MeTet modified eGFP <b>48</b> . ....	117
<b>Figure 81:</b> Structure of dextran-to-protein conjugate N <sub>3</sub> (4.3)-dextran-eGFP <b>49</b> . ....	117
<b>Figure 82:</b> Structure of final L17E(4.3)-dextran-eGFP conjugate <b>44</b> comprising dextran, decorated with on average 4.3 L17E at the glucose repeating units, and covalently bound eGFP at the polysaccharide reducing end. ....	118
<b>Figure 83:</b> Structure of MeTet modified eGFP <b>50</b> . ....	118
<b>Figure 84:</b> Structure of dextran-to-protein conjugate N <sub>3</sub> -(4.8)-dextran-eGFP <b>51</b> . ....	119
<b>Figure 85:</b> Structure of final L17E(4.8)-dextran-eGFP conjugate <b>52</b> comprising dextran, decorated with on average 4.8 L17E at the glucose repeating units, and covalently bound eGFP at the polysaccharide reducing end. ....	119
<b>Figure 86:</b> Structure of methyltetrazine modified eGFP <b>54, 55</b> , yielded upon site-specific introduction of methyltetrazine substrate mediated by LplA <sup>W37V</sup> . ....	120
<b>Figure 87:</b> Structure of methyltetrazine modified eGFP <b>56</b> , yielded upon site-specific introduction of methyltetrazine substrate mediated by LplA <sup>W37V</sup> . ....	121
<b>Figure 88:</b> Structure of protein-to-dextran conjugate N <sub>3</sub> (4.8)-dextran-eGFP <b>58</b> . ....	121
<b>Figure 89:</b> Structure of final L17E(4.8)-dextran-eGFP conjugate <b>57</b> comprising dextran, decorated with on average 4.8 L17E at the glucose repeating units, and covalently bound eGFP at the polysaccharide reducing end. ....	122
<b>Figure 90:</b> CLSM images (20×) of HeLa cells treated with 25 μM TAMRA-labeled dextran <b>38</b> (10 kDa). TAMRA-fluorescence channel (left), brightfield (middle) and merge (right). ....	123
<b>Figure 91:</b> CLSM images (20×) of HeLa cells treated with 25 μM TAMRA-labeled dextran <b>38</b> (10 kDa) and coincubated with solitary L17E <b>12</b> 40 μM. TAMRA-fluorescence channel (left), brightfield (middle) and merge (right). ....	123

<b>Figure 92:</b> CLSM images (20×) of HeLa cells treated with 3.13 μM construct <b>37</b> , TAMRA-labeled dextran (10 kDa) bearing 3.8 covalently conjugated L17E units per dextran on average. TAMRA-fluorescence channel (left), brightfield (middle) and merge (right).....	124
<b>Figure 93:</b> CLSM images (20×) of HeLa cells treated with 25 μM construct <b>36</b> , TAMRA-labeled dextran (10 kDa) bearing 4.5 covalently conjugated aurein1.2 units per dextran on average. TAMRA-fluorescence channel (left), brightfield (middle) and merge (right).....	124
<b>Figure 94:</b> CLSM images (20×) of HeLa cells treated with 12.5 μM construct <b>39</b> , doxorubicin-labeled dextran (10 kDa) bearing 5.2 covalently conjugated L17E units per dextran on average. Doxorubicin-fluorescence channel (left), brightfield (middle) and merge (right).....	125
<b>Figure 95:</b> CLSM images (20×) of HeLa cells treated with 4 μM L17E(4.3)-dextran-eGFP <b>44</b> . eGFP fluorescence channel (left), bright field (middle) and merge (right).....	125
<b>Figure 96:</b> CLSM images (63×) of HeLa cells treated with 4 μM L17E(4.3)-dextran-eGFP <b>44</b> . eGFP fluorescence channel (left), bright field (middle) and merge (right).....	125
<b>Figure 97:</b> Analytical RP-HPLC chromatogram of Ac-Orn(N <sub>3</sub> )-VC-aurein1.2-Lys(maleimide)-NH <sub>2</sub> <b>3</b> , 30 to 100% B (gradient 20 min), 220 nm, RT = 18.996 min. ....	126
<b>Figure 98:</b> MS (ESI) of Ac-Orn(N <sub>3</sub> )-VC-aurein1.2-Lys(maleimide)-NH <sub>2</sub> <b>3</b> , calculated: [M+H] <sup>+</sup> = 2211.60; [M+2H] <sup>2+</sup> = 1106.80; [M+3H] <sup>3+</sup> = 738.20; observed: [M+2H] <sup>2+</sup> = 1106.97; [M+3H] <sup>3+</sup> = 738.36.....	126
<b>Figure 99:</b> LC-chromatogram of Ac-Orn(N <sub>3</sub> )-VC-GS-Lys(maleimide)-NH <sub>2</sub> <b>6</b> , 10 to 100% B (gradient 13.5 min), 220 nm (black), 280 nm (red), RT = 10.25 min. ....	126
<b>Figure 100:</b> MS (ESI) of Ac-Orn(N <sub>3</sub> )-VC-GS-Lys(maleimide)-NH <sub>2</sub> <b>6</b> , calculated: [M+H] <sup>+</sup> = 893.97; [M+2H] <sup>2+</sup> = 447.49; observed: [M+H] <sup>+</sup> = 893.69; [M+2H] <sup>2+</sup> = 447.56.....	126
<b>Figure 101:</b> Analytical RP-HPLC chromatogram of Aurein1.2-Cys <b>33</b> , 20 to 100% B (gradient 20 min), 220 nm, RT = 15.824 min.....	127
<b>Figure 102:</b> MS (ESI) of Aurein1.2-Cys <b>33</b> , calculated: [M+H] <sup>+</sup> = 1583.93; [M+2H] <sup>2+</sup> = 792.47; [M+3H] <sup>3+</sup> = 528.64; observed: [M+2H] <sup>2+</sup> = 792.46; [M+3H] <sup>3+</sup> = 528.75. ....	127
<b>Figure 103:</b> Analytical RP-HPLC chromatogram of L17E <b>12</b> , 20 to 100% B (gradient 20 min), 220 nm (upper), 280 nm (lower), RT = 10.365 min. ....	127
<b>Figure 104:</b> MS (ESI) of L17E <b>12</b> , calculated: [M+H] <sup>+</sup> = 2859.47; [M+3H] <sup>3+</sup> = 954.16; [M+4H] <sup>4+</sup> = 715.87; [M+5H] <sup>5+</sup> = 572.89; observed: [M+3H] <sup>3+</sup> = 954.37; [M+4H] <sup>4+</sup> = 715.96; [M+5H] <sup>5+</sup> = 573.06.....	128
<b>Figure 105:</b> Analytical RP-HPLC chromatogram of L17E-Cys <b>34</b> , 20 to 100% B (gradient 20 min), 220 nm (upper), 280 nm (lower), RT = 10.555 min.....	128
<b>Figure 106:</b> MS (ESI) of L17E-Cys <b>34</b> , calculated: [M+H] <sup>+</sup> = 2962.61; [M+3H] <sup>3+</sup> = 988.53; [M+4H] <sup>4+</sup> = 741.65; [M+5H] <sup>5+</sup> = 593.52; [M+6H] <sup>6+</sup> = 494.76; observed: [M+3H] <sup>3+</sup> = 988.77; [M+4H] <sup>4+</sup> = 741.76; [M+5H] <sup>5+</sup> = 593.66; [M+6H] <sup>6+</sup> = 494.95.....	128
<b>Figure 107:</b> Analytical RP-HPLC chromatogram of L17E-Pra <b>41</b> , 20 to 100% B (gradient 20 min), 220 nm (upper), 280 nm (lower), RT = 11.849 min.....	129
<b>Figure 108:</b> MS (ESI) of L17E-Pra <b>41</b> , calculated: [M+H] <sup>+</sup> = 2955.57; [M+2H] <sup>2+</sup> = 1478.29; [M+3H] <sup>3+</sup> = 985.86; [M+4H] <sup>4+</sup> = 739.64; [M+5H] <sup>5+</sup> = 591.91; [M+6H] <sup>6+</sup> = 493.43; observed: [M+2H] <sup>2+</sup> = 1478.18; [M+3H] <sup>3+</sup> = 985.77; [M+4H] <sup>4+</sup> = 739.56; [M+5H] <sup>5+</sup> = 591.86; [M+6H] <sup>6+</sup> = 493.45.....	129
<b>Figure 109:</b> LC-chromatogram of Ac-Cys( <i>StBu</i> )-VC-Gly <b>7</b> , 10 to 100% B (gradient 13.5 min), 220 nm (black), 280 nm (red), RT = 11.53 min.....	129
<b>Figure 110:</b> MS (ESI) of Ac-Cys( <i>StBu</i> )-VC-Gly <b>7</b> , calculated: [M+H] <sup>+</sup> = 565.72; observed: [M+H] <sup>+</sup> = 565.38.....	130
<b>Figure 111:</b> Analytical RP-HPLC chromatogram of Ac-Cys( <i>StBu</i> )-VC-Gly-Dox <b>4-PG</b> , 00 to 100% B (gradient 20 min), 220 nm, RT = 17.869 min, (RT = 14.405: Ac-Cys( <i>StBu</i> )-VC-Gly <b>7</b> ).....	130
<b>Figure 112:</b> Analytical RP-HPLC monitoring of Ac-Cys-VC-Dox <b>4</b> synthesis, 00 to 100% B (gradient 20 min), 220 nm, RT = 16.137 min, (RT = 14.488: Ac-Cys( <i>StBu</i> )-VC-Gly <b>7</b> ; RT = 18.022: Ac-Cys( <i>StBu</i> )-VC-Gly-Dox <b>4-PG</b> ).....	130
<b>Figure 113:</b> LC-chromatogram of Ac-Cys-VC-Gly-Dox <b>4</b> , 10 to 100% B (gradient 13.5 min), 220 nm (black), 280 nm (red), RT = 12.16 min. ....	131

<b>Figure 114:</b> MS (ESI) of Ac-Cys-VC-Dox <b>4</b> , calculated: $[M+H]^+ = 1003.06$ ; $[3M+2H]^{2+} = 1504.09$ ; $[M-H]^- = 1001.06$ ; $[M-H+TFA]^- = 1115.06$ ; observed: $[M+H]^+ = 1002.77$ ; $[3M+2H]^{2+} = 1504.28$ ; $[M-H]^- = 1001.06$ ; $[M-H+TFA]^- = 1114.47$ .....	131
<b>Figure 115:</b> LC-chromatogram of azide equipped enzyme-cleavable aurein1.2-doxorubicin conjugate <b>8</b> , 10 to 100% B (gradient 13.5 min), 220 nm (black), 280 nm (red), RT = 16.16 min.....	131
<b>Figure 116:</b> MS (ESI) of azide-aurein1.2-doxorubicin conjugate <b>8</b> , calculated: $[M+H]^+ = 3214.66$ ; $[M+2H]^{2+} = 1607.83$ ; $[M+3H]^{3+} = 1072.22$ ; $[M+4H]^{4+} = 804.42$ ; $[2M+5H]^{5+} = 1286.46$ ; observed: $[M+2H]^{2+} = 1608.19$ ; $[M+3H]^{3+} = 1072.37$ ; $[M+4H]^{4+} = 804.56$ ; $[2M+5H]^{5+} = 1286.78$ .....	132
<b>Figure 117:</b> LC-chromatogram of azide-doxorubicin conjugate <b>9</b> w/o aurein1.2, 10 to 100% B (gradient 13.5 min), 220 nm (black), 280 nm (red), RT = 11.77 min. ....	132
<b>Figure 118:</b> MS (ESI) of azide-doxorubicin conjugate <b>9</b> w/o aurein1.2, calculated: $[M+H]^+ = 1896.03$ ; $[M+2H]^{2+} = 948.52$ ; $[M+3H]^{3+} = 632.67$ ; $[2M+3H]^{3+} = 1264.35$ ; $[3M+4H]^{4+} = 1422.27$ ; observed: $[M+H]^+ = 1896.30$ ; $[M+2H]^{2+} = 948.67$ ; $[M+3H]^{3+} = 632.86$ ; $[2M+3H]^{3+} = 1264.58$ ; $[3M+4H]^{4+} = 1422.58$ . ....	132
<b>Figure 119:</b> Coomassie stained SDS-PAGE analysis of Trastuzumab-aurein1.2-doxorubicin <b>1a-d</b> conjugation under different reaction conditions: Comparison of threefold and tenfold molar excess of azide-aurein1.2-doxorubicin <b>8</b> applying 16- or 48-hours reaction time. ....	133
<b>Figure 120:</b> HIC chromatogram of Trastuzumab-aurein1.2-doxorubicin <b>1a</b> conjugation product applying threefold molar excess of azide-aurein1.2-doxorubicin <b>8</b> and 16-hours reaction time; 0to100%B, 35 min, 0.9 mL/min, 220 nm. ....	133
<b>Figure 121:</b> HIC chromatogram of Trastuzumab-aurein1.2-doxorubicin <b>1b</b> conjugation product applying tenfold molar excess of azide-aurein1.2-doxorubicin <b>8</b> and 16-hours reaction time; 0to100%B, 35 min, 0.9 mL/min, 220 nm. ....	134
<b>Figure 122:</b> HIC chromatogram of Trastuzumab-LLQG; 0to100%B, 35 min, 0.9 mL/min, 220 nm. ..	134
<b>Figure 123:</b> Left: Coomassie stained SDS-PAGE analysis of Trastuzumab-aurein1.2-Dox <b>1e</b> ; Trastuzumab-Dox <b>10</b> ; Trastuzumab-BCN + TAMRA-N <sub>3</sub> as positive control for previous Trastuzumab-LLQG-BCN formation; Trastuzumab-LLQG-BCN as negative control. Right: Irradiated SDS-PAGE before staining: Doxorubicin fluorescent Trastuzumab-aurein1.2-Dox <b>1e</b> ; doxorubicin fluorescent Trastuzumab-Dox <b>10</b> ; TAMRA fluorescent Trastuzumab-BCN + TAMRA-N <sub>3</sub> positive control; Trastuzumab-LLQG-BCN negative control.....	135
<b>Figure 124:</b> Analytical RP-HPLC chromatogram of Ac-Ser-Val-Cit-Gly-Lys-OH <b>5</b> , 0 to 80% B (gradient 20 min), 220 nm, RT = 9.788 min. ....	135
<b>Figure 125:</b> MS (ESI) of Ac-Ser-Val-Cit-Gly-Lys-OH <b>5</b> , calculated: $[M+H]^+ = 589.66$ ; $[M+2H]^{2+} = 295.33$ ; observed: $[M+H]^+ = 589.49$ ; $[M+2H]^{2+} = 295.55$ .....	136
<b>Figure 126:</b> Analytical RP-HPLC chromatogram of cathepsin B mediated cleavage of test peptide <b>5</b> after 2 h incubation, 0 to 80% B (gradient 20 min), 220 nm, RT = 9.460 min (cleavage product <b>63</b> ).136	136
<b>Figure 127:</b> MS (ESI) of cathepsin B cleavage product <b>63</b> , calculated: $[M+H]^+ = 403.44$ ; observed: $[M+H]^+ = 404.46$ .....	136
<b>Figure 128:</b> <sup>1</sup> H NMR spectrum of dextran- <i>N</i> -Boc-cadaverine <b>13</b> . ....	137
<b>Figure 129:</b> <sup>1</sup> H NMR spectrum of <i>N</i> -Boc-ethylendiamine <b>65</b> . ....	137
<b>Figure 130:</b> <sup>1</sup> H NMR spectrum of 1-( <i>N</i> -Boc)- <i>N</i> -(2-aminoethyl)maleimide <b>66</b> . ....	138
<b>Figure 131:</b> <sup>1</sup> H NMR spectrum of <i>N</i> -(2-aminoethyl)maleimide <b>14</b> . ....	138
<b>Figure 132:</b> MS (ESI) of <i>N</i> -(2-aminoethyl)maleimide <b>14</b> , calculated: $[M+H]^+ = 141.14$ ; observed: $[M+H]^+ = 141.43$ . ....	139
<b>Figure 133:</b> <sup>1</sup> H NMR spectrum of maleimide(6.5)-dextran- <i>N</i> -Boc-cadaverine <b>18</b> . ....	139
<b>Figure 134:</b> <sup>1</sup> H NMR spectrum of maleimide(7.8)-dextran- <i>N</i> -Boc-cadaverine <b>19</b> . ....	140
<b>Figure 135:</b> <sup>1</sup> H NMR spectrum of maleimide(10.5)-dextran- <i>N</i> -Boc-cadaverine <b>20</b> . ....	140
<b>Figure 136:</b> Analytical RP-HPLC chromatogram of <i>N</i> -(5-aminopentyl)-2-azidoacetamide <b>21</b> , 00 to 80% B (gradient 20 min), 220 nm, RT = 3.319 min. ....	141
<b>Figure 137:</b> MS (ESI) of <i>N</i> -(5-aminopentyl)-2-azidoacetamide <b>21</b> , calculated: $[M+H]^+ = 186.23$ ; observed: $[M+H]^+ = 186.48$ . ....	141

<b>Figure 138:</b> $^1\text{H}$ NMR spectrum of unprotected $\text{N}_3(4.8)$ -dextran- <i>N</i> -Boc-cadaverine before removal of Boc protecting group.....	141
<b>Figure 139:</b> $^1\text{H}$ NMR spectrum of $\text{N}_3(4.8)$ -dextran-cadaverine <b>24</b> .....	142
<b>Figure 140:</b> IR spectrum of azide modified dextran-cadaverine <b>24</b> showing the corresponding azide band at a wavenumber of approximately $2116\text{ cm}^{-1}$ .....	142
<b>Figure 141:</b> $^1\text{H}$ NMR spectrum of $\text{N}_3(4.8)$ -dextran-cadaverine <b>25</b> .....	143
<b>Figure 142:</b> IR spectrum of azide modified dextran-cadaverine <b>25</b> showing the corresponding azide band at a wavenumber of approximately $2114\text{ cm}^{-1}$ .....	143
<b>Figure 143:</b> $^1\text{H}$ NMR spectrum of $\text{N}_3(4.3)$ -dextran-cadaverine <b>26</b> .....	144
<b>Figure 144:</b> $^1\text{H}$ NMR spectrum of $\text{N}_3(4.3)$ -dextran-norbornene <b>29</b> . ....	144
<b>Figure 145:</b> $^1\text{H}$ NMR spectrum of $\text{N}_3(4.8)$ -dextran-norbornene <b>31</b> . ....	145
<b>Figure 146:</b> $^1\text{H}$ NMR spectrum of $\text{N}_3(4.8)$ -dextran-biotin <b>32</b> . ....	145
<b>Figure 147:</b> Analytical RP-HPLC chromatogram of TAMRA-thiol <b>35</b> (both TAMRA isomers): 0 to 60% B (gradient 20 min), 220 nm (upper), 550 nm (lower), RT = 18.778 min; 19.753 min. ....	146
<b>Figure 148:</b> MS (ESI) of TAMRA-thiol <b>35</b> , calculated: $[\text{M}+\text{H}]^+ = 679.24$ ; $[\text{M}+2\text{H}]^{2+} = 340.12$ ; observed: $[\text{M}+\text{H}]^+ = 679.38$ ; $[\text{M}+2\text{H}]^{2+} = 340.46$ . ....	146
<b>Figure 149:</b> $^1\text{H}$ NMR spectrum of TAMRA-aurein1.2(4.5)-dextran- <i>N</i> -Boc-cadaverine <b>36</b> . ....	147
<b>Figure 150:</b> $^1\text{H}$ NMR spectrum of TAMRA-L17E(3.8)-dextran- <i>N</i> -Boc-cadaverine <b>37</b> . ....	147
<b>Figure 151:</b> Analytical RP-HPLC chromatogram of Ac-Cys( <i>StBu</i> )-OH <b>67</b> , 10 to 100% B (gradient 20 min), 220 nm, RT = 11.503 min. ....	148
<b>Figure 152:</b> MS (ESI) of of Ac-Cys( <i>StBu</i> )-OH <b>67</b> , calculated: $[\text{M}-\text{H}]^- = 250.36$ ; observed: $[\text{M}-\text{H}]^- = 250.24$ .....	148
<b>Figure 153:</b> LC-chromatogram of Ac-Cys-Dox <b>40</b> , 10 to 100% B (gradient 13.5 min), 220 nm (black), 280 nm (red), RT = 11.31 min. ....	148
<b>Figure 154:</b> MS (ESI) of of Ac-Cys-Dox <b>40</b> , calculated: $[\text{M}-\text{H}]^- = 687.70$ ; observed: $[\text{M}-\text{H}]^- = 687.08$ . ....	148
<b>Figure 155:</b> $^1\text{H}$ NMR spectrum of doxorubicin-L17E(5.2)-dextran- <i>N</i> -Boc-cadaverine <b>39</b> .....	149
<b>Figure 156:</b> $^1\text{H}$ NMR spectrum of TAMRA-dextran- <i>N</i> -Boc-cadaverine <b>38</b> . ....	149
<b>Figure 157:</b> IR spectrum of L17E(4.8)-dextran-cadaverine <b>42</b> . The azide band of the starting material at a wavenumber of $2116\text{ cm}^{-1}$ ( <b>Figure 140</b> ) disappeared after CuAAC.....	150
<b>Figure 158:</b> SEC chromatogram of L17E(4.8)-dextran-cadaverine <b>42</b> , 40% B (isocratic flow, 30 min, 0.6 mL/min.), 220 nm, RT = 9.800 min. ....	150
<b>Figure 159:</b> $^1\text{H}$ NMR spectrum of L17E(4.3)-dextran-norbornene <b>45</b> . ....	151
<b>Figure 160:</b> IR spectrum of L17E(4.3)dextran-norbornene <b>45</b> . Azide band no longer observable after CuAAC.....	151
<b>Figure 161:</b> $^1\text{H}$ NMR spectrum of L17E(4.8)-dextran-biotin <b>60</b> . ....	152
<b>Figure 162:</b> Coomassie stained SDS-PAGE analysis: <b>(1)</b> unmodified eGFP; <b>(2)</b> L17E(4.3)-dextran-eGFP <b>46</b> following ineffective IMAC purification.....	152
<b>Figure 163:</b> Coomassie stained SDS-PAGE of <b>(1)</b> unmodified eGFP, <b>(2)</b> $\text{N}_3(4.3)$ -dextran-eGFP <b>49</b> and <b>(3)</b> final L17E(4.3)-dextran-eGFP <b>44</b> . ....	153
<b>Figure 164:</b> Coomassie stained SDS-PAGE of <b>(1)</b> unmodified eGFP, <b>(2)</b> $\text{N}_3(4.8)$ -dextran-eGFP <b>51</b> and <b>(3)</b> final L17E(4.8)-dextran-eGFP <b>52</b> .....	153
<b>Figure 165:</b> HIC chromatogram of unmodified eGFP; 0to100%B, 35 min, 0.9 mL/min, 220 nm. ....	154
<b>Figure 166:</b> HIC chromatogram of eGFP-MeTet <b>54</b> conjugation product applying reference LpIA <sup>W37V</sup> ;0to100%B, 35 min, 0.9 mL/min, 220 nm. ....	154
<b>Figure 167:</b> HIC chromatogram of eGFP-MeTet <b>55</b> conjugation product applying LpIA <sup>W37V</sup> (batch 1); 0to100%B, 35 min, 0.9 mL/min, 220 nm. ....	155
<b>Figure 168:</b> Coomassie stained SDS-PAGE analysis of elution fraction of IMAC purified eGFP-L17E <b>11</b> . ....	155
<b>Figure 169:</b> Coomassie stained SDS-PAGE analysis of elution fraction of <b>(A)</b> IMAC purified LpIA <sup>W37V</sup> (batch 1) first attempt and <b>(B)</b> IMAC purified LpIA <sup>W37V</sup> (batch 2) second attempt. ....	156

---

## List of schemes

---

<b>Scheme 1:</b> Different strategies for chemical modification of hydroxy groups of glucose repeating units: (A) periodate oxidation and subsequent addressing of the dialdehyde with amine functionality; (B) cyanogen bromide activated amine conjugation; (C) glucose C2-hydroxy selective carboxyethylation followed by amide bond formation with amine-functionalities. <sup>[61, 71, 75b, 76]</sup> .....	13
<b>Scheme 2:</b> Modification of the polysaccharide reducing end via reductive amination: Schiff base formation followed by reduction into the stable amine. <sup>[77]</sup> .....	14
<b>Scheme 3:</b> General reaction scheme of (A) Cu(I)-catalyzed (CuAAC) <sup>[81]</sup> and (C) strain-promoted (SPAAC) <sup>[83]</sup> azide-alkyne cycloaddition. SPAAC shows cycloaddition applying BCN derivative; (B) Cu(I)-binding ligand BTAA. <sup>[82]</sup> .....	14
<b>Scheme 4:</b> General reaction scheme of maleimide-thiol conjugation <sup>[86]</sup> and inverse electron-demand Diels-Alder reaction. <sup>[88]</sup> .....	15
<b>Scheme 5:</b> mTG mediated bond formation between glutamine side chain, acting as acyl donor and $\epsilon$ -amine of lysine, acting as acyl acceptor. ....	16
<b>Scheme 6:</b> LplA-mediated amide bond formation between lipoic acid and $\epsilon$ -amine of lysine in the LAP recognition motif. ....	17
<b>Scheme 7:</b> mTG mediated synthesis of constituent A: Trastuzumab-LLQG-BCN <b>2</b> . ....	22
<b>Scheme 8:</b> Synthesis of dextran- <i>N</i> -Boc-cadaverine <b>13</b> via reductive amination. ....	32
<b>Scheme 9:</b> General synthesis of maleimide-dextran- <i>N</i> -Boc-cadaverine: Dextran- <i>N</i> -Boc-cadaverine <b>13</b> modification via carboxyethylation followed by EEDQ activated conjugation of <i>N</i> -(2-aminoethyl)maleimide <b>14</b> . ....	33
<b>Scheme 10:</b> General synthesis of $N_3$ -dextran-cadaverine: Dextran- <i>N</i> -Boc-cadaverine <b>13</b> modification via carboxyethylation followed by EEDQ activated conjugation of <i>N</i> -(5-aminopentyl)-2-azido-acetamid <b>21</b> and final removal of the Boc protecting group. ....	36
<b>Scheme 11:</b> General synthesis of $N_3$ -dextran derivatives bearing red-end functionalization: Amide-bond formation of $N_3$ -dextran-cadaverine with NHS-activated norbornene <b>27</b> or biotin <b>28</b> derivative. ....	39
<b>Scheme 12:</b> Synthesis of dextran compounds, decorated with TAMRA fluorophore and multiple copies of aurein1.2 <b>36</b> respectively L17E <b>37</b> via maleimide-thiol conjugation. ....	43
<b>Scheme 13:</b> Synthesis of L17E-decorated dextran <b>39</b> equipped with doxorubicin as fluorescent label. ....	44
<b>Scheme 14:</b> Cu(I)-catalyzed azide-alkyne cycloaddition, yielding L17E(4.8)-dextran-cadaverine <b>42</b> . ....	48
<b>Scheme 15:</b> iEDDA dextran-to-protein conjugation of red-end functionalized $N_3$ (4.3)-dextran-norbornene <b>29</b> and methyltetrazine modified eGFP <b>48</b> yielding dextran-to-protein conjugate $N_3$ (4.3)-dextran-eGFP <b>49</b> . ....	56
<b>Scheme 16:</b> Addressing the azide functionalities of $N_3$ (4.3)-dextran-eGFP <b>49</b> with L17E-Pra <b>41</b> in biocompatibilized Cu(I)-catalyzed azide-alkyne cycloaddition, yielding L17E(4.3)-dextran-eGFP <b>44</b> . ....	57
<b>Scheme 17:</b> LplA <sup>W37V</sup> mediated amide bond formation between lysine $\epsilon$ -amine of the LAP-tagged eGFP and a methyltetrazine substrate derivative derived of lipoic acid, yielding eGFP-MeTet <b>54</b> .....	62
<b>Scheme 18:</b> LplA <sup>W37V</sup> (batch 1) mediated amide bond formation between lysine $\epsilon$ -amine of the LAP-tagged eGFP and a methyltetrazine substrate derivative derived of lipoic acid, yielding eGFP-MeTet <b>55</b> . ....	63
<b>Scheme 19:</b> LplA <sup>W37V</sup> (batch 2) mediated amide bond formation between lysine $\epsilon$ -amine of the LAP-tagged eGFP and a methyltetrazine substrate derivative derived of lipoic acid, yielding eGFP-MeTet <b>56</b> . ....	64
<b>Scheme 20:</b> iEDDA dextran-to-protein conjugation of red-end functionalized $N_3$ (4.8)-dextran-norbornene <b>31</b> and eGFP-MeTet <b>56</b> , yielding conjugate $N_3$ (4.8)-dextran-eGFP <b>58</b> . ....	65
<b>Scheme 21:</b> Addressing $N_3$ (4.8)-dextran-eGFP <b>58</b> with L17E-Pra <b>41</b> in Cu(I)-catalyzed azide-alkyne cycloaddition, yielding L17E(4.8)-dextran-eGFP <b>57</b> . ....	66
<b>Scheme 22:</b> C-terminal NHS-activation of Ac-Cys( <i>St</i> Bu)-VC-Gly <b>7</b> and subsequent amide bond formation with doxorubicin. ....	89

<b>Scheme 23:</b> Removal of cysteine protecting group for generation of accessible thiol moiety in Ac-Cys-VC-Gly-Dox <b>4</b> . .....	90
<b>Scheme 24:</b> Maleimide-thiol conjugation of Ac-Orn(N <sub>3</sub> )-VC-aurein1.2-Lys(maleimide)-NH <sub>2</sub> <b>3</b> and Ac-Cys-VC-Gly-Dox <b>4</b> yielded azide-aurein1.2-doxorubicin <b>8</b> . .....	91
<b>Scheme 25:</b> Maleimide-thiol conjugation of Ac-Orn(N <sub>3</sub> )-VC-GS-Lys(maleimide)-NH <sub>2</sub> <b>6</b> and Ac-Cys-VC-Gly-Dox <b>4</b> yielded azide-doxorubicin <b>9</b> . .....	92
<b>Scheme 26:</b> mTG mediated BCN-modification of Trastuzumab-LLQG. ....	93
<b>Scheme 27:</b> Cathepsin B mediated cleavage of test peptide <b>5</b> . .....	95
<b>Scheme 28:</b> Synthesis of dextran- <i>N</i> -Boc-cadaverine <b>13</b> via reductive amination. ....	96
<b>Scheme 29:</b> General synthesis of 2-CE-dextran- <i>N</i> -Boc-cadaverine via carboxyethylation. ....	97
<b>Scheme 30:</b> General synthesis of maleimide-dextran- <i>N</i> -Boc-cadaverine via EEDQ activated conjugation of maleimide and amine bifunctionalized linker. Stated equivalents refer to 2-CE groups per dextran. ....	97
<b>Scheme 31:</b> General synthesis of N <sub>3</sub> -dextran- <i>N</i> -Boc-cadaverine via EEDQ activated conjugation of azide and amine bifunctionalized linker. Stated equivalents refer to 2-CE groups per dextran. ....	98
<b>Scheme 32:</b> Acidic removal of the Boc protecting group, resulting in accessible amine at the polysaccharide reducing end. ....	98
<b>Scheme 33:</b> Synthesis of maleimide and amine bifunctionalized linker <i>N</i> -(2-aminoethyl)maleimide <b>14</b> . ....	99
<b>Scheme 34:</b> Synthesis of maleimide(6.5)-dextran- <i>N</i> -Boc-cadaverine <b>18</b> : Dextran- <i>N</i> -Boc-cadaverine <b>13</b> modification via carboxyethylation followed by EEDQ activated conjugation of <i>N</i> -(2-aminoethyl)maleimide <b>14</b> . ....	100
<b>Scheme 35:</b> Synthesis of maleimide(7.8)-dextran- <i>N</i> -Boc-cadaverine <b>19</b> : Dextran- <i>N</i> -Boc-cadaverine <b>13</b> modification via carboxyethylation followed by EEDQ activated conjugation of <i>N</i> -(2-aminoethyl)maleimide <b>14</b> . ....	100
<b>Scheme 36:</b> Synthesis of maleimide(10.5)-dextran- <i>N</i> -Boc-cadaverine <b>20</b> : Dextran- <i>N</i> -Boc-cadaverine <b>13</b> modification via carboxyethylation followed by EEDQ activated conjugation of <i>N</i> -(2-aminoethyl)maleimide <b>14</b> . ....	101
<b>Scheme 37:</b> Synthesis of N <sub>3</sub> (4.8)-dextran-cadaverine <b>24</b> : Dextran- <i>N</i> -Boc-cadaverine <b>13</b> modification via carboxyethylation followed by EEDQ activated conjugation of <i>N</i> -(5-aminopentyl)-2-azidoacetamide <b>21</b> and final removal of the Boc protecting group. ....	102
<b>Scheme 38:</b> Synthesis of N <sub>3</sub> (4.8)-dextran-cadaverine <b>25</b> : Dextran- <i>N</i> -Boc-cadaverine <b>13</b> modification via carboxyethylation followed by EEDQ activated conjugation of <i>N</i> -(5-aminopentyl)-2-azidoacetamide <b>21</b> and final removal of the Boc protecting group. ....	102
<b>Scheme 39:</b> Synthesis of N <sub>3</sub> (4.3)-dextran-cadaverine <b>26</b> : Dextran- <i>N</i> -Boc-cadaverine <b>13</b> modification via carboxyethylation followed by EEDQ activated conjugation of <i>N</i> -(5-aminopentyl)-2-azidoacetamide <b>21</b> and final removal of the Boc protecting group. ....	103
<b>Scheme 40:</b> Synthesis of N <sub>3</sub> -dextran-norbornene derivative <b>29</b> and <b>30</b> bearing 4.3 azide groups per dextran and a norbornene functionality at the polysaccharide reducing end. ....	104
<b>Scheme 41:</b> Synthesis of N <sub>3</sub> -dextran-norbornene derivative <b>31</b> bearing 4.8 azide groups per dextran and a norbornene functionality at the polysaccharide reducing end. ....	104
<b>Scheme 42:</b> Synthesis of N <sub>3</sub> -dextran-biotin derivative <b>32</b> bearing 4.8 azide groups per dextran and a biotin functionality at the polysaccharide reducing end. ....	105
<b>Scheme 43:</b> Thiol-maleimide addition of maleimide(6.5)-dextran- <i>N</i> -Boc-cadaverine <b>18</b> with aurein1.2-Cys <b>33</b> and TAMRA-thiol <b>35</b> . Stated equivalents related to maleimide groups per dextran. ....	106
<b>Scheme 44:</b> Thiol-maleimide addition of maleimide(6.5)-dextran- <i>N</i> -Boc-cadaverine <b>18</b> with L17E-Cys <b>34</b> and TAMRA-thiol <b>35</b> . Stated equivalents related to maleimide groups per dextran. ....	107
<b>Scheme 45:</b> Synthesis of thiol-modified doxorubicin <b>40</b> . ....	108
<b>Scheme 46:</b> Thiol-maleimide addition of maleimide(6.5)-dextran- <i>N</i> -Boc-cadaverine <b>18</b> with L17E-Cys <b>34</b> and Dox-thiol <b>40</b> . Stated equivalents related to maleimide groups per dextran. ....	109
<b>Scheme 47:</b> Thiol-maleimide addition of maleimide(7.8)-dextran- <i>N</i> -Boc-cadaverine <b>19</b> with 1 eq. TAMRA-thiol <b>35</b> for generation of TAMRA labeled dextran <b>38</b> . ....	109

---

<b>Scheme 48:</b> Thiol-maleimide addition of maleimide(10.5)-dextran- <i>N</i> -Boc-cadaverine <b>20</b> with thiol-PNA and L17E-Cys <b>34</b> . Stated equivalents related to maleimide groups per dextran. ....	110
<b>Scheme 49:</b> Addressing N <sub>3</sub> (4.8)-dextran-cadaverine <b>24</b> with L17E-Pra <b>41</b> in Cu(I)-catalyzed azide-alkyne-cycloaddition. Stated equivalents related to azide groups per dextran. ....	111
<b>Scheme 50:</b> Addressing N <sub>3</sub> (4.3)-dextran-norbornene <b>30</b> with L17E-Pra <b>41</b> in Cu(I)-catalyzed azide-alkyne-cycloaddition. Stated equivalents related to azide groups per dextran. ....	111
<b>Scheme 51:</b> Addressing N <sub>3</sub> (4.8)-dextran-biotin <b>32</b> with L17E-Pra <b>41</b> in Cu(I)-catalyzed azide-alkyne-cycloaddition. Stated equivalents relating to azide groups per dextran. ....	112
<b>Scheme 52:</b> eGFP functionalization with methyltetrazine via NHS-activated methyltetrazine derivative <b>47</b> . ....	113
<b>Scheme 53:</b> LplA <sup>W37V</sup> mediated amide bond formation between lysine ε-amine of the LAP-tagged eGFP and a methyl tetrazine substrate derivative derived of lipoic acid. ....	113
<b>Scheme 54:</b> iEDDA dextran-to-protein conjugation of norbornene functionalized N <sub>3</sub> -dextran with MeTet modified cargo protein. ....	114
<b>Scheme 55:</b> Addressing N <sub>3</sub> -dextran-protein with L17E-Pra <b>41</b> in biocompatible Cu(I)-catalyzed azide-alkyne-cycloaddition. Stated equivalents related to number of azide groups per dextran. ....	115
<b>Scheme 56:</b> Alternative iEDDA dextran-to-protein conjugation applying pre-assembled L17E(4.3)-dextran-norbornene <b>45</b> and eGFP-MeTet <b>69</b> . ....	116

---

---

## List of tables

---

<b>Table 1:</b> Overview of maleimide-dextran- <i>N</i> -Boc-cadaverine compounds synthesized in the present work. R <sub>1</sub> = -(CH <sub>2</sub> ) <sub>5</sub> -NH-Boc; R <sub>2</sub> = -(CH <sub>2</sub> ) <sub>2</sub> -CO-NH-.....	35
<b>Table 2:</b> Overview of N <sub>3</sub> -dextran-cadaverine compounds synthesized in the present work. R <sub>3</sub> = -(CH <sub>2</sub> ) <sub>2</sub> -CONH-(CH <sub>2</sub> ) <sub>5</sub> ; R <sub>4</sub> = -(CH <sub>2</sub> ) <sub>5</sub> -.....	39
<b>Table 3:</b> Overview of N <sub>3</sub> -dextran-norbornene/biotin compounds synthesized in the present work. R <sub>3</sub> = -(CH <sub>2</sub> ) <sub>2</sub> -CONH-(CH <sub>2</sub> ) <sub>5</sub> ; R <sub>4</sub> = -(CH <sub>2</sub> ) <sub>5</sub> -.....	41
<b>Table 4:</b> Absorption measurement at 280 nm of serial dilutions of three different samples of L17E-Pra 41 for generation of a calibration curve and subsequent determination of the molar extinction coefficient. ....	49
<b>Table 5:</b> Overview of dextran-based compounds generated in the present work as modules for cytosolic or even nuclear delivery of different kinds of cargoes. In addition to the schematic structures, the abilities of the respective compounds to mediate cytosolic and nuclear uptake are given (+++ effective uptake; ++ medium uptake; + slight uptake; – no uptake). *Compounds differ in dextran-to-protein conjugation: Compound 52 based und unspecific and compound 57 based on site-specific LplA <sup>W37V</sup> -mediated dextran-to-protein conjugation.....	68
<b>Table 6:</b> Composition of applied buffers and solutions. ....	75
<b>Table 7:</b> Composition of separation and stacking gel solutions for preparation of polyacrylamide gels applied in SDS-PAGE.....	78
<b>Table 8:</b> Primer used for production of L17E-fusion genes. ....	79
<b>Table 9:</b> Components and final concentrations for LplA <sup>W37V</sup> -catalyzed ligation. ....	83
<b>Table 10:</b> Final concentrations for mTG mediated BCN-modification of Trastuzumab-LLQG. ....	93
<b>Table 11:</b> Components and concentrations for LplA <sup>W37V</sup> -mediated ligation. ....	120
<b>Table 12:</b> Components and concentrations for LplA <sup>W37V</sup> -mediated ligation. ....	121

---

## Danksagung

---

Meinen besonderen Dank möchte ich zuallererst meinem Doktorvater, Herrn **Prof. Dr. Harald Kolmar**, aussprechen. Ich möchte mich für die Aufnahme in die Arbeitsgruppe, die Möglichkeit meine Dissertation unter seiner Leitung anzufertigen, für das entgegengebrachte Vertrauen und natürlich seine wissenschaftliche Expertise sehr herzlich bedanken. Bei ihm als Chef möchte ich mich dafür bedanken, dass wir gemeinsam die ein oder anderen nennenswerten Resultate erzielen konnten und er mich unermüdlich motivierte, sowie bei ihm als Mensch dafür, dass wir uns trotz gelegentlicher (wissenschaftlicher) Diskussionen und Widerworte auch auf persönlicher Ebene immer sehr gut verstanden haben. Vielen Dank!

Bei Frau **Prof. Dr. Katja Schmitz** möchte ich mich für die Übernahme des Korreferats bedanken und bei Herrn **PD Dr. Tobias Meckel** sowie Herrn **Prof. Dr. Markus Biesalski** für ihr Engagement als Fachprüfer. Außerdem möchte ich mich bei Dr. Tobias Meckel für die große Hilfe beim Mikroskopieren und die unterhaltsamen Gespräche währenddessen bedanken!

Frau **Dr. Olga Avrutina** danke ich dafür, dass sie sich jederzeit Zeit für mich genommen hat und ich sehr viel durch ihre chemische Expertise, vor allem in der Peptidchemie, lernen konnte. Außerdem ein herzliches Danke dafür, dass sie sich unermüdlich darum bemühte und es schließlich schaffte mir das wissenschaftliche Schreiben auf Englisch erfolgreich beizubringen! Bei Herrn **Dr. Andreas Christmann** bedanke ich mich sehr herzlich dafür, dass ich jederzeit mit biologischen Fragen zu ihm kommen konnte und natürlich für viele Pausengespräche über Fahrräder, Kaffee oder allerhand andere spannende Themen. Vielen Dank auch an **Dr. Sascha Knauer**, sowohl für die Betreuung der Masterarbeit als auch dafür, dass man auch später immer mit Fragen zu chemischen Synthesen, HPLC oder LC-MS zu ihm kommen und viel von ihm lernen konnte.

Bei zwei meiner Chemikerkollegen möchte ich mich ganz besonders bedanken. Hendrik Schneider, mittlerweile **Dr. Hendrik Schneider**, für die gesamte gemeinsame Zeit, die bereits im ersten Semester des Bachelorstudiums begonnen hat. Viele Praktika haben wir gemeinsam absolviert, beide unsere Masterarbeiten im AK Kolmar angefertigt und dort schließlich auch unsere Doktorandenzeit gemeinsam verbracht. Dabei haben wir beide immer voneinander profitiert und, viel wichtiger als das, stets viel Spaß und eine wirklich gute Zeit zusammen gehabt! **Simon Englert** hat uns schließlich seit der Masterandenzeit verstärkt und während der gesamten Doktorarbeit haben wir drei super zusammengearbeitet, uns jederzeit gegenseitig geholfen und viel Spaß miteinander gehabt. Simon möchte ich besonders dafür danken, dass wir zwei schließlich unsere zusammen erarbeiteten Ergebnisse im gemeinsamen Paper veröffentlichen konnten! Dabei natürlich auch danke an Hendrik, ohne ihn wären unsere Ergebnisse so nicht möglich gewesen.

Vielen Dank an Thomas, Dessy und Arturo für die Hilfe in der Zellkultur, aber auch an alle anderen Mitglieder der Arbeitsgruppe Kolmar. Selbstverständlich darf die Kicker-Gruppe mit Hendrik, Sebastian, Lukas, Thomas, Ata, Arturo und Jan nicht unerwähnt bleiben und auch Julius nicht, der unermüdlich für ausgezeichnete musikalische Untermalung der Laborzeit sorgte.

Der größte Dank geht allerdings an meine Familie, die mich zu demjenigen gemacht hat, der ich bin und mich während des gesamten Studiums, der Doktorarbeit und bei den wirklich wichtigen Dingen des Lebens immer in großartiger Weise unterstützt hat.

Darmstadt,

**Erklärung**

Ich erkläre hiermit, dass ich meine Dissertation selbstständig und nur mit den angegebenen Hilfsmitteln angefertigt habe.

---

Bastian Becker, M.Sc.

---

Darmstadt,

**Erklärung**

Ich erkläre hiermit, noch keinen Promotionsversuch unternommen zu haben.

---

Bastian Becker, M.Sc.

---

Darmstadt,

**Erklärung**

Ich erkläre hiermit, dass die elektronische Version der Doktorarbeit mit der schriftlichen Version übereinstimmt. Die elektronische Version liegt dem Prüfungssekretariat vor.

---

Bastian Becker, M.Sc.